Multidimensional medical image analysis with automatic segmentation techniques

Dinesh Pandey

Submitted in total fulfilment of the requirements of the degree of

Doctor of Philosophy

August 2019

Institute for Sustainability and Innovation (ISI)
VICTORIA UNIVERSITY

Abstract

The advancement of medical imaging techniques such as fundus photography and breast magnetic resonance imaging (MRI) has shown tremendous improvement in the quality of multidimensional image produced. The image segmentation technology is used to partition the medical image into different regions for accurate identification and segregation of diseased area. Hence, the medical image is a vital entity to diagnose several pathological conditions. However, Multidimensional medical image analysis with automatic segmentation techniques these medical images have problems such as:

1. lack inherent spatial resolution;
2. contains different form of noise;
3. have boundary with the similar color intensity; and
4. populated with non-uniform illumination across the image and other imaging ambiguities.

In many clinical studies, the segmentation process can be carried out either manually or automatically. Manual segmentation for the identification of several landmarks in medical images has been popularly considered, but is time consuming, tedious, error prone and observer-dependent. On the other hand, automatic segmentation technique are highly desirable because of its robustness, improved efficiency, reliability and faster computation. Therefore, the development of an automatic segmentation technique for the medical images has become an integral part of the medical diagnosis system that yields a practical insight. However, achieving a desirable result from automatic segmentation is still challenging. This is because; variation is seen in image features for different cases, even when produced with same imaging technique. The broad aim of this thesis is to identify the robust and automatic segmentation technique overcoming the issues seen in medical images and hence can assist doctors for the evaluation and detection of several pathologies.

The objective is fulfilled by developing automatic segmentation algorithms and provide solutions to tackle challenges associated in two different imaging modalities: fundus photography (2D) and breast MRI (3D). The result is a series of work associated with the problem identification, analysis and a desirable solution with qualitative and quan-

titative validation. Specifically, we have strengthened the state-of-the-art by making the following novel contributions:

1. The analysis of retinal blood vessel is crucial for finding several pathological disorder that manifest through human eye. Therefore, blood vessel segmentation in fundus photography has great importance in medical image analysis. From the experiment, we observed that the retinal images with lesions, exudate's, non-uniformed illuminations and pathological artefacts have intrinsic problems such as the absence of thin vessels and detection of false vessels. In our work, we developed an automatic blood vessel segmentation framework, which is effective in analysing retinal blood vessels on noisy, pathological and abnormal retinal images. Initially, the noise is minimized with image subtraction technique using morphological operation. Then, we investigated thin and thick blood vessels separately. Thin vessels are detected using local phase-preserving denoising, line detection, local normalization, and maximum entropy thresholding. Local phase-preservation denoising removes the additional noise while preserving phase information (detailed) of the image. Thick vessels are segmented using maximum entropy thresholding. The performance of the proposed methods is carried in four popular databases (DRIVE, STARE, CHASE_ DB1, HRF). The result shows that the proposed segmentation method is automatic, accurate and computationally efficient. Furthermore, the proposed methods is found to be superior when compared with the other methods in the state of art.

2. The automatic optic disc (OD) segmentation is a challenging task for the images, which are under the influence of noise, uneven illumination and pathologies. As per the state-of-art, development of OD segmentation is still a challenging task because of several reasons such as 1) Ophthalmic pathologies causes the change of color, shape or depth of OD 2) Retinal pathologies (exudate, lesion), sometimes possess similar properties causing a false identification of OD. 3) Different factors like illuminations and contrast irregularities, boundary artefacts and blurred image edges makes segmentation complicated and requires pixel to pixel analysis. 4) Also the texture feature of OD vary for different images, adding more challenges, thus requiring a pre-processing step prior to the segmentation. 5) If the vessels are dense and around OD, the identification the OD boundary becomes difficult. To solve the above-mentioned challenges, a new method for the accurate localization and detection of the optic disc is developed. The process utilizes kmeans clustering over foreground and background estimated images to obtain the brightest cluster. The obtained results are merged together to estimate the OD center. The OD boundary is then estimated using circular Hough transform (CHT) using the radius and center obtained in the initial step. The boundary estimation is also obtained from superpixels method. Finally, the OD boundary pixels are identified with the geometrical model over the edge information obtained from superpixels and CHT. The experiments carried out on seven publicly available database verify the efficiency

of proposed methods. In addition, the outstanding results while compared with the other proposed methods in the current state of art proves the superiority of proposed methods.

3. A novel and accurate segmentation method of the breast region of interest (BROI) and breast density (BD) in breast MRI is proposed. The precise segmentation of BROI and BD is challenging, especially in noisy magnetic resonance images (MRI) due to similar intensity levels and the closely connected boundaries between BROI and other anatomical structure such as heart, lung and pectoral muscle. The segmentation of BROI is carried out in three major steps. Initially, we utilize adaptive wiener filtering and k-means clustering to denoised image by preserving edges and unwanted artefacts. Then, active contour based level sets is used to eliminate the heart area from the denoised image. Initial contour points for the active contour methods are determined by the maximum entropy thresholding and convolution method. Finally, a pectoral muscle is removed to obtain a BROI segmentation by using a morphological operations and local adaptive thresholding methods. The segmentation of BD is obtained with 4 level fuzzy c-means (FCM) thresholding methods on the result image obtained from BROI segmentation. The validation of proposed methods is performed using the 1350 breast images from 15 female subjects. The obtained result show that the proposed method is automatic, fast and efficient.

4. The segmentation of breast lesions in breast MRI is considered as a important and challenging task in medical image analysis. Noise, intensity similarity of lesions and other tissues, and variable shape and size of lesion are the primary challenges during the process of lesion segmentation. Hence, the framework for the accurate segmentation of breast lesion from the DCE MRI image is proposed. The framework is built using max flow and min cut problems in the continuous domain over the denoised image. The proposed method is achieved in three steps. Firstly, in the pre-processing step, the post contrast and pre-contrast image are subtracted. This is followed by image registration that benefits by enhancing the tumor area. Secondly, a phase preservation denoising and pixel-wise adaptive Wiener filtering technique are used which is followed by max flow and min cut problems in the continuous domain. A denoising mechanism clears the noise in the image by preserving the useful and detailed features such as edges. Then, a tumor detection is done using continuous max flow. Finally, morphological operation is used as a post-processing step to further delineate the obtained results. The efficiency of the proposed method is verified with the series of qualitative and quantitative experiments carried out on 21 cases with two different MR image resolution. The obtained results when compared with the manually segmented results demonstrates the quality of segmentation obtained from the proposed method.

The segmentation experiments for all above-mentioned four proposed algorithms are performed on Matlab R2013b running under Intel(R) core(TM) i5-4570s CPU@ 2.90 Ghz

with 8GB of RAM. In an effort to test the performance of the proposed algorithms, both the public and private datasets with the manually drawn ground truth image are used. Moreover, the qualitative and quantitative measurements were used as a way to verify the robustness of the proposed algorithms. Also, the result were compared with the recent state-of-art which demonstrate the enhanced performance and advancement of the proposed methods. Finally, our overall results on the proposed methods show that the proposed algorithms are automatic, accurate and computationally efficient.

Declaration

I, Dinesh Pandey, declare that the PhD thesis entitled "Multidimensional medical image analysis with automatic segmentation techniques" is no more than 100,000 words in length including quotes and exclusive of tables, figures, appendices, bibliography, references and footnotes. This thesis contains no material that has been submitted previously, in whole or in part, for the award of any other academic degree or diploma. Except where otherwise indicated, this thesis is my own work

Dinesh Pandey, 27th October 2019

Preface

This thesis research has been carried out in the Institute for Sustainability and Innovation (ISI), Victoria University. The main contributions of the thesis are discussed in Chapters 3-6 and are based on the following publications:

- **D. Pandey**, X. Yin, H. Wang, and Y. Zhang, "Accurate vessel segmentation using maximum entropy incorporating line detection and phase-preserving denoising" *Computer Vision and Image Understanding*, Volume 155, Pages: 162-172, 2017. **(Q1 Journal)**

- **D. Pandey**, H. Wang, M. Su, J. Chen, J. Wu and Y. Zhang, "Automatic and fast segmentation of breast region-of-interest (ROI) and density in MRIs," *Heliyon*, Volume 4, Pages: e01042, 2018, doi: 10.1016/j.heliyon.2018 **(Q1 Journal)**

- **D. Pandey**, X. Yin, H. Wang, and Y. Zhang, "Automated optic disc localization and segmentation based on superpixel method incorporating clustering and Hough transform using retinal fundus images" *Artificial Intelligence in Medicine*,2019.(Under Review) **(Q1 Journal)**

- **D. Pandey**, X. Yin, H. Wang, and Y. Zhang, "Automatic breast tumor segmentation in denoised MRIs using continuous max-flow algorithm" *IEEE access*,2019.(Submitted) **(Q1 Journal)**

Acknowledgements

Foremost, I would like to express my sincere gratitude to my Supervisor, Professor Hua Wang for his continuous support, encouragement, and patience during my Ph.D. research work. His guidance has helped me in improving the quality of my research work. I would like to acknowledge with much appreciation for the help that I got from my co-supervisor Dr. Xiaoxia Yin. Her constant support, motivation and enthusiasm have greatly contributed to the successful completion of my PhD thesis. I could not have imagined having a better advisor and mentor for my Ph. D study. Without their support, my PhD journey would not have been possible.

I take this opportunity to express my gratitude to Professor, Yanchun Zhang and Prof. Yuan Miao for teaching me knowledge and research skills and providing guidance not only for research but also for life.

The research presented in this thesis was undertaken in the Institute for Sustainable Industries and Liveable Cities at Victoria University (2015-2019). I thank Victoria University for providing the services and facilities in terms of access to the internet, scholarly articles and necessary software. The various learning, enriching, networking, professional and personal development experiences that I was able to receive from the University is also appreciated. I acknowledge the University for providing VU Postgraduate Research Scholarship funding.

I would like to record my appreciation to my seniors and friends Dr. Quan Vu, Mr. Santosh Kaini, Mr. Saurav Dahal, Ms. Irina and Mr. Ravindeer for their generous support and pleasant company.

Nobody has been more important to me in the pursuit of this project than the members of my family. I would like to thank my parents Mr. Hari Prasad Pandey and Bhagawati Pandey, for giving birth to me at the first p lace a nd s upporting m e spiritually throughout my life. They are the ultimate role models. I wish to thank my loving and supportive wife, Sika, and my adorable son, Eivan, who provide unending inspiration.

Last but not the least; I would like to thank my sisters, Muna, Ena and brother-in-law, Mr. Anil Karki for their motivation and encouragement throughout my study.

Dinesh Pandey
Melbourne, Australia
October, 2019

Contents

List of Figures

List of Tables

Chapter 1

Introduction

THE study on life science is pondered as a dynamic field with the utilization of the biological and medical information. Prior to the advancement of digital computers and technology, the experienced specialists were responsible in analysis and processing of medical images and had to entirely rely on their heuristic experience [9]. Moreover, such manual analytical process are limited on extracting and detecting features from the signals and suffers from other factors such as human errors and lack of detailed analysis. In the last few decades, due to the advancements of medical sensing and imaging technologies such as fundus photography [10] [11], magnetic resonance imaging (MRI) [12] [13], ultra sound [14], computed tomography (CT) [15] have provided an adequate amount of details about the interior of human body [16].

For efficient and precise diagnosis, the medical image should be clear and noise free [17]. Noise in the medical images is the primary challenge during image analysis. Hence, it's essential to understand the pattern of noise and often desirable to eliminate the noise for enhancement of useful features before further analysis. Moreover, the unclear and closely connected boundaries between anatomical structures, non-uniform illumination through the image and other imaging ambiguities adds an complexity during the image analysis [18].

Image analysis can be done either manually (medical experts) or automatically (via software) [19]. Manual analysis of medical image is a time consuming, tedious and error prone process. On the other hand, automatic analysis carried out by using computational resource which is immeasurably faster, more accurate and leading to significant improvement in disease diagnosis of MRI medical disorders. There are many different techniques used for the analysis of medical images such as segmentation [20] [21] [22], quantification

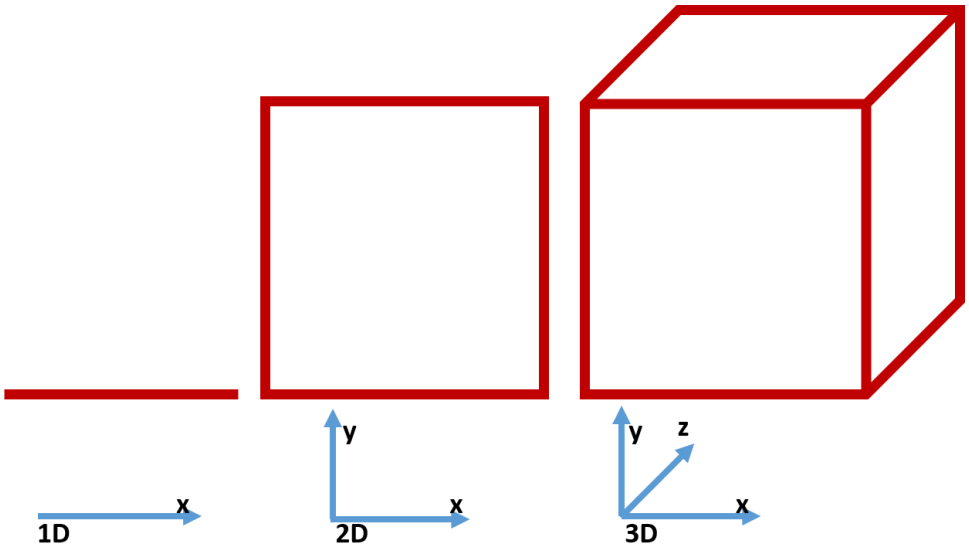

Figure 1.1: Illustration of image representation in 1D, 2D and 3D.

[23], registration [24], visualization [25] etc. Among MRI medical image analyzing techniques, segmentation is the primary and most crucial step. Segmentation is an process of partitioning an image into regions based on the common features of each pixel or voxel of image which is useful in various clinical applications [20]. This thesis is focused on the development of automatic segmentation algorithms for the identification of anatomical structures assisting doctors in detecting MRI pathological disorders. The developed algorithms are unsupervised, computationally efficient, robust and demonstrates higher accuracy.

1.1 Understanding the multi-dimensional image

The dimension of the image depends upon the dimensional number which can be referred as the number of independent input variable. In one dimensional space $I(x)$, the amplitude $j = I(x)$ is the dependent variable (output), and there is only one independent variable x. In two dimensional space (2D) space, an image is defined as $I(x, y)$. The x and y are two independent variables which denote the position at any point. A 2D image is usually formed with thousands of tiny dots generally called pixels. The position of pixels is fixed and is displayed together as an image. We can introduce more independent variable to represent the image is higher dimension which allows better visualization of

image. For instance, a three dimensional (3D) image include additional dimension such as depth z. Hence, 3D image can be defined as a function $I(x, y, z)$. Figure 1.1 show the image representation in different dimension.

$1D : j = I(x)$

$2D : j = I(x, y)$

$3D : j = I(x, y, z)$

Where, $x = 0 \ldots M-1$, $y = 1 \ldots N-1$ and $z = 0 \ldots .D-1$ denotes the spatial coordinates. The values of the x, y, and z are represented as the intensity values. In digital imaging, pixel (x and y) is the number of smallest addressable element created by phase and frequency values [26]. Similarly, voxel is created with phase and frequency values in addition to the slice thickness (z) [27].

1.2 Medical Imaging Systems

Medical imaging is the technique to create images of various part of human body which can be utilized for the diagnostic and treatment purposes. Data in the form of images are considered as an important asset in medical imaging. Medical imaging creates a visual representation of the body interior by non-invasive methods, which are used for diagnosis, or assist diagnosis for several medical conditions [28]. The basic concept of the medical imaging system is shown in Figure 1.2.

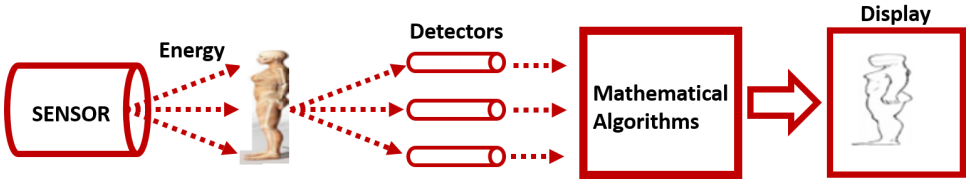

Figure 1.2: Illustration of medical imaging system.

A source of energy is passed through the human body using special device which are observed in the form of signal by the detector. The signal vary according to the different tissues and an image is reconstructed based on these signals. Various imaging techniques can be found in modern medical technology. Each imaging technique uses a different technology and source of energy to reconstruct the image. Magnetic resonance imaging (MRI) [12] [29], computed axial tomography (CAT) [30], ultrasound [14] and

x-ray [31] are the popular imaging techniques. MR imaging technique can detect conditions such as cysts, lesions, structural abnormalities and problems with blood vessels. Some pathological disorder can be detected via retina. There is a special camera with low power microscope which captures a detailed fundus image of human eye known as retinal imaging. Based on the condition of various landmark inside the eye, diagnosis is carried out. The retinal imaging is used to monitor several diseases such as diabetic retinopathy and hypertension in the early stages that manifest through human eyes. This thesis mainly focuses on the automatic segmentation of different landmarks which assist medical professionals for the identification of human diseases via MRI and retinal imaging techniques.

1.2.1 Medical Resonance Imaging (MRI)

Magnetic resonance imaging (MRI) is a technique to develop high quality images of the human body parts. Originally, the MRI is based on the principles of spectroscopic technique, nuclear magnetic resonance (NMR) [32]. NMR is a technique to obtain microscopic chemical and physical information about molecules. MRI scanner uses radio waves, magnetic fields and gradients to produce a detailed image as shown in Figure 1.3. It does not involve x-rays and ionization radiation, hence posses low risk. The main component of the MR scanners are main magnet, shim coils and the computer control. Main magnets polarizes the sample and the shim coils is used for correcting shifts in the homogeneity of the main magnetic fields.

To generate an MRI, a person is placed in the MRI scanner which creates a strong magnetic field around the object to be imaged. Initially, the energy generated from the oscillating magnetic field is applied to the object at the appropriate resonance frequency to excite the hydrogen atom that is available inside the human body. The excited hydrogen atom produces the radio frequency signal which is measured by the receiving coil. The radio signal is used to produce the position information using the gradient coils by varying the magnetic field. The intensity of the received signal is measured and plotted. Hence, an image slices is reconstructed from the RF signal.

The coils that produce RF pulse are rapidly switched on and off, to produce an MRI scan. The transmitted RF pulses can focus on particular tissues or abnormalities. The

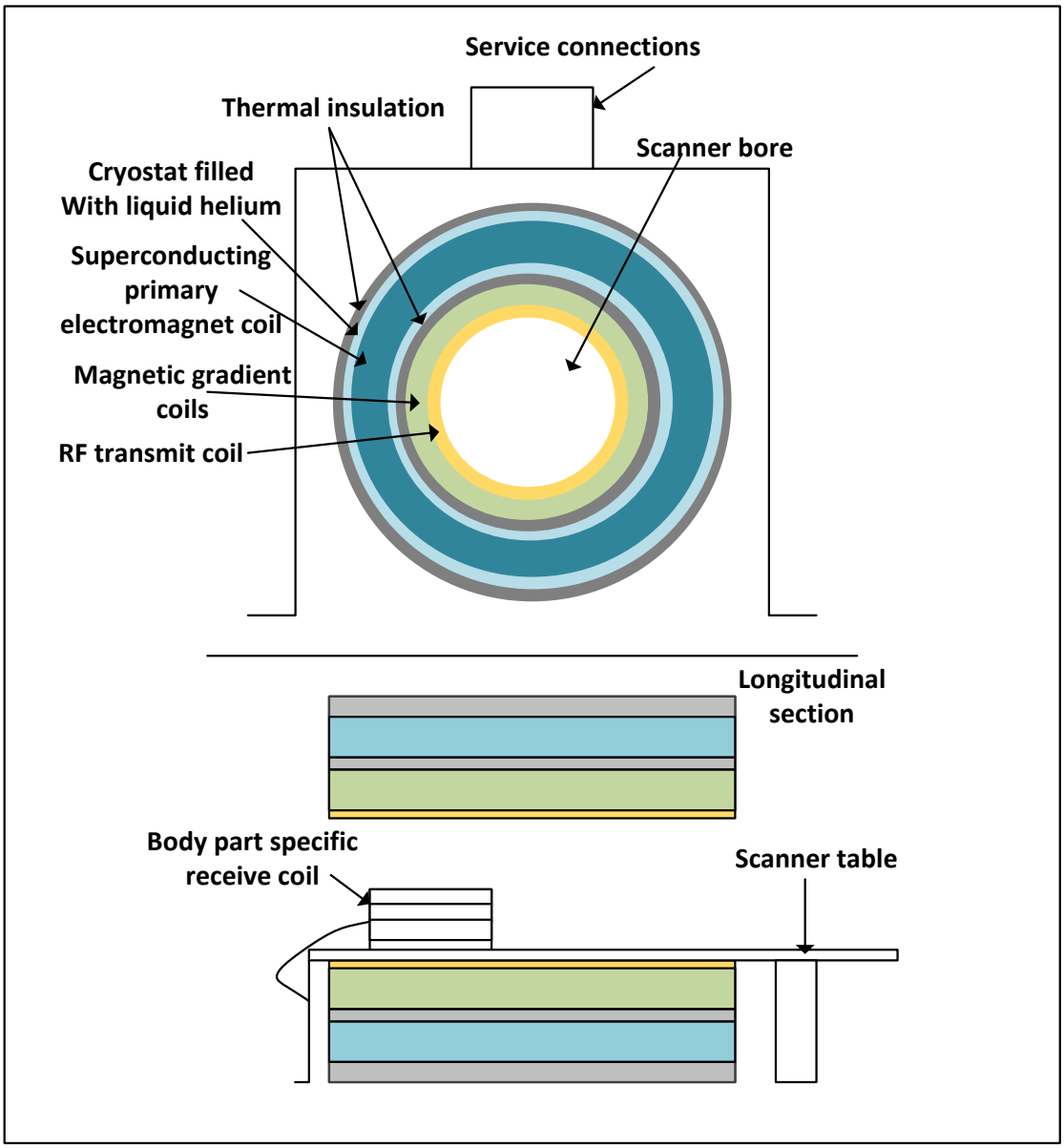

Figure 1.3: Illustration of MR scanner [1].

different tissues relax at different rates when RF pulse is switched off. The relaxation time is measured in two ways. $T1$ relaxation and $T2$ relaxation. $T1$ and $T2$ relaxation are the time taken by the magnetic vector and axial spin to return to its resting state respectively.

For a breast MRI, an object is place in the table and the breast is positioned on the opening of the table. Breast MRI requires an injection of contrast agent in the left or right arm which goes into the vein during the scanning process. The agent increases the quality of images where the tissues are clearer and the abnormalities are detected more easily.

On the other hand, Dynamic contrast-enhanced magnetic resonance imaging (DCE-MRI) [33] [34] is the series of 3D MRI scans. It is generated to from 4D (3D spatial + time) before and after the injection of contrast agent. The analysis is carried out through the intensity variation of MR signals before and after the injection of contrast agents over time.

Image acquisition of MRI

The process of acquisition is carried out with a breast surface coil. Initially, T1 weighted high quality image sequence is collected and the process is repeated for MRI frames before Gadolinium (Gd)- based contrast agent is injected. The process continues for several minutes. This method is commonly known as T1 measurement. A multiple frames with DCE 3D gradient echo sequence (GRE) is utilized to measure the kinetics of contrast agents in the lesions. To distinguish this kinetic feature, a high temporal resolution in the range of 40 to 120 seconds per dynamic acquisition is required. Moreover, for retrieving morphological features such as margins, shapes and internal structures, high spatial resolution is desirable that is acquired up to 512 in many clinical scanners. To identify structures such as cysts, fibro adenomas, and lymph nodes, a pre-contrast T2-weighted image sequence is acquired. The above-mentioned method provides MR image sequences with different properties and can be used for the analysis and segmentation of lesions [65].

Figure 1.4 shows the image before and after the contrast agent is injected. DCE MRI without injecting contrast agent is shown in Figure 1.4 (a). Since the lesion has not been enhanced, it is difficult to differentiate between lesions and healthy tissues. After injection of contrast agent, the intensity of lesion is changed. The enhanced lesion is high-

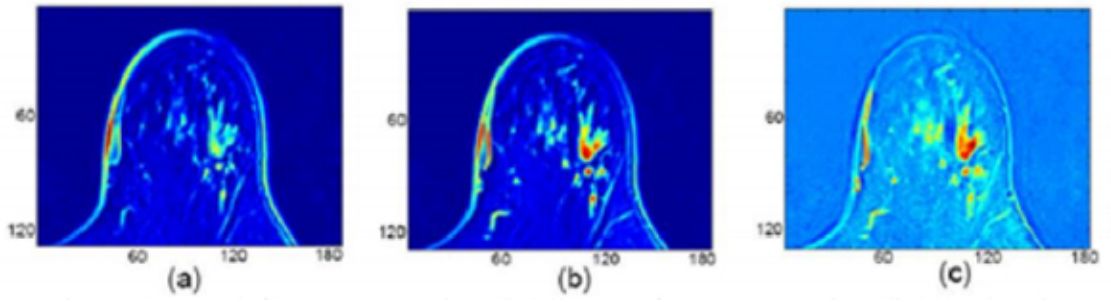

Figure 1.4: (a) Image before contrast agent is applied (b)Image after contrast agent is applied (c)Subtraction between (b) and (a)

lighted by a red color as shown in Figure 1.4 (b). The images obtained before and after the injection of contrast agent are subtracted. Hence, it produces an image with distinct lesion as shown in Figure 1.4 (c). The above displayed images in Figure 1.4 is simple and lesion can be easily labeled. Normally, artificial noise is found all over the images. When the lesion is labeled, some of the noise from the tissue region is also highlighted and detected as a lesion resulting in the requirement of the development of a computer aided method to analyze the lesion.

1.2.2 Fundus photography

Retinal imaging is the technique of capturing a photograph of th interior of the human eye using a low powered microscopic camera. The images produced by this technique provides reproducible high resolution images. The image are easily available and compliant to the image enhancement. The important anatomical structures such as blood vessel, optic disc, optic cup, fovea and macula can be visualized in the image. The characteristics of these structures are studied to document the presence of disorder and monitor their change over time. Furthermore, the identification of lesions is also important for the detection of pathology.

Image acquisition of retinal image

Fundus photography is captured with a fundus camera specialized with a low powered microscope. The fundus cameras are described by the optical angle of acceptance of the lens. The angle of acceptance vary from 20° to 140°. The angle of 30° is considered as the

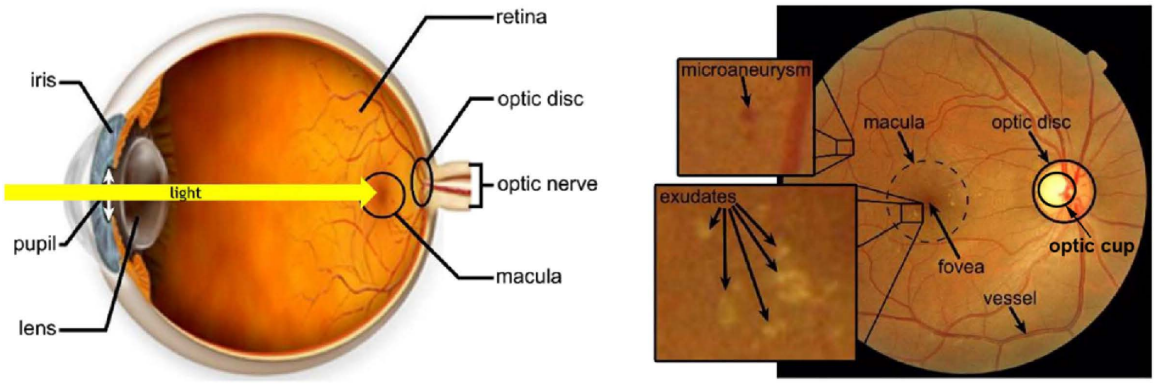

(a) (b)

Figure 1.5: Basic structure of human eye (a) fundus photography (b) different anatomical structure of fundus photography [2]

normal angle of view which creates a magnification of 2.5 times. Moreover, 45° to 140°is a wide angle view, however provides less retinal magnification. An angle of view less than 20° is narrow angle view. The advantage of considering the larger wide angle view is to provide a thorough documentation for the improved detection of retinal pathology. However, the image disadvantages, such as deformation of image due to the spherical shape of globe, misrepresentation of color intensity and higher equipment cost make it less popular. Hence, 30°, angle of acceptance trends to be standard methods during fundus photography.

1.3 Motivation

The image generated from wide variety of medical imaging system are interpreted manually by the expert radiologist [35]. The obtained information are used by the doctors for the diagnosis of several diseases.

The interpretation of result is time consuming for the doctors as it requires trials, repetitions and validations. The medical image generated from different medical imaging techniques includes huge amount of information. With the advancement of the technology, the number of size and dimension is increased where more information are available. The increased size and dimension makes it challenging for the expert radiologist to accurately diagnose the disease. For doctors, it's a tedious and time consuming work. Hence,

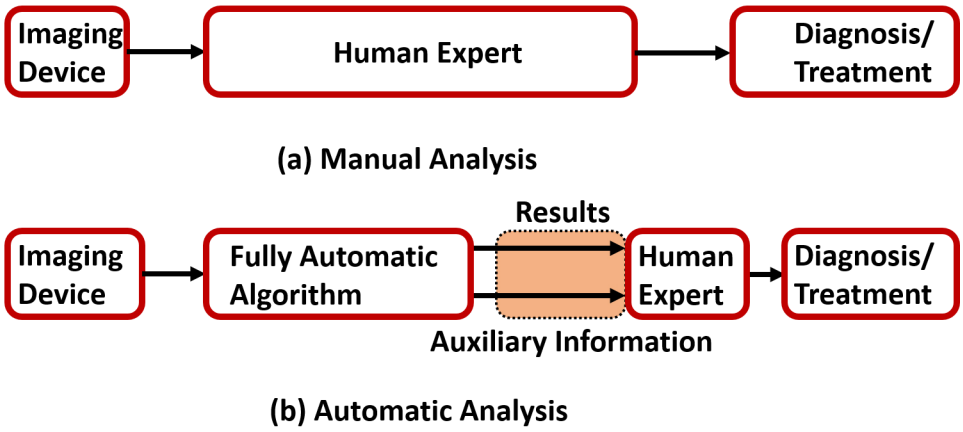

Figure 1.6: (a) Illustration of (a) Manual Analysis (b) Automatic Analysis

a finely tuned automatic segmentation algorithms needs to be developed which can assist doctors to accurately diagnose the disease with less effort. Also, it can be used for the early detection of disease and diagnostic error. The illustration of manual and automatic analysis is shown in Fig.1.6.

The image processing techniques involves efficient extraction of various information such as volume, shape, and motion by preserving the original data precision. MRI research efforts are done in different fields such as pre-processing, enhancement, segmentation, feature extraction and classification, for processing and analyzing the medical images. Among them, segmentation is considered as the most important and challenging area in medical analysis. Hence, this thesis will mostly focus on the automatic segmentation frameworks to identify varieties of landmarks in fundus photography and breast MRI.

Segmentation is the process of classifying pixels/voxels that are homogeneous and later extracting these regions of interest. The accurate and automatic segmentation of medical images is considered as the vital step during diagnosis, clinical studies and treatment planning. Automatic segmentation methods assist to provide solution for larger number of cases with the same accuracy. The automatic segmentation can be done with different type of machine learning approach. These approach can be divided into supervised and unsupervised segmentation methods.

The supervised segmentation method is the technique in which the system is trained based on the training set of image and the inferred function is produced. If the output of the function is discrete, it's called classifier and if it's continuous, it's called as regression

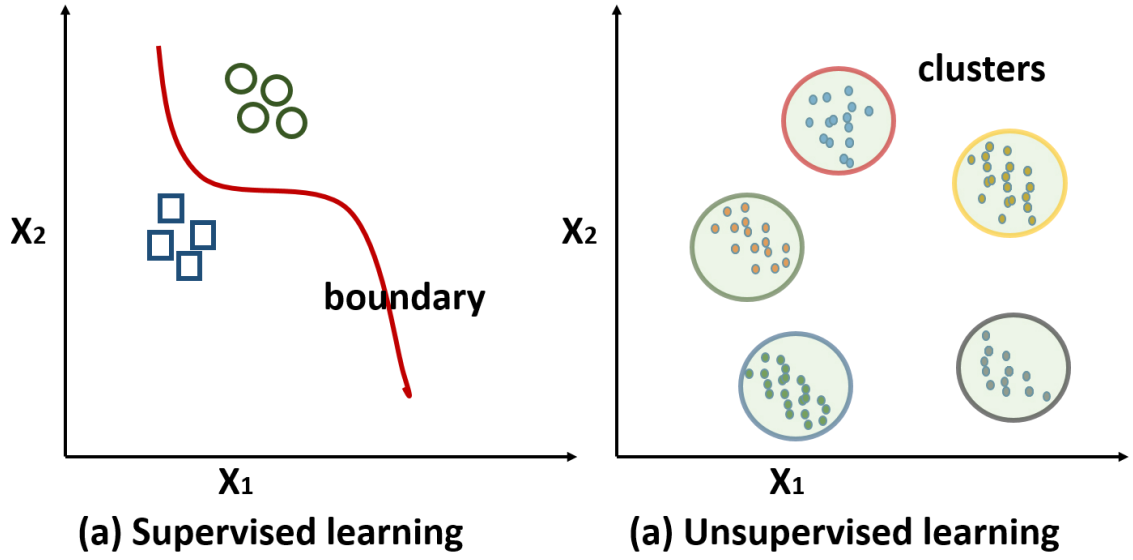

Figure 1.7: (a) Illustration of (a) Supervised Learning and (b) Unsupervised Learning

function. Hence, the supervised learning approach requires the ground truth before the training process and the output is predicted based on it. To solve the problems using supervised algorithm, a series of steps is followed as shown below:

1. Prepare the training set.
2. Determine the features of the prepared training data set. This set is prepared after gathering the information, either from human expert or measurements. Thereafter, the features are transformed into feature vectors. The number of feature vectors should be appropriate to achieve effective high dimensional data processing.
3. Select the learning algorithm, and run the learning algorithm in the training data set. We can fix and adjust the parameters to optimize the performance which is known as validation set. This validation set is obtained after cross validation with training set.
4. Finally, the performance is analyzed by testing with test dataset.

In unsupervised segmentation method, initially dataset is not labeled. Hence, this method does not require human intervention. They are more subjective and there is no simple goal for the analysis. It is used to find the indirect hidden structures, patterns or

features to analyze new data. Unsupervised segmentation methods are computationally efficient. It is not always possible to obtain labeled data for training purpose and create the supervised segmentation model. However, with unsupervised learning, a model can be created which can solve MRI problems with less computation and without the prior knowledge of labels.

Automatic segmentation techniques for medical images rely on the properties and feature of the images extracted from the imaging system. For example, MRI, mammography or fundus photography will require a different segmentation algorithm. The challenge is due to the contrast in image quality and drastic variation in shape and size of the landmarks to be segmented. Moreover, images are often corrupted with different kind of noise and artifacts which adds complexity in accurate segmentation. Medical images are often observed with low contrast and similar intensity values between different anatomical structures. It becomes considerably difficult to produce the desirable segmentation results. Hence, the development of accurate and automatic segmentation frameworks is a absolute necessity.

1.4 Challenges

Image segmentation can be used in the medical imaging field to study about body structure, identification of the pathological region and assist doctors for the diagnosis of disease. Automatic segmentation also aids medical experts to accurately achieve a reliable results while using a larger data sets.

Automatic segmentation of different anatomical structures from medical image is always a difficult task. Prior to the segmentation, one should always take care of image conditions and quality. Moreover, noise developed during acquisition period makes automatic segmentation tough. Several other factors such as illumination, insufficient resolution and low contrast also make it challenging and difficult in distinguishing the different anatomical structures. Hence, an accurate results are difficult to obtain from a simple segmentation algorithms. Furthermore dealing with the high dimensional images is also an challenging job where segmentation process often requires high computational time. The appearance and features of the image acquired from different acquisition tech-

niques differs markedly. Hence, a automatic method developed for one type of image for the segmentation of various shapes and structures cannot be applied to the other type of image acquired from different imaging techniques. However, it can be done with the modification of parameters used in the algorithm.

This thesis contributes to addressing different segmentation challenges in multidimensional images. Especially in two imaging modalities: fundus photography (2D) and Breast MRI (3D) which are explained below.

1.4.1 Fundus photography

Fundus photography captures a digital image of the back portion of human eye. The image captures a different landmarks such as optic nerve, blood vessels, macula and fovea. The analysis of these landmarks is carried for wide variety of ophthalmic conditions that manifest through human eye.

For example, a increased pressure inside the eye can severely damage the optic nerve which is refereed as glaucoma. Experts can use fundus photography to detect the changes and recommend the appropriate solutions [36]. With the study of fundus photography, doctors can observe the details in retina and detect the damage caused to the retina from diabetes (diabetic retinopathy) [37]. Some retinal landmarks which are not visible on a flurescein angiogram can be easily observed in fundus photography. As a result, the interpretation of fluorescein angiography can be done accurately.

Fundus photography is also used to assist the interpretion of fluorescein angiography because certain retinal landmarks visible in fundus photography are not visible on a fluorescein angiogram.

The retinal images with lesions, exudate's, nonuniform illuminations and other pathological artifacts have intrinsic limitations under which unreliable results such as wrongly identified blood vessels, optic nerve, macula and fovea during segmentation. Manual segmentation of these landmarks is a tedious and the result may vary between the experts. Hence, automatic segmentation of these landmarks should be the primary requirement either for diagnosis or early detection of the disease that manifest through retina. In order to deal with the challenges, we have proposed a robust and accurate framework for the segmentation of two important structures 1) blood vessels and 2) optic disc (OD)

from the fundus photography.

1.4.2 DCE MRI

DCE MRI is utilized for detection, diagnosis and staging of the breast cancer. Based on the evaluation of multiple risk factors, 15% to 20% lifetime risk is associated with women to get cancer [38] [39]. American Cancer society (ACS) has recommended screening from DCE MRI, to reduce the risk of cancer by detecting it in the early stage [40]. Cancer at an early stage is curable. Manual delineation is tedious, time consuming because of large amounts of data to be analyzed. Hence, the segmentation of breast lesions is becoming popular to improve the diagnostic accuracy and computation time. It is observed that the cancer detection sensitivity in DCE MRI is high, but specificity is low [41]. The improved system with the lowest false positive (high specificity) will save a cost for additional treatment and biopsies [42] [43]. Also, it reduces a woman's anxiety and tension. DCE MRI inherits low SNR, motion artifacts and high inter-patient variability.

As the performance of the existing techniques are moderate, the is still a requirement of segmentation accuracy. Hence, we have developed a novel algorithms for accurate and automatic segmentation of 1) breast region of interest (BROI) 2) breast density (BD) and 3) breast lesions.

1.5 Thesis aim and objectives

This thesis is aimed to develop novel framework for addressing the aforementioned challenges in automatic segmentation of medical images. The segmentation challenges are addressed in two imaging modalities.

Fundus photography (2D)

- Automatic segmentation of blood vessels
- Automatic segmentation of optic disc

MRI (3D)

- Automatic Segmentation of BROI and BD
- Automatic Segmentation of breast lesions

1.5.1 Automatic segmentation of blood vessels

Each retinal image shows unique properties with respect to retinal boundaries, optic discs and different diseases. Moreover, vessel crossing, bright or dark lesions, low contrast, uneven illumination, and noise further complicate the segmentation process for an accurate result. The major limitations in state-of art methodologies which makes automatic segmentation more complicated are 1) Extraction of thin vessels in retinal images is difficult 2) Both non-uniform illumination and noise in the image are responsible for false 3) closer vessels are merged. 4) Retina is assumed to be healthy and free of bright and dark lesions in the most of the segmentation techniques reported in the literature. However, the existence of bright or dark lesions can considerably degrade the quality of retinal vessel detection and even make the result unusable. (5) The existing algorithms are validated and tested on a small number of retinal images, which are not enough for algorithms justification. Hence, we aimed to develop a fully automated and novel blood vessel segmentation algorithm to remove above mentioned complications.

1.5.2 Automatic segmentation of optic disc (OD)

In the state-of-art, development of accurate OD detection and segmentation are still facing challenges because of several reasons such as 1) Ophthalmic pathologies causes the change of color, shape or depth of OD 2) Retinal pathologies (exudate, lesion), sometimes possess similar properties causing a false identification of OD. 3) Different factors like illuminations and contrast irregularities, boundary artifacts and blurred image edges makes segmentation complicated and requires pixel to pixel analysis. 4) Also the texture feature of OD vary for different images, adding more challenges, thus requiring a preprocessing step prior to the segmentation. 5) If the vessels are dense and around OD, the identification the OD boundary becomes difficult. Although, the results obtained from the proposed localization techniques of OD in the state of the art is considerable, the precise and automatic segmentation of OD boundary is still a challenging task and requires a detailed analysis around the boundary of OD. Hence, we aimed to develop a fully automatic algorithm that accurately segments the optic disc especially from pathological images.

1.5.3 Segmentation of Breast region of interest (BROI) and breast density (BD)

Fully automatic, accurate and fast segmentation of BROI still require much attention because of several reasons: 1) Breast structures in different breast MR images are unsymmetrical 2) Manual correction is required around the boundary area of breast. 3) A bilateral asymmetry between left and right breast region requires separate analysis. 4) Pectoral muscle and breast region which is found to be closely attached possesses similar color intensity. This results in high false positive. 5) Several methods in the state-of-art are supervised and require prior information before the segmentation. Similarly for BD segmentation, we note that there is a significant range of studies carried out in a semi-automated segmentation using an interactive thresholding method and user-assisted clustering methods. These non-automated methods are subjective and create inter and intra-reader variability. Hence, to address this above mentioned challenges, we aim to develop a fully automated framework for the segmentation of BROI and BD.

1.5.4 Automatic segmentation of Breast lesions

Early detection of tumors from breast MR images is significant because it saves life. The segmentation of breast MR image provides a detailed and accurate information such as shape, size and type of lesion which is vital in diagnosis of breast cancer. Manual segmentation of lesions from the DCE MRI is a tedious and time consuming task even for a qualified specialist. Hence, it is difficult to include in the clinical routine. On the other hand, automatic segmentation is fast and can include MRI quantitative information of the breast area for the accurate results. This process will assist doctor for the accurate identification of the problem in the early stage. However,the automatic segmentation is a challenging task because of the irregular shape, boundaries and similar intensity distributions across the image. Hence, accurate segmentation of lesions is still a challenging task and requires a detailed analysis around the boundary of lesions. Prior to the segmentation, it is essential to enhance the MR image because the current image technique produces a low contrast image which makes hard to differentiate between normal and lesion area especially around the boundary. Moreover, the removal of noise plays a vital role while preserving the important information such as boundary and edges of MR im-

age to produce the accurate segmentation with computational efficiency. Hence, we aim to develop a fully automatic framework for the segmentation of breast lesion.

1.6 Thesis contribution

This thesis offers an innovative analytical and methodological framework for the automatic segmentation in two different imaging modalities. The developed algorithm will assist for the segmentation of different areas in images. The **major contribution** in terms of theoretical and practical aspects in two different imaging modalities are as listed below:

1. The detailed review on the most important automatic segmentation techniques in multidimensional medical images is demonstrated.

1.6.1 Retinal Imaging

2. Accurate and robust algorithm for the segmentation of blood vessels is developed using maximum entropy incorporating line detection and phase-preserving denoising. The study shows potential to assist medical doctors in improving screening accuracy of retinal imaging.

    - An automatic, accurate and computationally efficient framework for retinal blood vessel segmentation is proposed.
    - A preprocessing step that includes background estimation and subtraction to eliminate non-uniform illumination and noise.
    - Local phase preserving denoising works efficiently for thin vessel extraction.
    - Treating thin and thick vessels separately allows accurate segmentation of retinal vessels.

3. An algorithm for the accurate segmentation of optic disc is developed. The algorithm is capable of dealing with the images with retinal pathologies which shares similar color intensity causing the false identification of OD and its boundary. This requires a preprocessing prior to the segmentation.

- An automatic, accurate and computationally efficient framework for optic disc segmentation is proposed.
- A pre-processing step that reduce the noise, and uneven illumination across the images is developed
- Estimation of optic disc region of interest (OD-ROI) is done with kmeans clustering and circular hough transform (CHT) incorporating linear filtering.
- Edge information are obtained from simple linear iterative clustering (SLIC) Superpixels and CHT.
- Developing a geometrical model over the edge information obtained from SLIC Superpixels and CHT allows accurate segmentation.

1.6.2 Breast MRI

4. An algorithm for automatic and fast segmentation of breast region-of-interest (ROI) and density in 3D MRIs is developed. This study proposes an innovative, fully automatic and fast segmentation approach to identify and remove landmarks such as the heart and pectoral muscles before BROI and BD segmentation.

    - An automatic, accurate and computationally efficient framework for breast region of interest (BROI) and breast density (BD) segmentation is proposed.
    - A machanism to minimize the influence of noises, preserve edges and remove unwanted artifacts for accurate results is developed.
    - The segmentation of heart area is obtained with active contour level set method. The method involves calculation of initial contour by using maximum entropy thresholding and convolution technique, to develop accurate segmentation.
    - The pectoral muscle is closely connected and possess similar color intensity with BROI. This results in false positives and requires manual corrections. The segmentation method to automatically and efficiently detect pectoral muscle is developed

5. An algorithm that automatically segments breast lesion from the MR images is developed

- An automatic and efficient unsupervised segmentation method is proposed.
- Breast MR image is enhanced using image registration followed by image subtraction.
- An mechanism to reduce the noise while preserving important information of breast MR image is developed.
- A fast segmentation approach using using max flow and min cut problems in continuous domain is developed.
- A post processing step using morphological approach is developed to further delineate the obtained result.

1.7 Thesis Organization

The organization of the chapters in this thesis is shown in Fig. 1.8.

A brief description of each chapter is outlined below.

- **Chapter 1** identifies the challenges of automatic segmentation methods in two imaging system 1) Fundus photography and 2) MRI Image. The objectives of the thesis are then defined accordingly to solve the mentioned challenges. Afterward, a brief summary of the methodology followed in each proposed algorithms for solving different problems throughout the thesis is listed. Finally, the contribution of the conducted research is presented.
- The literature review of existing work falling into the scope of multidimensional medical images is explained in **Chapter 2**. The literature review helped to analyze the effectiveness and advantage of different techniques. To solve the segmentation problem, these techniques are used in the proposed framework as per the requirement. State of art for each proposed segmentation is explained in detail in each chapter.
- The retinal images with lesions, exudates, non-uniformed illuminations, and pathological artifacts have intrinsic problems such as the absence of thin vessels and false vessels detection. To solve these problems, **Chapter 3** proposed a novel algorithm which involves separation of background images to minimize the influence of

noise, non-uniformed illuminations, and lesions. We develop two different strategies to segment thin and thick blood vessels. Thin blood vessels are identified by taking benefits of local phase-preserving denoising, line detection, local normalization, and maximum entropy thresholding. To remove noise and preserve detailed blood vessels information, phase-preserving denoising technique is used. The technology takes advantage of log-Gabor wavelet responses in the complex domain to preserve the phase information of the image. Thick vessels are extracted and binarized via maximum entropy thresholding. The performance of the proposed algorithm is tested on four popular databases (DRIVE, STARE, CHASE_DB1, HRF). The results demonstrate that the proposed segmentation process is automatic, accurate and computationally efficient.

- Optic disc (OD) localization and segmentation is an important procedure for the automatic screening of optic nerve head abnormalities. There are several methods proposed for the localization and segmentation of OD. However, precise boundary segmentation is still challenging for the images, which are under the influence of noise, uneven illumination, and pathologies. Hence, to solve this problem, we proposed a novel algorithm that includes identification of the OD region of interest (OD-ROI) and boundary pixels in **Chapter 4**. The process begins with the Kmeans clustering algorithm, which is applied to the foreground and background estimated images, to obtain the brightest cluster. The resulting clusters are merged together and the highest weight value is calculated as the approximation of the OD center. Secondly, the OD-ROI is estimated by comparing the radius and center information obtained using a circular Hough transform (CHT) with the approximated center from the initial step. Finally, the OD boundary pixels are identified with the geometrical model over the edge information obtained from superpixels and CHT. We have verified our method for segmenting OD using seven databases and shown to be superior while compared with the other proposed methods in state of the art.

- **Chapter 5** proposed a novel and accurate segmentation of the breast region of interest (BROI) and breast density (BD) which is considered as a significant challenge during the analysis of breast MR images. Most of the existing methods for breast segmentation are semi-automatic and limited in their ability to achieve accurate re-

sults. This is because of difficulties in removing landmarks from noisy magnetic resonance images (MRI) due to similar intensity levels and the close connection to BROI. This study proposes an innovative, fully automatic and fast segmentation approach to identify and remove landmarks such as the heart and pectoral muscles. The BROI segmentation is carried out with a framework consisting of three major steps. Firstly, we use adaptive Wiener filtering and k-means clustering to minimize the influence of noises, preserve edges and remove unwanted artifacts. The second step systematically excludes the heart area by utilizing active contour based level sets where initial contour points are determined by the maximum entropy thresholding and convolution method. Finally, a pectoral muscle is removed by using morphological operations and local adaptive thresholding on MR images. Prior to the elimination of the pectoral muscle, the MR image is subdivided into three sections: left, right, and central, based on the geometrical information. Subsequently, a BD segmentation is achieved with 4 level fuzzy c-means (FCM) thresholding on the denoised BROI segmentation. The proposed method is validated using the 1350 breast images from 15 female subjects. The pixel-based quantitative analysis showed excellent segmentation results when compared with manually drawn BROI and BD. Furthermore, the presented results in terms of evaluation metrics: Acc, Sp, AUC, MR, P, Se, and DSC demonstrate the high quality of segmentation using the proposed method. The average computational time for the segmentation of BROI and BD is 1 minute and 50 seconds.

- Segmentation of lesions in breast MR images is an important task in medical image analysis, which plays a significant role in detecting abnormal lesions. Detection of breast lesions is usually done by the manual process by expert radiologist, which is a long and tedious process. Therefore in **Chapter 6**, the development of computerized segmentation method will assist doctors for the quicker identification of the problem in the early stage saving unnecessary biopsies and expensive tests. The automatic segmentation of lesion from the diseased breast MR image is still a challenging task because of the irregular shape, boundaries and similar intensity distributions across the image. Furthermore, the presence of noise adds complexity to achieve accurate segmentation results. The supervised techniques

are considered effective, but its efficiency depends upon a large amount of labeled dataset used for the training purpose beforehand. On the other hand, the unsupervised technique does not require labeled dataset and produce results without prior knowledge. In this chapter, we propose a fully automatic unsupervised method using max flow and min cut problems in the continuous domain over the denoised image. It is observed that a graph model over the denoised model is efficient in producing an accurate result using fewer iteration. The proposed framework is divided into three parts. In the pre-processing step, the post contrast and pre-contrast image are subtracted which is followed by image registration. This potential benefit of this process is to enhance the lesion area. The second step is lesion detection where max flow and min cut problems in the continuous domain are applied after noise removal. The useful features of the image are preserved using the phase preservation denoising and pixel-wise adaptive Wiener filtering technique. Finally, the unwanted area in the obtained result is removed in a post-processing step using morphological operation. The performance of the proposed method is tested qualitatively and quantitatively on 21 cases with two different MR image resolution. The result obtained from the proposed method when compared with the manually segmented images demonstrates the high quality of segmentation results.

- **Chapter 7** concludes the thesis which includes research objectives and the task accomplished to achieve the thesis aims. Also, we provide a brief description on future enhancement in the algorithm development for medical image segmentation.

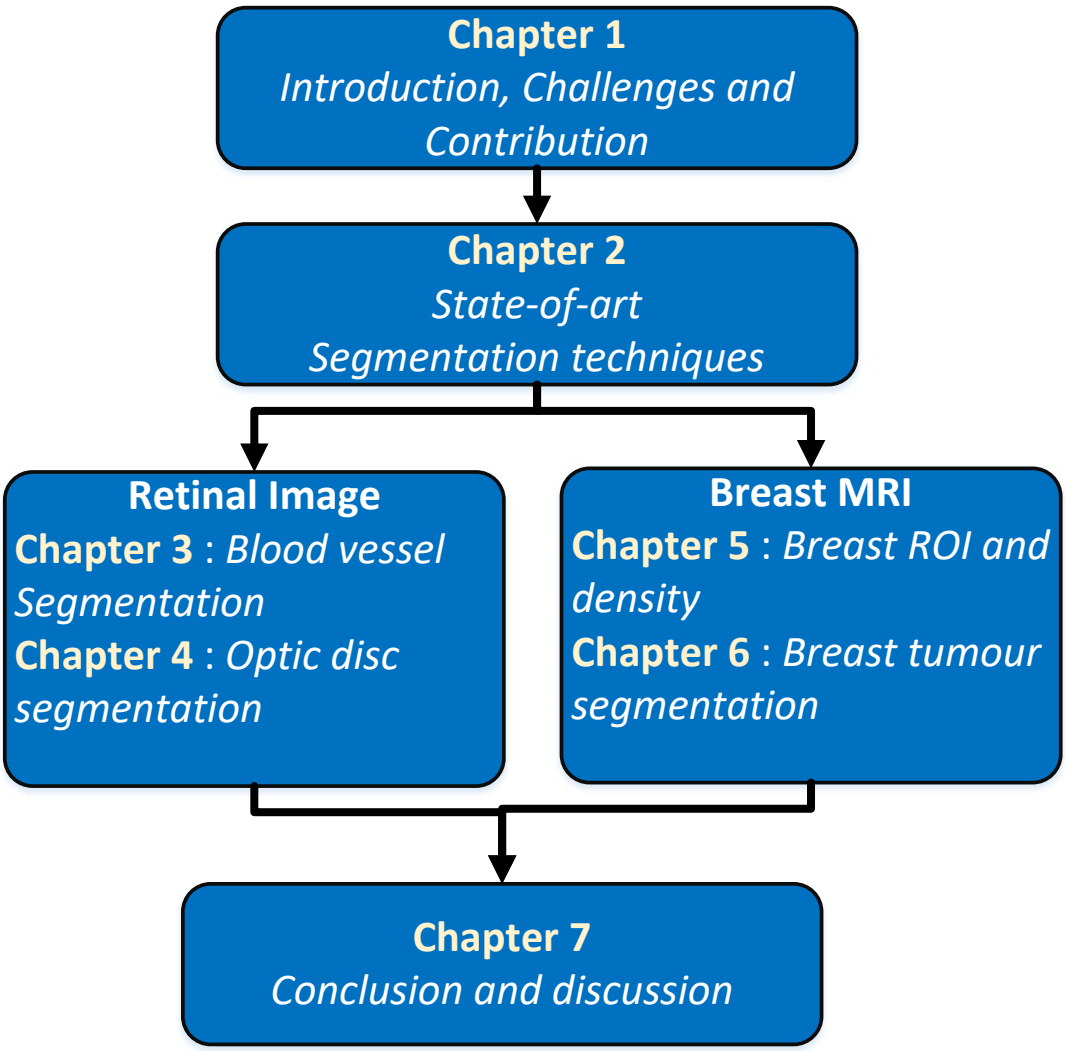

Figure 1.8: The thesis organization

Chapter 2

Segmentation techniques in multidimensional medical images

IMAGE segmentation is one of the most important step for the extraction the important areas from medical image [44] [20]. Moreover, automatic segmentation of the desired region of interest (ROI) assist doctors at diagnosing diseases accurately in less time [45]. Moreover, this system can help to reduce the diagnostic errors that are inevitable in human [46].

There are several automatic segmentation methods which has been applied in the recent medical images analysis. Some of the popular and important image segmentation techniques are thresholding based technique [47] [48], region based technique [49] [50], edge based technique [51] [52], clustering based methods [53] [54], and deformable models [55] [56].

In the remainder of this section, we will review in detail about the above-mentioned image segmentation techniques. The organization of this chapter is summarized in Fig. 2.1

2.1 Thresholding based segmentation technique

Thresholding is one of the most popular and simple image segmentation technique. The pixels of an image is divided with respect to the threshold value which is calculated using the intensity level. Thresholding technique is basically divided into three categories. Global thresholding [57], Local adaptive thresholding [58], and Maximum entropy thresholding [59].

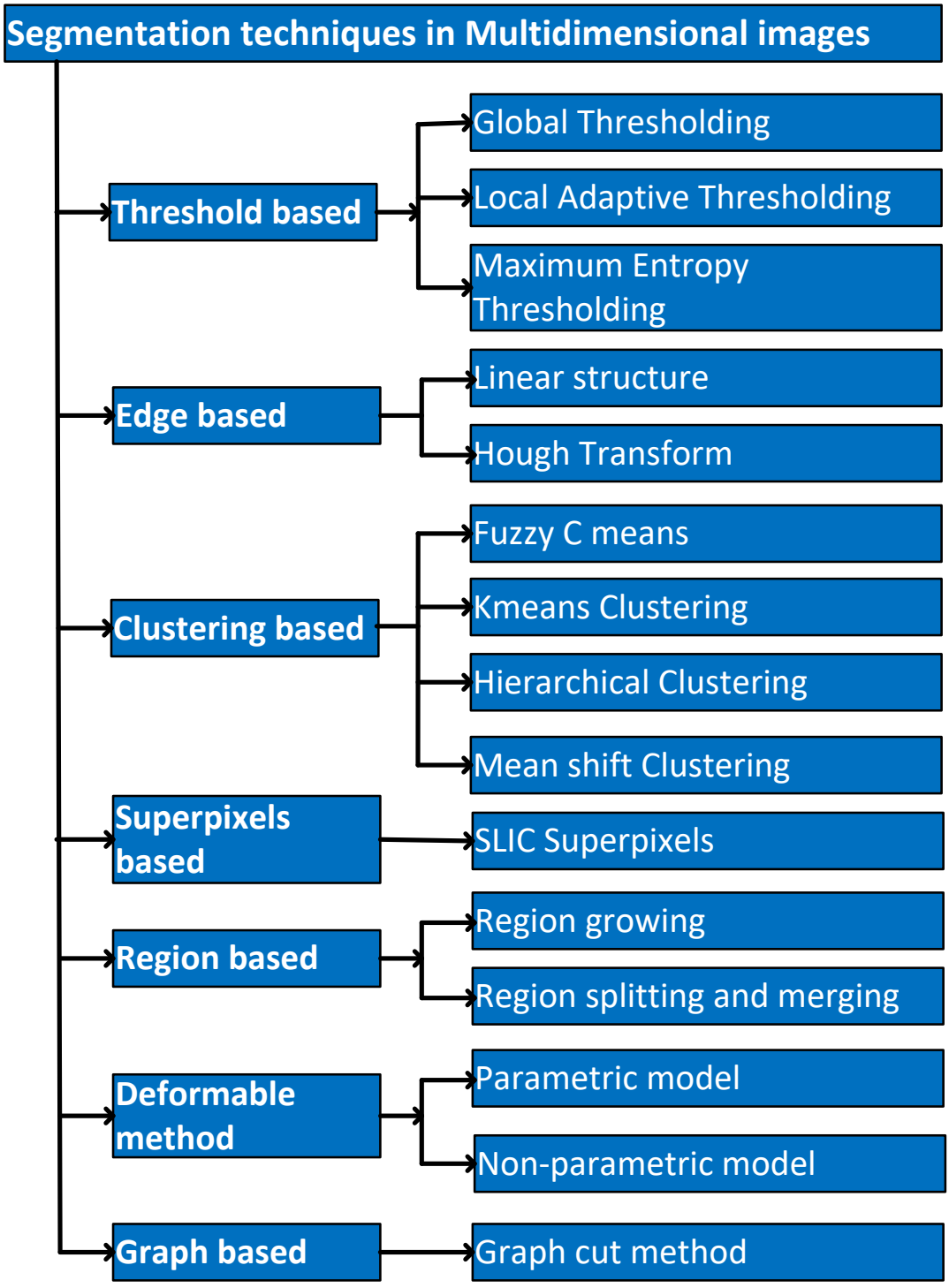

Figure 2.1: Organisation of literature review

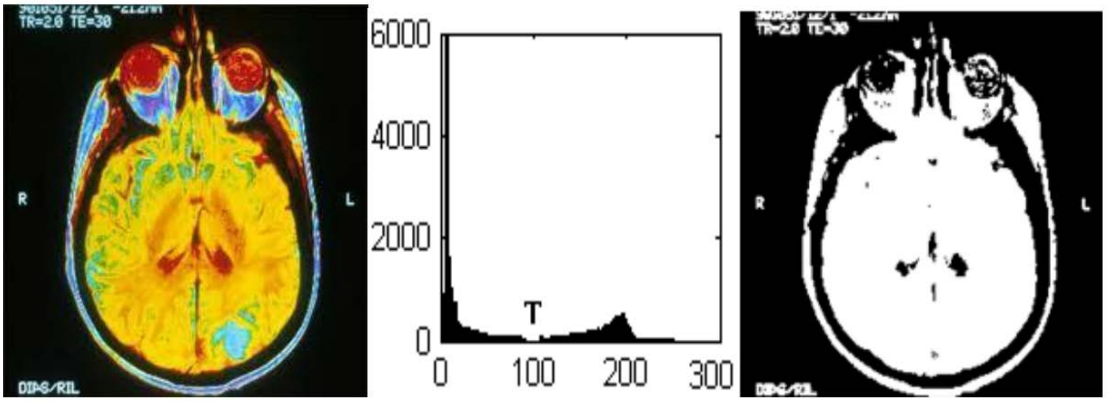

Figure 2.2: Example of global thresholding [3]

2.1.1 Global Thresholding

Global thresholding is considered to be effective when the intensity distribution between background and foreground is highly distinct. In this technique, a single threshold value is applied to all the pixels in the image. Let us consider a single threshold value, 'T' for the input image $I(x,y)$. 'T' is calculated using the image features. The output image, $O(x,y)$ is obtained as the binary image after thresholding. The output image is obtained as shown in Eq. (2.1)

$$O(x,y) = \begin{cases} 1 & if\ I(x,y) > T \\ 0 & if\ I(x,y) \leq T \end{cases} \tag{2.1}$$

This thresholding technique works very well if the histogram has a clear valley between two regions as shown in Fig. 2.2

The thresholding value T can be calculated using several techniques such as Otsu, Histogram analysis, iterative, maximum correlation and clustering. The goal of the Otsu thresholding method [60] is to find the optimal thresholding value for global thresholding technique. Initially, the image is divided into two-pixel class. Next, the bimodal histogram and the threshold is selected to minimize the intra-class variance of black and white pixels which is carried out to measure the pixel distribution in each side of the threshold(background or foreground) by the iterative process for all the possible threshold values. Let the variance of the two-class be σ_0 and σ_1, then the Otsu method searches

the threshold the minimizes the intraclass variance as shown in Eq. (2.2)

$$\sigma_w^2(T) = w_0(T)\sigma_0^2(T) + w_1(T)\sigma_1^2(T) \tag{2.2}$$

where w_0 and w_1 are the weight probabilities of the classes separated by threshold T as shown in Eq. (2.3) and Eq. (2.4) respectively. The class probability is calculated from the 'L' bins of histograms.

$$w_0(T) = \sum_{i=0}^{T-1} p(i) \tag{2.3}$$

$$w_1(T) = \sum_{i=T}^{L-1} p(i) \tag{2.4}$$

Histogram-based technique [61] is used to calculate the thresholding value by plotting the histogram of the image. The image is thresholded to separate the two regions: foreground and background. Moreover, this technique can be used to separate the regions with all possible homogeneous region in the image. Let us consider the two peaks $H1$ and $H2$ of the histogram. The threshold value, T is calculated as shown in Eq. (2.5) and Eq. (2.6):

$$T = (H1 + H2)/2 \tag{2.5}$$

$$T = minH(u) \tag{2.6}$$

where, $u \in [P1, P2]$ and $H(u)$ is the histogram value at greylevel u between $P1$ and $P2$.

Iterative thresholding [62] is the improved version of Otsu thresholding technique the includes iteration. During the first iteration, the threshold value from the traditional otsu method is derived and the mean greyscale values of the two classes is calculated. In the second iteration, instead of two class separation, the image is separated into three class based on the two mean greyscale value calculated in the previous step. The three classes are defined as background, foreground and the region to be determined (TBD). The classless than the smaller mean is categorized as background. Similarly, the class larger than

the bigger mean is categorized as foreground and the remaining class is categorized as TBD. The next iteration is carried out by keeping the pre determined background and foreground area unchanged and the same procedure is repeated in the TBD region. The iteration is stopped after fulfilling the pre-set criteria.

2.1.2 Local Adaptive Thresholding

This thresholding technique calculates different thresholds for each pixel. The calculated threshold value is dependent upon the intensity information of neighboring pixels. This technique typically takes greyscale or color images as an input and outputs a binary image. This technique works well with the images having strong illumination gradient. For the estimation of the threshold, two approaches (i) the Chow and Kaneko approach [63] and (ii) local thresholding are used.

Chow and Kaneko initially classify an image into overlapping sub-images. The histogram of sub-images is investigated and finally, the optimum threshold for sub-image is calculated. This method is computationally expensive, hence not suitable for the real-time application. On the other hand, local thresholding approach calculates the threshold value by calculating the mean and median of the sub-image. A function that calculates the mean and median of local intensity distribution is utilized. This technique works well when there are enough foreground and background pixels in the neighborhood. However, on the image margins, there won't be enough pixels in the neighborhood so the mean will be close to the mean of center pixels. Hence, to solve this problem, a constant value C can be introduced. The new threshold value is calculated with using mean and C. As a result, all the pixels which do not have background pixels in their neighborhood are set to background. Hence, produce an segmentation. The following step is followed for the calculation of local threshold.

1. The image is convolved with the statistical operator: mean or median.
2. The original images are subtracted from the convolved image.
3. Finally, a threshold from the resultant image with mean and constant, C is calculated.

2.1.3 Maximum entropy thresholding

This thresholding technique is based on maximizing the Shannon entropy [64] i.e. the maximization of the information measure between object and background. Entropy is considered as one of the effective information to describe an image. Hence, we can calculate the entropy information of the distribution of gray levels to partition the target image to produce a thresholded image. Evidence shows that the performance of 2D maximum entropy method is effective than 1D maximum entropy method. 2D maximum entropy thresholding is based on the normalized histogram of the gray image whose value ranges from 0 to 255.

Let us consider an image that required binarization. Let $I_h(i)$ be the normalized histogram of that image and t indicates the threshold to be determined.

$$\sum_{i=0}^{\mathrm{i_{max}}} I_{\mathrm{h}}(i) = 1 \tag{2.7}$$

The Entropy of vessel pixel $H_{vessel}(t)$ is given by Eq. (2.8)

$$H_{\mathrm{vessel}}(t) = -\sum_{i=0}^{\mathrm{t}} \frac{I_{\mathrm{h}}(i)}{\sum_{j=0}^{\mathrm{t}} I_{\mathrm{h}}(j)} log \frac{I_{\mathrm{h}}(i)}{\sum_{j=0}^{\mathrm{t}} I_{\mathrm{h}}(j)} \tag{2.8}$$

Similarly, the entropy of background pixel $H_{bg}(t)$ is given by Eq. (2.9)

$$H_{\mathrm{bg}}(t) = -\sum_{i=\mathrm{t}+1}^{i_{max}} \frac{I_{\mathrm{h}}(i)}{\sum_{j=\mathrm{t}+1}^{i_{max}} I_{\mathrm{h}}(j)} log \frac{I_{\mathrm{h}}(i)}{\sum_{j=\mathrm{t}+1}^{\mathrm{t}} I_{\mathrm{h}}(j)} \tag{2.9}$$

Hence, Optimal threshold by maximizing the background and vessel pixels can be calculated as Eq. (2.10)

$$\mathrm{T_2} = \mathrm{arg}_{t=0.....\mathrm{i_{max}}} \mathrm{Max} H_{\mathrm{vessel}}(t) + H_{\mathrm{bg}}(t) \tag{2.10}$$

The final binary image using T is calculated as Eq. (2.11)

$$I_4 = \begin{cases} 1, & \mathrm{I_3} < \mathrm{T_2} \\ 0, & \text{otherwise} \end{cases} \tag{2.11}$$

Maximum entropy thresholding [65] can be an important technique during the seg-

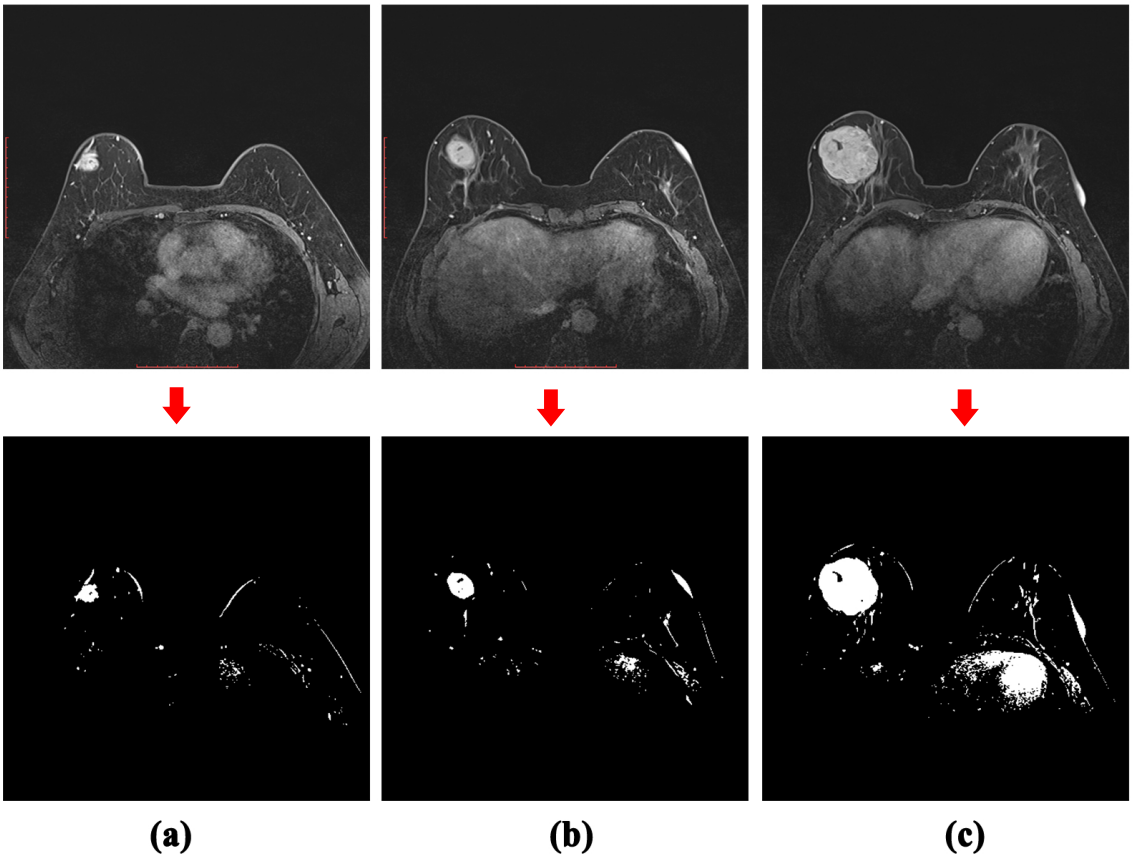

Figure 2.3: Illustration of segmentation carried out with maximum entropy thresholding in breast MRI image.

mentation process in the medical imaging area. Fig. 2.3 illustrates the effectiveness of maximum entropy thresholding during the segmentation of medical images. We have experimented this technique with the breast MRI image having a tumor. The experiment shows that if the parameter is adjusted, a good segmentation result can be obtained.

2.2 Edge based Segmentation technique

Edge is considered as one of the most important information regarding the shapes of the objects in an image. The images contain several objects in different forms such as linear and circular. The different objects have a variety of image gray level and geometric properties. Using these image features, the extraction of important areas is carried out incorporating computer vision, image processing algorithms and object recognition ap-

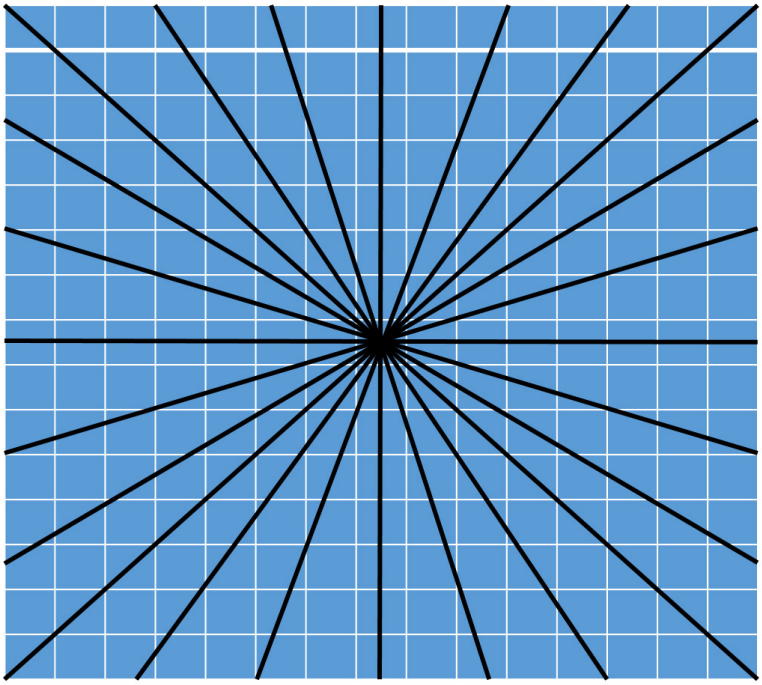

Figure 2.4: A generalized line detection [4]

plications. There are several edge detection techniques [66]. This section describes some of the important edge based technique.

2.2.1 Linear structure detection

Linear structure detection is an effective method to segment linear structures in medical image [67]. The basic line detection is illustrated in Fig. 2.4. At each pixel position (i, j), an average gray level is computed on the window of size WxW pixels. Twelve lines of length W pixels at 12 different orientations with an angular resolution of 15 degrees passing through the centered pixels are identified as shown in Fig. 2.4. The gray level of each line is calculated and the line with the highest level is selected as the winning line [4].

On the other hand, the line detection operation is carried out by using the kernel as per the orientation and particular width of the line [4]. Let us consider a line response of single pixel width and line kernels with directions of $0°$, $45°$, $90°$and $135°$as shown below,

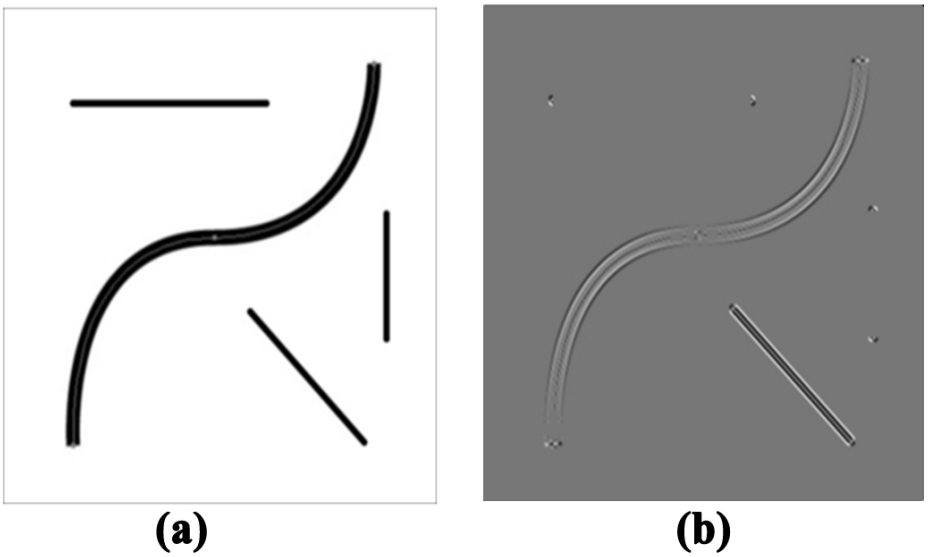

Figure 2.5: Illustration of line detection:single pixel width and +45°orientation

respectively.

$$\begin{bmatrix} -1 & -1 & -1 \\ 2 & 2 & 2 \\ -1 & -1 & -1 \end{bmatrix}, \begin{bmatrix} -1 & -1 & 2 \\ -1 & 2 & -1 \\ 2 & -1 & -1 \end{bmatrix}, \begin{bmatrix} -1 & 2 & -1 \\ -1 & 2 & -1 \\ -1 & 2 & -1 \end{bmatrix}, \begin{bmatrix} 2 & -1 & -1 \\ -1 & 2 & -1 \\ -1 & -1 & 2 \end{bmatrix}$$

Fig. 2.5 shows the illustration of general line detection. Fig. 2.5 (a) and (b) are the original image and the response image using kernel +45°and single pixel width respectively. It is observed that the horizontal and vertical lines are not detected however, the lines with the 45°orientations are clearly detected. In the medical image, segmentation of thread-like structures such as blood vessels is vital. Hence this technique can be used for the detection of such structures. Fig. 2.6 show the blood vessel detected in different orientations. Fig. 2.6 (a) is the original green channel retinal image. (b),(c), (d) and (e) is the response images in four different orientation. This method is especially effective in detecting the thin structures which are difficult to segment.

2.2.2 Hough transform

Hough transform is the popular feature extraction technique which can be used for the segmentation of certain shapes such as line, circle and eclipse by the voting process [68] [69]. Furthermore, the algorithm can be extended to extract a more complicated shape. In medical image segmentation, Hough transform can be a used to extract several important

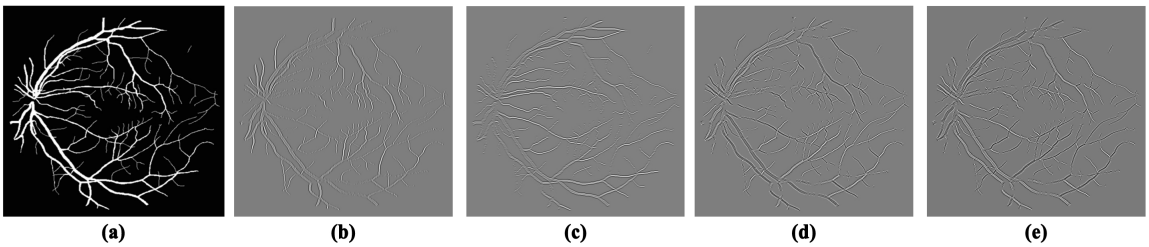

Figure 2.6: Illustration of line detection in 4 orientation: medical image (fundus photography). Line kernels with directions of (a)90°(vertical) (b)180°(horizontal) (c) 45°(d) 135°as shown below, respectively

landmarks.

Let us consider a line segment AB as shown in the Fig. 2.7 and a single edge point (x, y) in a line segment AB. There could be the infinite number of lines which passes through this selected point. Each line can be represented as shown in Eq. (2.12)

Figure 2.7: A generalized line segment

$$y = mx + b \tag{2.12}$$

Where m is a slope, b is a y-intercept. Any line that passes through the edge points (x, y) can be characterized in the slope-intercept space (m, b). Therefore, all lines that pass through points (x, y) have a unique value for y intercept b, for every m. The y intercept is derived from the equation as shown in Eq. (2.13)

$$b = y - mx \tag{2.13}$$

In (m, b) space, the set of (m, b) values forms a line in (m, b) space. The voting process is carried out on every point for each possible line passing through it and counted in the accumulator. The line with the highest number of vote is then selected. The process can be extended to detect the circle as well. Initially, we need to parameterize the circle of the

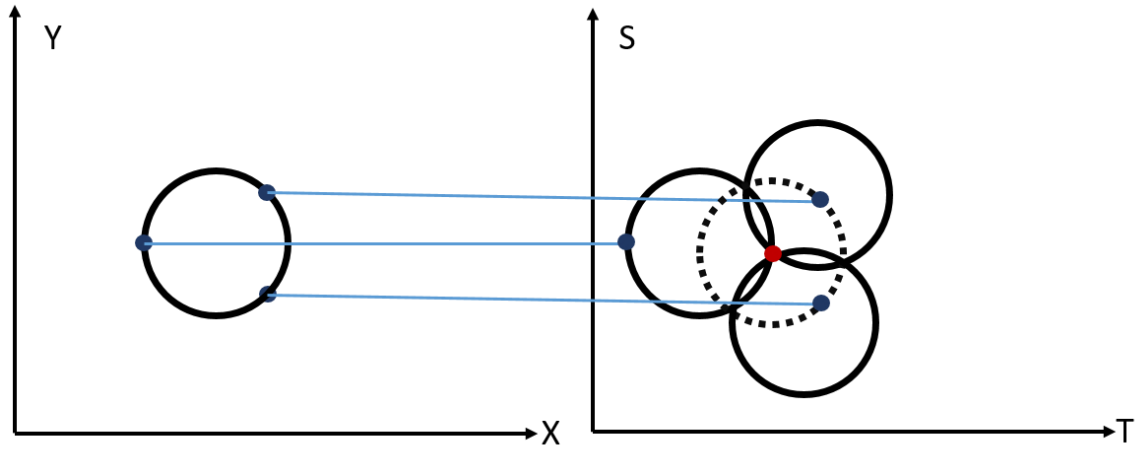

Figure 2.8: A generalized line segment

arbitrary size (x, y, R). Now the objective is to find the (a, b) coordinates of the centers which are calculated as shown in Eq. (2.14).

$$\begin{aligned} a &= x - Rcos(t) \\ b &= y - Rsin(t) \end{aligned} \tag{2.14}$$

The locus of point (a, b) of the circle should have the center of the circle at one point. The circle around the edge point with the common center is counted in the accumulator. The object with the highest vote will be selected as a required circular object.

The common steps that are followed by the Hough transform are given below:

1. Estimate the anticipated feature points in the image.
2. For each feature point, observe the possibility that passes through the feature point and counts the vote in the accumulator. Every shape has to be parameterized accordingly.
3. Find the local maxima of the vote. Select the desired one and reconstruct it into image space.

The illustration of the most prominent circular object detected using Hough transform in the given radius limit is shown in Fig. 2.9. In this figure, the optic disc is detected from the retinal fundus image using a circular Hough transform.

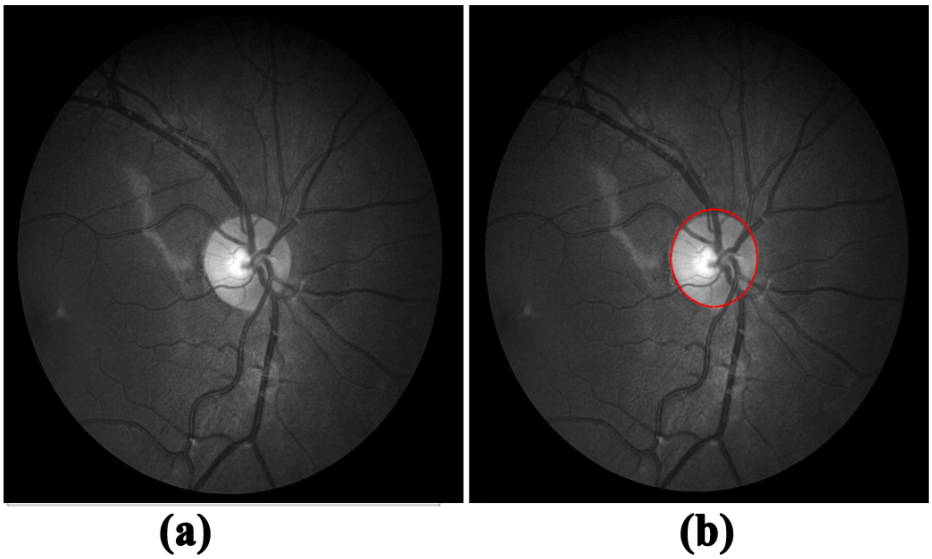

Figure 2.9: Illustration of circular object detection using hough transform in medical image.

2.3 Clustering based segmentation technique

Clustering is an unsupervised learning problem which deals with detecting a structure in a collection of unlabeled data [70]. The objects which are similar in some way are grouped together as shown in Fig. 2.10. Here the object is identified with the two criteria 1) distance and 2)color. If the distance of the two or more object is close, they are clustered in the same class. This clustering technique based on the closeness of the object is referred to as distance-based clustering. Clustering can be done based on the features of two or more objects. If the features of objects are similar, they are clustered at the same cluster. In Fig. 2.10, it is clustered according to the color intensity feature of objects. The main purpose of clustering is to determine an inherent group from unlabeled data. The clustering requires the criteria to be defined by a user so that it fits a problem to produce the best result.

Clustering algorithms are classified as 1)Exclusive clustering [71] 2)overlapping clustering [72] 3)hierarchical clustering [73] 4)probabilistic clustering [74]. Firstly, the object belonging to the definite cluster cannot be assigned to another cluster. i.e the data are clustered in an exclusive way. Secondly, in overlapping clustering, each point may belong to the different cluster but with the different degrees of membership. It used fuzzy sets of cluster data. Thirdly, the hierarchical clustering algorithm is based on the union

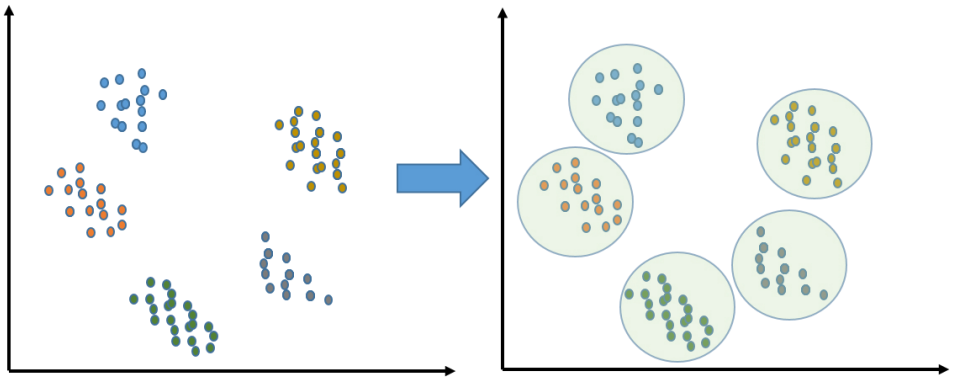

Figure 2.10: Representation of cluster

between the two nearest clusters. Finally, if the clustering is based on a completely probabilistic approach, then it's called probabilistic clustering.

In the following section, some of the important clustering approach used for the segmentation is explained.

2.3.1 Fuzzy C means clustering

Fuzzy C means (FCM) clustering is based on the minimization of the following objective function Eq. (2.15) [75] [76]. The center of the cluster is calculated as shown in Eq. Eq. (2.16) using the membership matrix, U_{xy}. The membership matrix is updated according to the position of the cluster centre. The change in the membership matrix is calculated and compared with old membership matrix. If the objective function is minimized, the process is stopped otherwise a new center of clusters is determined and membership matrix is updated according to the new centers. The process continues until the objective function is minimized as shown in Eq. Eq. (2.15).

$$O_m = \sum_{x=1}^{N} \sum_{y=1}^{C} U_{xy}^{m} ||z_x - C_y||^2, 1 \leq m \leq \infty \tag{2.15}$$

where N and C are the number of data points and number of cluster centers respectively. U_{xy} represents the membership function of $x^(th)$ data and $y^(th)$ cluster center.m and C_y are the fuzziness index ≥ 1 and $y^(th)$ cluster center. The membership function U_{xy} and

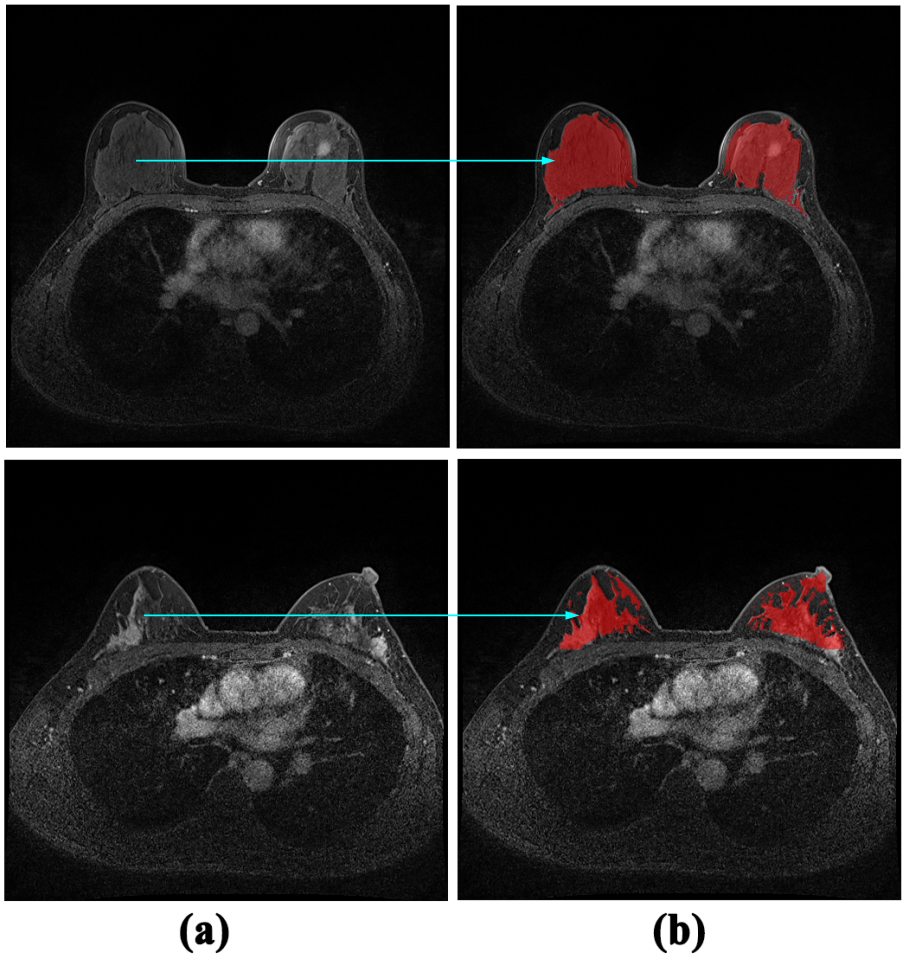

Figure 2.11: Illustration of 3 level FCM. (a) Original MRI image (b) Segmentation of breast density using FCM

cluster centers C_y are calculated as shown in Eq. (2.16) and Eq. (2.17):

$$U_{xy} = \frac{1}{\sum_{z=1}^{C} \left(\frac{||z_x - C_y||}{||z_x - C_z||}\right)^{\frac{2}{m-1}}} \tag{2.16}$$

$$C_y = \frac{\sum_{x=1}^{N} U_{xy}^{m} . z_x}{\sum_{x=1}^{N} U_{xy}^{m}} \tag{2.17}$$

The membership function U_{xy} and cluster centers C_y is calculated and repeated unless $max_{ij}\{|U_{xy}^{z+1} - U_{xy}^{z}|\} < \epsilon$, where ϵ is the termination iteration between 0 and 1. Each pixel of the image is assigned to the respective cluster with the highest membership value. FCM can be used for the segmentation of various landmarks in medical images. Figure Fig. 2.11 shows the illustration of breast density segmented using level 3 FCM [77]. First

column depict the original breast MRI and the result obtained from FCM is shown in second column. The experiment shows that FCM could be a useful tool for medical image segmentation.

2.3.2 Kmeans clustering

Kmeans clustering is a simple clustering technique with low computational complexity and the produced cluster do not overlap [78]. This unsupervised technique is widely used to solve low-level image segmentation problems. For 'K' clusters, the algorithm calculates the initial cluster centers 'Ck' randomly. Then, the distance between cluster centers and each pixel is calculated. There are several methods to calculate the distance. However one of the most used methods is Euclidean distance. The pixel is assigned to the nearest cluster. Once all the pixels are assigned to the initial centers, the centroid is updated and the distance between the updated center and the pixels are calculated [79]. The process is repeated until there is no change. Let us consider an image $I(x, y)$. The image has to be divided into k number of cluster. Kmeans clustering is applied according to the following steps.

1. Initialize the number of cluster k, randomly. Also the centre for each cluster C_k is calculated.

2. For each pixel, Euclidean distance d is calculated between the centre and each pixel of an image as shown in Eq. (2.18).

$$d = ||p(x, y) - c_k|| \tag{2.18}$$

3. The pixels are assigned to the nearest centre.

4. After all the pixels are assigned to the clusters, the new centroid is calculated as shown in Eq. (2.19)

$$C_k = \frac{1}{k} \sum_{y \in C_k} \sum_{x \in C_k} p(x, y) \tag{2.19}$$

5. Repeat the process until same results are obtained.

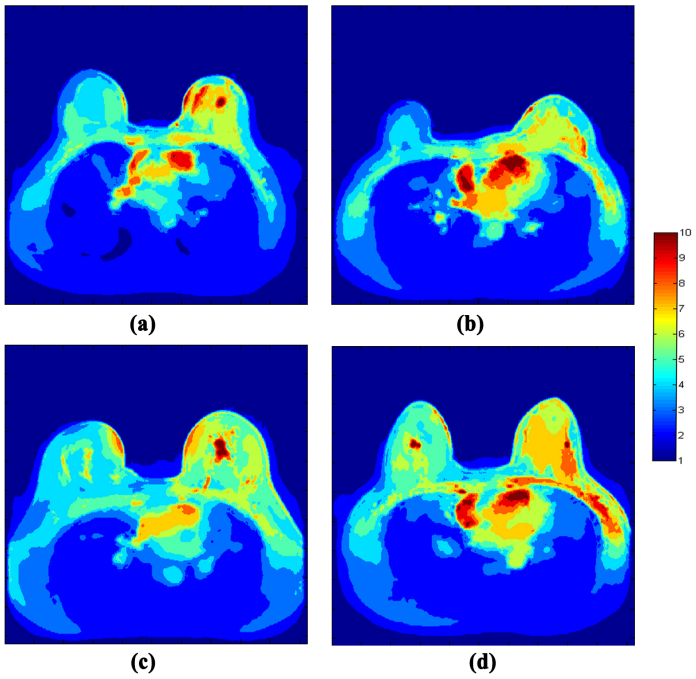

Figure 2.12: Illustration of 10 cluster K-means in Breast MRI image

Figure Fig. 2.12 presents the color distribution of cluster produced by 10 cluster K-means. This algorithm seems to be very effective for medical images and is widely used. In Figure Fig. 2.12, blue color in the color bar (k=1) signifies the darkest and red color (K=10) represents the brightest intensity. The 1st and 2nd cluster represent air background and partial lung area respectively. Moreover, clusters 3 to 10 characterize breast region of interest (BROI), pectoral muscle, heart, some region of lung and breast density (BD). Hence, most of the useful information can be represented above cluster 3.

2.3.3 Hierarchical clustering

The hierarchical clustering is an algorithm that clusters similar pixels into the same clusters [73]. Each cluster is distinct from each other and the object within the cluster are broadly similar. The process begins by considering each observation as a separate cluster. Secondly, closer clusters are identified and merged together. The similarity of the clusters is measured using different distance metrics. One of the popular and widely used distance metric methods is Euclidean distance. The output of the hierarchical clustering is a dendrogram. A dendrogram is a diagram which shows the hierarchical relationship

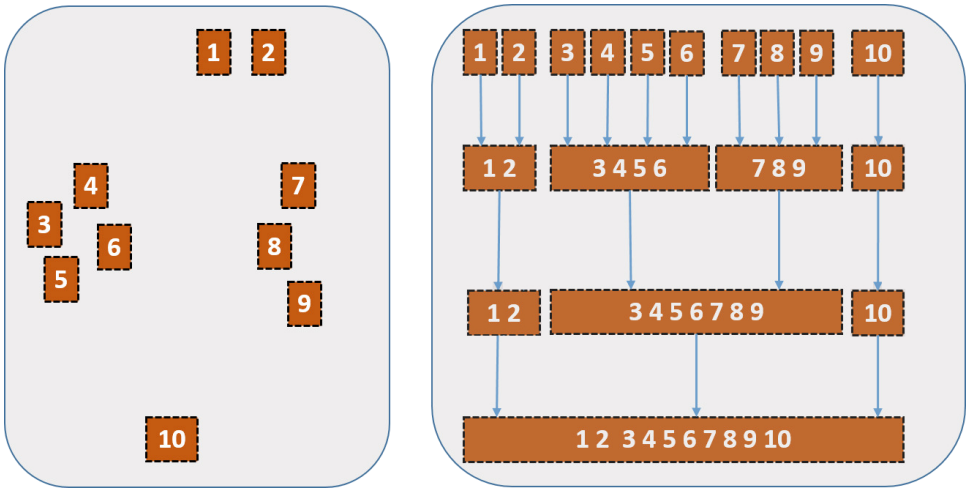

Figure 2.13: Representation of cluster

between the objects in the image. The initial step in the hierarchical clustering is to determine which elements to be merged as a cluster [80]. Hence, we take the closest element considering the shortest distance using the Euclidean distance. Fig. 2.13(a) show the example of hierarchical clustering where raw data are merged together in different steps. After partitioning the second row, the dendrogram provides clusters as {1 2} {3 4 5 6} {7 8 9} and {10} as shown in Fig. 2.13(b). The clustering of third row yields cluster as {1 2} {3 4 5 6 7 8 9} {10}. The measured distance between two clusters can be either complete linking clustering or single linking cluster. Let us consider the two clusters be A and B. The maximum distance between the objects is referred to as complete linking clustering as shown in the Eq. (2.20).

$$\max\{d(x,y) : x \in A, y \in B\} \tag{2.20}$$

Moreover, the minimum distance between the objects of the cluster is also measured which is referred to as a single linking cluster as shown in the Eq. (2.21).

$$\min\{d(x,y) : x \in A, y \in B\} \tag{2.21}$$

2.3.4 Mean shift clustering/segmentation

Mean shift algorithm begins with specifying a window around the data point and calculating the mean of the data point citeaminikhanghahi2017surveyṪhereafter, the center

of the window is shifted according to the mean. It's repeated until it converges. This advanced and powerful clustering technique is used for image segmentation using the generalized kernel approach. During the image segmentation, the image features such as color, gradient, textures, etc is extracted. Based on these features, we initialize windows at the individual pixel locations and the mean is calculated. Finally, until convergence, the mean shift is performed for each window. Also, the windows with the same peak are merged together to produce the final result.

The process of the mean shift algorithm is explained. Let us consider n data points X_i, where $i = 1, ..., n$ on a d dimensional space R_d. The Kernel density estimator calculated with kernel $K(x)$ and window radius h is given by Eq. (2.22).

$$\hat{f_K} = \frac{1}{nh^d} \sum_{i=1}^{n} K(\frac{x - x_i}{h}) \tag{2.22}$$

The mean shift is performed on the class with radially symmetric kernels satisfying the Eq. (2.23)

$$K(x) = c_k k(||x||^2) \tag{2.23}$$

where k(x) is defined as the profile of the kernel for x $\geq$ 0 and c_k represents the normalization constant. Hence, the density gradient estimation is carried out with further algebraic manipulations to achieve as the Eq. (2.24):

$$\hat{\nabla f(x)} = \underbrace{\frac{2c_{k,d}}{nh^{d+2}}[\sum_{i=1}^{n} g(||\frac{x - x_i}{h}||^2)]}_{term1} \underbrace{[\frac{\sum_{i=1}^{n} x_i g(||\frac{x-x_i}{h}||^2)}{\sum_{i=1}^{n} g(||\frac{x-x_i}{h}||^2)} - x]}_{term2} \tag{2.24}$$

where g(x) = -k'(x) represents the derivative of the selected kernel. The term1 is the density estimator at x. The term2 is the mean shift vector (m). m is proportional to the density gradient estimate at point x calculated using kernel k. The mean shift process is summarized in three steps;

Firstly, calculate the mean shift vector $m(x_i^t)$.

Secondly, translate density estimation window: $x_i^(t+1) = x_i^t + m(x_i^t)$.

Finally, iteration of the first and second step is carried out until convergence i.e. $\nabla f(x_i) = 0$.

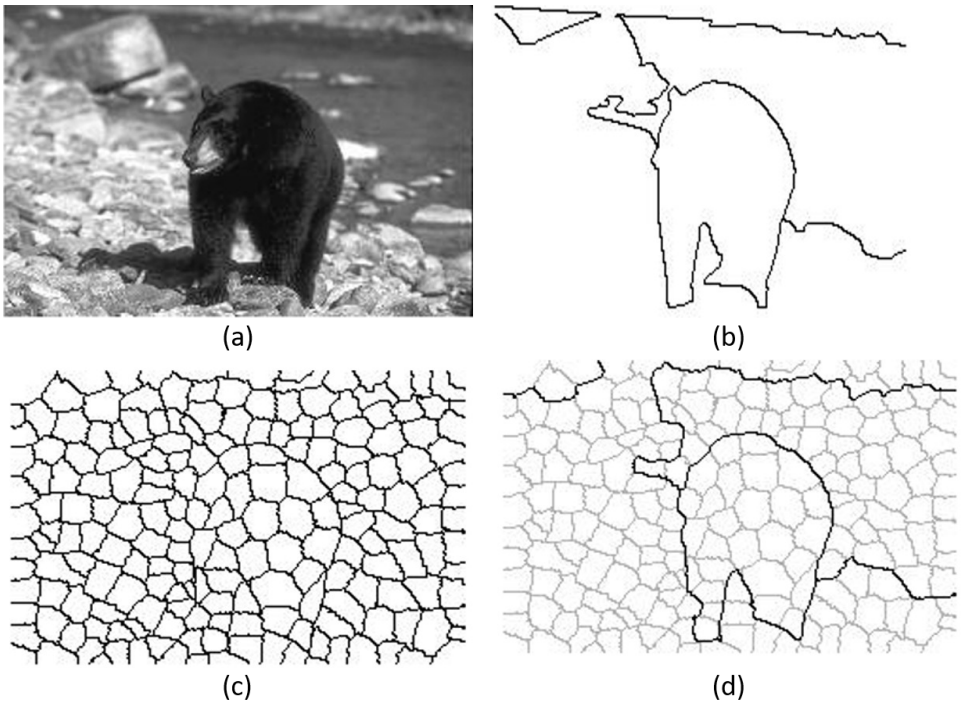

Figure 2.14: Representation of superpixel maps (a) Original Image (b) manual segmentation by expert (c) superpixel map (k=200) (d) reconstruction of the segmentation from superpixel map [5]

2.4 Superpixels based segmentation

In computer vision, many algorithms use pixel-grid representation which cannot represent the real boundary or edges. It would be efficient to detect the meaningful entities by partitioning an image into segments not in grids which are called as superpixels [81]. IT is observed that superpixel map has various advantages during segmentation. First, the complexity of the image is reduced since hundreds of thousands of pixels are converted to few hundreds of superpixels. Hence, it is computationally efficient. Second, most of the structures in the image is preserved because superpixels have resulted from over-segmentation. Hence, while moving from pixel-grid to superpixels map, there will be a little loss.

The example of super pixels is depicted in Fig. 2.14. The comparison of the segmentation obtained from the ground truth is shown in Fig. 2.14 (b). The superpixels in Fig. 2.14 (d) show that most of the structures are preserved i.e. can produce highly accurate segmentation.

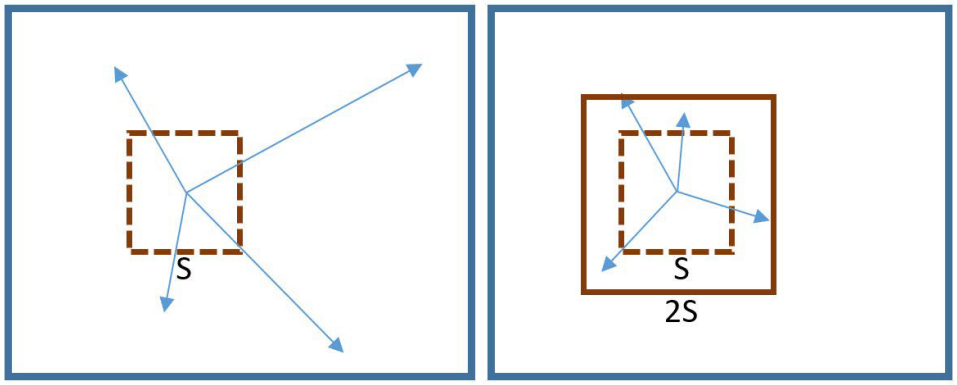

Figure 2.15: Difference between search criteria between standard k-means and SLIC. (a) Kmeans algorithm : distance is calculated from cluster centre to every pixel in the entire image.(b) SLIC computes distance from each cluster centre to pixels and the pixel search are narrowed down within 2S X 2S region.

2.4.1 SLIC superpixels

The superpixels should be fast, easy to implement and produce efficient results. However, the existing state of the art does not satisfy the above-mentioned criteria [82] [81]. Simple linear iterative clustering (SLIC) is a technique to produce superpixels utilizing the local clustering of pixels by adopting kmeans with an important distinction. Firstly, the rate of distance calculation during optimization is reduced. The search space is limited for the area proportional to the superpixels size as shown in the Fig. 2.15. Secondly, the color and spatial contiguity are combined while calculating the weighted distance. This results in control over the size and compactness of superpixels.

In SLIC, the K is considered as the input parameter, which is a preferred number of equal sized superpixels. Let us consider the number of pixels in the image is N. N/K can be considered as the approximate size of each superpixel and $S = \sqrt{(N/K)}$ is the grid interval.

The cluster generation is carried out in $[labxy]$ which is a 5-dimensional space. $[lab]$ is the pixel color vector in CIELAB color space [83] and xy is a normal pixel position. The clustering process begins by choosing the clustering center $C_K = [l_K, a_K, b_K, x_K, y_K]^T$ with the regular grid interval S.

The approximate area of the superpixel is SxS. Hence, we can safely assume that pixels allied with the current cluster centre lie within the area of $2Sx2S$ on xy plane as

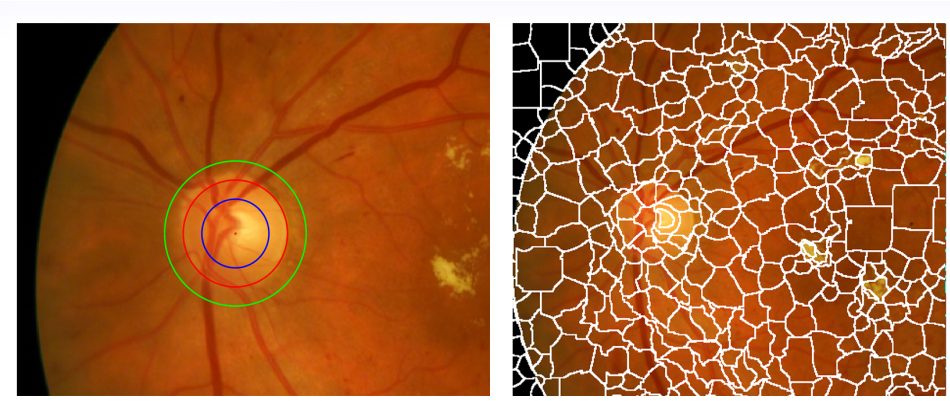

Figure 2.16: Illustration of SLIC algorithm on medical image (Fundus photography)

shown in Fig. 2.15. The search is carried out within this area for the pixel which is near to this cluster centre. Once all the pixels are allied to the nearest cluster centre, the cluster centre is updated and adjusted by calculating the mean vector [lk,ak,bk,xk,yk]T of all the pixels associated within the cluster. The residual error is calculated using L2 norm between new and previous cluster. Finally, the process is repeated until the error converges and Euclidean distances are the popular distance measure in most of the clustering techniques. The, Euclidean distances in CIELAB space are meaningful and works well for the small distance. If the distance surpasses the limit, it begins to outweigh the similarities resulting bad boundaries. Hence, the distance measured in SLIC is followed instead of simple Euclidean norm in 5D:

The distance measure, DMs is defined as follows in Eq. (2.25):

$$\begin{aligned} DM_s &= d_{lab} + (m/S)Xd_{xy} \\ d_{lab} &= \sqrt{(l_k - l_i)^2 + (a_k - a_i)^2 + (b_k - b_i)^2} \\ d_{xy} &= \sqrt{(x_k - x_i)^2 + (y_k - y_i)^2} \end{aligned} \tag{2.25}$$

where, DM_s is the summation of lab distance and the xy plane distance normalized by the grid interval S. m controls the compactness of the superpixels.

Fig. 2.16 show that superpixels generated by SLIC algorithm for the retinal image.

2.5 Region based segmentation technique

The region in the images are defined as the group of connected pixels which has similar properties [84] [61]. Segmentation comprises of partitioning an image into a set of regions based on the similarity. The appropriate thresholding technique is also required for region-based segmentation. The region-based methods are effective with the images having some common properties such as 1) the image with intensity values 2) the unique pattern and textures for each region and 3)spectral profiles of multidimensional image data. These properties are combined and used to produce efficient segmentation. Also, the effectiveness of these techniques depends upon the type of data. The region-based segmentation techniques mainly include the following methods.

2.5.1 Region growing

In the region growing method, the pixels are associated or disassociated to the region [85] [86]. Pixels within the same region are compared for the similarity with the neighboring pixels. The similarity of pixels is measured based on the different features such as intensity, texture, and shape. If the result is positive, the pixel is added to grow the region.

The growing process starts from initially selected pixels from the user. Thereafter, the pixels in the neighborhood are verified whether they belong to the same region. The process is repeated until all the pixels are classified. The process is terminated based on the termination criterion defined by the user. Region growing method often works efficiently then edge-based segmentation.

2.5.2 Region splitting and merging

In this method, two basics techniques: splitting and merging are used for the segmentation of the image into various regions [61] [87]. Firstly, splitting refers to the iteratively dividing an image into several regions having similar characteristics. Secondly, merging refers to combining similar adjacent regions.

Let I be the original image to be segmented. Let all pixels in the region satisfy some similarity constraint. Based on the similarity, the region is split. The process of region

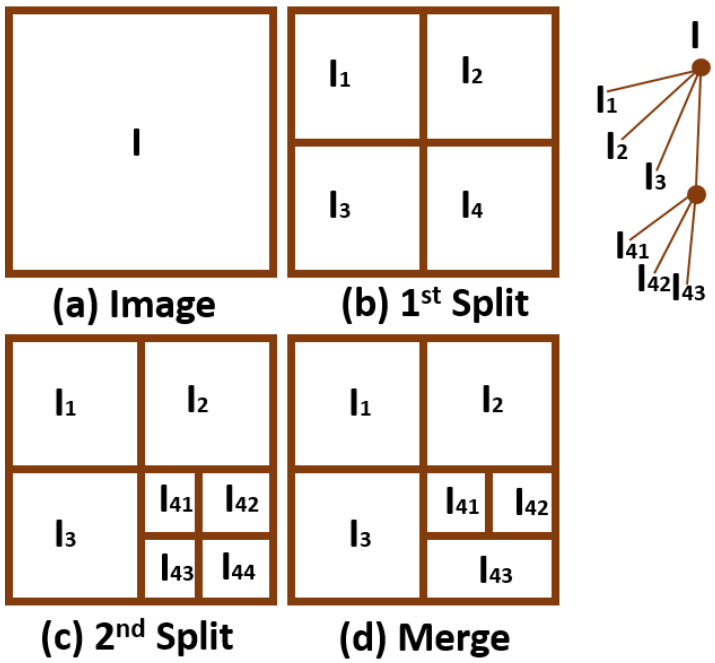

Figure 2.17: Region splitting and merging tree.

splitting and merging is carried out in the following step.

Step1: The region R_1 equals to I.

Step2: Split the images into the different regions $(R1, R2, R3)$ based on the similarity between the pixels in the image, I. However, I_4 is not divided in the step.

Step 3: Let's split I_4, which are not divided in the previous step. Split I_4 based on the similarity between the pixels.

The process is repeated to obtain the best segmentation.

2.6 Deformable method

In the image domain, the defined curve or surfaces are deformed under the influence of internal or external forces. The internal force is defined within the curve or surface and designed to keep the smooth model. The external force is computed from the image data and it assists to move the curve or surface towards an object boundary or features. Deformable models offer robustness against image noise and boundary gaps over the extracted boundary information by integrating coherent and consistent boundary information. The deformable model can achieve sub-pixel accuracy which is highly desirable

for medical imaging application [88] [89].

2.6.1 Parametric deformable model/ Active contour/surfaces

Traditionally known as an active contour model, a parametric deformable model also referred to as snakes are used for delineating the outline of the objects in a noisy image [90]. This model has been widely used in different medical imaging areas for applications like shape recognition, edge detection and especially on segmentation [91]. An active contour model defines a curve or surface that changes its shape and position to satisfy the predefined conditions [92]. Initially, snakes were introduced by Kass et al [93] and use the energy minimization spline guided by the internal elastic energy (constraint force) and external elastic energy (image force) which pulls towards the different shape and edges.

Snake Model

An snake is a curve that changes its location and shape until it satisfies predefined conditions to produce a segmentation [93]. A simple elastic snake C is defined as the parametric curve $C(s) = (x(s).y(s)$. The parameter C varies from A to B, hence all the intermediate points fall within the range. The total energy E uses the sum of three energy terms during the energy minimization process as shown in Eq. (2.26).

$$E = \int_A^B E(C(s))ds = \int_A^B E_int(C(s)) + E_extt(C(s)) + E_c(C(s))ds \tag{2.26}$$

where E_int and E_extt is the internal and external force of the snake. The internal force increases when its bent or stretched. The external force decreases when the snake moves closer to a part of the image.

$$E = \int_A^B \alpha||\gamma^{'}(s)||^2 + \int_A^B \beta||\gamma^{''}(s)||^2 ds - \delta \int_A^B || \bigtriangledown (G_n x I)||^2(\gamma(s))ds + E_c \tag{2.27}$$

Internal elastic energy take into account 1) contour behavior in terms of smoothness and 2) curvature model of the curve. These two terms are defined as the first and second

derivatives of the contour respectively as as shown in Eq. (2.28)

$$E_int = \begin{cases} \oint_C ||\gamma'(s)||^2 + \int_A^B \beta||\gamma''(s)||^2 ds, & \text{if the contour is closed.} \\ \int_A^B ||\gamma'(s)||^2 + \int_A^B \beta||\gamma''(s)||^2 ds, & \text{if the contour is not closed.} \end{cases} \tag{2.28}$$

The movement of the curve depends upon the application and user. Hence, to determine the influence of the movement, the constants α and β are introduced as shown in Eq. (2.29):

$$E_int = \int_A^B \alpha||\gamma'(s)||^2 + \int_A^B \beta||\gamma''(s)||^2 ds \tag{2.29}$$

External elastic energy is defined by the behavior where the snake is attracted by some shapes and edges of the original image. For this purpose, the gradient information can be used since it possesses local extrema and monotonic behavior. Hence, the external elastic force is represented as shown in Eq. (2.30)

$$E_int = \begin{cases} \oint_C || \bigtriangledown I)||^2(\gamma(s))ds, & \text{if the contour is closed.} \\ \int_A^B || \bigtriangledown I)||^2(\gamma(s))ds, & \text{if the contour is not closed.} \end{cases} \tag{2.30}$$

Where I is an input image and $\bigtriangledown$ is the gradient function.

$$\bigtriangledown I = (\frac{\partial I}{\partial x}, \frac{\partial I}{\partial y}) \tag{2.31}$$

To enforce the convergence to the local minimum, Gaussian smoothing, G_n is introduced as shown in Eq. (2.32)

$$E_extt = -\delta \int_A^B || \bigtriangledown (G_n x I)||^2(\gamma(s))ds \tag{2.32}$$

where δ is a weighting parameter which allows increasing the visibility of the gradient field by the snakes.

Active contour without edges

The segmentation of different landmark from medical images is a tedious task. In traditional active contour methods, the evolution of the contour depends upon the gradient of the image [94] [95]. Active contour without edges is the technique based on Mumford–Shah functional [96] and can evolve and detect boundaries that are not necessarily defined by the gradient. This method can produce an accurate segmentation even for the noisy image [97].

Let us consider two forces of the initial contour C, be $F_1(C)$ and $F_2(C)$. $F_1(C)$ is the force to shrink the contour and $F_2(C)$ is the force to expand the contour. These two forces are balanced when they reach the desirable boundary of the interested object. The minimal partition problem used to minimize an energy is represented in Eq. (2.33) :

$$F(c_1, c_2, C) = F_1(C) + F_2(C) = \int_{inside(C)} |I_o - c_1|^2 dx + \int_{outside(C)} |I_o - c_2|^2 dx \tag{2.33}$$

The iteration process is controlled by level set formulation as shown in Eq. (2.34).

$$\begin{gathered} C = \{(x,y)|\phi(x,y) = 0 \\ F(c_1, c_2, C) = \int_\Omega (I_o(x,y) - c_1)^2 H(\phi) dxdy + \int_\Omega (I_o(x,y) - c_2)^2 (1 - H(\phi)) dxdy \\ + v \int_\Omega |\nabla H(\phi)| \end{gathered} \tag{2.34}$$

Where $H(.)$ is the heaviside function and $I_o(x,y)$ is the input image. To obtain the minimum of F, F's derivatives is found and set to zeros and c_1 and c_2 and ϕ is updated in Euler-Lagrange as shown in Eq. (2.35).

$$\begin{aligned} c_1(\phi) &= \frac{\int_\Omega I_o(x,y) H(\phi(t,x,y)) dxdy}{\int_\Omega H(\phi(t,x,y)) dxdy} \\ c_2(\phi) &= \frac{\int_\Omega I_o(x,y)(1 - H(\phi(t,x,y))) dxdy}{\int_\Omega (1 - H(\phi(t,x,y))) dxdy} \\ \frac{\partial \phi}{\partial t} &= \delta(\phi)[v div(\frac{\nabla \phi}{|\nabla \phi|}) - (I_o - c_1)^2 - (I_o - c_2)^2] \end{aligned} \tag{2.35}$$

where $\delta(.)$ is the Dirac function.

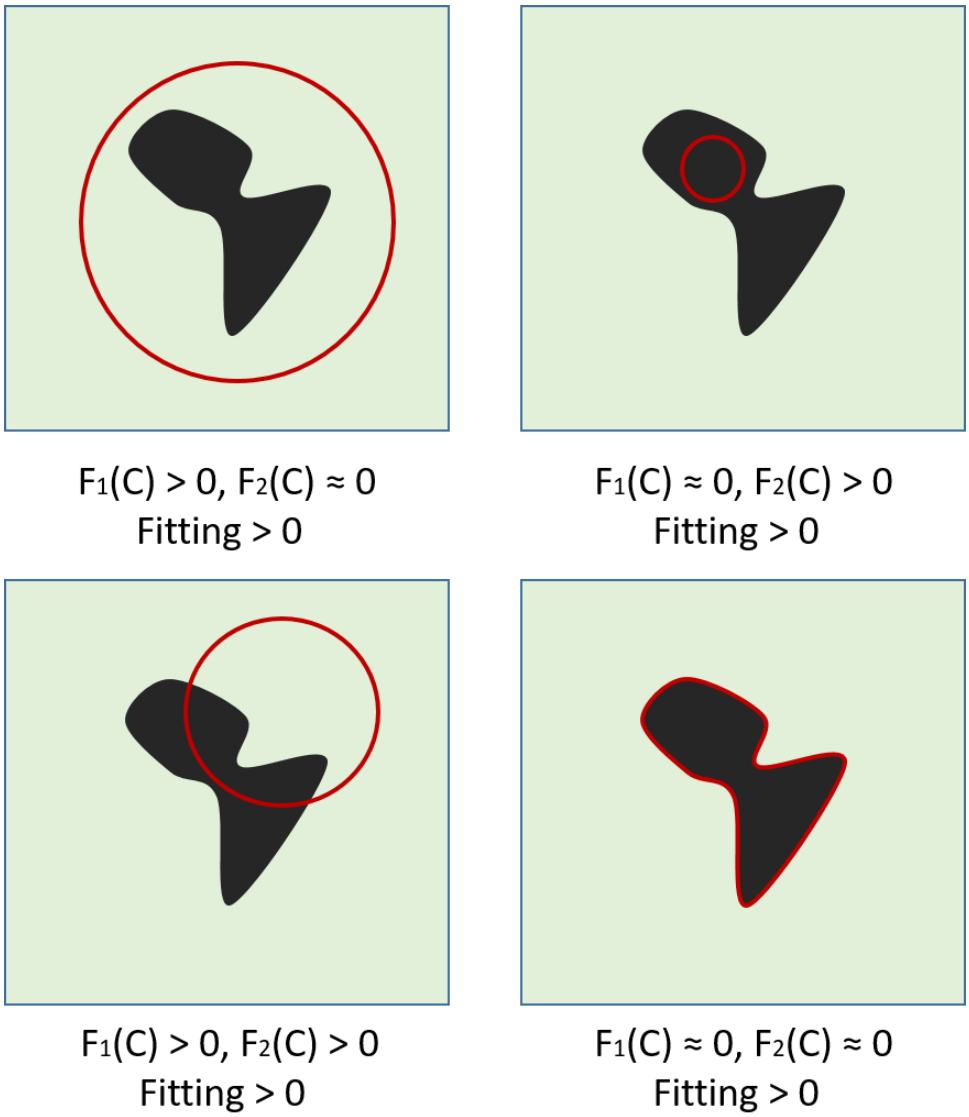

Figure 2.18: Region splitting and merging tree.

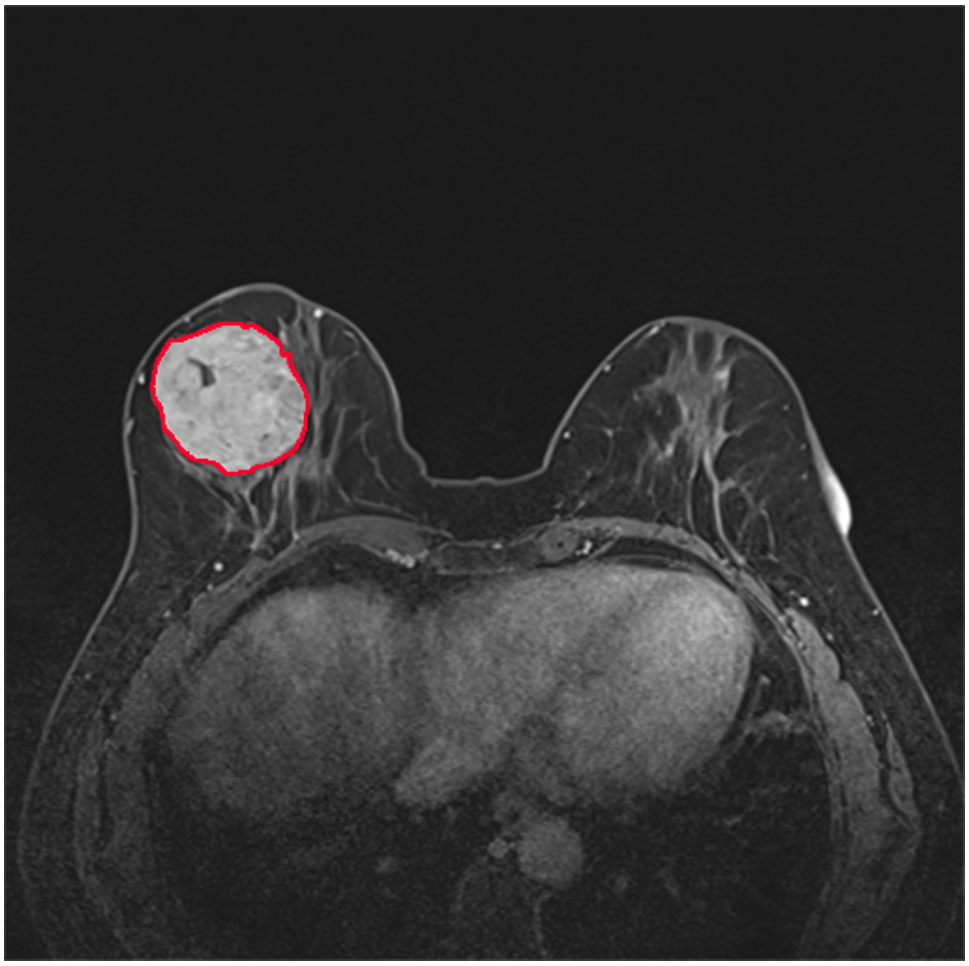

Figure 2.19: Boundary extraction using Active contour without edges.

Fig. 2.18 shows the evolution of contour in different scenarios. Let us consider everything in black as -1 and rest as $+1$. C_1 and C_2 in the Eq. (2.33) is interpreted as the mean value within and outside the contour C respectively. The I_o represents the entire image. Fig. 2.19 shows the minimization of energy. There are four different cases discussed.

1. If the initial contour C is outside the object, $F_1(C) > 0$ and $F_2(C) \approx 0$.

2. If the initial contour C is inside the object, $F_1(C) \approx 0$ and $F_2(C) > 0$.

3. If the initial contour C is both inside and outside of the object, $F_1(C) > 0$ and $F_2(C) > 0$.

4. IF the initial contour C is on the boundary of the object i.e the energy is minimized $C = C_0$, $F_1(C) = 0$ and $F_2(C) = 0$.

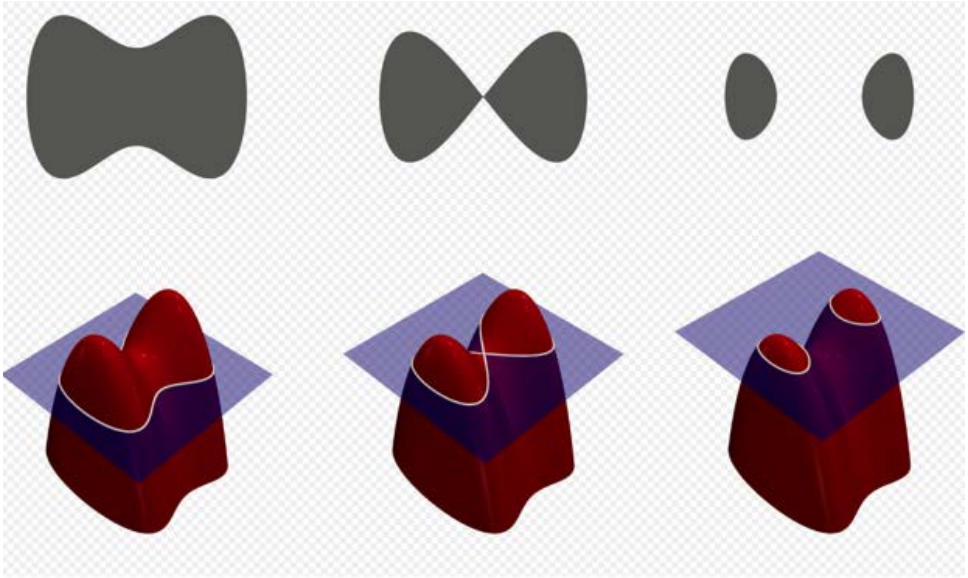

Figure 2.20: Region splitting and merging tree.

Fig. 2.19 shows the segmentation obtained from active contour without edges. the boundary of the lesion from breast MRI image is obtained in 10 iterations.

2.6.2 Non-parametric deformable model/ Level set method

The non-parametric deformable model/ Level set method is used as a tool for the numerical analysis of surfaces and shapes without using object parameterization [98][99]. This method is effective especially for the shapes that changes its topology i.e. time-varying objects. When the object splits into two it's difficult to describe the transformation by parameterizing the boundary of the shape.

The illustration of level set methods can be explained from Fig. 2.20.In the figure, the first object in the upper left corner has a distinct and well-behaved boundary. Below that object, a graph of the level set function ψ is plotted that determines the shape of the object depicted by red surface. Similarly, the xy plane is depicted by the blue flat surface. When the shape or contour itself is a set of points in the boundary, the boundary of the shape is then the zero level set of ψ. The object in the upper row is changing its shape and finally splits into two as seen in the Fig. 2.20. The Level set method would be very effective to detect during such deformations.

For a given image I, let $\psi(x, y)$ be the level set function to define the shape or contour. If the contour is zero level set of the level set function, then the contour C becomes

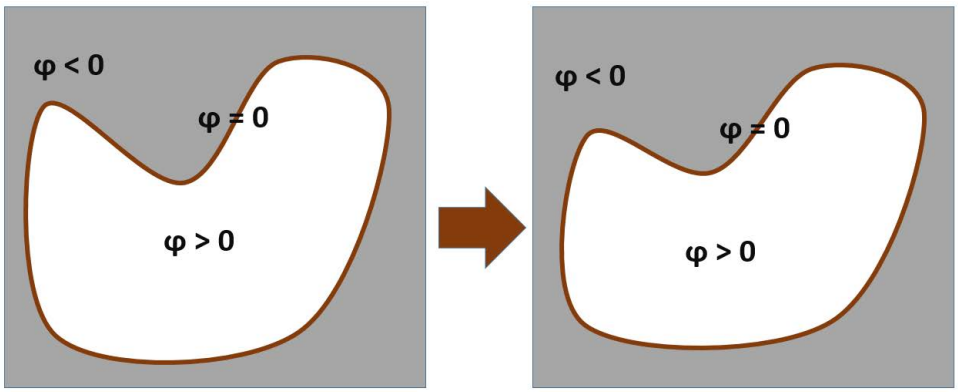

Figure 2.21: Contour change in level set method.

Eq. (2.36):

$$C = \{(x,y)|\psi(x,y) = 0\} \tag{2.36}$$

Moreover, the inside and outside region of the curve are explicitly defined as:

$$\psi(x,y) = \begin{cases} > 0, & \text{inside the contour.} \\ = 0, & \text{contour.} \\ < 0, & \text{outside the contour.} \end{cases} \tag{2.37}$$

The level set function is updated as the values of ψ is changed to fit on the shape of the object as shown in the Fig. 2.21. Some region which has negative values will transform into positive and vice versa.

2.7 Graph based methods

The graph-based method rely on graph partitioning [100] [101]. Image is initially treated as graph G and the vertices of the graph are composed of pixels. The edge of each object in the image has a weight and is determined by the related vertices. Let G be the graph of the image I. Let set of subgraph $SG_1, SG_2, SG_3, ..., SG_n$ is extracted from graph G such that $K \in 1, 2, 3, ..., n, \forall i, j, v_i, v_j \in SG_k$ between v_i and v_j.where $i \neq j$ and v is the vertices. The demonstration of the image segment into the graph is shown in Fig. 2.22. Initially, the pixel of image is assigned with the vertices's to represent the image as graph. Based

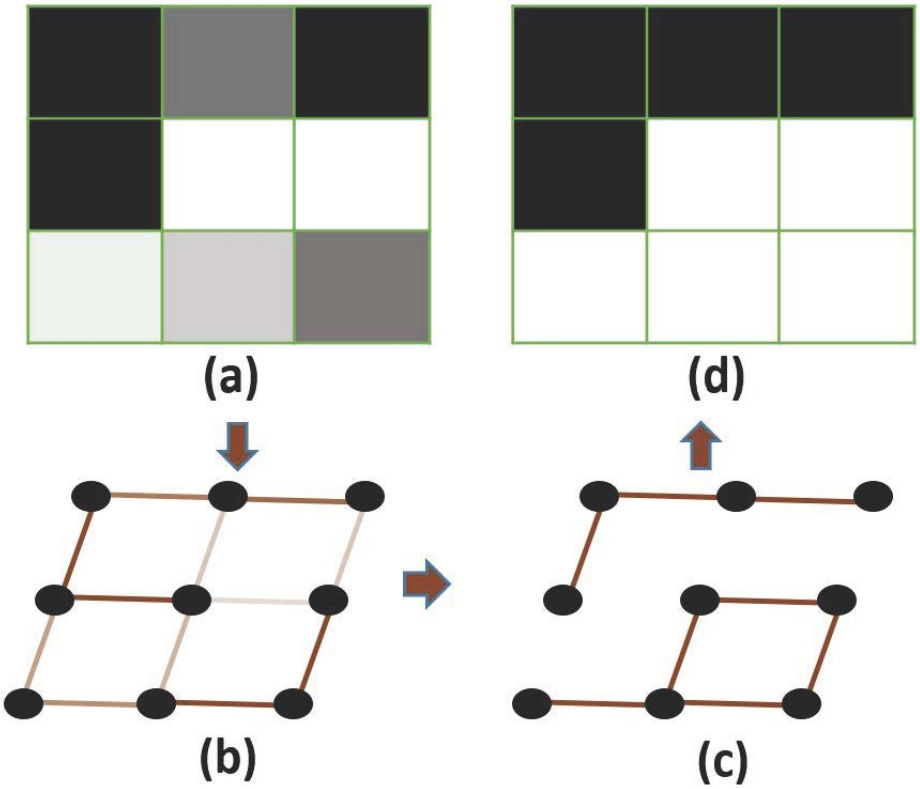

Figure 2.22: Demonstration of graph partitioning (a) Original Image (b) Graph with vertices (each pixel is assigned with vertices) (c) Graph partitioning according to the weight of vertices. (d) Final segmentation image

on the weight of vertices's the graph is either connected or disconnected to create the segment.

2.7.1 Graph cut methods

The graph cut method is popular because of its good mathematical basis and successfully obtained good results in another field of image processing. Graph cut constructs an image-based graph and provides a global optimal solution of energy minimization functions. However, it is computationally expensive because it uses global optimum. Also, the graph cut is known for over-segmentation. Several works have already been done to improvise the graph cut algorithm. To improve the speed of graph cut methods, the algorithms based on the reduction of graph nodes have been proposed in the literature [102]. Watershed algorithm [103] is the widely used approach in the graph cut method that is applied to the gradient image. The watershed algorithm can be used on certain

image section instead of the whole image. Interactive based graph cut method is incorporated with the user interaction to improvise the segmentation results. It is considered to be more effective especially for the target image whose accuracy requirement is high. In this method the interested object areas can be selected either by choosing the interested object area or by selecting the seed point [104]. In [105] [106] follows the interactive graph cut method where seeds are iteratively added until the accurate segmentation is obtained. Similarly, [107] chooses object and background seeds are selected for only one time to construct graphs with a reasonable weight. The graph cut approach is considered better for the objects with a weak background.

Active contours, level sets, live wire, and graph cut are categorized as energy base segmentation methods that establish an objective (energy) function [105] [108]. The energy function reaches a minimum level when the image is segmented. In live wire, users identify seeds and have to be located at the object boundary. The constructed energy function is minimized for the optimization of the curve position. Moreover, in the level set and active contour, the initial curve is provided and based on the predefined curve; a minimum valued energy function is generated. These methods are very sensitive to the initially set curve and utilize boundary information. Also, these methods cannot obtain global optimal results. However, graph cut is a segmentation method where energy function is constructed based on the boundary and region information and can achieve global optimal results.

Consider a graph $G = (V, E)$ where V denotes a series of vertices and E denotes edges of the graph. Each vertex V is composed of two types of nodes. 1. Neighborhood node (pixel in the image) and 2. Terminal node (s-source and t-sink). Neighborhood node relates the pixels and terminal node consists of a source (s) and sink (t). The graph is called a $s - t$ graph where s is a foreground (an object that is segmented) and t is the background mode.

Edges E are also of two types 1. $n - link$ that are related to neighboring pixel and $t - link$ that are related to the terminal pixel. Each edge is assigned to a non-negative weight, which is also known as cost. Cost is a summation of all weights W_e of edges and denoted by $|C|$.

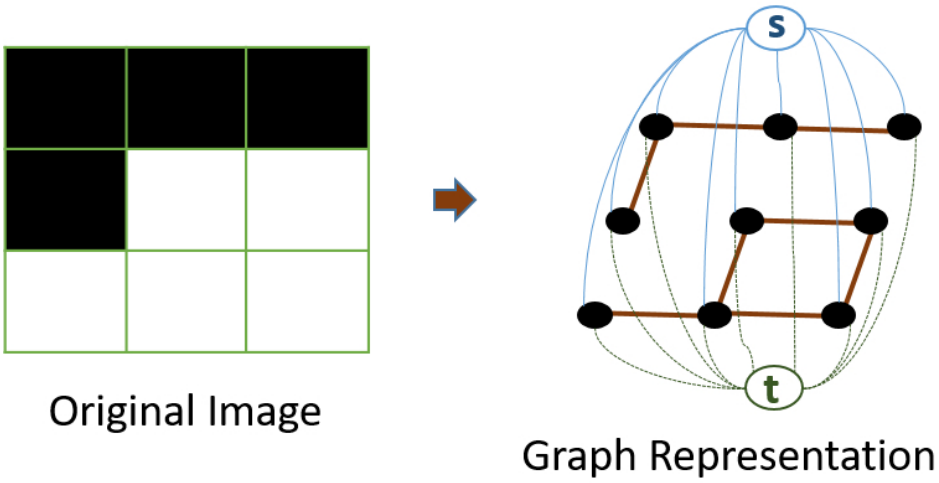

Figure 2.23: Illustration of s-t graph

$$|C| = \sum_{e \in C} W_e \tag{2.38}$$

The cut with the minimum cost is called min-cut calculated by achieving maximum flow. Fig. 2.23 shows the graph obtained from the s-t graph to get the minimum cut by dividing the graph. The curve is divided into two disjoint subsets S and T $s \in S$, $t \in T$ and $S \cup T = V$. S and T corresponds to the object and background.

2.8 Conclusion

In this chapter, we reviewed popular segmentation techniques which are widely used in the analysis of multidimensional medical image analysis. Multidimensional image analysis is becoming more popular and can be used for the identification of several diseases from the image generated from the different imaging source.The algorithms should be carefully designed so that the final anatomical structure is not lost in the image. Also, robustness, precision, accuracy and time consumption to produce result should be considered while developing algorithm. Hence, we take an advantage of several methods to develop a framework to produce the required output. Some of the important techniques which are explained in this chapter are being used in our work. Hence, we will get into more details about some techniques in the succeeding chapters.

Chapter 3
Accurate Blood Vessel Segmentation

3.1 Introduction

THE manifestation of diseases in retinal images is an important investigative indicator of various medical syndromes in relation to eye and body. The ophthalmic diseases such as diabetic retinopathy [109], [110], retinal artery occlusion [111] and choroidal neovascularization [112] could be identified from the different characteristics of blood vessels. To identify these features, blood vessel segmentation is an important and primary step. There are two ways of blood vessel segmentation: manual and automatic [113]. Manual segmentation of blood vessels in an image is complex and exceptionally time consuming that requires training and skill. Hence it is commonly acknowledged by the medical community that automatic segmentation is significantly valuable for accurate and speedy identification of blood vessels. It is vital to have automatic and accurate segmentation algorithm for retinal images to develop a diagnostic system for the treatment of ophthalmic disorders.

Several solutions have already been proposed for segmentation of retinal vessels. Preceding research on the development of methods for blood vessel segmentation can be categorized as supervised [114], [115] or unsupervised segmentation [116] - [117]. Segmentation with supervised methods is basically reliant on training sets such as manually

This chapter is derived from:

- **D Pandey**, X. Yin, H. Wang, and Y. Zhang, "Accurate vessel segmentation using maximum entropy incorporating line detection and phase-preserving denoising" *Computer Vision and Image Understanding*, Volume 155, Pages: 162-172, 2017.

segmented gold standard classifications. The information is used to differentiate retina images as vessels or non-vessels. In supervised segmentation methods, a training process such as support vector machines (SVMs) [118], [119], k-nearest neighbors [120], artificial neural networks (ANN) [121], Gaussian mixture models (GMM) [122], [123] are implemented. In contrast, unsupervised segmentation methods are independent of training datasets, hence are more appropriate to a broader range of imaging modalities. Unsupervised segmentation techniques have been proposed by a wide range of approaches such as texture mapping [117], thresholding techniques [124], vessel tracing/tracking [125], [126], multi-scale approaches [127], model based approaches [128], [129], active contour models [130], morphological processing [131], [132], and matched filter approaches [133]. Also, each retinal image shows unique properties with respect to retinal boundaries, optic discs and different diseases [134]. Moreover, vessel crossing [135], bright or dark lesions [136], low contrast [137], uneven illumination [138], and noise [139] further complicate the segmentation process for an accurate result.

A line detector proposed by [118] calculates the average pixel intensity of lines in different orientations and the line with highest average intensity is selected. This technique is effective in dealing with the vessels comprising central light reflex, especially for the long lines. In [118], the length of line detector is fixed. Hence, when two vessels are closer, it tends to merge together. Also, it produces false vessels at vessel crossovers. A solution was proposed by [8] using generalized multiscale line detector by varying a length. A shorter line length can be detected efficiently but introduces background noise in the segmented results. Moreover, the same weight assigned for the different line length in [8] produces considerably higher noise and the false vessels near optic disc. It is also observed that the method is ineffective in dealing with the pathological images with bright or dark lesion. Hence the issues observed in the current state of the art that restrict in developing an accurate vessel segmentation algorithm can be summarized as: I) Both non-uniform illumination and background noise of the images are responsible for false vessels. II) Detection of dim and thin vessels in retinal images is a greater challenge. Very few researcher treat thick and thin vessels separately, which results in higher false positives. III) Closer vessels are merged. IV) Most of the blood vessel segmentation algorithms assume that retina is healthy and free of bright and dark lesions [7]. How-

ever, the existence of bright or dark lesions can considerably degrade the performance of blood vessel segmentation and even make the result unusable due to detected lesions. To overcome the aforementioned problem, we propose an accurate retinal blood vessel segmentation method. The underlying technique of proposed solution involves summation of filter responses while detection of centerlines in different orientations. Generally, for line detection twelve different orientations are involved [8], [140], [141]. However, it is suggested in [142], four different orientations are sufficient to detect the blood vessels with reduced computational complexity. In addition, phase-preserving denoising technique before the centerline detection is highly effective especially for the accurate detection of thin and dim vessels with significantly reduced noisy pixels.

The original RGB retinal images consist of red, green and blue channels. Red channel is the brightest color channel and blue channel displays poor dynamic range. Thus, detailed blood vessels are not represented. In contrast, green channel exhibits highest contrast between blood vessels and background. Hence, green channel image is selected for retinal blood vessels segmentation method [143]. The process begins with a preprocessing step to eliminate non-uniform illumination and noise in fundus image. This step includes background estimation and subtraction. The background estimation is carried out with a morphological opening approach and subtracted from the green channel fundus image. It aims in reduction of drastic variation of illumination and noise existed in the fundus images during pixel classification. Furthermore, optic disc and pathological regions such as bright lesion are treated as background during estimation since these pixels are brighter than the blood vessels and background. Additionally, we contribute a method to accurately segment thin and thick blood vessels from retinal fundus images. Thick blood vessels are clear, distinct and easier to detect while thin vessels are smaller in size, dim and show bad contrast. It is also observed that the gray level intensity and geometrical correlations between thin and thick vessels are different. Hence, thick and thin blood vessels have different characteristics and needs to be segmented using separate approaches. To handle thick vessels, our approach uses threshold technique which can change the threshold value according to the image property. However, in order to detect thin vessels, the proposed approach utilizes a basic line detection method incorporating a phase-preserving denoising technique, local normalization and maximum entropy.

phase-preserving denoising method significantly removes the noise closer to the blood vessels and line detection methods detects the detailed blood vessel from the denoised image. Local normalization is further used to correct the remaining non-uniform illumination in an image. Our algorithm is efficient, computationally fast and evaluated with four publicly available databases: the DRIVE database [144], the STARE database [145], the CHASE_DB1 [146] and High-resolution fundus image (HRF) [147]. The outcome of our method is compared with the recent results produced in the literature which confirms that our method outperforms the existing solutions.

Rest of the chapter is structured as follows. A detailed review of the models used for retinal vessel segmentation is discussed in Section 3.2. Section 3.3 provides an explanation of the new proposed method. In section 3.4, experimental results are analyzed and compared to the methods in the literatures. Section 3.5 concludes the work in the chapter.

3.2 Overview of the Approach

In the following section, we explain our motivations to use MRI different models for retinal vessel segmentation.

3.2.1 Retinal background estimation and subtraction

The important and primary pre-processing step in our algorithm is background estimation. This process normalizes and reduces the non-uniformed intensity distribution. The normalized image is obtained by the subtraction of background estimation from an inverted green image. The background estimation is acquired by performing a morphological opening operation. The normalized image is computed using Eq. (3.1).

$$I_1 = I_g - I_{bg} \tag{3.1}$$

where I_1 labels normalized images , I_g labels inverted green images and I_{bg} labels background estimations. The background estimation satisfies Eq. (3.2).

$$I_{bg} = \cup\{(S_e) \mid (S_e) \subseteq I_s\}, \tag{3.2}$$

where S_e indicates a disc shaped structuring element with radius of R, I_s is the set of I_g and $\cup$ denotes union of set. The background estimation I_{bg} is given by geometric interpretation where unions of all translations of structuring elements S_e fit the entire image I_g. Therefore, the size of S_e must be estimated such that its value is larger than the width of the blood vessel. The width of the vessels is not likely greater than 15 pixels as per our observation, so we have considered the size of S_e as 15.

3.2.2 Local Phase-Preserving denoising of retinal images

Denoising process involves transformation of noisy images into some domain where noise components are more easily recognized. To remove noise, a thresholding procedure is implemented and the transformation is reversed to reconstruct a noise-free image. The denoising method is associated with a complex valued log Gabor wavelet filter where amplitude information is decomposed while preserving important phase information of an image [148]. The process begins with calculating amplitude and local phase data at each point of a retinal image. This is performed by utilizing log-Gabor wavelet filter [149] that has a Gaussian transfer function viewed on a logarithmic frequency scale. The amplitude information of the wavelet filtered image depicts that most of the energy is concentrated in the middle. However, the local phase information is distributed throughout the image over all frequencies. The amplitude or phase information alone is not capable of reconstructing the image efficiently. Hence, we follow the phase-preserving technique while shrinking the amplitude information in different scaling factors and orientations. Let us consider an image $I(x, y)$. The image response for even symmetric (M_n^e) and odd symmetric (M_n^o) wavelets at scale n is given by Eq. (3.3). The amplitude $A_n(x, y)$ and phase $\phi_n(x, y)$ at a wavelet scale n are calculated as Eq. (3.4) and Eq. (3.5) respectively.

$$[Re_n(x, y), Im_n(x, y)] = [I(x, y) \times M_n^e, I(x, y) \times M_n^o] \tag{3.3}$$

where $Re_n(x, y)$ and $Im_n(x, y)$ are the real and imaginary parts of the complex valued frequency component.

$$A_n(x, y) = \sqrt{Re_n(x, y)^2 + Im_n(x, y)^2} \tag{3.4}$$

$$\phi_n(x,y) = \text{atan2}(Im_n(x,y)/Re_n(x,y)) \tag{3.5}$$

While denoising, a noise threshold at each wavelet scale is determined and the amplitude of the filtered vector is shrinked leaving the phase unchanged. Hence, we calculate the complex valued wavelet response by preserving the phase information while shrinking the amplitudes over different wavelet scales and orientations. An image can be reconstructed by summing the remaining even-symmetric filter responses over all scales and orientations. The estimation of noise threshold is determined from mean and variance of Rayleigh distribution. The mean and variance of the Rayleigh distribution $R(x)$ in Eq. (3.7) are given by μ_R and σ_R^2 in Eq. (3.7).

$$R(x) = x/\sigma^2 e^{-(x)^2/2\sigma^2} \tag{3.6}$$

$$\mu_R = \sigma\sqrt{\pi/2}, \sigma_R^2 = \frac{4-\pi}{2}\sigma^2 \tag{3.7}$$

where σ is the scale parameter of the rayleigh distribution.The noise threshold τ_1 is calculated as,

$$\tau_1 = \mu_R + c\sigma_R \tag{3.8}$$

where, c specifies the standard deviation values of noise to reject. It is related to an ideal wave shape. It is assumed that lower value of c produces an ideal wave shape [148]. If the value of c is high, thin vessels are treated as noise and removed. Hence, we tuned the value of c equal to 1.

To make a robust estimation, mean (μ_R) is replaced with the median (M) response of rayleigh distribution,

$$M = \sigma\sqrt{2\ln(2)} \tag{3.9}$$

where M labels median responses. At each scale and orientation, noise threshold is calculated and processed. Finally the reconstructed image which is labeled as I_2.

3.2.3 Linear structure detection

Blood vessels can be observed in all possible orientations and size. It is necessary to select the set of directional filters, whose responses can be merged together, in order to detect retina vessels at all the possible directions. After observation, we found that the particular line kernels with horizontal (0°), diagonal (45°, 135°), and vertical (90°) directions can be used as an alternative to any other conventional line detection solutions [142].

Let us consider line kernels with directions of 0°, 45°, 90°and 135°as shown below, respectively.

$$\begin{bmatrix} -1 & -1 & -1 \\ 2 & 2 & 2 \\ -1 & -1 & -1 \end{bmatrix}, \begin{bmatrix} -1 & -1 & 2 \\ -1 & 2 & -1 \\ 2 & -1 & -1 \end{bmatrix}, \begin{bmatrix} -1 & 2 & -1 \\ -1 & 2 & -1 \\ -1 & 2 & -1 \end{bmatrix}, \begin{bmatrix} 2 & -1 & -1 \\ -1 & 2 & -1 \\ -1 & -1 & 2 \end{bmatrix}$$

We convolve each matrix with the denoised image I_2 to obtained the four different image responses in four directions. All of the filtered responses are merged together to produce final image I_3. Using k_{0°, k_{45°, k_{90° and k_{135° to label the line kernels, the image I_3 can be expressed as:

$$I_3 = k_{0^\circ} * I_2 + k_{45^\circ} * I_2 + k_{90^\circ} * I_2 + k_{135^\circ} * I_2. \tag{3.10}$$

However, there are MRI weaknesses in relation to basic line detection. For example, surrounding vessels are likely to get merged and the extension produced around the cross-sections tends to generate false vessels. To address the above mentioned problems, a phase-preserving denoising method is used, which allows elimination of noise for an image without losing the properties of blood vessels. Because of center light reflex [135], some of the vessels tend to be torn apart that can be observed in the Fig. 3.6(a). In addition, since the width of a line detector is equal to single pixel, some thick vessels cannot be detected. To address these problems, we perform thick vessel detection that will be represented in Section 3.3.

3.2.4 Local normalization

This process uses mean and variance in a local neighborhood to correct the non-uniform illumination or shading artifacts [150] after line detection. In this process, mean and vari-

ance are calculated in each pixel within the locally defined block size of 10×10. Local mean map of the image carries low frequency information and local variance map represents high-frequency information specifically the edge information of image. It is observed that the pixels around the edges show higher local variance values and local mean map is dominated by uneven illumination. After subtracting local mean map from a retinal image, we can adjust the global uneven illumination from the image. Similarly, after dividing it by its variance map, the resultant retinal image allows clear edge with reduced uneven illumination. The local normalization $L(x, y)$ of the image $I_3(x, y)$ that corrects non-uniform illumination or shading artifacts is computed according to Eq. (3.11).

$$L(x, y) = \frac{I_3(x, y) - \mu_{\mathrm{L}}(x, y)}{\sigma_{\mathrm{L}}(x, y)} \tag{3.11}$$

where $\mu_{\mathrm{L}}(x, y)$ and $\sigma_{\mathrm{L}}(x, y)$ are the estimation of local mean and local standard deviation of the input image. After local normalization, denoising technique is used again, which further removes noise with preserved edges as shown in Eq. (3.12).

$$I_4(x, y) = \mathrm{denoise}(L(x, y)) \tag{3.12}$$

3.2.5 Maximum Entropy Thresholding for Binarization

The segmentation of blood vessels from the background images requires an appropriate threshold technique which can change threshold value according to image property. We use maximum entropy to select the optimal thresholding value to binarize the final image. This method utilizes normalized histogram of an image whose value ranges from 0 to 255 to determine the threshold value. Let us consider an grayscale image that requires binarization and let $I_{\mathrm{h}}(i)$ be the normalized histogram of that image where i takes values from 0 to 255 and t indicates the threshold to be determined.

$$\sum_{i=0}^{i_{\max}} I_{\mathrm{h}}(i) = 1 \tag{3.13}$$

Entropy of vessel pixel $H_{\mathrm{vessel}}(t)$ is obtained as:

$$H_{\text{vessel}}(t) = -\sum_{i=0}^{t} \frac{I_{\text{h}}(i)}{\sum_{j=0}^{t} I_{\text{h}}(j)} \log \frac{I_{\text{h}}(i)}{\sum_{j=0}^{t} I_{\text{h}}(j)} \tag{3.14}$$

Similarly, entropy of background pixel $H_{\text{bg}}(t)$ is given as:

$$H_{\text{bg}}(t) = -\sum_{i=t+1}^{i_{\max}} \frac{I_{\text{h}}(i)}{\sum_{j=t+1}^{i_{\max}} I_{\text{h}}(j)} \log \frac{I_{\text{h}}(i)}{\sum_{j=t+1}^{t} I_{\text{h}}(j)} \tag{3.15}$$

Hence, optimal threshold τ_2 by maximizing the background and vessel pixels, can be calculated as:

$$\tau_2 = \arg\max(H_{\text{vessel}}(t) + H_{\text{bg}}(t)) \tag{3.16}$$

The final binary image I_5 using τ_2 is computed as:

$$I_5(x,y) = \begin{cases} 1, & I_4(\text{x,y}) < \tau_2 \\ 0, & \text{otherwise} \end{cases} \tag{3.17}$$

3.3 Proposed vessel segmentation method

The proposed approach to segment retinal blood vessels consists of four steps: A) image pre-processing, B) thin blood vessel detection, C) thick blood vessel detection, and D) image post-processing, as shown in Fig. 3.1. The green channel inverted image is used because it exhibits better contrast between vessels and background.

3.3.1 Image pre-processing

This image pre-processing strategy is to achieve normalized images via separating background images from inverted green channel images. This aims to improve retina image quality via correcting non-uniform illumination. Fig. 3.2 illustrates the effectiveness of the image pre-processing approach. Fig. 3.2 (a), (b), (c) are the inverted green channel image, the background estimated image and the resultant image after subtraction of (b) from (a), respectively. The blood vessels as seen in Fig. 3.2 (a) have been dissolved after estimation of background using morphological opening operation, the result of which is

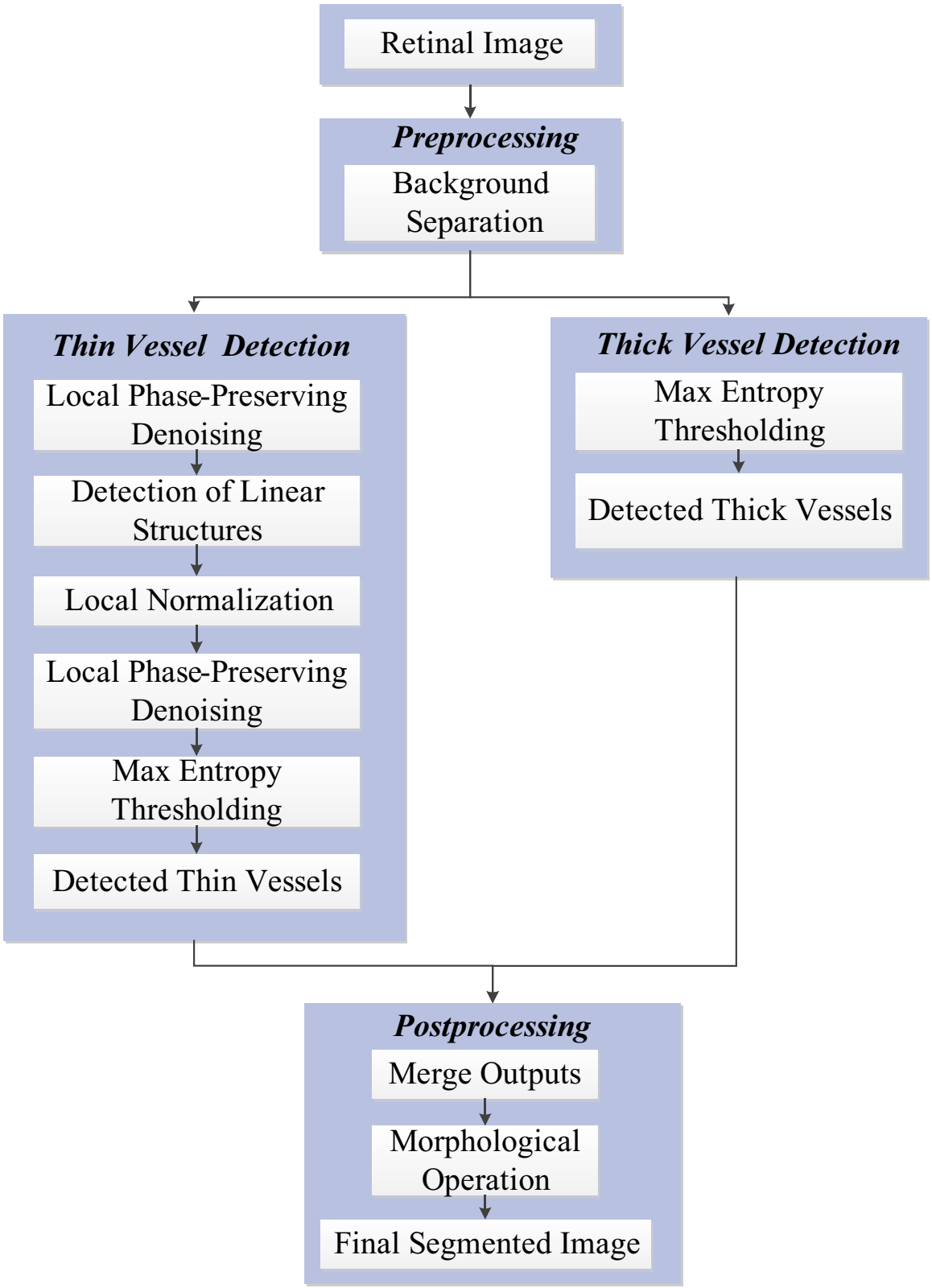

Figure 3.1: The proposed functional diagram of retinal vessel segmentation.

illustrated in Fig. 3.2 (b). After subtracting the estimated background image i.e. subtracting Fig. 3.2 (b) from Fig. 3.2 (a), we obtain the clear blood vessels as shown in Fig. 3.2 (c), where the influence of noise and non-uniform illumination has been reduced and does not contain strong lesions or bright spots as seen in the original image (Fig. 3.2 (a)).

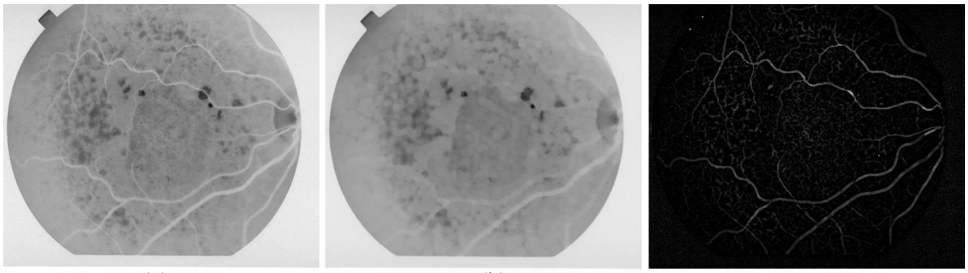

(a) (b) (c)

Figure 3.2: Subtraction of the estimated background from an inverted green channel image. (a) The inverted green channel image. (b) The estimated background image. (c) The resultant image after subtraction of the estimated background from the inverted green channel image.

3.3.2 Thin Vessel Detection

The original retinal image contains MRI types of noises such as photo-electronic noise, impulse noise and structured noise. It is necessary to remove these noises to identify and preserve detailed blood vessel. Therefore, following the preprocessing step, the phase-preserving denoising method is applied before and after the analysis of line structure and local normalization. According to [142], four orientations of the line structure detector (filter) are sufficient to extract the blood vessels from the noise reduced image. To further remove the illumination inequality existing in the extracted blood vessels, local normalization is utilized for image enhancement with corrected and smooth edges of the blood vessels. Furthermore, the resultant image is binarized with the threshold value generated from a maximum entropy method [117], represented in section 2.5. After binarization, the area of each connected component is calculated. At this point, most of the blood vessel pixels are connected with each other. The binarized image contains smooth edged blood vessels including some background noise. To remove the background noise, a morphological dilation operation is performed and the area of each connected component is calculated. According to our experiment with four databases as mentioned before, we found that small areas with size less than 20 pixels were envisioned as noise and are

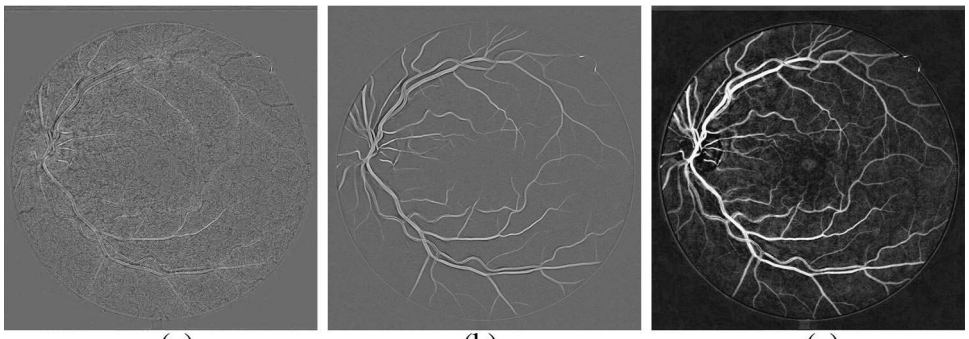

Figure 3.3: Filter responses of the retinal images obtained according to different scaling factors. (a) Scaling factor of 1. (b) Scaling factor of 2. (c) Scaling factor of 8.

removed. Finally, we convolve the dilated image with the binarized image in order to extract the thin blood vessels.

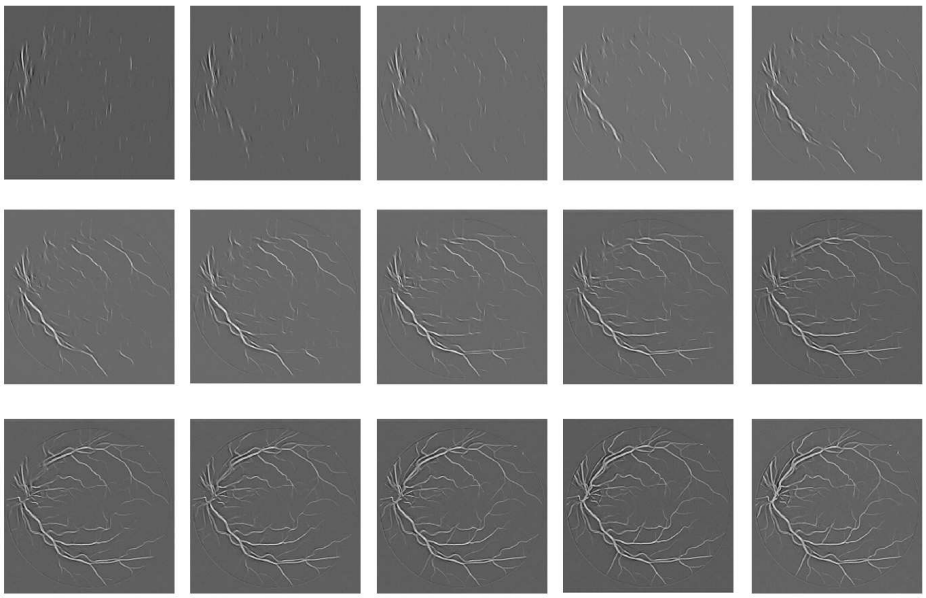

Figure 3.4: Illustration of denoised retinal image after reconstruction with scaling factor of 2 and 15 orientations using Gabor wavelet filter.

For phase-preserving denoising, wavelet scaling factor and orientation are two important prospects. When the scaling factor is low, filter response to noise is high and could treat useful information as noise. With the increased value of the scaling factor, filter response to the noise is decreased. Hence, scaling factor should be chosen carefully. Before the line structure detection, scaling factor should be low with an aim to remove noise. After local normalization, preservation of blood vessels is important requiring high scaling factor.

With several experiments and optimization, we choose a scaling factor of 2 before line structure detection, for optimum noise removal. After local normalization, as the noise is already removed, we use high scaling factor of 8 to preserve blood vessel information and to provide contrast between vessels and background. Fig. 3.3 (a), (b), and (c) demonstrates the filter response of a retinal image via phase-preserving denoising with the scaling factors of 1, 2, and 8, respectively.

The high quality of the reconstructed retinal image undeniably depends on the feature extraction with Gabor wavelet filters that use scaling factors and orientations. Larger scaling factors and orientations tradeoff with the computational time. The process begins with constructing a Gabor features by taking 2 scales and 15 orientations using Gabor wavelet filters. The image to be denoised is now convolved with the constructed Gabor features, thus generating 15 different feature vector responses with the same size as shown in Fig. 3.4. The final image is obtained by summing the responses over all scales and orientations.

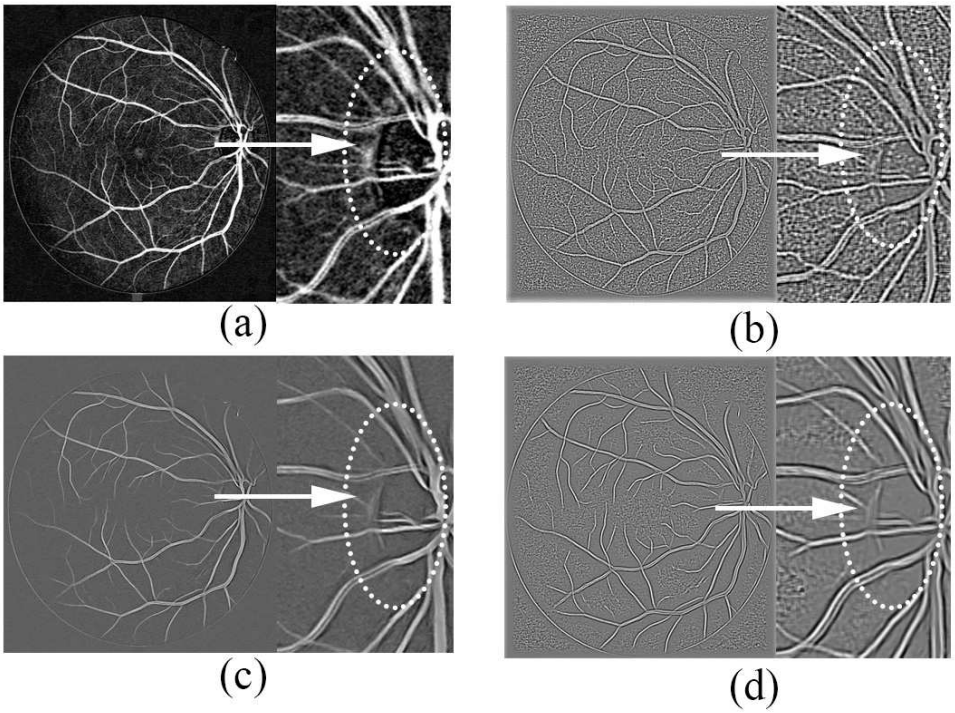

Figure 3.5: Illustration of resultant images obtained without (as shown in (a) and (b)) and with (as shown in (c) and (d)) phase-preserving denoising. (a) The resultant image before using line detection. (b) The resultant image after using local normalization. (c) The denoised image with scale factor of 2 and 15 degrees of orientation before using line detection. (d) The denoised image with scaling factor of 8 and 15 degrees of orientation.

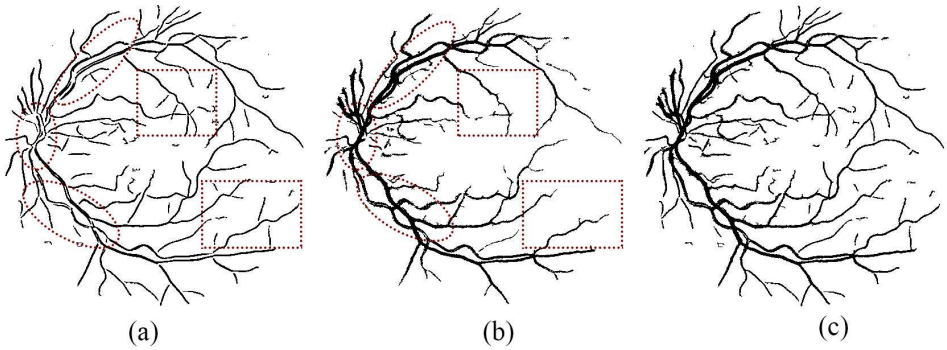

Figure 3.6: Illustration of blood vessel segmentation results by using the proposed methods according to (a) thin vessel detection; (b) thick vessel detection; (c) post-processing for improved image quality by superimposing of the image between (a) and (b). Red-dotted rectangles in (a) show detected thin blood vessels that is not discovered using thick vessel detection as shown in red dotted rectangles in (b). Red-dotted circles in (a) demonstrate the limitation of the proposed thin vessel detection where thick blood vessels are torn apart. The limitation is solved when conducting thick vessel detection as illustrated in the red dotted circles in (b).

Thin vessel detection in a noisy image shows greater challenge. The procedure to remove noise will lead to the loss of true blood vessel information. Also, the noisy pixels are merged with true vessels resulting in the false positives. Fig. 3.5 compares the resultant images with or without using phase-preserving denoising. Fig. 3.5 (a) and (b) are the results before using line detection and after the local normalization, both of which are processed with absence of phase-preserving denoising. Similarly, Fig. 3.5 (c), (d) are the results before using line detection and after using local normalization operation but with phase-preserving denoising. It is clearly seen that, denoising technique is able to remove a tremendous amount of noise without losing vessel properties as shown in Fig. 3.5 (c), (d).

3.3.3 Thick Vessel Detection

Thick blood vessel detection is conducted in parallel with thin vessel detection following the pre-processed step. The image after being processed is binarized with the threshold value obtained from the maximum entropy. The result image contains blood vessels and noise. We calculate the area of each connected component and remove the components whose areas consist of 20 pixels or less. The resultant image obtained after this process contains only thick vessels.

3.3.4 Post-processing

The detected thin and thick vessels are merged together via superimposition. The noise in the merged image is not always removed especially to the image with lesions and unusual illumination. Hence, we perform morphological dilation operations using a disc shaped structuring element with radii of 3 pixels. This morphological operation allows the remaining component to grow by 3 pixels from the edge along all the direction, which connects all the vessels nearby. The area of each connected component is searched. We remove the area with 500 pixels or less as noise areas from the dilated image. Finally, we convolve the dilated image with the merged image. The obtained segmented image is compared with manually drawn ground truth images available at the experimented databases.

Fig. 3.6 shows the resultant images from phase 1 (thin vessel detection) and phase 2 (thick vessel detection). The red dotted circles in Fig. 3.6 (a) illustrate that thick vessels are torn apart due to center light reflex. However, thin vessels can be detected effectively as shown in red dotted boxes in Fig. 3.6 (a). Fig. 3.6 (b) demonstrates the results from phase 2 where thick vessels are efficiently detected. We merge the two solutions from both phases to overcome the noise issues. Fig. 3.6 (c) is the final results where resultant images from both phases are superposed together. As a result, the final images contain most of vessels including both thick and thin vessel trees.

3.4 Performance Evaluation and Results

3.4.1 Image Source and Experimental Evaluation Criteria

The performance of this proposed segmentation is evaluated through images taken from publicly available databases: the DRIVE, the STARE, the CHASE_DB1 and HRF. These databases are widely used, popular and contain varieties of images including both healthy and pathological images that are taken using different cameras under different environmental conditions. These databases consist of ground truth and masks that have been manually segmented by experts. The DRIVE database is composed of total 40 color retinal images. The images were collected from diabetic retinopathy screening program in

the Netherlands. These images were taken from canon CR5 non-mydriatic 3-CCD camera with 45 degree field of view (FOV). Among the 40 images, 20 images are categorized as test databases and the remaining as training databases. The images were compressed and kept in JPEG format. The STARE database contains 20 images. Out of these images, 10 are pathological images. The images were captured with TopCon TRV-50 fundus camera at 35 degree field of view. Two observers were involved in the segmentation manually. The CHASE_DB1 database contains 28 retinal images from 14 patients. Among them 14 images were taken from Child Heart and Health Study. The HRF database contains three categories of images : 15 images of healthy images, 15 images of diabetic retinopathy retinas (DR) and 15 images of patients with glaucoma (G).

Among two types of the images in the DRIVE database, 20 images from the test database are utilized for the qualitative assessment of proposed algorithm. Also, we utilize the entire sets from STARE and CHASE_DB1 databases that contain 20 and 28 images respectively. Among three categories of HRF database, we have utilized the images with DR and G which includes pathological retinal images.

Two different ground truth images were provided that were manually segmented by two experts in the first three databases. The ground truth image that were manually segmented by the first observer of each database are used to verify the result. For HRF, only one set of manually segmented ground truth images are available. Also, the performance of these experiments using our algorithms is compared with the results via existing methods in state of the art, in terms of sensitivity (Se), specificity (Sp), area under ROC curve (AUC), accuracy (Acc), and Matthews correlation coefficient (MCC). This quantitative assessment is performed with pixel based classification technique. Every pixel is classified either as a vessel or background. As the result, there are 4 combinations: two classifications and two misclassifications. Classification refers to true positive (TP) and true negative (TN) whereas misclassification refers to false positive (FP) and false negative (FN) [113]. These measures are defined as the following equations.

$$\text{Acc} = \frac{\text{TP+TN}}{\text{TP+FP+TN+FN}} \tag{3.18}$$

$$\text{Se} = \frac{\text{TP}}{\text{TP+FN}} \tag{3.19}$$

$$\text{Sp} = \frac{\text{TN}}{\text{TN+FP}} \tag{3.20}$$

Note that TP and TN specify the correctly acknowledged vessel pixels and background pixels whereas FP and FN specify the incorrectly acknowledged vessel pixels and background pixels. The symbols Se and Sp are respectively the proportion of positives and negatives that are correctly identified.

We use MCC as another metric to measure the quality of binary classification that takes two values (normally 0 and 1) among resultant analyzed images (prediction values) and the ground truth images (actual values). It satisfies Eq. (3.21)

$$\text{MCC} = \frac{\frac{\text{TP}}{\text{N}} - \text{S} \times \text{P}}{\sqrt{\text{P} \times \text{S} \times \text{(1-S)} \times \text{(1-P)}}} \tag{3.21}$$

where, $\text{N} = \text{TN+TP+FN+FP}$, $\text{S} = \frac{\text{TP+FN}}{\text{N}}$, $\text{P} = \frac{\text{TP+FP}}{\text{N}}$

This measurement method is commonly considered as one of the best ways to describe the confusion matrix [151] of TP, TN, FP, and FN where the amount of samples in the two classes differs noticeably. As an example, the non-vessel pixels are significantly varied compared with the vessel pixels. The value of MCC varies between -1 to +1 and prediction is efficient if the value is high.

To achieve the non-parametric performance measurement, receiving operating characteristics (ROC) curve [151] is used, which estimates tradeoff between sensitivity and specificity. It is a binary classifier that is plotted by using different values of the independent threshold in a certain interval. The value is calculated in each threshold point and represents the false positive rate i.e. (1-Sp) on x-axis and true positive rate (Se) on y-axis. The ROC curve is regarded as an ideal curve as a point (0, 1) when it is closer to the top left corner, which offers perfect value i.e. 1 as area under curve (AUC) and considered as an excellent result when AUC value is above 90%. Note that, AUC is the measure of predictive performance.

3.4.2 Results and Discussion

This section presents the experiment executed to evaluate the performance of the designed algorithm for the segmentation of retinal blood vessels. These experiments are

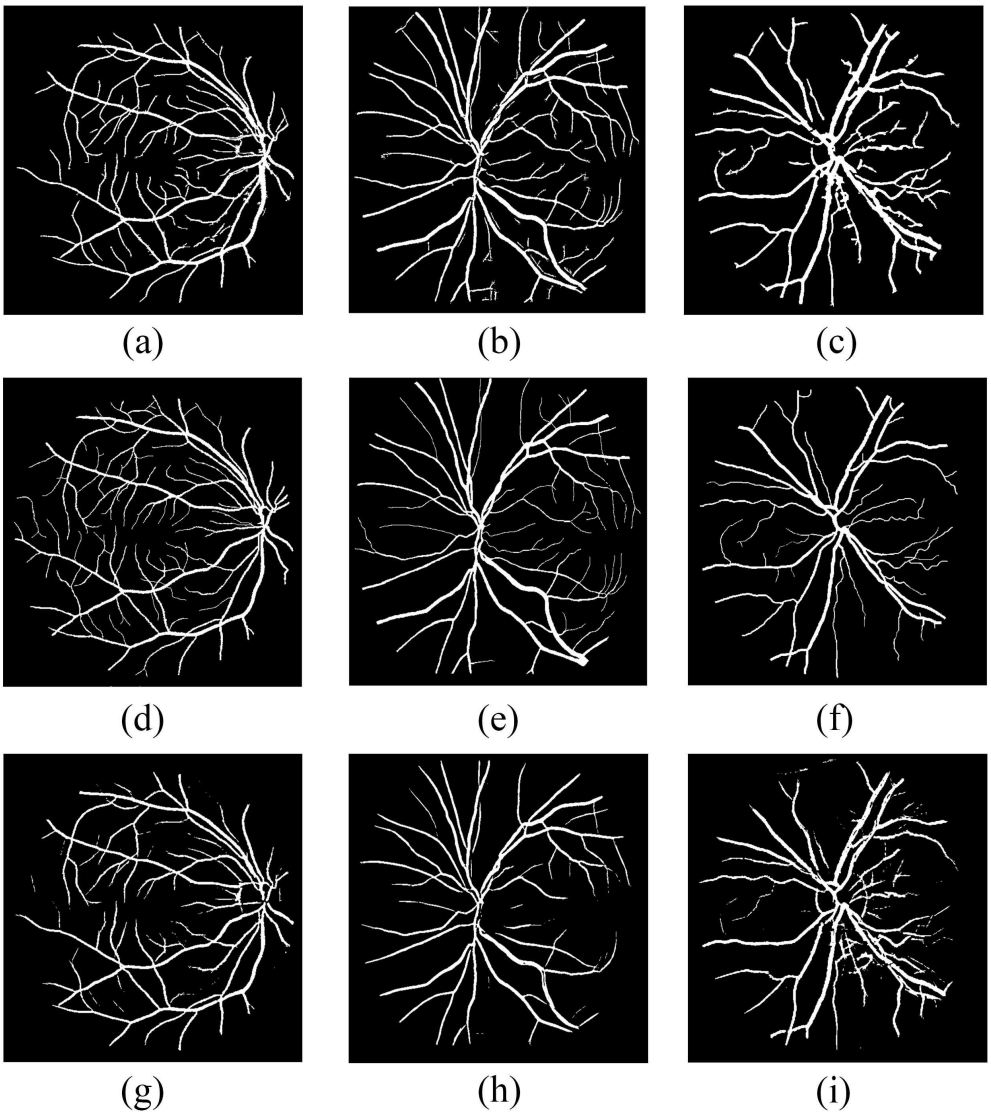

Figure 3.7: (a), (b), (c) are the final retinal vessel segmentation results for three databases, DRIVE, STARE and CHASE DB1. Similarly (d), (e), (f) are the manually segmented ground truth result. (g), (h), (i) are the result from B-COSFIRE [6].

carried out on each image from mentioned databases. All experiments are performed on Matlab R2013b running under Intel(R) core(TM) i5-4570s CPU@ 2.90 Ghz with 8 GB of RAM.

Table 3.1: This table lists the resultant performance using DRIVE database in terms of sensitivity, specificity, AUC, accuracy (Acc) and MCC. The results using the proposed algorithm are compared with the results using the methods in literature.

Methods	Se	Sp	AUC	Acc	MCC
Supervised Method					
Staal emphet al.[114]	-	-	0.9520	0.9441	-
Soares *et al.*[152]	0.7332	0.9782	0.9614	0.9466	-
Ricci and Perfetti *et al.*[118]	-	-	0.9633	0.9595	-
Marin *et al.*[153]	0.7067	0.9801	0.9588	0.9452	-
Fraz *et al.*[154]	0.7406	0.9807	0.9747	0.9480	-
Unsupervised Method					
Martinez-perez *et al.*[155]	0.7246	0.9655	-	0.9344	-
Al-Rawi *et al.*[140]	-	-	0.9435	0.9535	-
Ricci and Perfetti *et al.*[118]	-	-	0.9558	0.9563	-
Al-Diri *et al.*[156]	0.7282	0.9551	-	-	-
Lam *et al.*[157]	-	-	0.9614	0.9472	-
Fraz *et al.*[154]	0.7150	0.9760	0.8460	0.9430	-
Nguyen *et al.*[8]	-	-	-	0.9400	-
Yin *et al.*[117]	0.7556	0.9656	-	0.9475	-
B-COSFIRE [6]	0.7655	0.9704	0.9614	0.9442	0.7475
Zhao *et al.*[158]	0.7420	0.9820	0.8620	0.9540	-
PROPOSED METHOD	**0.8106**	**0.9761**	**0.9650**	**0.9623**	**0.7681**

The improved segmentation results can also be observed visually. Resultant segmentation is automatically acquired using our approach, which is compared with the manually segmented images by the first observer for each database (ground truth). To demonstrate the improvement, the results obtained are compared with the B-COSFIRE segmentation results. Fig. 3.7 (a), (b), (c) are the results using the proposed automatic segmentation from randomly selected images associated with DRIVE, STARE and CHASE_DB1 respectively. Fig. 3.7 (d), (e), (f) illustrates the manually segmented ground truth images and Fig. 3.7 (g), (h), (i) are the segmented results from B-COSFIRE [6]. The results obtained from our methods, while compared with ground truth and B-COSFIRE results, show that the proposed algorithm is able to pick up fine details of blood vessels, and allows least errors compared with the ground truth. It is further validated according to the resultant quality metrics listed in Table 3.1 - Table 3.3.

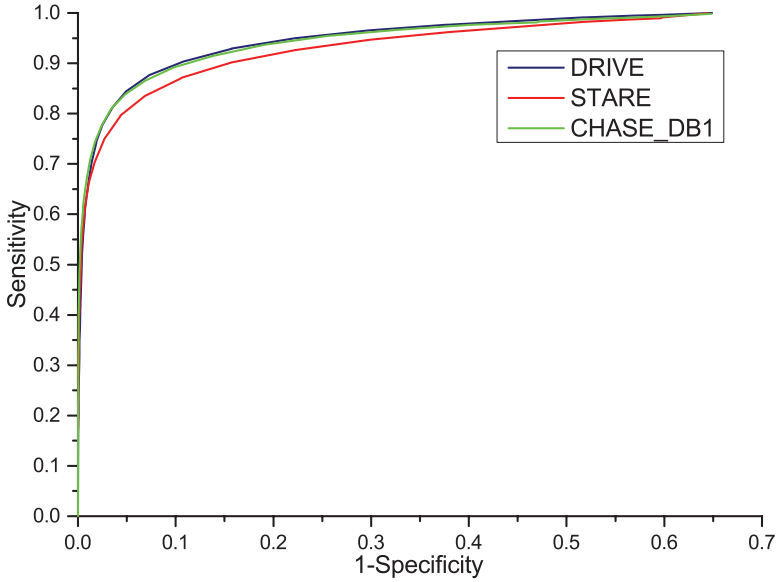

Figure 3.8: ROC curves for DRIVE, STARE and CHASE_DB1, represented by blue, red and green lines, respectively, using the proposed algorithm.

Table 3.2: This table lists the resultant performance using STARE database in terms of sensitivity, specificity, AUC, accuracy (Acc) and MCC. The results using the proposed algorithm are compared with the results using the methods in literature.

Methods	Se	Sp	AUC	Acc	MCC
Supervised Method					
Staal *et al.*[114]	-	-	0.9614	0.9516	-
Soares *et al.*[152]	0.7207	0.9747	0.9671	0.9480	-
Ricci and Perfetti *et al.*[118]	-	-	0.9680	0.9646	-
Marin *et al.*[153]	0.6944	0.9819	0.9769	0.9526	-
Fraz *et al.*[154]	0.7548	0.9763	0.9768	0.9534	-
Unsupervised Method					
Mendonca *et al.*[142]	0.6996	0.9730	-	0.9479	-
Martinez-perez *et al.*[155]	0.7506	0.9569	-	0.9410	-
Ricci and Perfetti *et al.*[118]	-	-	0.9602	0.9584	-
Al-Diri *et al.*[156]	0.7521	0.9681	-	-	-
Lam *et al.*[157]	-	-	0.9739	0.9567	-
Fraz *et al.*[154]	0.7310	0.9680	0.8500	0.9440	-
Nguyen *et al.*[8]	-	-	-	0.9320	-
B-COSFIRE [6]	0.7716	0.9701	0.9563	0.9497	0.7335
Zhao *et al.*[158]	0.7800	0.9780	0.8740	0.9560	-
PROPOSED METHOD	**0.8319**	**0.9623**	**0.9547**	**0.9444**	**0.7523**

Table 3.1, Table 3.2 and Table 3.3 further endorse the effectiveness of the proposed algorithm in terms of Acc, AUC, Sp, Se, and MCC using all the three databases. The

Table 3.3: This table lists the resultant performance using CHASE_DB1 database in terms of sensitivity, specificity, AUC, accuracy (Acc) and MCC. The results using the proposed algorithm are compared with the results using the methods in literature.

Methods	Se	Sp	AUC	Acc	MCC
Supervised Method					
Fraz *et al.*[154]	0.7224	0.9711	0.9712	0.9469	-
Unsupervised Method					
B-COSFIRE [6]	0.7585	0.9587	0.9487	0.9387	0.6802
PROPOSED METHOD	**0.8106**	**0.9530**	**0.9633**	**0.9494**	**0.6922**

results we achieve on all the three databases outperform the results using most of existing literature.

We choose five supervised methods designed by research groups such as [Staal emphet al. [114], Soares *et al.* [152], Ricci *et al.* [118], Marin *et al.* [153], Fraz *et al.* [154]] and ten unsupervised methods from the research work carried out by [Martinez-Perez *et al.* [155], Al-Rawi *et al.* [140], Ricci *et al.* [118], Al-Diri *et al.* [156], Lam et. al [157], Fraz *et al.* [154], Nguyen et al. [8], Yin *et al.* [117], B-COSFIRE [6], Zhao *et al.* [158]] to analyze the DRIVE database, the results of which are compared with our segmentation results. In terms of sensitivity, AUC and accuracy, our method outperforms almost all of the recent research outcomes. The results regarding specificity are similar when using the proposed algorithm and the algorithms in literature. According to STARE databases, results associated with specificity, accuracy and AUC using our algorithm are highly comparable with most of the results using the state of the art methods. Especially, sensitivity using the proposed segmentation is significantly high. Similarly, for the CHASE_DB1, sensitivity is marginally better and specificity, AUC and accuracy calculated using our method is highly comparable with two existing methods such as [Fraz et al. [154], B-COSFIRE [6]]. Fig. 3.8 shows the ROC curve for DRIVE, STARE and CHASE_DB1, respectively, using our algorithm. The x-axis represents the value of (1-specificity), and y-axis represents the value of sensitivity. The parameter AUC can be further calculated by measuring the area under the ROC curve.

The parameter MCC is calculated according to the mentioned three databases using the proposed algorithm and B-COSFIRE. Our result shows improved vessel segmentation performance and outperforms B-COSFIRE [6]. In the work represented by Zhao *et al.*[158], AUC was defined as $(\text{Se} + \text{Sp})/2$. If we follow this definition, our results re-

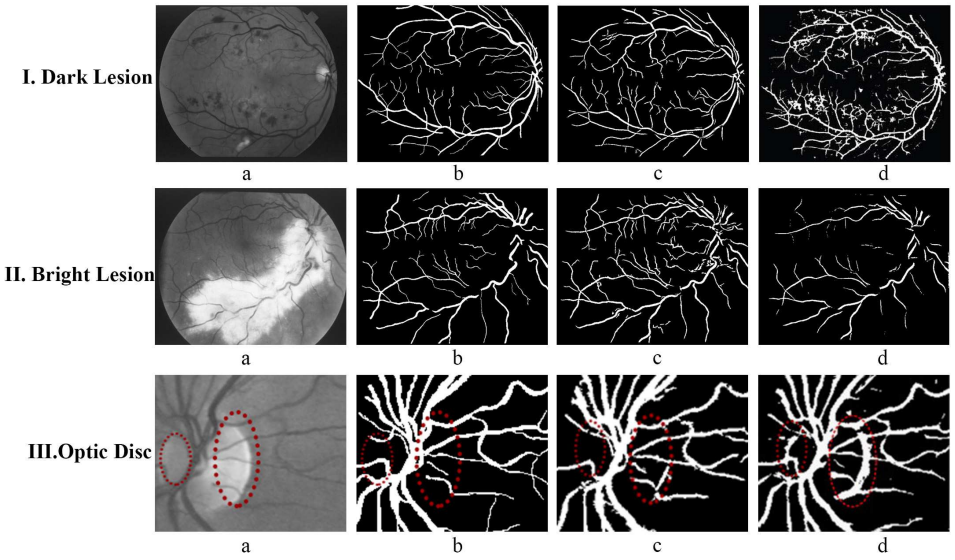

Figure 3.9: Comparison of resultant blood vessel segmentation on the abnormal retinal images. (I) The image with dark lesion, (II) The image with bright lesion, and (III) The image with optic disc. The images on the first column are the inverted green channel images. Similarly second, third, and fourth columns are the manually segmented ground truth images, segmented results using proposed methods and the results achieved by I. (d), Saffarzadeh *et al.* [7]; II. (d), B-COSFIRE [6]; and III. (d), Nguyen *et al.* [8] respectively. We use red dotted circles in III to spot the optic disc regions.

lated to DRIVE and STARE are 0.8933 and 0.8971, respectively, which are still higher than 0.8620 and 0.8740(the results represented in Zhao *et al.* [158]).

3.4.3 Computation time

The computational time in the proposed algorithm mainly depends upon the number of orientations and scales. The number of scales and orientations should be determined so that most of the blood vessels are preserved. We execute our experiments for MRI times to optimize the solution and the experiment takes less than 7 seconds for processing each of the images selected from DRIVE and STARE databases and the analysis of each image from CHASE_DB1 database takes less than 16 seconds. The total time required to process a single image of HRF database was less than 22 seconds. The experiment mentioned in Table 3.4 is conducted using our computer system. The configuration of the system is mentioned in Section 4.2. Table 3.4 shows that the execution time of our algorithm is significantly less than the other recent approaches tested on the same hardware.

Table 3.4: Performance analysis in terms of execution time for processing single image of databases (Drive and Stare).

Methods	Computation Time
PROPOSED METHOD	**7s**
B-COSFIRE [6]	10s
Yin *et al.*[117]	24s

3.4.4 Performance on Bright lesion, Dark lesion and Optic Disc

It is important to know that presence of bright and dark lesions will degrade the performance of resultant image segmentation. Non-uniformed bright or dark lesions with diverse intensity patterns are incorrectly classified as blood vessels. In addition, the imaged optic disc region appears to be brighter than the other portions in a retinal image, which tends to produce false vessels. In our framework, three steps are designed to reduce the amount of noise and the influence of uneven illumination artifacts. As an initial step, we adopt background estimation and subtraction operations to weaken the influence of noise and uneven illumination. After that, the phase-preserving denoising and local normalization methods are used to further remove artifacts. Finally, the areas of connected components in the binarized image are calculated and smaller areas are deleted. However, most of the existing literature only represents their work based on the retinal images and does not analyze pathological retinal images. In order to make comparison with our proposed algorithm, we use recent techniques in literature to analyze pathological images. The results show that our method is much advanced in processing retinal images with pathology. Fig. 3.9 shows the comparison of our results with three of the recent algorithms and ground truth images using DRIVE and STARE databases. We select the pathological images in terms of dark lesions as shown in Fig. 3.9 I(a), bright lesions in Fig. 3.9 II(a) and imaged optic disc in Fig. 3.9 III(a). The resultant segmented image according to the method afforded by Saffarzadeh *et al.* [7] is illustrated in Fig. 3.9 I(d). In this figure, most of the dark lesions are wrongly detected as blood vessels. Fig. 3.9 II(d) shows the segmented result produced by the algorithm developed by B-COSFIRE [6]. It is observed that in the region of bright lesion, thin and dim blood vessels are incorrectly removed. The segmented result from Nguyen *et al.* [8] is illustrated in Fig. 3.9 9 II(d), which shows false blood vessel detection near the optic disc. Our segmentation

enables to correctly detect both thin and thick vessels with clearly removed dark lesions as shown in Fig. 3.9 I(c). In the region of bright lesions, our algorithm allows both thin and dim vessels to be detected without missing details, as shown in Fig. 3.9 II(c). In the optic disc region indicated by red dotted circles as shown in Fig. 3.9 III(c), false blood vessels in the circled regions that are wrongly detected in Fig. 3.9 III(d) have been noticeably removed via using the proposed algorithm. Our approach provides accuracy of the detected blood vessels as illustrated in Fig. 3.9 (I-III)(c), which well match the ground truth images displayed in Fig. 3.9 (I-III)(b).

Table 3.5: This table lists the resultant performance using two sets of pathological images on the HRF database (Diabetic Retinopathy (DR) and Glaucomatous (G)) in terms of sensitivity, specificity, AUC, and accuracy (Acc). The results using the proposed algorithm are compared with the results using the methods in literature.

Methods	Se	Sp	AUC	Acc
DR				
Yu *et al.*[159]	0.7604	0.9625	-	0.9460
Roberto *et al.*[160]	0.6997	0.9787	-	0.9554
Odstrcilik *et al.*[147]	0.7463	0.9619	0.9589	0.9445
PROPOSED METHOD	**0.8025**	**0.9629**	**0.9590**	**0.9576**
G				
Yu *et al.*[159]	0.7890	0.9662	-	0.9518
Roberto *et al.*[160]	0.7566	0.9785	-	0.9603
Odstrcilik *et al.*[147]	0.7900	0.9638	0.9704	0.9497
PROPOSED METHOD	**0.8224**	**0.9781**	**0.9697**	**0.9641**

To further study the performance of our method in pathological images, we have conducted an experiment on the two sets of HRF databases which includes pathological images. Table 3.5 show the results in terms of Se, Sp, AUC and Acc. For both sets of pathological images(DR and G), Se and acc are marginally better. Sp and AUC are highly comparable with the results presented by the existing algorithms. Hence, the performance results that we achieve are significantly better than most of the results demonstrated by recent algorithms.

3.5 Conclusion

In this chapter, we propose a novel framework for automatic retinal vessel segmentation by combining line detection and phase-preserving denoising with an application of mor-

phological reconstruction and maximum entropy. This framework has been tested on the four popular and publicly available databases, DRIVE, STARE, CHASE_DB1 and HRF. The quantitative analysis in terms of different evaluation metrics (Se, Sp, AUC, Acc, and MCC) demonstrates significantly improved segmentation quality using our algorithm when compared to the recent retinal image segmentation techniques. Particularly, our experimental investigation shows that the proposed method can be used for effective analysis of retinal vessels on abnormal retinal images with bright or dark lesions and optic disc since the recent techniques seldom perform quantitative analysis of retinal images with pathology. The presented approach can act as a strong tool for the retinal blood vessel segmentation.

Chapter 4

Automated optic disc localization and segmentation using retinal fundus images

4.1 Introduction

Human retina manifests several systemic diseases such as glaucoma, diabetic retinopathy (DR), etc. that causes abnormalities like blurred central vision or a blind spot in the center of the visual field finally leading to blindness [161][162]. Therefore, early diagnosis of these diseases is essential to identify the changes in anatomical structures, such as the optic disc (OD), optic cup, vasculature, and retinal pathologies [163]. During the screening of glaucoma and DR, the shape and the visual aspects of OD are considered as important features. Hence, the detection and segmentation of OD is the preliminary step for the development of computer-assisted diagnosis (CAD) system [164][165].

Several solutions have already been proposed for segmentation of optic disc detection and segmentation. A morphological based segmentation [166][167] have been proposed that extracts OD contour by using techniques such as stochastic watershed algorithms, connected component, and adaptive mathematical morphology. [168][169] discusses the deformable model that uses active contour, template matching and supervised gradi-

This chapter is derived from:

- **D Pandey**, X. Yin, H. Wang, and Y. Zhang, "Automated optic disc localization and segmentation based on superpixel method incorporating clustering and Hough transform using retinal fundus images" *Artificial Intelligence in Medicine*, 2019.(Under Review)

ent vector flow snake. Pixel based classification methods using k-nearest and super pixels classifiers are discussed in [170]. Some of the remarkable works have been explained. Zhu et al. [171] proposed a segmentation method using edge detection and Circular Hough Transform (CHT) to detect the center and radius of the circle. The author concluded that the performance of the CHT depends upon the circular shape and showed a weak performance in non-circular OD. A new approach using iterative thresholding method incorporating connected component analysis to approximate the center of OD followed by the OD extraction by using an active contour model was proposed by Siddalingaswamy et al [172]. The model based approach using CHT, and the statistical model was proposed by Yin et al. [173]. After pre-processing, CHT is used to approximate the center and radius of OD. A disc boundary is fine-tuned using statistical deformable model. Lu et al [174] proposed an automatic OD segmentation method utilizing a circular transformation. The transformation is based on circular boundary and color formation through the OD boundary concurrently. The accuracy was increased via the preprocessing step, median filtering, and OD probability map. A modified Chan-Vese model using the red channel and texture features is proposed by Joshi et al [168]. Hsiao et al. [169][13] proposed a method that detects the contour using a canny edge detector and Hough transform. In the next step, supervised gradient vector flow (SGVF) snake model is used for segmentation by updating and classifying the contour points in each iteration. Moreover, Tjandrasa et al. [175][33] have proposed a new OD segmentation method using Hough transform as an initial level set for contour detection in a grayscale image. A morphological approach using mathematical morphology is proposed by Welfer et al. [166]. First, the coarse detection of OD boundary is performed and later results are improved in the second step. Morales et al. [167] used principal component analysis (PCA) to extract the gray scale image and segmentation is carried out using generalized distance function, stochastic watershed, and geodesic transformations. This method achieved an accuracy of 86.89% with 110 retinal images of DRIONS dataset. Cheng et al.[170] proposed a method that classifies each super pixel as disc or non-disc using histogram and texture features. The process is followed by the deformable model to achieve the final contour of OD. Abdhullah et al. [176] proposed an algorithm based on morphological operations, the circular Hough transform and the grow-cut algorithm. To enhance the

OD and remove the retinal vasculature and other pathologies, morphological operators are used. The center of OD is determined by the Hough transform and the segmentation of OD boundary is achieved using a graph-cut algorithm. Marin et al. (2015) [177] proposed a two-step automatic thresholding on a morphologically processed bright enhanced region to get a reduced region of interest, followed by the application of circular Hough transformation (CHT) to get the OD center and OD region. Superpixels provides information about local and coherent regions. Cheng et al. [170] proposed a statistical approach OD segmentation using a histogram based superpixels method.

The literature study shows the challenges of OD detection and segmentation as (1) Ophthalmic pathologies causes of the changes of color, shape or depth of OD. (2) Retinal pathologies (exudates, lesions) sometimes possess similar properties causing a false identification of OD [178]. Several factors like boundary artifacts, blurred image edges, illuminations, and contrast irregularities make segmentation difficult and require pixel to pixel analysis [176]. A texture of OD varies from images, adding more challenges, thus requiring a preprocessing step prior to the segmentation [179]. Also, the vessels around an OD creates difficulty during segmentation [176]. Although the localization process of OD in the state of the art is considerable, the precise and automatic segmentation of OD boundary is still a challenging task and requires a detailed analysis around the boundary of OD [165]. Superpixel algorithm has been widely used for the medical image segmentation and displays an excellent segmentation ability of the images with strong structures and clear edge information [180]. However, it is less likely that OD with pathologies and uneven illumination can posses above mentioned properties [176][165]. Hence to overcome these problems, we propose a novel framework based on superpixel incorporating CHT, morphological operation, and Kmeans clustering.

The process begins with the pre-processing step to estimate the background (BG) image and foreground (FG) image utilizing the morphological operation to separate the blood vessel from the inverted green channel image [65][181]. The image without the blood vessel is termed as BG image and the image only with blood vessel is termed as FG image. In the second step, the algorithm estimates the optic disc region of interest (OD-ROI) and are carried out in two separate steps 1) Localization of OD and 2) Approximation of OD boundaries. The localization process utilizes the clustering information

based on the intensity of images obtained from Kmeans clustering on BG and FG images [182]. The obtained information from BG and FG images are merged together to find the pixel with maximum weight using linear filtering [183]. Thirdly, the circular Hough transform (CHT) is used to approximate the OD boundary over the Kmeans clustered BG image. This process helps to obtain the potential radius and the center of OD. However, the center obtained from CHT is not always effective for the diseased retinal image which has dim OD, bright and dark lesion and the image with uneven illumination. Hence, we compared the centers obtained from CHT with the center calculated from the localization of OD. After finalizing the center, we draw the OD boundaries using the radius obtained from CHT. The concurrent circle with 20 pixels is drawn on the obtained OD boundaries to achieve the OD-ROI. Finally, the segmentation of OD begins with the extraction of edge information using superpixels [184][82]. Unlike other methods [170] [180], the classification steps are not adopted to determine the OD or non-OD superpixels. However, the geometrical model is constructed over the edge information obtained from superpixels and CHT within OD-ROI. This process incorporates the pixel by pixel comparison between the obtained edges within OD-ROI and eventually, the final boundary of OD is extracted.

The rest of the chapter is organized as follows. In section 4.2, the proposed methodology is presented. Performance evaluation and experimental results are discussed in section 4.3. Conclusion and discussion are given in section 4.4.

4.2 Methods

The proposed method for OD segmentation consists of three stages: 1) Preprocessing using morphological operation. 2) Localization and detection of OD based on edge detection, using Kmeans clustering algorithm and Hough transform and 3) the segmentation of optic disc acquired by comparison of the edges from super pixels and Hough transform. Fig. 4.1 shows a schematic of the method's work-flow.

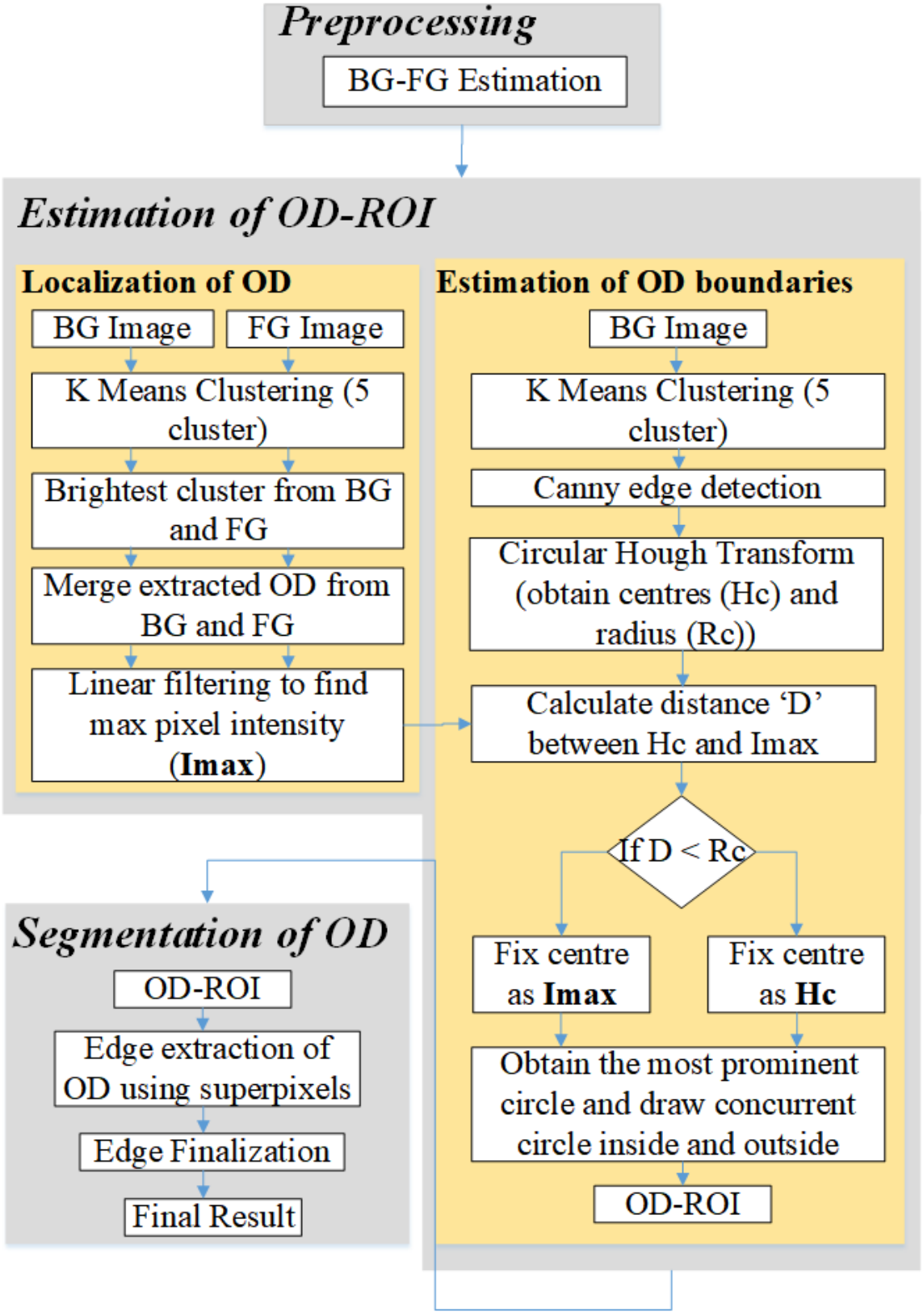

Figure 4.1: The schematic representation of a OD segmentation algorithm.

4.2.1 Retinal Background and Foreground Estimation

This is an important pre-processing step to reduce the noise and uneven illumination across the images. First, we resize the fundus image to make the process computationally efficient especially for the images with high resolution. The resized image has the 565 rows whereas the columns are calculated accordingly to preserve the aspect ratio. Since the original fundus image contains unwanted noise and uneven illumination. Noise suppression and smoothing can be done with Gaussian filtering. However, the gaussian filter can create edge distortion and vanishing problem. Hence, to preserve edges during noise reduction, we use a pixel-wise adaptive Weiner filtering technique [185]. The method estimates the mean and standard deviation of the local neighborhood of each pixel and preserves detailed edges. Thereafter, the morphological opening operation is performed in the inverted green channel image to obtain the background estimation which excludes the retinal blood vessels and uneven illumination. FG image includes main blood vessels and is obtained after subtracting BG image with the inverted green channel image as shown in Eq. (4.1).

$$I_{\mathrm{FG}} = I_{\mathrm{G}} - I_{\mathrm{BG}} \tag{4.1}$$

where I_{FG} = Normalized image , I_{G} = Inverted green image, I_{BG} = Background estimation

Background estimation I_{BG} is provided by geometric interpretation via a union of all translations of structuring elements S_{e} that fit entirely within the image I_{G} as shown in Eq. (4.2). The size of S_{e} is estimated such that its value is larger than the width of the blood vessel. Since the width of the vessels is not likely greater than 15 pixels, we consider the size of S_{e} as 15 [65]. The background is estimated that cannot completely fit the objects larger than 15 pixels to achieve the background image.

$$I_{\mathrm{BG}} = \cup\{(S_{\mathrm{e}}) \mid (S_{\mathrm{e}}) \subseteq I_{\mathrm{s}}\}, \tag{4.2}$$

where S_{e} = Structuring element with radius R , I_{s} is the set of I_{G} and $\cup$ is the union of set.

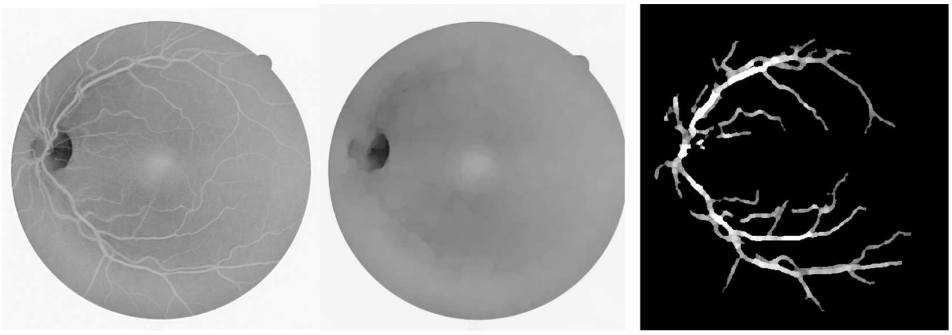

Figure 4.2: Background and Foreground estimation from the inverted green channel image. (a) The inverted green channel image. (b) The background estimated image. (c) The foreground estimated image obtained after the subtraction of estimated background from the inverted green channel image.

4.2.2 Estimation of OD-ROI

After the preprocessing step, the ROI extraction is performed in two steps. 1) Localization of OD and 2) Estimation of OD boundaries.

Localization of OD

In the healthy retinal image, the OD region is considered as the brightest area of fundus green image. Most of the information about OD in contained in BG and can be easily localized using BG image. However, retinal pathological images with bright, dark lesions and non-uniform illuminations resemble similar color intensity properties which adds complexity during the localization of OD ROI. Hence, the intensity feature from the BG image stand-alone is not sufficient for the accurate result. Hence, we analyze the intensity information from BG as well as FG images separately to achieve the efficient output. We utilized the kmeans clustering technique to cluster the whole image on the basis of intensity properties. The brightest clusters are used to select a pixel with maximum weight score in OD.

K-means clustering technique is an unsupervised, yet very powerful clustering method that produces results which are close to the human observations [186]. The K-means clustering technique is used to partition the image into the number of k clusters according to the color intensity value of each pixel. K-means clustering method follows two major steps to divide an image into k number of clusters. Initially, k centroid points are calcu-

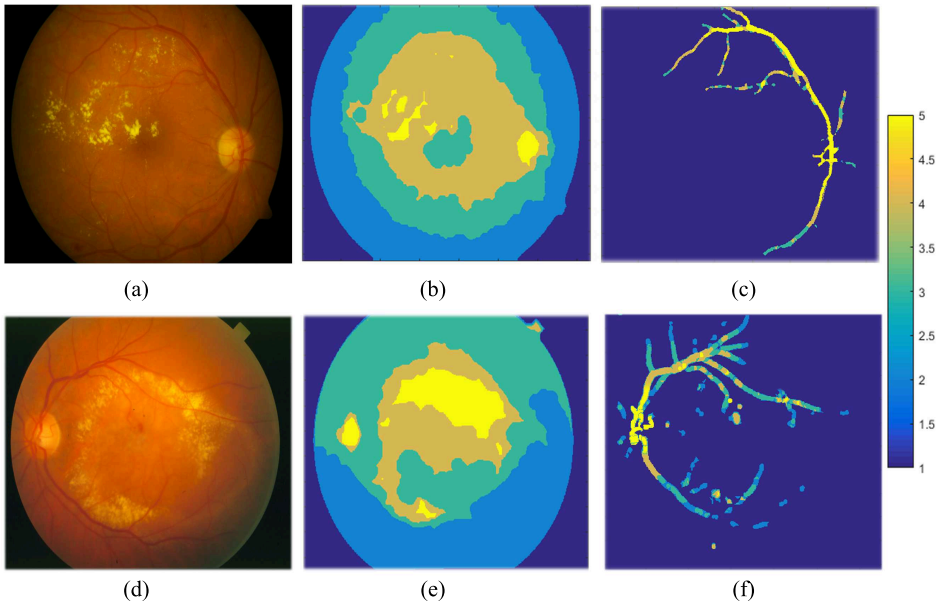

Figure 4.3: Illustration of resultant images obtained with 5 cluster Kmeans clustering method from BG and FG images in-terms of pixel intensity. (a),(d) are the original images. (b),(e) are the clustering results obtained from BG image. (c),(f) are the clustering results form the FG image.

lated for the provided k clusters and each pixel in an image is allocated to the nearest cluster. The Euclidean distance between each pixel and the nearest centroid is calculated and the centroid is updated until the convergence has been reached.

$$\begin{aligned} I_{\text{kmeans1}} &= kmeans(I_{\text{BG}}) \quad for \quad BG \quad image \\ I_{\text{kmeans2}} &= kmeans(I_{\text{FG}}) \quad for \quad FG \quad image \end{aligned} \tag{4.3}$$

where, I_{kmeans1} and I_{kmeans2} are the edge map image after K-means clustering for BG and FG images.

The number of cluster in our case is fixed as 5 because the experimented images show that 5 clusters have sufficient intensity information of OD. Fig. 4.3 shows the result obtained from the kmeans clustering method with 5 clusters. The resultant image of kmeans clustering algorithm in BG and FG images separately is shown in Fig. 4.3 (b)(e) and (c),(f) respectively. Thereafter, the brightest cluster is selected in the resultant image and the weight of each pixel is calculated using linear filtering method. From the experiment,

the window size is considered as 50 x 50. The pixel which has maximum weight score is selected as the location of OD. I_{kmeans1} and I_{kmeans2} are the resultant image after kmeans clustering for BG and FG images respectively as shown in Eq. (4.3).

Although OD is the brightest area of the retinal images, the areas that contain pathologies and uneven illumination sometimes posses the similar properties of OD [187]. As a result, the pixel outside the OD is sometimes identified as the location of OD. Hence, the brightest cluster obtained after kmeans clustering in BG and FG images alone may not be accurate enough to identify the correct location of OD. To overcome this problem, the resultant brightest cluster from BG and FG images are merged together before calculating the maximum weight score. In FG images, the central part is the brightest area due to the presence of dense blood vessel. Hence, the combined weight score of the pixel within the OD region is maximum when compared with the pixel from other areas.

Illustration of the selection of maximum weight score obtained using BG, FG, and BG+FG is depicted in Fig. 4.4. It is observed that maximum weight score calculated using separate BG and FG image increases the possibility of wrong OD localization. This is because of the similar color intensity in different areas and OD. However, the weight score, if calculated after superimposing BG and FG image, is able to produce the weight score for the accurate detection of OD.

In the Fig. 4.4, blue, green and red dots show the maximum weight score calculated from BG, FG and BG + FG images respectively. As observed in Fig. 4.4 (a) and (b), maximum weight score calculated using FG and BG separately is not within the OD location. However, the weight calculated using BG + FG images in both cases is within OD location. The BG and FG images are combined and the maximum weight score is calculated as shown in Eq. (4.4).

$$
\begin{aligned}
I_{\text{kmeans}} &= I_{\text{kmeans1}} + I_{\text{kmeans2}} \\
I(u,v) &= \sum_{i=-k/2}^{k/2} \Big(\sum_{j=-l/2}^{l/2} w(s,t) I_{\text{kmeans}}(u+s, v+t) \Big) \\
I_{\text{max}}(u,v) &= \max(I(u,v))
\end{aligned}
\tag{4.4}
$$

where, I_{kmeans} is the merged resultant image. $I(u,v)$ is the output image pixel as the linear combination of intensity value in the local neighborhood of the pixel $I_{\text{kmeans}}(u,v)$

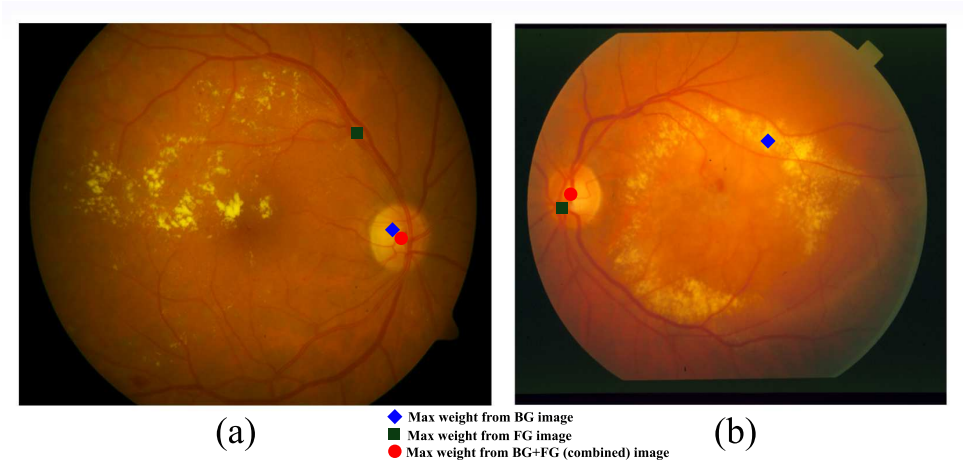

Figure 4.4: Illustration of the selection of maximum weight using BG, FG and BG+FG. Blue diamond shape represents the resultant maximum weight from BG images. Green rectangle shape represents the resultant maximum weight from FG image. Red circular shape represents the resultant maximum weight from (BG+FG) combined image.

and mask, k = 50. $I_{\max}(u, v)$ is the pixel inside the OD.

Estimation of OD boundaries

The localization of OD is followed by the estimation of OD boundary. The estimation process is done using BG image with circular hough transform (CHT) where the edges are initially extracted by K-means clustering and canny edge detection. CHT is the algorithm that detects the circular objects in the image based on the Eq. (4.5).

$$\begin{aligned} X &= a + Rxcos(\theta) \\ Y &= b + Rxsin(\theta) \end{aligned} \tag{4.5}$$

where (a, b) is the central point of the detected circle and R is the radius of the most prominent circle selected from the circles obtained using CHT [188]. The experimental analysis from the databases shows that the size of OD is approximately between 40 to 80 pixels in the resized fundus images. The circle candidates are obtained by a voting method in the Hough parameter space and stored in an accumulator matrix. We search the circular shape within the range and select the most prominent circles.

Let us consider a location obtained from OD localization as $L(a, b)$. The prominent circles are obtained using CHT as shown in Eq. (4.6):

$$(i, j, r) = CHT(I_{\text{kmeans1}}, R_{\text{min}}, R_{\text{max}}) \tag{4.6}$$

where, $h(x_o, y_o)$ and r are the centers and radius of prominent circles. I_{kmeans1} is the edge map image after K-means clustering in BG image. R_{min} and R_{max} denotes the minimum and maximum radius limit of OD to search.

We choose 3 prominent circles out of which one should be selected to fix the radius, r and estimated boundary of OD, as displayed in Fig. 4.5. Moreover, we measure the distance from the center to the point obtained from the previous step (localization of OD). The circle with the closest distance is selected to fix the radius of OD. It is also validated with the experiment that the localization of OD is accurate for most of the images. However, for the few difficult images, there are probabilities of incorrect OD localization. Hence, the localization is further validated by comparing the distance between the points obtained from localization and the center of the most prominent circle from CHT methods. We validate the obtained result as accurate if the calculated distance is within the radius of the selected prominent circle. For the cases, where distance is greater than the radius, the point obtained from CHT is considered as a center. The experiment shows that the proposed localization methods are very efficient in detecting the OD location.

The distance between two points $L(a, b)$ from CHT and $I_{\text{max}}(u, v)$ from OD localization is calculated as in Eq. (4.7):

$$D = \sqrt{(I_{\text{max}}u - a)^2 + (I_{\text{max}}v - b)^2} \tag{4.7}$$

If $D < r$, draw circle with $(I_{\text{kmeans}}(u, v), r)$ else $(L(a, b), r)$.

Finally, we draw two concentric circles with 20 pixels inside and outside the obtained circle which is the estimated OD region of interest (OD-ROI) as shown in Fig. 4.6(a).

4.2.3 Segmentation of OD

After the estimation of ROI, the edges of the OD should be determined. The obtained edge information from the detection process only provides the estimation of OD bound-

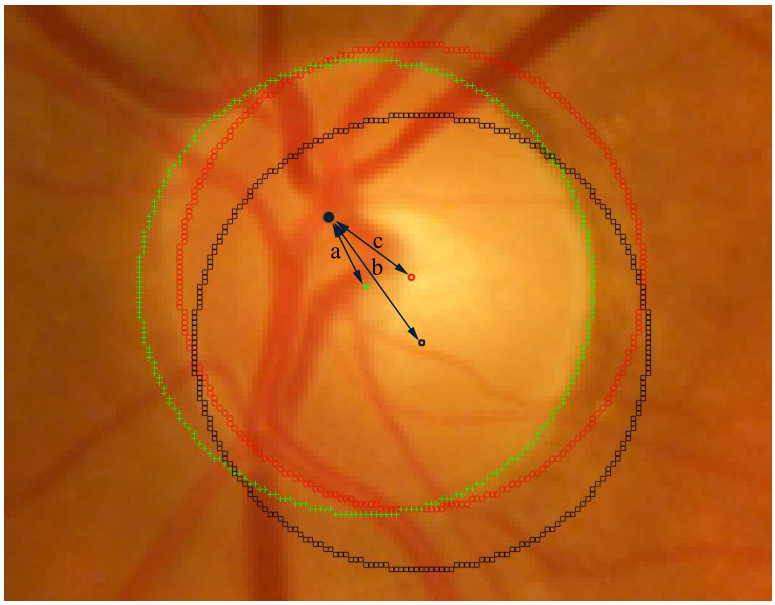

Figure 4.5: Illustration of three prominent circle obtained from CHT. a,b and c are the distance measured from the centre of each prominent circle to the point calculated from localization of OD.

ary which is not accurate. Hence, for optic disc segmentation, we use the edge feature obtained from SLIC (Simple Linear Iterative Clustering) based superpixels method and the CHT. thereafter, a geometrical model is created on the edge information obtained from the SLIC and CHT.

SLIC based super pixel method performs a local clustering of pixels in 5-D space on CIELAB color space which is perceptually uniform color space [170]. This color space uses pixel color vector (L, a, b) and pixel coordinate (x, y) while clustering. SLIC generates a superpixel built over the color intensity similarity and the proximity in the image plane, resulting in a better segmentation. The distance measured in 5D space using Euclidean distance is not possible without normalizing the spatial distances. Hence, SLIC uses a new distance measure considering the size of a super pixel which generates approximately equal super pixels. For superpixels generation, SLIC is the adaptation of K-Means but avoids redundant distance calculation. A weighted distance measure is the combination of color and spatial proximity and compactness of super pixels which delivers control over the size.

Let us consider input as the desired number of approximately equal-sized superpixels K. For an image with N number of pixels, the size of super pixels is N/K and the center

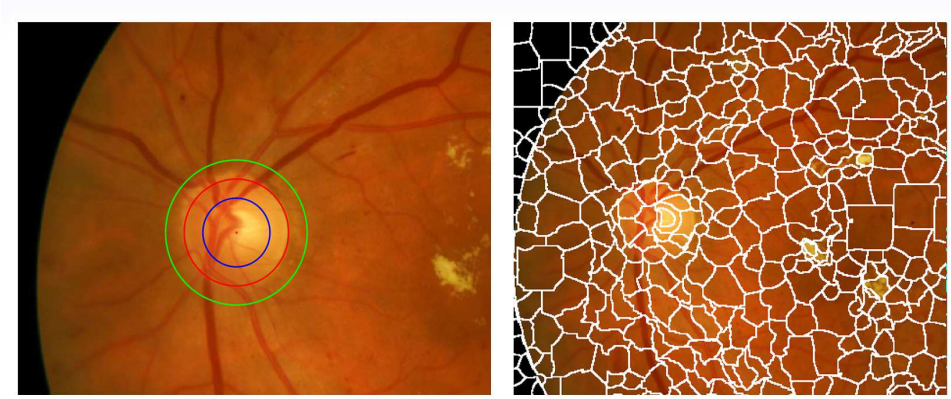

Figure 4.6: Illustration of results obtained from CHT and SLIC. (a) Red circle is the result from CHT. The green and blue circles are the concurrent circles which are drawn 20 pixels inside and outside of the circle obtained from CHT. (b)The resultant segmentation obtained from SLIC.

of the superpixel at every grid interval is $S = \sqrt{N/K}$. Let us initialize a cluster C_k. This algorithm choose I super pixels with cluster centers, $C_k = [L_k, a_k, b_k, x_k, y_k]^T$ where, $k = [1, K]$ at regular interval S.

After initializing the cluster centers C_k, it is necessary to move seed locations corresponding to the lowest gradient position in a 3 x 3 neighborhood to select an edge ignoring a noisy pixel. Hence, the image gradient $I_{SP}(x, y)$ is calculated as in Eq. (4.8).

$$I_{SP}(x, y) = \| I_{BG}(x+1, y) - I(x-1, y) \|^2 + \| I_{BG}(x, y+1) - I(x, y-1) \|^2 \quad (4.8)$$

where, $I_{SP}(x, y)$ is the lab vector corresponding to the pixel position (x, y) and $||.||$ is the L_2 norm which takes both color and intensity information in consideration.

Each pixel in the image I_{BG} is associated with the nearest cluster center according to the distance measured as shown in Eq. (4.8). Then the cluster centers are updated based on the average labxy vector of all the pixels of that particular cluster. The process is repeated until the residual error E meets the threshold $E \leq threshold$.

The distance measure, DMs is defined as follows Eq. (4.9):

$$\begin{aligned} DM_s &= d_{lab} + (m/S)Xd_{xy} \\ d_{lab} &= \sqrt{(l_k - l_i)^2 + (a_k - a_i)^2 + (b_k - b_i)^2} \\ d_{xy} &= \sqrt{(x_k - x_i)^2 + (y_k - y_i)^2} \end{aligned} \tag{4.9}$$

where, DM_s is the summation of lab distance and the xy plane distance normalized by the grid interval S. m controls the compactness of the superpixels.

Fig. 4.6 (b) shows the result of segmentation produced by SLIC superpixel algorithm in the BG image. It is observed that SLIC is able to provide accurate segmentation since it produces several partitions near the object boundary. The features such as color, appearance, the texture should be extracted for the superpixels classification as OD or non OD region. The classification technique is performed with several procedures requiring enormous processing time and memory. Hence, to get rid of these processing steps, the developed method constructs the geometrical model over the segmentation results obtained from SLIC and CHT within OD-ROI as shown in Fig. 4.7. The process begins by drawing the straight line intersecting the center and concentric circle from each point of hough circle. Secondly, we search the nearest possible edge pixel from each point of hough circle within the OD-ROI by measuring the euclidean distance between each point. We record the nearest point as the edge pixel. The process is repeated for all the available points of hough circle. Finally, an updated boundary for OD is acquired and curve fitting is applied to best fit the series of boundary pixels.

Let us consider a centre point of the hough circle as $h(x_0, y_0)$ as Fig. 4.7 (b). An concentric circles $C1$ and $C2$ is drawn outside and inside the hough circle C respectively and termed as OD-ROI. From each point of hough circle, a line that intersects the centre point, $h(x_0, y_0)$, $C1$ and $C2$ is drawn. The illustration of the geometrical model is seen in Fig. 4.7(b). For each line, $C(x_0, y_0)$ is the point on hough circle, $C2(x_{min}), y_{min}))$ is the point on inner circle and $C1(x_{max}, y_{max})$ is the point on outer circle. We search the nearest edge points on both the direction from each hough point i.e. $(x_{min}, y_{min}) \leftarrow (x_0, y_0) \rightarrow (x_{max}, y_{max})$. All the obtained points are connected to get the OD boundary. The boundary is further improvised by applying curve fitting [189].

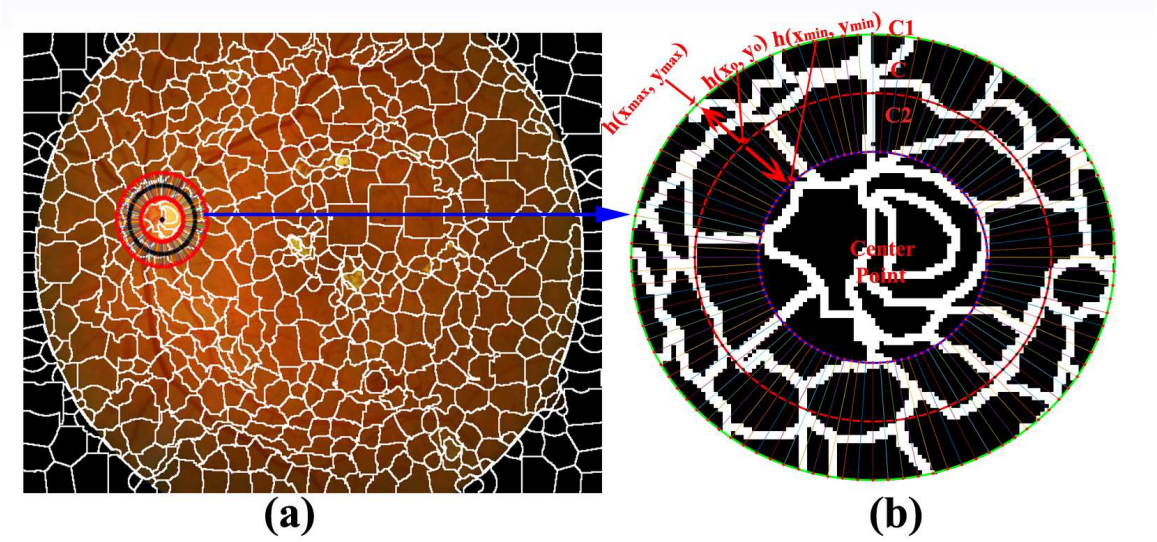

Figure 4.7: Illustration of geometrical model constructed over the edge information obtained from CHT and SLIC.

4.3 Performance evaluation and results

4.3.1 Image databases and performance metrics

The experiments are performed on Matlab 2016b running under Intel(R) core(TM) i5-4570s CPU@ 2.90 Ghz with 8GB of RAM. The performance of the proposed method is evaluated on the publicly available 7 databases. DRIONS_DB [190], MESSIDOR [191], INSPIRE_AVR [192], DRIVE [193], CHASE_DB [194], DIARETDB0 [195], DIARETDB1 [196]. These databases contain healthy as well as pathological images that are taken using different camera and environmental conditions. DRIVE is a publicly available database which has 40 color fundus images out of which 7 images have pathology. The images are divided into two groups, training set, and test set. MESSIDOR database contains 1200 images among which 540 are healthy and 660 with diabetic retinopathy. The images in this databases are captured in three ophthalmological departments by a research program sponsored by the French Ministries of Research and Defense using the 3CCD color video camera on Topcon TRC NW6 non-mydriatic retinograph, with 45 degrees of FOV. DIARETDB0 and DIARETDB1 are acquired in Kuopio University Hospital, Finland using the digital fundus camera with 50 degrees of FOV. DIARETDB0 contains 130 color fundus images that include 20 normal and 110 pathological images. DIARETDB1 contains 89 color fundus images with 4 normal and 84 pathological images. CHASE_DB

database contains 28 retinal images from 14 patients obtained from the Child Heart and Health study. This database includes 9 and 10 years old children of different ethnic origin. DRIONS_DB is the public database which consists of 110 color digital retinal images. Among 110 images, 50 images are pathological. For evaluation, we have to use the manually labeled OD which is available online for each database. The manual segmentation of OD as the groundtruth is available.

The ground truth of DRIONS_DB and INSPIRE_AVR database is provided by [190] and [192]. Also the ground truth of MESSIDOR, DRIVE, CHASE_DB, DIARETDB0, DIARETDB1 is publicly available from [197]. The performance of the proposed algorithm is experimented and compared with the existing methods in-terms of eight parameters: area under ROC curve (AUC), accuracy (Acc), sensitivity (Se) or Recall, Specificity (Sp), precision (P), misclassification rate (MR), DICE coefficient (DSC) and Overlap coefficient (Oc) [198][199]. This quantitative analysis is the pixel-based classification method where each pixel are either classified as OD or non-OD region. As a result, there are 4 possibilities: True Positive (TP), True Negative (TN), False Positive (FP) and False Negative (FN) [200]. TP and TN refer to the classification whereas FP and FN refer to the misclassification. TP and TN denote the pixel which is correctly identified as OD region pixels. Similarly, FP and FN signify the pixels which are incorrectly identified as OD region pixels. A signify the segmentations obtained from the proposed methods and G'' signify the ground truth which is manually segmented. These metric are defined as the following equations.

$$\text{Acc} = \frac{\text{TP+TN}}{\text{TP+FP+TN+FN}} \tag{4.10}$$

$$\text{P} = \frac{\text{TP}}{\text{TP+FP}} \tag{4.11}$$

$$\text{Se} = \frac{\text{TP}}{\text{TP+FN}} \tag{4.12}$$

$$\text{Sp} = \frac{\text{TN}}{\text{TN+FP}} \tag{4.13}$$

$$\mathrm{MR} = \frac{\mathrm{FP+FN}}{\mathrm{TP+FP+TN+FN}} \tag{4.14}$$

$$\mathrm{DSC} = \frac{2(\mathrm{A} \cap \mathrm{GT})}{\mathrm{A} + \mathrm{GT}} * 100\% \tag{4.15}$$

$$\mathrm{OC} = \frac{(\mathrm{A} \cap \mathrm{GT})}{\mathrm{A} \cup \mathrm{GT}} * 100\% \tag{4.16}$$

Acc is defined as the total number of classified pixels which are correctly identified to the number of total pixels in an image. Se and Sp are the metrics which are derived from the proportion of positive and negative pixels in the ground truth image that is truly identified. P is the ratio of correctly predicted positive observations and total predicted positive observations.P indicates the reproducible measurements even the value is far from the acceptable range which distinguishes it from the accuracy. A metric MR is the misclassification rate which measures the frequency of the wrong prediction. MR rate is considered excellent when the value is close to zero and positive. DSC is the overlap based metric that measures the similarity between segmented OD via automatic and manual method. To further verify the efficiency of the proposed algorithm, we calculated a metric known as Oc. This metric is the similarity measure related to the jaccard index which measures the overlap between automatically and manually segmented OD. We calculate metric, AUC from receiving operating characteristics (ROC) curve, which is used to estimate the trade-off between Se and Sp [201]. To achieve this non-parametric performance measurement, the curve is plotted with a false positive rate (1-Sp) on the x-axis and true positive rate (Se) on y-axis using different threshold values within a certain interval. The value greater than 90% is considered to be an excellent result and the ROC curve is considered as an ideal curve when its closer to the top left corner which offers a perfect value i.e. 1.

4.3.2 Results and Discussion

OD Localization

This section presents the results of automatic localization of the OD localization and is listed down in Table 4.1. The proposed method was able to locate the OD with high ac-

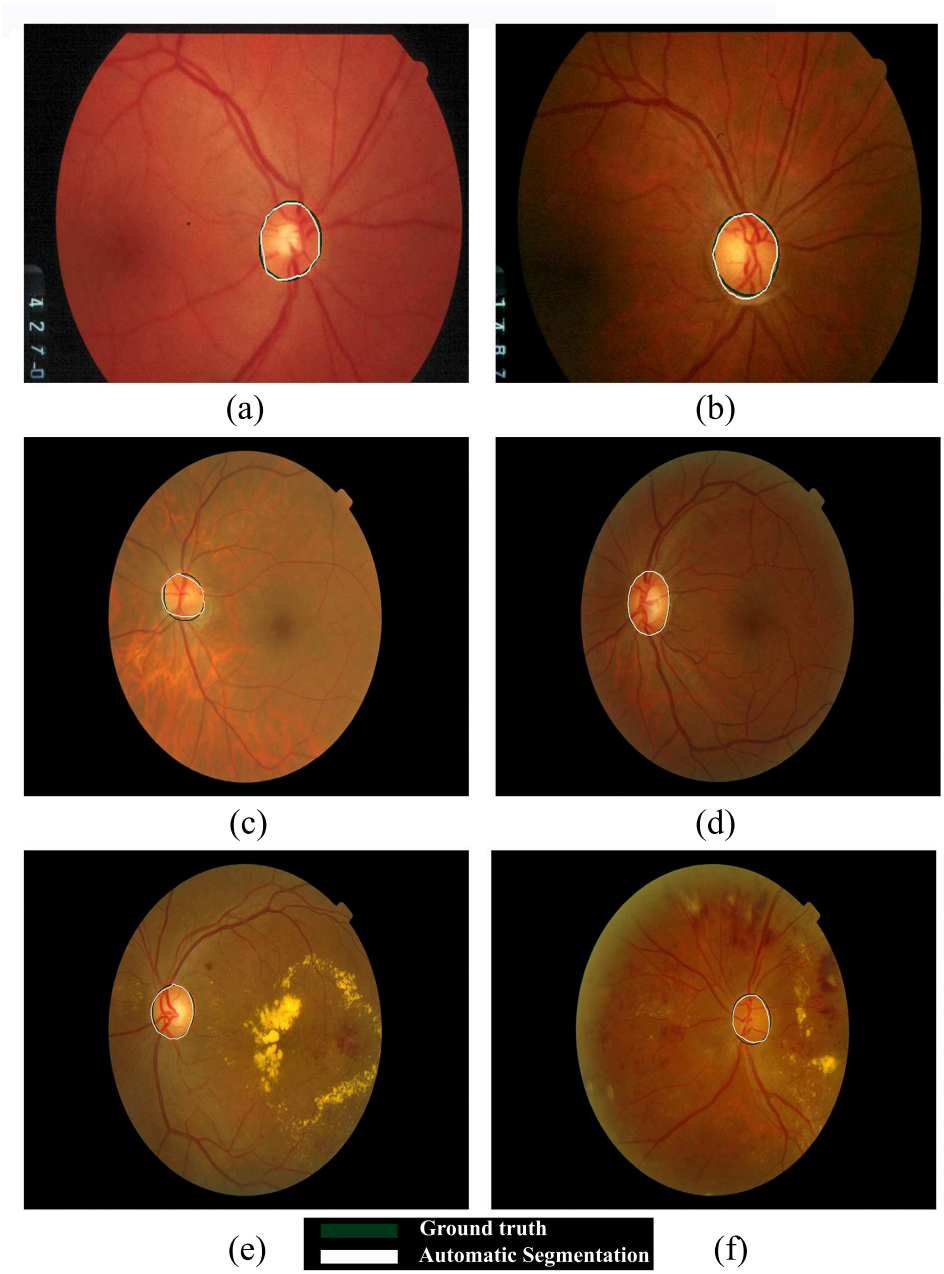

Figure 4.8: Illustration of experimental results on different types of images form different databases. Automatic segmentation is represented with the white colour and the ophthalmologist labelled boundary is represented with the green colour.

Table 4.1: Performance analysis of OD localization.

Database	No. of Image	OD detected	Accuracy (%)
DRIONS	110	109	99.09
INSPIRE_AVR	40	39	97
MESSIDOR	1200	1190	99.1
DRIVE	40	40	100
DIARETDB0	110	108	99.18
DIARETDB1	89	89	100
CHASE_DB1	28	28	100

Table 4.2: Performance measure of OD segmentation in different databases in terms of accuracy, sensitivity, specificity, precision, misclassification rate, DICE coefficient (DSC), Overlap coefficient (Oc) and AUC.

Database	Acc	Se	Sp	P	MR	DSC	Oc	AUC
DRIONS-DB	0.9981	0.9402	0.9988	0.9676	0.0030	0.9246	88.42%	0.9800
INSPIRE	0.9977	0.9377	0.9991	0.9638	0.0022	0.9496	90.43%	0.9721
MESSIDOR	0.9985	0.9581	0.9989	0.9300	0.0013	0.9411	88.99%	0.9788
DRIVE	0.9965	0.9079	0.9988	0.9876	0.0030	0.9046	82.7%	0.9965
DIARETDB0	0.9971	0.9119	0.9986	0.9358	0.0027	0.9208	85.40%	0.9596
DIARETDB1	0.9973	0.9546	0.9983	0.9306	0.0026	0.9408	88.82%	0.9758
CHASE_DB1	0.9954	0.9520	0.9968	0.9034	0.0043	0.9270	86.28%	0.9779

curacy. The experiments are conducted with seven databases which have approximately 1600 images and with several challenging conditions due to pathologies such as a bright, dark lesion, non-uniform illuminations. It is clear that under any challenging circumstances, the proposed method is able to locate the OD with high accuracy. The accuracy is close to 100% on most of the experimented databases. It is worth mentioning that the detection of OD is an important initial step to achieve efficient OD segmentation results.

OD Segmentation

The segmentation results achieved from the proposed OD boundaries estimation method is presented in this section. Fig. 4.8 shows the example of visual comparison of automatically and manually acquired OD segmentation. The green oval shaped boundary is the manually segmented ground truth results of OD whereas the white oval shaped boundary is the automatically obtained segmentation results. It is observed that the automatically segmented results have good agreement with manually segmented ground

Table 4.3: The results using the proposed algorithm are compared with the results using the methods in literature in terms of accuracy, sensitivity, specificity, precision, misclassification rate, DICE coefficient (DSC), Overlap coefficient (Oc) and AUC.

Database	Acc	Se	Sp	P	MR	DSC	O	AUC
DRIONS-DB								
Morales et al. 2013 [167]	0.9934	-	-	0.9281	-	0.9084	-	-
Abdullah et al. 2016 [176]	0.9549	0.8508	0.9966	0.9966	-	0.9102	85.1%	-
Zahoor et al. 2017 [202]	0.9986	0.9384	0.9973	0.9463	-	-	87.40%	-
Proposed Method	**0.9987**	**0.9402**	**0.9988**	**0.9676**	**0.0030**	**0.9246**	**88.42%**	**0.9800**
INSPIRE								
Behdad et al. 2014 [203]	0.9958	0.9144	0.9980	-	-	0.9168	-	-
Proposed Method	**0.9977**	**0.9377**	**0.9991**	**0.9638**	**0.0022**	**0.9496**	**90.43%**	**0.9721**
MESSIDOR								
Morales et al. 2013 [167]	0.9949	-	-	0.9300	-	0.8950	-	-
Sohini et al. 2015 [197]	0.9956	0.9043	-	-	-	-	83.73%	0.9710
Abdullah et al. 2016 [167]	0.9989	0.8950	0.9995	0.97946	-	0.9339	87.93%	-
Zahoor et al. 2017 [202]	0.9980	0.8309	0.9993	0.9136	-	-	75.61%	-
Proposed Method	**0.9985**	**0.9581**	**0.9989**	**0.9300**	**0.0013**	**0.9411**	**88.99%**	**0.9788**
DRIVE								
Welfer et al. 2013 [166]		0.8354	0.9981	0.8876	-	0.9084	39.40%	-
Salazar et al. 2014 [204]	0.9412	0.7512	0.9982	-	-	-	-	-
Morales et al. 2013 [167]	0.9903	-	-	0.8544	-	0.8169	-	-
Sohini et al. 2015 [197]	0.9960	0.8780	-	-	-	-	80.67%	0.9561
Basit et al. 2016 [205]	-	0.8921	0.9921	0.6930	-	-	61.88%	-
Abdullah et al. 2016 [176]	0.9672	0.8188	0.9966	0.8728	-	0.8720	78.60%	-
Zahoor et al. 2017 [202]	0.9980	0.8309	0.9993	0.9136	-	-	75.61%	-
Proposed Method	**0.9965**	**0.9079**	**0.9988**	**0.9876**	**0.0030**	**0.9046**	**82.7%**	**0.9965**
DIARETDB1								
Welfer et al. 2013 [166]	-	0.6341	0.9981	0.8704	-	0.9084	57.16%	-
Morales et al. 2013 [167]	0.9957	-	-	0.9229	-	0.8930	-	-
Sohini et al. 2015 [197]	0.9963	0.8815	-	-	-	-	80.22%	0.9596
Basit et al. 2016 [205]	-	0.7347	0.9944	0.7049	-	-	54.69%	-
Abdullah et al. 2016 [176]	0.9772	0.8510	0.9984	0.9263	-	0.8910	85.1%	-
Zahoor et al. 2017 [202]	0.9937	0.9706	0.9949	0.8991	-	-	87.34%	-
Proposed Method	**0.9973**	**0.9546**	**0.9985**	**0.9306**	**0.0026**	**0.9408**	**88.82%**	**0.9758**
DIARETDB0								
Sohini et al. 2015 [197]	0.9956	0.8660	-	-	-	-	77.61%	0.9333
Proposed Method	**0.9971**	**0.9119**	**0.9986**	**0.9358**	**0.0027**	**0.9208**	**85.40%**	**0.9596**
CHASE_DB1								
Sohini et al. 2015 [197]	0.9914	0.8962	-	-	-	-	80.82%	0.9467
Abdullah et al. 2016 [176]	0.9579	0.8313	0.9971	0.9261	-	0.9050	83.2%	-
Proposed Method	**0.9954**	**0.9520**	**0.9968**	**0.9034**	**0.0043**	**0.9270**	**86.28%**	**0.9779**

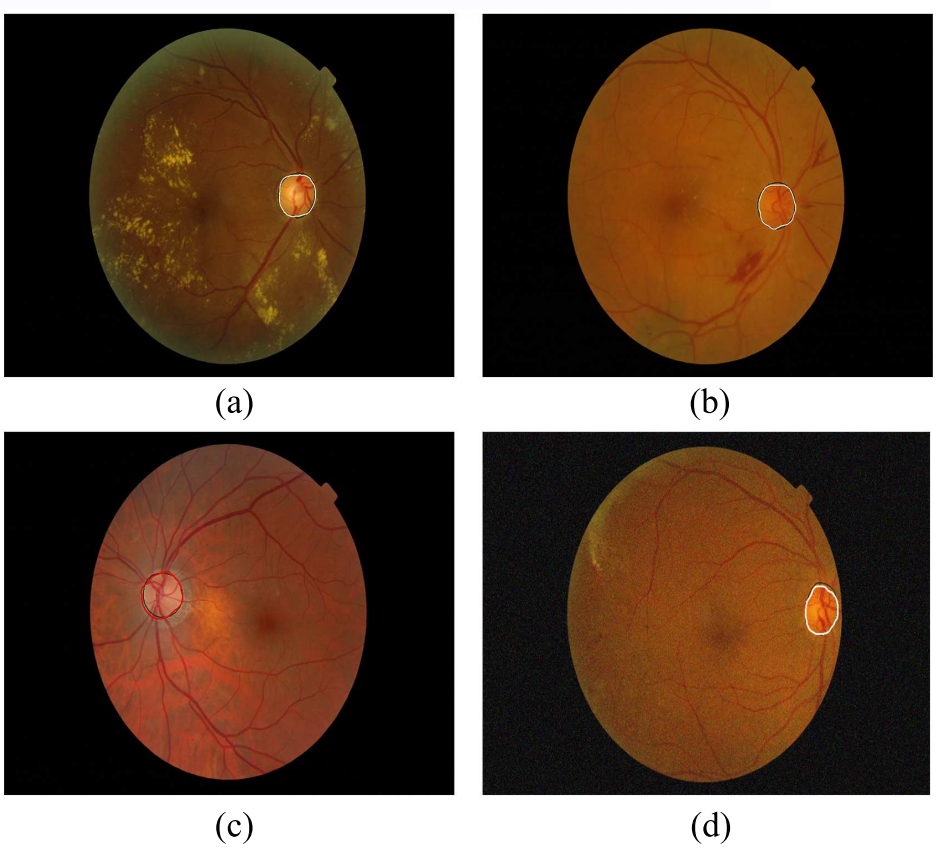

Figure 4.9: Illustration of segmentation performance (a) Presence of pathologies (b) poor contrast (c)uneven illumination (d) noisy images.

truth. Hence, the proposed algorithm efficiently extract the edge information of OD with negligible error. The segmented results are further validated with the evaluation matrices (AUC, Acc, Se, Sp, P, MR, DSC, O) as shown in Table 4.2 and are evaluated for seven databases. The obtained results using the proposed method outperform most of the existing literature as shown in Table 4.3.

We choose the few existing methods reported recently from 2013 to 2017 as shown in Table 4.3. As observed in the literature, the accuracy calculated from Zohoor et al 2017 [202] in the DRIVE database is slightly high compared with the proposed method. However, the other results achieved by the proposed algorithm are better. Also, the welfare et al 2013 [166] result associated with DSC in the DRIVE database is seen better but is highly comparable with the proposed method. According to Chase DB1 database, the results associated with specificity is highly comparable with the results obtained with the proposed method. Other than that, the results obtained from the proposed method are

marginally better than the results calculated with the existing methods.

The computational time of the proposed work mainly depends upon the kmeans clustering, obtaining hough circle and superpixels. Since the images are resized while maintaining aspect ratio, the execution time differs slightly on different databases. The experiment takes on an average of 6.3s, 10.2s, 8.8s, 5.8s 7.2s, 7.3s, and 6.8s for DRIONS, INSPIRE, MESSIDOR, DRIVE, DIARETDB1, DIARETDB0, and CHASE_DB1 respectively which is considerably low. The total computational time is highly dependent upon the configuration of the computer system and simulation software version. Hence, the comparison of computational time with other methods are not shown.

Performance on the presence of pathologies, noise and uneven illumination

It is important to know that the presence of pathologies, noise, and uneven illuminations reduce the performance of OD segmentation. Initially, we use the Weiner filter to reduce the influence of noise and uneven illumination artifacts. Although the effect of noise and uneven illumination is reduced after filtering, the lesions that posses the similar properties of OD make the detection and segmentation difficult. The proposed method combines the edge information obtained from background and foreground image to detect the OD location. We compare the location obtained from the kmeans clustering method and CHT to further verify whether the detected point is within the OD and finalize a location of OD. For the segmentation, we merge the edge information obtained from superpixel and CHT. This process allows us to compare the edge information of OD obtained from CHT and superpixels in-depth and select the right edge pixel. Hence, our method turns out to be robust against noise, lesions, and uneven illumination. Some examples are displayed in Fig. 4.9 where (a) is an image with the presence of a lesion (b) with poor contrast (c) with uneven illumination and (d) with a Gaussian and salt pepper noise. Out methods is able to detect and accurately segment the OD in all the four cases successfully.

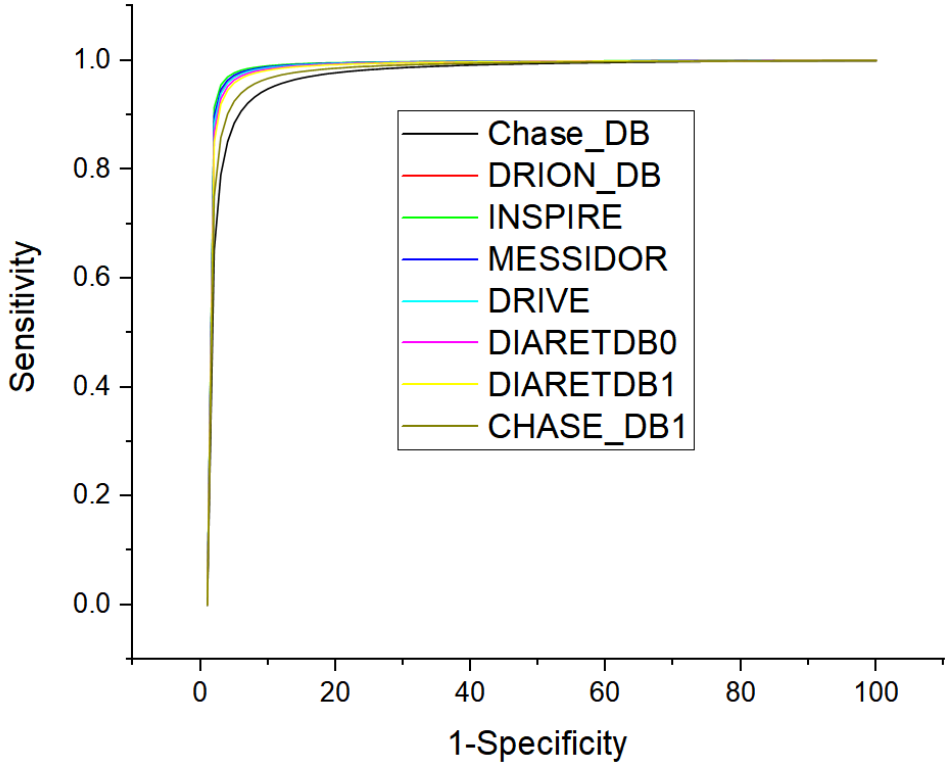

Figure 4.10: ROC curve using the proposed algorithm.

4.4 Conclusion and Discussion

In this chapter, we propose a novel framework for automatic estimation of OD-ROI and segmentation of OD. OD-ROI is achieved by the application of kmeans clustering. CHT and OD segmentation are obtained using the geometrical model over the edge information acquired from SLIC and CHT. This framework has been tested on seven publicly available databases, DRIONS-DB, INSPIRE, MESSIDOR, DRIVE, DIARETDB1, DIARETDB0, and CHASE_DB1. These databases include images with different resolutions and pathological conditions. The experiment shows that the proposed method is accurate, computationally efficient and is effective for abnormal retinal images with uneven illumination and several pathological conditions. The quantitative analysis in terms of eight evaluation metrics(Acc, Se, Sp, P, MR, DSC, O, and AUC) shows the outstanding segmentation results when compared with the recent OD segmentation techniques. This method can be used as a part of automatic computer aided diagnosis systems for early detection of glaucoma.

To obtain the robust OD segmentation, we considered several factors that degrade

the fundus images such as noise, uneven illumination and the pathologies such as bright and dark lesions. Initially, our approach incorporates the noise removal technique while preserving edges. The estimation of OD-ROI is carefully considered utilizing the clustering algorithm on separate BG and FG images obtained from morphological steps. Later, the obtained location points are compared with the results obtained from CHT to optimize the produced results. For final segmentation, our method utilizes edge information which is obtained from SLIC and CHT algorithms. The edge information obtained alone from SLIC or CHT cannot contribute a precise segmentation. Also, the over-segmentation from SLIC could provide a false edge and has to be identified properly. Hence, our approach i.e by using a geometrical model over the edges obtained from SLIC and CHT is able to find the boundary of OD accurately resulting reliable and robust segmentation. The necessity of feature extraction for the classification of OD and non-OD pixels are eliminated saving the processing time and memory.

In the future, we will concentrate on measuring the variation of cup-to-disc ratio for the automated detection of glaucoma. Moreover, we will direct our research for fovea detection that is partially dependent on the result of OD segmentation

Chapter 5

Automatic and fast segmentation of breast region-of-interest (ROI) and density in Magnetic Resonance Imaging (MRI)

5.1 Introduction

Breast cancer is a major cause of death in women [206]. It is reported that, in a lifetime of women worldwide, one in eight will develop breast cancer [207, 208]. Also, the reported statistics reveal that over 2 million women are suffering from breast cancer in the US alone [209]. To reduce the mortality rate from breast cancer, early diagnosis and treatments are essential [210]. MRI is a well-established imaging technique to identify and mitigate breast diseases by generating a series of 3D images that a radiologist uses to manually detect the diseased part and identify problems[211, 212]. The manual process is time consuming because of the high number of images [213, 214]. Hence, automatic computer-algorithm based image analysis has become essential for performing computer-aided detection and diagnosis, which aim to provide prompt output and help radiologist to accurately locate the diseased area.

This chapter is derived from:

- **D. Pandey**, X. Yin, H. Wang, M.-Y. Su, J.-H. Chen, J. Wu, and Y. Zhang, "Automatic and fast segmentation of breast region-of-interest (roi) and density in MRIs" Heliyon, vol. 4, no. 12, p. e01042, 2018..

The main objective of this study is to segment the breast region of interest (BROI) and breast density (BD) from breast MRIs. First, BROI segmentation can serve as the fundamental step for avoiding irrelevant structures such as unwanted background and organs like the heart, liver, and chest, improving efficiency and accuracy during further analysis like tumor segmentation [215]. Tumor segmentation in breast MRIs is considered to be a laborious and error-prone procedure. Also, tumors normally reside inside the BROI. Therefore, prior to tumor segmentation, it is essential to identify the BROI [216]. BROI segmentation is also useful for applications such as BD measurement [217] and performance improvement of DCE-MRI in terms of pharmacokinetics-model calibration (PMC) [217, 218]. During PMC, the properties of the interior chest wall should be determined, which requires pectoral muscle segmentation [219]. Second, the ratio of BD can be considered as a strong indicator for the estimation of breast cancer risk. Also, breast tissue pattern asymmetry in left and right breast is considered to be an abnormal biological process that leads to cancer [220]. BD does not have a distinct shape and pattern and may be found anywhere within the image. Moreover, intensity inhomogeneity is a common problem within breast MRIs since the bias field adds more challenges by producing similar intensity around the BROI.

For BROI segmentation, different techniques have been reported in the literature. Ertas et al. [221], performed morphological operation and intensity thresholding for the segmentation. However, the results are better when the chest wall has high contrast. Several other methods such as intensity histogram [222, 223], wavelet analysis [224, 225] and active contour [226,227], fuzzy c-means [228,229], region growing [230,231] are proposed. The performance of these methods rely on the contrast between the border regions and can fail in the cases that have similar intensity distribution. A fully automated method reported by Wang et al. [232] extracts breast area on non-fat-suppressed MRI images. The author explained that the properties of pectoral muscle and the breast-air boundaries are similar in 3D and exhibit smooth sheet like surfaces and use a Hessian-based filter to suppress the lower contrast and non-specific shapes. However, this method does not include breast density segmentation and may not produce an accurate mask. Khalvati et al. [233] reported a multi-atlas segmentation algorithm that creates a breast atlas with the help of phase congruency. This segmentation process is reliant upon the shape and intensity

based registration prior to the segmentation. Gubern-Merida et al. [234] proposed a probabilistic atlas based approach for breast segmentation. However, the accuracy depends upon the size and variability of the database and requires an atlas that is representative of the population, which is computationally expensive. An edge based approach was proposed by [235] that is independent from the visible contrast between the breast ROI and chest wall. This method calculates cost function using edge information obtained from tunable Gabor filter. The precision of this method depends upon the information from the adjacent slices and accurate initial-border determination. Despite the advancement in BROI segmentation, fully automatic, accurate and fast segmentation of BROI still require much attention. This is because: 1. MR breast imaging contains breast structures in different shapes and no clear boundary of breast landmarks, which requires manual correction [236]. 2. There is a bilateral asymmetry between left and right breast regions requiring separate analysis [237]. 3. The pectoral muscle is closely attached and possesses similar intensity to the BROI which gives false positives and requires manual corrections [238]. 4. It is observed from the literature that several existing methods are supervised and require prior information before the segmentation process which results in computational complexity [239]. For BD segmentation, we note that there is a significant range of studies carried out in a semi-automated segmentation using an interactive thresholding method [240][241] and user-assisted clustering methods [242]. These non-automated methods are subjective and create inter- and intra-reader variability [243]. It can be time-consuming, and therefore unsuitable for processing larger databases. To cope with above-mentioned difficulties, some attempts on automated methods have been studied such as adaptive thresholding [244], atlas-based method [245], Gaussian distribution curve fitting [246], hierarchical support vector machine [247], and Otsu thresholding algorithm [248]. It is observed that supervised methods provide more accurate results, but require a complex and costly labelling and analysis by expert radiologists prior to segmentation. Hence, for automatic segmentation of BD, unsupervised methods produce efficient results. Also, the most effective way to minimize computation time is to reduce the number of pixels processed. To overcome these problems, we propose a novel framework which is fully automatic, unsupervised, fast and efficient. The proposed model is divided into two steps: 1. BROI segmentation 2. BD segmentation.

During BROI segmentation, First, we aim to de-noise the MR image and precisely remove air-background using pixelwise adaptive wiener filtering (PAWF) technique [249] [250] and k-means clustering [251]. PAWF technique can preserve the edges and high frequency parts of an image unlike a normal filtering technique and k-means clustering will automatically cluster the whole image on different group, based on the correlation of pixels intensity. Second, the heart area, a brighter part of image is segmented using active contour level-set method [252]. The novelty in this method involves the calculation of initial contour by using maximum entropy thresholding and convolution technique [117, 253], which provides accurate segmentation and reduction of computation speed. Third, the segmentation of the pectoral muscle is performed. The orientation of the pectoral muscle and breast density of the left, right, and central area of the breast are different. Hence, we apply a morphological operation on a different orientation to enhance the gap between the pectoral muscle and breast density. The resultant image is binarized using an adaptive thresholding technique to exclude the pectoral muscle. Finally, we use polynomial curve fitting [254] to smoothen the acquired BROI segmentation. During BD segmentation, initially, we de-noise the result image from BROI segmentation. It is observed from the experiment that, the volume and intensity of BD in left and right breasts are different, hence, the single threshold value could not provide accurate segmentation. We divide the BROI segmentation image according to its geometrical information and calculate a different threshold value for left and right breast using four level FCM [255]. This study calculates FCM within the BROI rather than on an entire image.

Rest of the chapter is organized as follows. A detailed methodology of the segmentations (BROI and BD) is reported in Section 5.2 which includes the explanation of eliminating unwanted landmarks. In section 5.3, the experimental results are analyzed and discussed. Finally, a concluding remark drawn in this study is given in Section 5.4.

5.2 METHODS

The general workflow for BROI and BD segmentations is illustrated in Fig. 5.1. Each step is successively explained in the following sections.

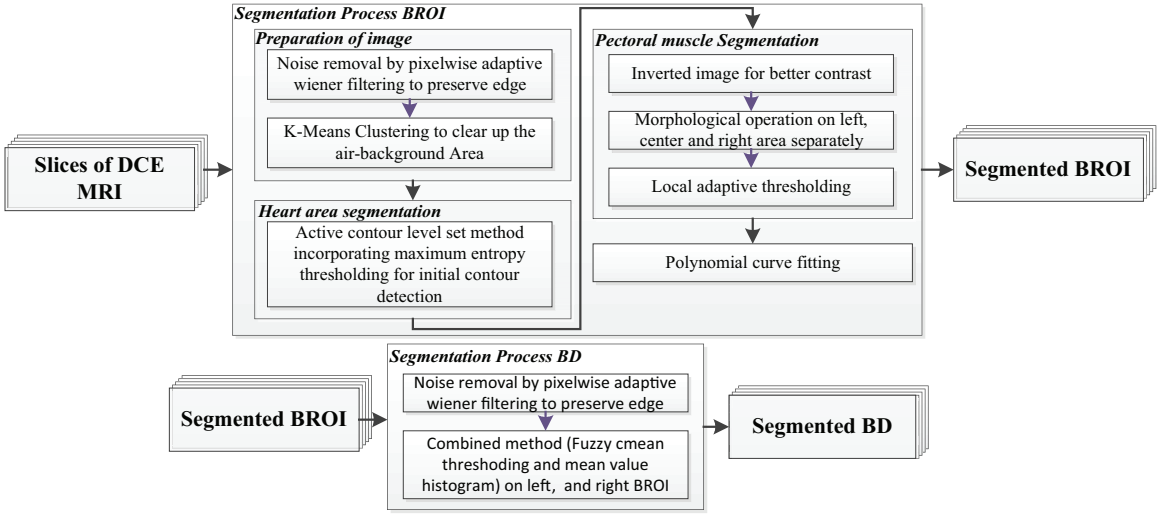

Figure 5.1: General workflow of segmentation procedure to extract BROI and BD.

5.2.1 SEGMENTATION METHODOLOGY OF BROI

Pre-processing Step

The process begins with rescaling the image to the fixed size so that each image in the different databases posses similar properties. The rescaled image dimension equals 328 on the row whereas the columns are calculated accordingly, to preserve the aspect ratio. The original breast MRIs are fundamentally corrupted by random noise from the image acquisition process that leads to uncertainties during the measurement of any quantitative biomarker [256]. Hence, pre-processing the rescaled image is an important step for removing undesirable noise such as additive white Gaussian noise (AWGN) and irrelevant details that affect the BROI segmentation. Gaussian filtering has been thoroughly studied for noise suppression and smoothing [257]. This process blurs an image with Gaussian function and involves a convolution mask where pixel values are modified according to the neighboring pixels. However, the Gaussian filter is not always suitable for denoising since it also removes high-frequency signal components leaving a blurred edge or boarder as shown in Fig. 5.2(a) [258]. The edge preserving denoising technique should be adopted as the edges are the important features during segmentation. Hence, we apply a pixelwise adaptive wiener filtering technique that effectively removes the noise while preserving the edges [259][260]. The denoised result image obtained from Gaussian filter has blurred edges. However, the result from pixelwise adaptive wiener

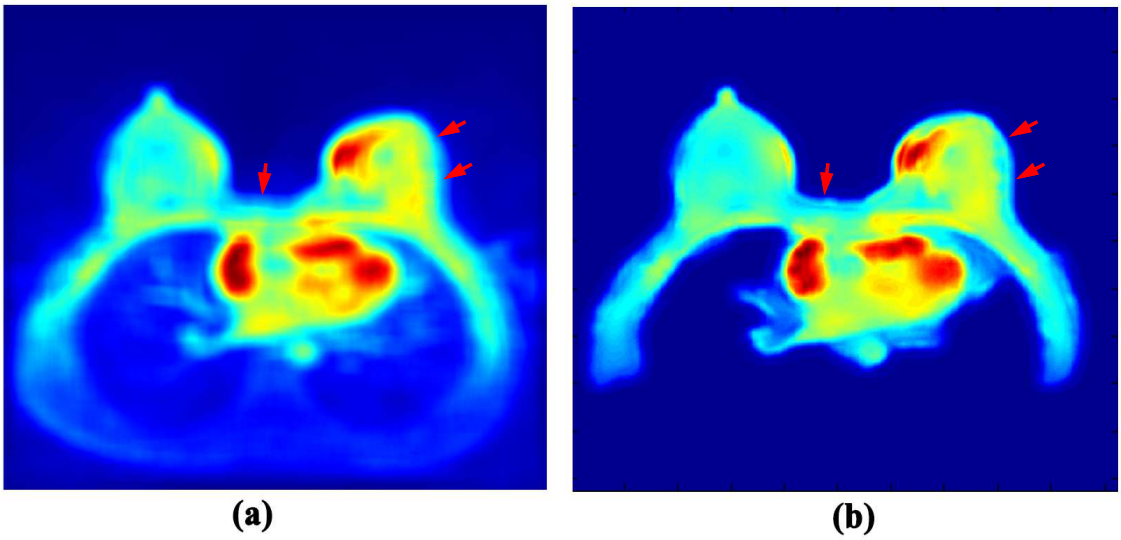

Figure 5.2: Illustration of filtering technique in regards to the accurate edge preservation (a) Gaussian filter (b) pixelwise adaptive wiener filter.

filtering technique show that sharp edges are preserved as shown by the red arrowhead in Fig. 5.2(a) and (b).

Let us consider the pixel position (i, j) and the window mask of W_M around its neighborhood. We conducted experiments to see the effect of different window size in the MR images. We found out that the use of larger window size clears the noise but destroys the useful edge information. On the other hand, the use of smaller window size are not capable of clearing the noise from the image. Based on our experiment, we fixed the window size (W_M) as 10x10. The value presented is suitable for the database we have used. However, it can be slightly optimized to suit the other database of MR image.

The pixelwise adaptive wiener filter is given by Eq. (5.1) [261]:

$$I_{\text{denoised}}(i,j) = m_{\text{f}} + \frac{\sigma_{\text{f}}^2 - v^2}{\sigma_{\text{f}}^2}(I_{\text{noisy}}(i,j) - m_{\text{f}}) \tag{5.1}$$

where, m_{f} and σ_{f}^2 is the local mean and variance. v^2 is the average value of σ_{f}^2 across noisy image i.e. I_{noisy}. The computation of local mean and m_{f} and variance σ_{f}^2 is provided Eq. (5.2):

$$
\begin{aligned}
m_{\mathrm{f}} &= (XY)^{-1} \sum_{i,j \in M} I_{\mathrm{noisy}}(i,j) \\
\sigma_{\mathrm{f}}^2 &= (XY)^{-1} \sum_{i,j \in M} (I_{\mathrm{noisy}}^2(i,j) - m_{\mathrm{f}}^2)
\end{aligned}
\tag{5.2}
$$

where X and Y are the horizontal and vertical arrays of pixels in the window mask.

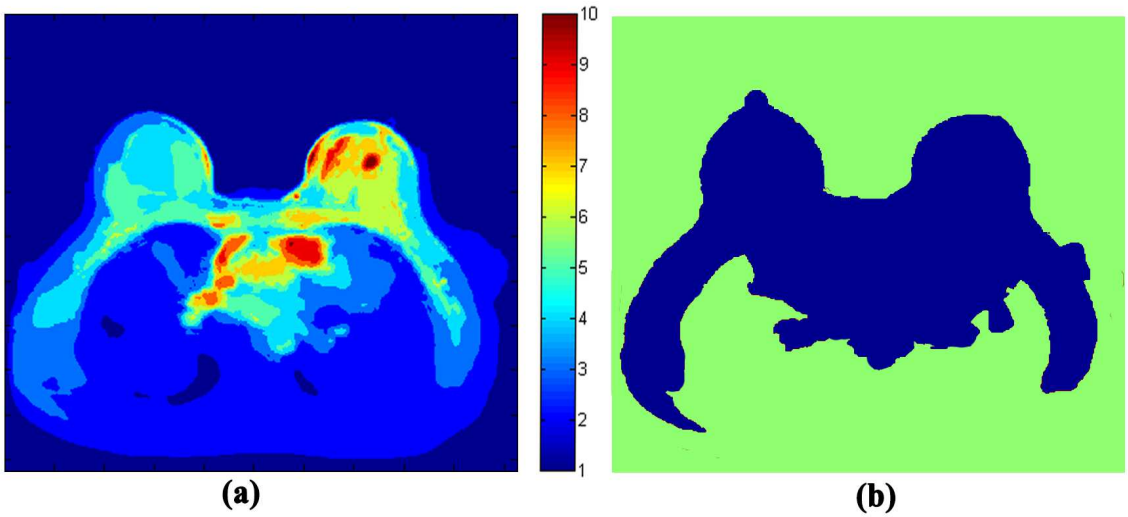

Figure 5.3: Illustration of (a)Color distribution of MRI image using 10 clusters of the K-means clustering algorithm. (b) Resultant binarised image after removing noise and first two layers.

The color distribution of the denoised MRI image is studied using K-means clustering method as presented in Fig. 5.3. This method follows two steps that divide a set of data into k number of clusters. Initially, k centroid is calculated and the data point is allocated to the cluster as the nearest centroid from the particular data point. The distance between the centroid and the data point is calculated with the Euclidean distance. Once the data point is clustered, a new centroid is recalculated and the procedure is repeated until convergence has been reached [262]. We clustered an image into 10 different colors (k=10) which is sufficient to observe the level of detail of landmarks and their color distribution. In Fig. 5.3(a), blue color in the color bar (k=1) signifies the darkest and the red color(k=10) represents the brightest intensity area. Let us consider a set of n data points as $d_1, d_2, ...d_n$ and k cluster has centroid as $c_1, c_2, ...c_k$. The number of clusters in our case is 10. Initially, we select random centroid points and assign elements d_i to the cluster O_j as presented in the Eq. (5.3). Now, update the center of cluster O_j and repeat until the centroid converges

using Eq. (5.3).

$$O_j = \{d_i : ||d_i - c_j||^2 \leq ||d_i - c_t||^2, 1 \leq t \leq k\} \tag{5.3}$$

During the experiment conducted on 15 MR breast scans, we discovered that 1st and 2nd cluster always represent air background and partial lung area. These clusters do not possess useful information and can be eliminated. Moreover, clusters 3 to 10 characterize BROI, pectoral muscle, heart, some region of lung and BD. This means that most of the useful information can be represented above cluster 3 and is preserved as shown in Fig. 5.3(b). Note that we have conducted experiments with different cluster numbers and is empirically set as 10.

Heart area segmentation

In the MR images, heart area, the central part of the image appears to have the brightest intensity in the image and differs in shape and size. It is observed that some images have low contrast and close boundaries which creates complication in the segmentation process. The elimination of this area is vital for the accurate segmentation of the BROI. We obtained 10 clusters in the previous section. From our experiment, we noticed that the last four clusters are the brightest clusters in terms of color intensity and cover heart area and gradually spread towards the pectoral muscle and BROI as shown in Fig. 5.4(a), (b). Hence, we combine these clusters and use the active contour level set method [252] to segment heart area. The active contour model uses level set method to evolve its initial contour. The detection of boundaries rely on the mumford–Shah segmentation technique [263] for the evolution process of contour. Hence, the objects with discontinuous and undefined boundaries can be detected with this model. The process begins by detecting an initial contour point for the evolution process. The initial contour point is detected using maximum entropy thresholding and convolution method [253][117]. Initially, a preprocessed image is binarized with maximum entropy thresholding. A convolution process is carried out between the binarized image and a square window of 50 pixel x 50 pixel. Note that, we fixed our window size from several experiments. The convolution

between image $I(i,j)$ and the mask image $h(u,v)$ is given by Eq. (5.4):

$$C(i,j) = \sum_{u=-\infty}^{\infty} (\sum_{v=-\infty}^{\infty} I(i-u, j-v)h(u,v)) \tag{5.4}$$

where (i,j) is the dimension of the image to be convolved and (u,v) is the dimension of mask image. $h(u,v)$ is the coefficient of mask image at position (u,v). The centre of the window point provides a weighted sum of each pixel in the binarized image. The pixel that gives the highest weighted sum as an initial contour point is considered. We draw a circle (initial contour, C) from the initial contour points. Let us consider two forces of the initial contour C, be $F_1(C)$ and $F_2(C)$. $F_1(C)$ is the force to shrink the contour and $F_2(C)$ is the force to expand the contour. These two forces are balanced when they reach the desirable boundary of the interested object. The minimal partition problem used to minimize an energy is represented in Eq. (5.5):

$$F(c_1, c_2, C) = F_1(C) + F_2(C) = \int_{inside(C)} |I_o - c_1|^2 dx + \int_{outside(C)} |I_o - c_2|^2 dx \tag{5.5}$$

In this work, the initial contour is located around the mid section of the heart area as shown in Fig. 5.4(b). Moreover, $F_1(C)$ is always zero and $F_2(C)$ is greater than 0, hence, we always expand initial contour (C). When the initial contour C reaches the equilibrium, $F_1(C)$ and $F_2(C)$ becomes zero, and segmentation is achieved. The iteration process is controlled by level set formulation as shown in Eq. (5.6).

$$\begin{gathered} C = \{(x,y) | \phi(x,y) = 0 \\ F(c_1, c_2, C) = \int_\Omega (I_o(x,y) - c_1)^2 H(\phi) dxdy + \int_\Omega (I_o(x,y) - c_2)^2 (1 - H(\phi)) dxdy \\ + v \int_\Omega |\nabla H(\phi)| \end{gathered} \tag{5.6}$$

Where $H(.)$ is the heaviside function and $I_o(x,y)$ is the input image. To obtain the minimum of F, F's derivatives is found and set to zeros and c_1 and c_2 and ϕ is updated in

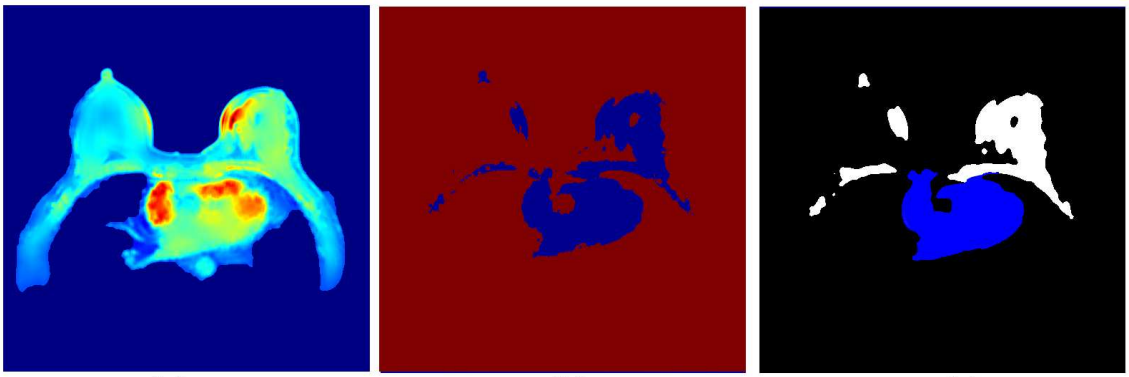

Figure 5.4: Elimination process of heart area. a)10 clustered MRI image b)Four brightest cluster c)Final segmented heart area.

Euler-Lagrange equation as shown in Eq. (5.7):

$$\begin{aligned} c_1(\phi) &= \frac{\int_\Omega I_o(x,y)H(\phi(t,x,y))dxdy}{\int_\Omega H(\phi(t,x,y))dxdy} \\ c_2(\phi) &= \frac{\int_\Omega I_o(x,y)(1-H(\phi(t,x,y)))dxdy}{\int_\Omega (1-H(\phi(t,x,y)))dxdy} \\ \frac{\partial\phi}{\partial t} &= \delta(\phi)[vdiv(\frac{\nabla\phi}{|\nabla\phi|}) - (I_o - c_1)^2 - (I_o - c_2)^2] \end{aligned} \tag{5.7}$$

where $\delta(.)$ is the Dirac function. The experiment shows that, the heart area normally resides within this circular radius of 80 pixels from the initial contour points. Hence, we permit the evolution process only on the circular area of 80 pixel radius from the initial contour point and will stop automatically. This process improves accuracy and saves computational time. The final segmented heart area is represented by blue as shown in Fig. 5.4(c).

Pectoral muscle segmentation

The other important step is identifying the pectoral muscle. This step is vital because pectoral muscle and BROI shares a similar pixel intensity especially in the presence of dense BD [264][265], making segmentation difficult and inaccurate. Hence, we include shape and geometrical information of the pectoral muscle and BD in MRIs obtained using the several experiments. The pectoral muscle is attached just below the BROI and above the lung and heart region ans spreads towards the bottom left and right corner as shown

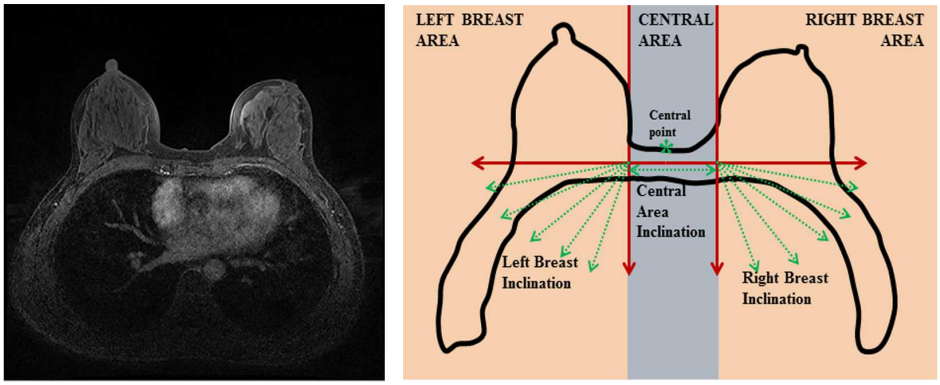

Figure 5.5: Identification of pectoral muscle area using a morphological operation. (a) MRI image. (b) A 2D image slice is divided into three different areas : 1) left 2) right and 3) central breast area. Each area is processed with a morphological operation in different orientation that develops a response image. These response images are merged to produce a single image.

in Fig. 5.5(a). Also, the BD is found to be thick in the BROI region and gradually becomes narrower and ends at the left and right corner. In the narrow section, the pectoral muscle and BD are closely connected. However, there is a small space between these two regions in MR images. We use a morphological opening operation to make this gap smooth and clear. Moreover, we use local adaptive thresholding for the binarization of the resultant image obtained from morphological opening operation. Finally, the greatest area from the connected-component labeling is selected as a pectoral muscle.

Fig. 5.5(b) depicts the model for producing a response image in each orientation. It is observed that the angle of inclination of left breast tissue near the pectoral muscle varies between 180 to 270 degrees and right breast tissue near the pectoral muscle varies between 270 to 360 degrees as demonstrated by the green lines in Fig. 5.5(b) respectively. Similarly, the breast tissue inclination in the central area is 0 degree. To generate a response image using morphological opening operation in different orientation, we divide a denoised image obtained after eliminating the heart area into 1. Left breast area 2. Right breast area and 3. Central breast area using shape and geometrical information. Hence, a five response image on the left and right breast areas with 15 degree increment in angle of inclination and 1 response image on central breast area with 0 degree orientation is generated. The separate response images are generated using morphological opening operation with the structuring elements in terms of lines in different orientations and the

response images are merged together. The morphological opening operation is found to be very effective in smoothing the space between the breast tissue and pectoral muscle. This operation eliminates the objects that are smaller than the line structuring element with the scale of 5 pixel in different orientations to reconstruct the remaining shape of the objects. Let I_h be the denoised image after eliminating the heart area. Morphological opening operation performs both erosion and dilation using the same structuring elements on the image and satisfies Eq. (5.8):

$$I_{\mathrm{rs}} = \cup\{(S_{\mathrm{e}}) \mid (S_{\mathrm{e}}) \subseteq I_{\mathrm{s}}\}, \tag{5.8}$$

where S_{e} indicates a line shaped structuring element with the scale of 5 pixel in different orientations, I_{s} is the set of I_{h} and $\cup$ denotes union of set. The response image I_{rs} is given by geometric interpretation where unions of all translations of structuring elements S_{e} fit the entire image I_{h}. The important thing to noticed here is that the brightest feature smaller than the scale of line structuring elements in their respective orientation is greatly reduced in terms of intensity. Also,it eliminates small specularities and textural fluctuations.

Fig. 5.6 show the images, before and after the morphological opening operation in the left and right breast areas. Fig. 5.6 I ((a) and (b)) are the original image of left and right breast areas respectively. After the morphological opening operation, the gap between the pectoral muscle and BD is clear and smooth as shown in Fig. 5.6 II ((a) and (b)) on the left and right breast areas. After the morphological opening operation, an adaptive local thresholding is used separately in three different areas to segment the pectoral muscle. In the global thresholding approach, a single thresholding value is produced for a whole image based on the global characteristics of the image. In contrast, adaptive local thresholding calculates a local thresholding value based on the characteristics of the window around the pixel, i.e. it changes the threshold value dynamically in the image. Since the calculation of a local threshold based on the histogram is computationally expensive, we have chosen a local threshold value calculated using the statistical parameter, mean and local intensity distribution. Adaptive local thresholding typically takes a grayscale input image and produces a binary image $I_b(x, y)$ as an output as shown in Eq. (5.9) which is

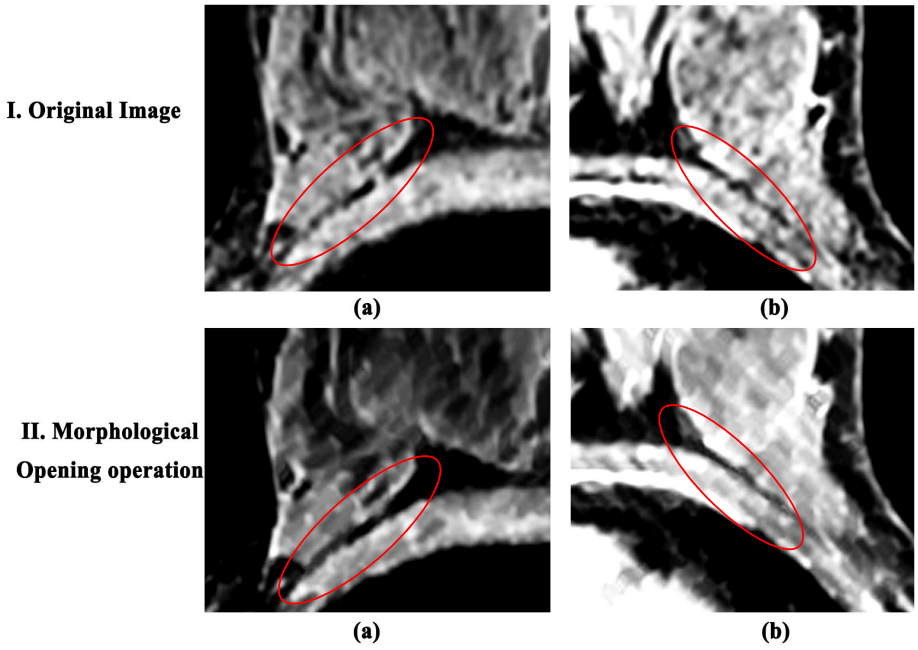

Figure 5.6: Illustration of morphological opening operation to obtain a separation between pectoral muscle and breast tissues. (I) The original image of left and right breast area (II) The resultant image after using morphological opening operation on left and right breast area.

dependent upon the window size.

$$I_b(x,y) = \begin{cases} 0 & I(x,y) \leq T(x,y) \\ 1 & \text{otherwise} \end{cases} \tag{5.9}$$

$I_b(x,y)$ is the binarized image, $I(x,y) \in [0,1]$. The threshold value $T(x,y)$ is achieved using sauvola's technique. This technique uses mean, $m(x,y)$ and standard deviation $\delta(x,y)$ to calculate the threshold value of each pixel within a defined window size as shown in the Eq. (5.10):

$$T(x,y) = m(x,y)[1 + k(\frac{\delta(x,y)}{R})] \tag{5.10}$$

where R is the maximum value of standard deviation and fixed as 128 for the grayscale image. k is the bias and takes the positive value between [0.2,0.5]. Since the algorithm is not very sensitive of k , we calculate the threshold value without involving k as shown in Eq. (5.11):

$$T(x,y) = m(x,y)[1 + (\frac{\delta(x,y)}{R})] \tag{5.11}$$

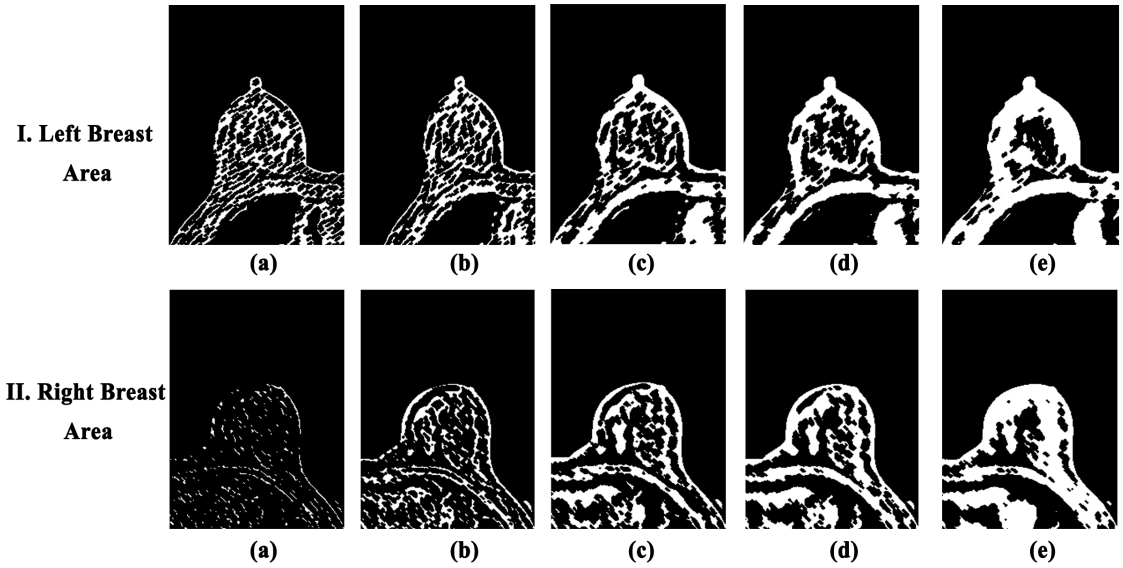

Figure 5.7: Response of different window size during adaptive thresholding. Resulting image obtained from adaptive thresholding using different window size (5, 10, 20, 30, and 50) respectively I) on left breast area II) on right breast area.

The smaller window size is found to be more sensitive to noise and generates unusable white pixels around the image. Increasing the window size will produce a denoised and clear image and tends to merge the edges. Hence it is necessary to select the right window size of our requirement for the segmentation of the pectoral muscle. We have conducted an experiment to find the right window size as shown in Fig. 5.7. The first and second row in Fig. 5.7 shows a resulting image from adaptive thresholding using different window size on left and right breast respectively. A window size of 5, 10, 20, 30, and 50 pixels are considered, which is depicted in Fig. 5.7 I ((a), (b), (c), (d), and (e)) on left breast and Fig. 5.7 II ((a), (b), (c), (d), and (e)) on right breast respectively. It is observed that a window size of 20 pixels is found to be suitable to produce an accurate results.

A resultant image from left, right and central part of the image are merged together to produce a single image. To segment the pectoral muscle, we remove the area above the central point which is highlighted in blue as shown in Fig. 5.8(a). Note that the central point is already detected in the previous steps. Fig. 5.8(b) shows the remaining part after the upper region is removed. Finally, a pectoral muscle is segmented by extracting the greatest area using the connected-component labeling as shown in Fig. 5.8(c).

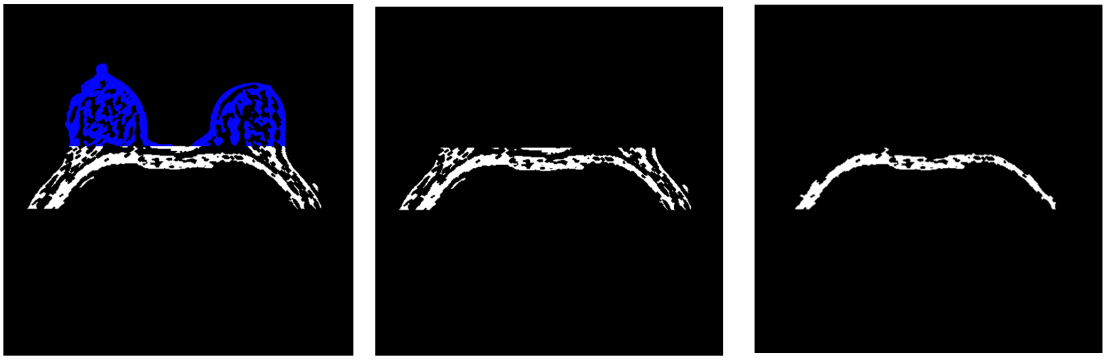

Figure 5.8: Illustration of extraction of pectoral muscle after local adaptive thresholding. (a) Resultant image of local adaptive thresholding. The blue in upper part represents the area above the central point of breast image and lower part represents the heart area (b) Resultant image after removing a area above the central point and heart area. (c) Extraction of pectoral muscle by selecting the greatest area of connected-component labeling.

5.2.2 SEGMENTATION METHODOLOGY OF BD

We segmented a BD with thresholding method using fuzzy c-means clustering technique. The MRI images are noisy and the literature reveals that the conventional FCM is not efficient to produce a threshold for noisy image and sometimes produces false positives in the segmented images [266]. Hence, we denoised the obtained BROI segmentation. Also, high-level FCM is required to produce efficient results which are computationally expensive. To cope with the computing problem, we used conventional FCM clustering method within the BROI area.

FCM clustering is based on the minimization of the following objective function [267] as shown in the Eq. (5.11). First of all, we define a number of clusters, C = 4 and the random initialization of membership matrix in Eq. (5.13) is done. The centre of the cluster is calculated as shown in Eq. (5.14) using the membership matrix, U_{xy}. The membership matrix is updated according to the position of the cluster centre. The change in the membership matrix is calculated and compared with old membership matrix. If the objective function is minimized, the process is stopped otherwise a new center of clusters is determined and membership matrix is updated according to the new centers. The process

continues until the objective function is minimized as shown in Eq. (5.12).

$$O_m = \sum_{x=1}^{N}\sum_{y=1}^{C} U_{xy}^{m}||z_x - C_y||^2, 1 \leq m \leq \infty \tag{5.12}$$

where N and C are the number of data points and number of cluster centers. U_{xy} represents the membership function of $x^(th)$ data and $y^(th)$ cluster center.m and C_y are the fuzziness index ≥ 1 and $y^(th)$ cluster center. The membership function U_{xy} and cluster centers C_y are calculated as shown in Eq. (5.13) and Eq. (5.14):

$$U_{xy} = \frac{1}{\sum_{z=1}^{C}(\frac{||z_x - C_y||}{||z_x - C_z||})^{\frac{2}{m-1}}} \tag{5.13}$$

$$C_y = \frac{\sum_{x=1}^{N} U_{xy}^{m}.z_x}{\sum_{x=1}^{N} U_{xy}^{m}} \tag{5.14}$$

The membership function U_{xy} and cluster centers C_y is calculated and repeated unless $max_{ij}\{|U_{xy}^{z+1} - U_{xy}^{z}|\} < \epsilon$, where ϵ is the termination iteration between 0 and 1. Each pixel of the image is assigned to the respective cluster with the highest membership value. We conducted the experiment on FCM with several clusters. According to the experiment, FCM with 4 clusters is found to be effective for producing an accurate thresholding value. A threshold value is produced by averaging the mean of maximum and minimum value of the third cluster. Moreover, it is observed that the mean histogram intensity of left and right BROI is different. Hence, we calculated separate thresholds by using 4 level FCM of left and right BROI. The obtained segmentation result is accurate with faster computation.

Fig. 5.9 shows the mean histogram of intensity information in the left and right BROI. For demonstration, we choose six MR images and observed that the right BROI has a higher intensity level as compared with the left BROI. Thus, we came to the conclusion that a single thresholding value produced by thresholding would not be sufficient to achieve high accuracy in the segmentation of BD. To solve this problem, we divided a BROI image into three different areas following similar steps during BROI segmentation. Since, the central area has no BD, we focus on the left and right BROI. Fig. 5.10 demonstrates the left (blue solid arrowhead) and right (blue dotted arrowhead) BROI re-

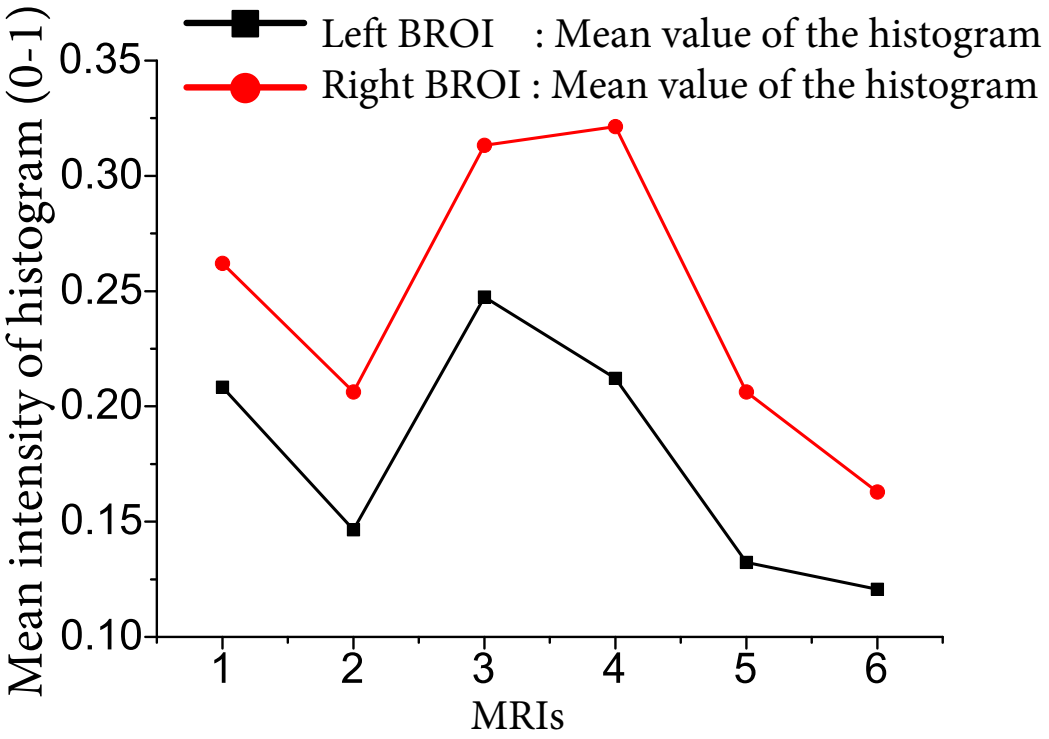

Figure 5.9: Mean value of histogram in terms of intensity of the left and right BROI.

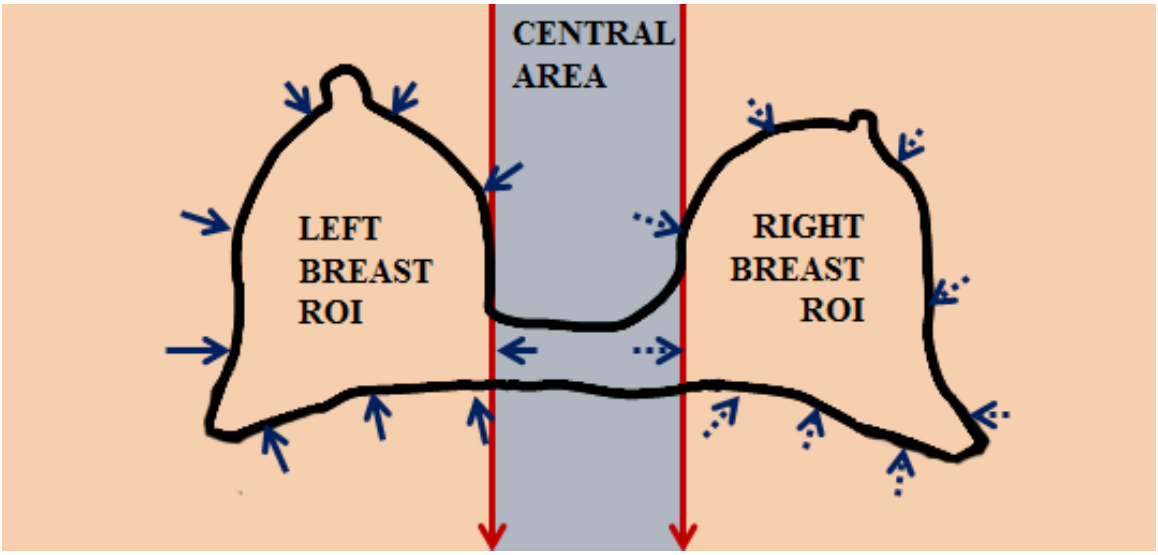

Figure 5.10: A process to obtain BD from BROI from breast slices.

spectively. We conducted our experiment separately on the left and right BROI to extract BD and later resultant images are merged to produce the final result.

Ethics statement

Human studies were approved by Victoria University Committee and by the Institutional Review Board. MR imaging was conducted in accordance with guidelines defined by Affiliated Zhongshan Hospital of Dalian University to achieve safe and reliable scanning. The experiment was approved specifically by the ethics committee. Written consent was obtained from each case subject after the imaging procedures had been conveyed.

5.3 RESULTS AND DISCUSSION

5.3.1 Image source and evaluation criteria

The experiment was performed on 15 female subjects (T1-weighted MR scans) with an age range between 22 and 54 years without any symptom of breast diseases. It was performed on a Philips Achieva 3.0T scanner using the turbo spin echo pulse sequence without fat suppression. Each patients MR scan covers entire breast with the total number of 90 image slices with 2 mm thickness. The other imaging parameters considered are: TR/TE = 645/9.0 ms, echo train = 5, slice gap = 0, phase encoding R-L, bandwidth per pixel = 174 Hz, field of view = 330 mm, imaging matrix = 328 $\times$ 384, and parallel imaging with SENSE factor = 2. The presented database consist of the variety of breast sizes, shapes, and breast tissues patterns. The proposed algorithm is applied to the individual slices to complete a 3D breast volume using Matlab R2013b running under Intel(R) core(TM) i5-4570s CPU@ 2.90 GHz with 8GB of RAM.

The performance of the proposed algorithm is tested with the quantitative analysis using a pixel-based classification technique where pixels are classified as BROI, BD or background. As a result, each pixel in the images are classified as classification (true positive (TP) and true negative (TN)) and misclassification (false positive (FP) and false negative (FN)). Based on these classified prediction, the performance of our algorithm is compared in terms of Accuracy (Acc), Precision (P), Sensitivity (Se) or Recall, Specificity (Sp), Area under ROC curve (AUC), Misclassification rate (MR), Dice similarity coefficient (DSC) and Jaccard Coefficient [268][269][270][271]. These performance metrics are

defined as shown in Eq. (5.15) to Eq. (5.21):

$$\text{Acc} = \frac{\text{TP+TN}}{\text{TP+FP+TN+FN}} \quad (5.15) \qquad \text{P} = \frac{\text{TP}}{\text{TP+FP}} \quad (5.16)$$

$$\text{Se} = \frac{\text{TP}}{\text{TP+FN}} \quad (5.17) \qquad \text{Sp} = \frac{\text{TN}}{\text{TN+FP}} \quad (5.18)$$

$$\text{MR} = \frac{\text{FP+FN}}{\text{TP+FP+TN+FN}} \quad (5.19) \qquad \text{DSC} = \frac{2(\text{A} \cap \text{GT})}{\text{A} + \text{GT}} * 100\% \quad (5.20)$$

$$\text{JC} = \frac{\text{A} \cap \text{GT}}{\text{A} \cup \text{GT}} * 100\% \quad (5.21)$$

TP and TN denote the pixel that is correctly identified as BROI/BD or background pixels. Similarly FP and FN represent the incorrectly identified BROI or BD, and background pixels. A and GT denotes automatically and manually obtained segmentations. Acc is the measure of the total number of correctly classified pixels (sum of true positives and true negatives) to the number of total pixels in an image [253, 272]. Precision is the proportion of correctly predicted positive observations to the total predicted positive observations [269]. Although both accuracy and precision depict the closeness of measurement to an actual value, precision reflects the reproducible measurements even if they are far from accepted value. The metrics Se and Sp are derived respectively from the proportion of positive and negative pixels in the ground truth image that are truly identified [273, 274]. A result with high sensitivity and specificity are considered as an accurate segmentation. A metric misclassification rate or error rate MR is the measure of how often the predictions are wrong. The best misclassification rate is 0.0 and the worst is 1.0. Also, receiving operating characteristics (ROC) curve [151] is used to estimate the trade-off between Se and Sp that is considered as non-parametric performance measurement. The ROC curve can be considered as a binary classifier and is plotted with the different values of independent threshold values within a certain interval. A curve representing a false positive rate (1-Sp) on the x-axis vs true positive rate (Se) on the y-axis is plotted. The ROC curve is the measure of predictive measure and is considered as an ideal curve when it is closer to the top left corner. The value of AUC greater than 90% is considered to be an excellent result. To further validate the performance of the developed algorithm, we have calculated an overlap based metrics known as Dice similarity coefficient (DSC) and Jaccard coefficient (JC) (DSC) [275]. It is the measure of overlap between two binary images to demonstrate the segmentation performance. The value of

these overlap based metrics ranged from 0 (no overlap) to 1 (perfect overlap).

5.3.2 BROI segmentation results

Fig. 5.11 shows the comparison of results produced by the proposed BROI segmentation method with the ground truth image which is manually segmented by an expert radiologist. The images with different size and shape are considered for the demonstration and yield the accurate segmentation results. First column ((a) (d) and (g)) shows the ground truth image whereas second column ((b), (e), and (h)) and third column ((c), (f), and (i)) shows the automatically segmented results respectively. In order to further validate the robustness of the proposed BROI segmentation, we performed the quantitative analysis using 8 metrics. Table 5.1 shows the performance of the proposed model in terms of accuracy, specificity, area under ROC curve, misclassification rate, precision, sensitivity and Dice similarity coefficient. Note that the values presented is the table are the average value of each slice in the MR image. Experiment shows that the obtained results are accurate while compared with the manual segmentation. In terms of accuracy, specificity and AUC, all the results are above 95%, proving the effectiveness of the proposed algorithm. It is observed that, the algorithm demonstrates a very good result with a minimum of 88% and maximum of 96% precision rate. The sensitivity of the proposed algorithm is high with an average value of 95.73%. The overlap ratio demonstrated by the Dice similarity and Jaccard coefficient is high with an average of 96.35% and 92.86% respectively.

5.3.3 BD segmentation results

Fig. 5.12 shows the comparison of results produced by the proposed BD segmentation method and ground truth image which is manually segmented by an expert radiologist. The images with different level of breast tissue are considered for the demonstration and yield the accurate segmentation results. First column ((a) (d) and (g)) shows the ground truth image whereas second column ((b), (e), and (h)) and third column ((c), (f), and (i)) shows the automatically segmented results respectively. In order to further validate the robustness of the proposed BD segmentation, we performed the quantitative analysis using 8 metrics. Table 5.2 shows the performance of the proposed model in terms of

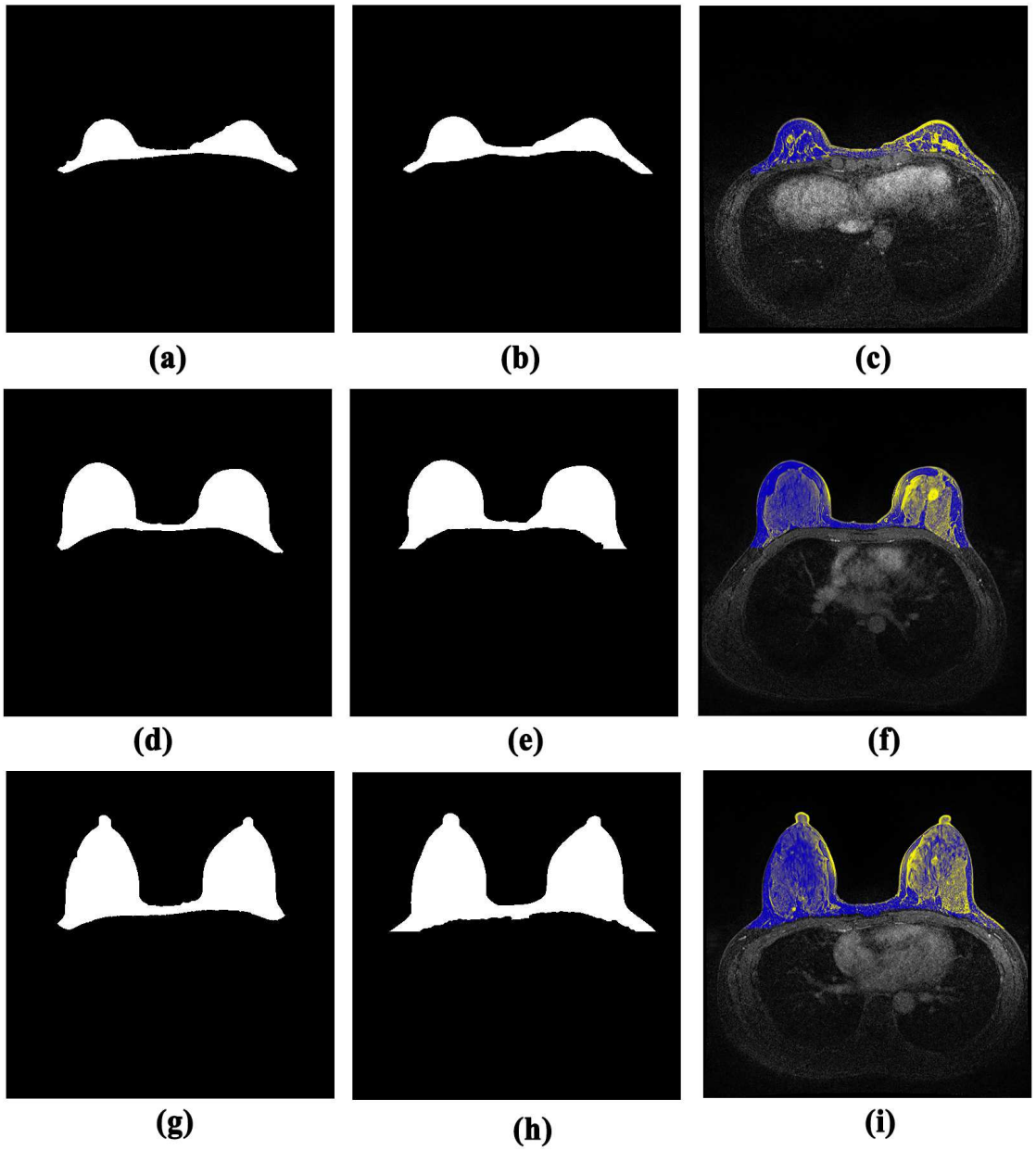

Figure 5.11: Results of BROI segmentation on the MRI images with different levels of BD and different breast shapes. The images in the first column are the manually segmented ground truth images. Similarly, second and third columns are the automatically segmented results with the proposed method and its mask on the original image to visually inspect the accuracy.

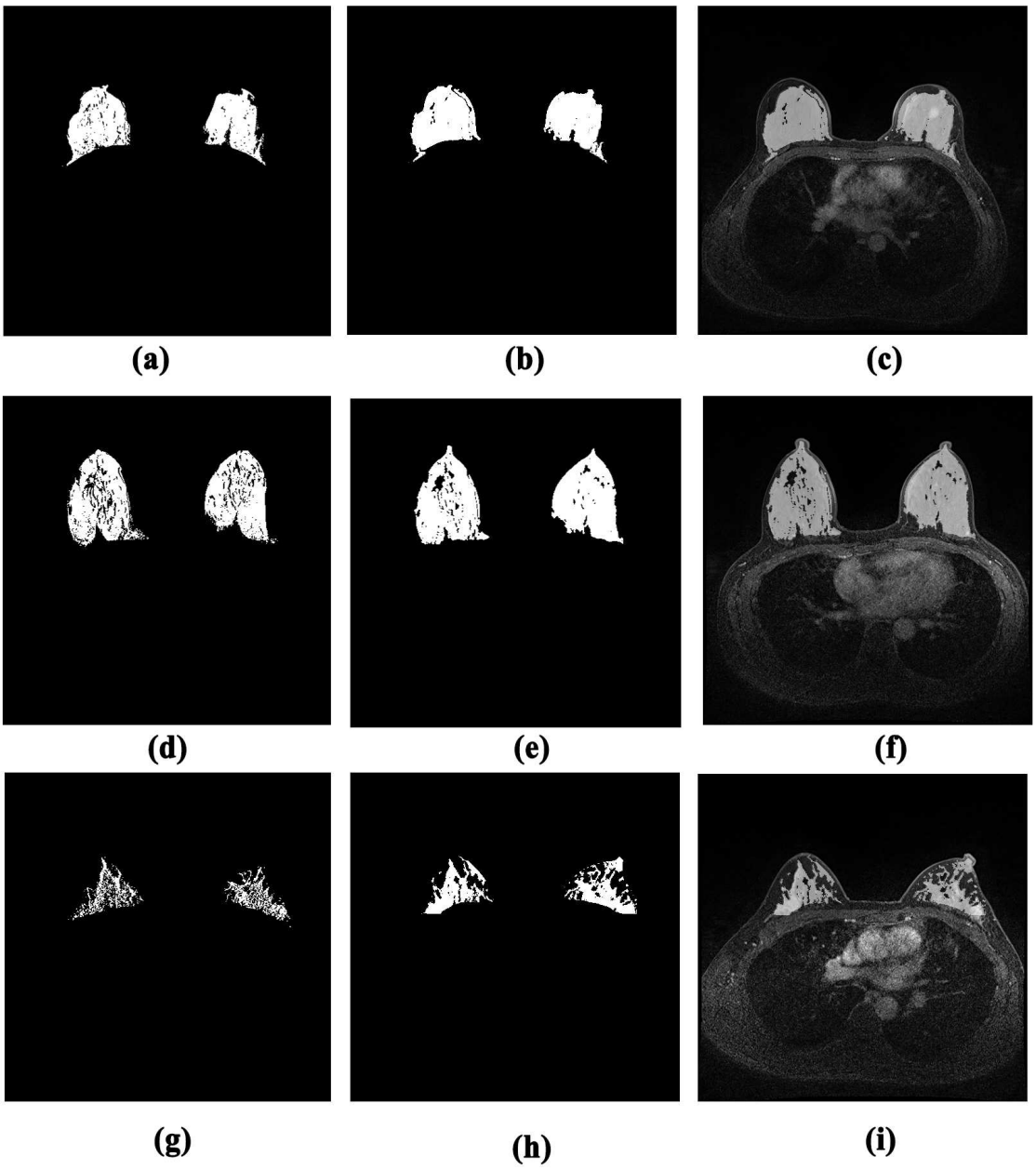

Figure 5.12: Results of BD segmentation on the MRI images with different levels of BD and different breast shapes. The images in the first column are the manually segmented ground truth images. Similarly, second and third columns are the automatically segmented results with the proposed method and its mask on the original image to visually inspect the accuracy.

Table 5.1: This table shows the resultant performance of BROI segmentation using the proposed method in 15 different cases in terms of accuracy (Acc), specificity (Sp), area under the curve (AUC), misclassification rate (MR), precision (P), sensitivity (Se) or recall, and Dice similarity coefficient (DSC).

DB	Acc	Sp	AUC	MR	P	Se	DSC	JC
1	0.9776	0.9830	0.97	0.0224	0.9425	0.9473	0.9555	0.9147
2	0.9648	0.9740	0.96	0.0398	0.8921	0.9413	0.9475	0.9002
3	0.9803	0.9783	0.99	0.0197	0.8800	0.9937	0.9564	0.9164
4	0.9871	0.9898	0.98	0.0129	0.9588	0.9591	0.9888	0.9778
5	0.9578	0.9554	0.95	0.0389	0.8960	0.9602	0.9599	0.9024
6	0.9819	0.9848	0.97	0.0181	0.9402	0.9414	0.9424	0.8910
7	0.9814	0.9845	0.97	0.0174	0.8873	0.9501	0.9647	0.9318
8	0.9897	0.9912	0.96	0.0122	0.9347	0.9123	0.9674	0.9368
9	0.9699	0.9671	0.97	0.0301	0.8945	0.9733	0.9542	0.9124
10	0.9829	0.9824	0.99	0.0171	0.9489	0.9868	0.9874	0.9751
11	0.9682	0.9644	0.99	0.0318	0.9421	0.9928	0.9867	0.9737
12	0.9834	0.9866	0.98	0.0166	0.9246	0.9420	0.9632	0.9290
13	0.9709	0.9728	0.98	0.0291	0.9272	0.9468	0.9568	0.9171
14	0.9795	0.9800	0.98	0.0205	0.9021	0.9679	0.9548	0.9135
15	0.9853	0.9888	0.98	0.0147	0.9301	0.9447	0.9673	0.9366
Avg	**0.9773**	**0.9789**	**0.97**	**0.0228**	**0.9201**	**0.9573**	**0.9635**	**0.9286**

accuracy, specificity, area under ROC curve, misclassification rate, precision, sensitivity and Dice similarity coefficient. Note that the values presented is the table are the average value of each slice in the MR image. Experiment shows that the obtained results are accurate and highly comparable with results obtained from the manual segmentation. In terms of 3 metrics (accuracy, specificity and AUC), the results are above 95%, proving the effectiveness of the proposed algorithm. It is observed that, the algorithm demonstrates an outstanding result with an average of 95.05% precision rate. The overlap ratio demonstrated by the Dice similarity and Jaccard coefficient is high with an average of 91.60% and 84.53% respectively. In terms of sensitivity, resultant values are slightly low but satisfactory values compared with other parameters. This is because some part of the BD has very low intensity and could be missed during the segmentations.

5.3.4 Discussion

Obtaining automatic, fast and accurate segmentation of the BROI and BD from MR images is a significant and challenging problem. The breast images can be found in different

Table 5.2: This table shows the resultant performance of BD segmentation using the proposed method in 15 different cases in terms of accuracy (Acc), specificity (Sp), area under the curve (AUC) and misclassification (MR), precision (P), sensitivity (Se) or recall, and Dice similarity coefficient (DSC).

DB	Acc	Sp	AUC	MR	P	Se	DSC	JC
1	0.9879	0.9898	0.96	0.0133	0.9514	0.8140	0.9046	0.8260
2	0.9799	0.9854	0.96	0.0321	0.9701	0.8190	0.9321	0.8728
3	0.9874	0.9872	0.97	0.0126	0.9549	0.8199	0.8946	0.8092
4	0.9912	0.9897	0.96	0.0088	0.9301	0.8145	0.8984	0.8155
5	0.9478	0.9701	0.93	0.0522	0.9647	0.8075	0.9141	0.8417
6	0.9885	0.9819	0.97	0.0115	0.9611	0.8110	0.9231	0.8571
7	0.9749	0.9814	0.97	0.0354	0.9302	0.8297	0.9145	0.8424
8	0.9845	0.9989	0.94	0.0155	0.9482	0.8176	0.9108	0.8362
9	0.9855	0.9676	0.96	0.0212	0.9444	0.8412	0.9402	0.8871
10	0.9788	0.9701	0.97	0.0277	0.9589	0.8250	0.9001	0.8183
11	0.9612	0.9627	0.98	0.0388	0.9628	0.8555	0.9374	0.8821
12	0.9888	0.9797	0.97	0.0112	0.9494	0.8002	0.9045	0.8256
13	0.9659	0.9645	0.97	0.0341	0.9579	0.8109	0.9141	0.8417
14	0.9873	0.9823	0.96	0.0127	0.9312	0.8125	0.9214	0.8542
15	0.9898	0.9781	0.95	0.0102	0.9415	0.8212	0.9306	0.8702
Avg	**0.9800**	**0.9793**	**0.96**	**0.0225**	**0.9505**	**0.8199**	**0.9160**	**0.8453**

shapes, sizes and density patterns. Moreover, the pectoral muscles are closely connected and shares similar intensity distribution with BROI. Hence, the initial identification of landmarks such as lung, heart and pectoral muscle is a vital step to facilitate the efficient BROI and BD segmentation process.

This study performs a stepwise analysis on landmarks such as lung, heart, and pectoral muscle and gradually eliminates them to achieve the final segmentation results. Prior to the landmark identification, we utilized the pre-processing step which improves the segmentation process. During the heart segmentation, an active contour level set method is used on the last 4 clusters from k-means clustering obtained during the pre-processing step. These 4 clusters are the brightest and the experiment shows that the heart region lies within these clusters. Active contour uses the level set method to create a force to either shrink or expand the contour from the initial contour point. The initial contour point is always selected approximately around the centre of the heart region using the maximum entropy thresholding and convolution method. We fix the initial contour (circle) at the radius (5 pixel) from the initial contour point. This is because we wanted to expand the contour from the central area of heart and limit it beyond the circu-

Table 5.3: Comparison of accuracy using three and four clustered FCM on BROI after segmentation.

Database	ACC with 4 level FCM (single threshold)	ACC with 4 level FCM (double threshold)
1	0.9601	0.9776
2	0.9421	0.9648
3	0.9656	0.9803
4	0.9611	0.9871
5	0.9594	0.9578
6	0.9658	0.9819
7	0.9470	0.9814
8	0.9523	0.9897
9	0.9349	0.9699
10	0.9231	0.9829
11	0.9451	0.9682
12	0.9532	0.9834
13	0.9475	0.9709
14	0.9546	0.9795
15	0.9529	0.9853
Avg	**0.9509**	**0.9773**

lar radius of 80 pixels. We observed that circular radius of 80 pixel is sufficient to identify the heart area from the rescaled image. Furthermore, the segmentation is obtained within a few iterations which results in faster computation time.

During pectoral muscle segmentation, the image is divided into three sections. The angular orientation of the pectoral muscle and breast density boundary is different in three different sections. So, each segment needs to be analysed separately. Also, the analysis of smaller segments reduces the processing time. Finally, the resultant image from the three segments are merged to generate the final segmented image. In the next step, we preserved the breast area above the central point to have fewer components for the extraction of the pectoral muscle as shown in Fig. 5.8 (a), (b).

The image obtained from BROI segmentation is further processed for BD segmentation. In the conventional method, the 4 level FCM thresholding technique is used to develop a single threshold valve for the entire image which includes both breasts. However, the analysis of the mean histogram based on the intensity of left and right breasts showed that the left and right breast have dissimilar mean intensity. Hence, the BROI is divided into three sections based on their geometrical information and the 4 level FCM threshold-

Table 5.4: Quantitative comparison of performance of BROI and BD segmentation using the proposed method with the recently developed other approaches.

	Acc	Sp	Se	DSC	JC
BROI					
Gallego et al. 2012 [276]	-	-	0.8900	0.8800	0.7900
Wu et al. 2013 [271]	-	-	-	0.9500	-
Ivanovska et al. 2014 [**?**]	-	0.9900	0.9800	0.9600	-
Gubern et al. 2015 [234]	-	-	-	0.9400	-
Jose et al. 2015 [248]	-	-	-	0.9220	-
Khalvati et al. 2015 [233]	-	-	-	0.9400	-
Milenkovic et al. 2015 [235]	-	-	-	0.961	-
Doran et al. 2017 [277]	-	-	-	0.924	0.8590
Aida et al. 2017 [278]	0.9733	0.9810	0.9491	0.9630	0.9290
PROPOSED METHOD	**0.9773**	**0.9789**	**0.9573**	**0.9635**	**0.9286**
BD					
Ivanovska et al. 2014 [**?**]	-	0.9900	0.8100	0.8300	-
Gubern et al. 2015 [234]	-	-	-	0.80	-
Thakran et al. 2018 [279]	-	-	0.8900	0.9000	0.8400
PROPOSED METHOD	**0.9800**	**0.9793**	**0.8199**	**0.9160**	**0.8453**

ing is applied separately to develop two threshold values for left and right breasts. It is observed that accuracy of separate thresholding in left and right BROI is better than the single thresholding technique as shown in Table 5.3. Furthermore, since varied thresholding uses smaller area, the process became faster.

The proposed method was tested with 15 different MR images developed form the same imaging technique with different scenarios i.e variety of breast sizes, shapes and BD patterns. The result demonstrates that, our method accurately segments BROI and BD in the different scenarios which can also be observed with the segmentation result as shown in Fig. 5.11 and Fig. 5.12. To evaluate the performance of the proposed method, eight evaluation metrics are calculated. The obtained results shows that the proposed method is efficient for the segmentation of BROI and BD from MR images.

We choose nine recent methods in the literature such as [276], [271], [**?**], [234], [248], [233], [235], [277], and [278] to analyze the BROI segmentation and three methods such as [**?**], [234] and [279] for the BD segmentation, the results of which are compared with the proposed method. The quantitative comparison is done with the available five metrics (Acc,Sp,Se,DSC and JC) as shown in Table 5.4. In terms of Acc and DSC, our method outperforms all the recent results for both BROI and BD segmentation. JC obtained from

the proposed method is marginally better or comparable with the existing literature. The results associated with Sp and Se are highly comparable with most of the results.

For automatic BROI and BD segmentation, we have compared our DSC value with different methods in the literature. In the model based method followed by Gallego et al. [276], a mean Se, DSC and JC obtained was 89%, 88% and 79%. The processing time taken to run was less than a minute to segment BROI per volume with the size of 256 x 128 x 45. The edge based approach followed by Wu et al. [271] demonstrates an average DSC rate of 95%. The processing time taken for BD segmentation was 4.5 minutes with MR image of 256 x 256 x 56 per volume. Gubern et al. [234] and Kalvati et al. [233] use the atlas based method and showed that the mean DSC obtained was 94%. Gubern-Merida et al. [234] reported a computational time of 8 min for BROI and BD segmentation for the image of 256 x 128 x 96 per volume. Similarly, Kalvati et al. [233] showed that the processing time for his method was 2 min for BROI segmentation for the MR image of 94 x 94 x 44 per volume. A automatic BROI segmentation in the axial breast MR images proposed by Milenkovic et al. [235] obtained a overall DSC value of 96.1% and the computational time was 4.1 minutes on the MR image of 448 x 448 x 144 per volume for BROI segmentation.

The computation time in the proposed algorithm mainly depends upon the resolution of the MR images and the clusters for the Kmeans and Fuzzy cmean clustering technique used for the experiments. The number of clusters should be determined so that the BROI and BD regions can be preserved with faster execution of the algorithm. We execute our algorithm for the several times to optimize the solution and the experiments takes an average of 1 minute and 50 seconds for BROI and BD segmentation with the resolution of 384 x 384 x 90 per volume. The execution time of our algorithm is significantly less than the other recent approaches tested on the similar hardware. The performance can be further improved with the implementation of GPU.

Breast MR databases are not available online. Results presented in the state of art are calculated from their own private databases. Hence, it is not always suitable to compare the results developed from different databases. Furthermore, during the segmentation process, the various methods might have several assumptions and considerations that make direct comparison problematic. For instance, Wang et at. [232] results are dependent upon the presence of fat in the anterior side of chest wall and Wu et al. [271] does

not consider challenging cases. Also, the processing speed depends upon the resolution of MR image of different databases.

5.4 CONCLUSION

In this chapter, we proposed an automatic method for the accurate segmentation of the BROI and BD. BROI segmentation is achieved by combining pixelwise adaptive filtering, k-means clustering and morphological operations with the application of local adaptive thresholding. BD segmentation is obtained by a combined method using fuzzy c means thresholding and mean value histogram. These frameworks have been tested on 15 different cases that comprised of different shapes and density patterns. Furthermore, quantitative analysis was carried with different evaluation metrics (Acc, Sp, AUC, MR, P, Se, DSC and JC) to demonstrate the segmentation quality when compared with manually segmented results by an expert. Most particularly, it is observed that the proposed algorithm is highly effective on breast MRIs with dense BD that has an similar intensity level to the area near the pectoral muscle. The presented model can act as a preliminary step that further assists in the diagnosis of breast cancer.

Chapter 6

Automatic breast lesion segmentation in denoised MRIs using continuous max-flow algorithm

6.1 Introduction

BREAST cancer occurred due to the abnormal growth of cells around the breast lobules or ducts [280]. The growth of the cell is uncontrollable and can spread to the other part of the body. Hence, breast cancer is the most common cancer diagnosed in women that causes death after lungs cancer. Early diagnosis and treatment of such cancer are essential to improve the survival rate. There are several medical imaging modalities used for the diagnosis of breast cancer, which may include mammography [281], ultrasound [282], biopsy CT scan [283] and MRI scan [284] [285]. Among imaging techniques, dynamic contrast-enhanced magnetic resonance imaging (DCE-MRI) provides a three dimensional high resolutions images with the accurate anatomical information that is not available with the other two widely used techniques: mammography and ultrasound. Therefore it is the most common and important tool for breast cancer diagnosis which provides relatively accurate results. However, manual segmentation of such imaging techniques for the suspicious breast lesion is a tedious and time-consuming task due to

This chapter is derived from:

- **D Pandey**, X. Yin, H. Wang, and Y. Zhang, "Automatic breast lesion segmentation in denoised MRIs using continuous max-flow algorithm" *IEEE access*,2019.(Under review)

the large number of data [286]. Hence, automatic lesion segmentation method is essential for accurate and efficient lesion delineation [287]. The development of the algorithm for automatic lesion segmentation is challenging mainly due to the noise, the similar intensity in different tissues and variability of shape and size between patients [288].

In the literature, several methods have been proposed using supervised and unsupervised methods for lesion segmentation on MRI images. Supervised methods require a large amount of previously labeled data by an expert. The goal is to develop a trained system to classify different objects labels. Initially, the dataset is divided into training and testing data. Some of the popular supervised approaches are K-Nearest Neighbors (KNN) [289], random forests (RF) [290], SVM [291] [292], Bayesian and deep learning, which is one of the advance supervised technique [293] [294]. Since the labeled and big datasets are required, the process is complex and computation expensive to achieve an efficient result. In contrast to that, the unsupervised method requires training models or prior knowledge of the required segmentation labels [50]. The algorithm framework relies on the different features such as region, boundary texture, and edges that are presented on the image. Although supervised techniques are popular, it requires a large volume of labeled data. In real clinical application, it's challenging to get sufficient labeled data because of limited patients and time constraints. It is likely that neighboring pixels tend to take the same label and has a low number of connected components. This is because labeling has are highly structured and correlated with complex dependencies that are hard to train as there are pixels or voxels up to millions. Moreover, optimization becomes complex since the whole labeling should be expressed as one optimization problem. Hence, if the input feature vector has a high dimension, it's hard to model the learning problems.

On the other hand, unsupervised techniques rely on the patterns (feature vectors) belonging to the same object. The features can be studied and defined as per the requirement. Among several unsupervised segmentation techniques, some of the important techniques are 1) Clustering based such as fuzzy Cmeans and Kmeans [295] 2) Edge based segmentation that relies on the fact that pixels are distinct in the background and foreground [296]. 3) Region-based segmentation such as region growing and region splitting-merging [297]. Here the seed selection is considered as an important step.

Another important and popular segmentation technique is energy-based segmentation where the result is obtained by minimizing the constructed energy function [298]. Several methods, which relies on energy function. Some of the popular segmentation methods includes Live wire [299], active contour [97], level sets [300] and graph-based [301]. Active contour and level set methods use the boundary information to construct the energy function and the performance relies on the initial curve. However, graph-based segmentation utilizes region and boundary information to produce a globally optimal solution [51]. Also, the discrete optimization graph-based methods have become popular because of its performance in medical image segmentation [302] [303]. In this method, the images are partitioned into several sub-graphs that represents a meaningful object in the image. Initially, the image is transformed in the form of a graph where pixels, region or voxel represents the structured grid of the graph. One of the main drawbacks of such method is the grid bias by penalizing the spatial directions resulting in the adverse effect on computation. The study shows that such a problem can be solved by formulating max flow and min cut problems in continuous domain [304].

Also, the unsupervised segmentation techniques currently face several difficulties. The presence of unavoidable noise during the breast DCE MRI acquisition has a greater effect of the accurate segmentation. The task is further complicated by geometric distortions and non-uniform illumination in the tissues. Furthermore, patient movement during acquisition may blur or even wipe out the border between the lesion and background tissue. Hence, prior to the segmentation process, a good denoising algorithm to eliminate noise while preserving the useful information and structure is required. Manual segmentation is not only tedious but also subject to intra observer and inter observer variability especially with the breast with dense breast tissues. Image features of the other structures such as lymph, breast tissues, and the blood vessel may resemble with the breast lesion with ends with false negative results. Hence, to solve the aforementioned challenges, we proposed a fully automatic and unsupervised framework that is able to produce an accurate lesion segmentation. The framework incorporates a graph method (solved by formulating max flow and min cut problems in the continuous domain) with denoising methods and morphological operations. It is observed that although the continuous max flow (CMF) algorithm is able to reduce the iterations avoiding the computational load,

the segmentation quality heavily depends upon the denoising process prior to the execution.

The lesion segmentation begins with the preprocessing step to eliminate the common background signals and to improve the contrast of breast lesions. This step is carried out by using image registration followed by the subtraction between pre and post-contrast images. Thereafter, we use the phase preservation denoising and adaptive Weiner filtering, significantly reducing noise and unwanted artifacts while preserving the important features such as edge and boundary required for the segmentation. A process is followed by CMF algorithm to obtain the segmentation. Finally, we use a morphological operation on the resultant image to remove the unwanted region to obtain the final result.

Rest of the chapter is organized as follows. A detailed review of used methods used for the breast lesion segmentation is discussed in section 6.2. In section 6.3, the proposed lesion segmentation method is explained. Section 6.4 discusses the experimental results and discussion. Finally, a concluding remark drawn in this study is given in Section 6.5.

6.2 Materials and methods

6.2.1 Image subtraction after registration

The important and primary pre-processing step in our algorithm is subtraction between pre and post contrast images [305]. This process makes it easier to characterize lesions by eliminating common background signals. The resultant image is obtained with the improved contrast in breast lesion. However, the performance of subtraction depends upon the image pre and post images acquisition. The patient should not between the whole imaging session, which is not always feasible. These unintended movements creates a misalignment of images sequence [306]. Hence, it requires image registration prior to the segmentation. Image registration is the geometrical transformation of one image to the other. The normalized image is obtained from the subtraction of pre contrast image from the post contrast image after the registration.

$$I_{\text{sub}} = I_{\text{post}} - I_{\text{pre}} \tag{6.1}$$

where, I_{post} and I_{pre} are the post and pre contrast image sequence. I_{sub} labels the image obtained from the subtraction of I_{pre} from the I_{post} after registration.

Let I_{reg} is the registered image. The Post-contrast image is registered with respect to the pre-contrast image. The misalignment between pre and post contrast image is removed using the registration algorithm "imregtform" routine in Matlab. Furthermore, "imregconfig" defines the similarity metric and optimization method. The registration procedure is based on the affine transformation and bicubic interpolation.

$$I_{\text{reg}} = registration(I_{\text{post}}) \tag{6.2}$$

$$I_{\text{sub}} = I_{\text{reg}} - I_{\text{pre}} \tag{6.3}$$

Affine transformation model This section discusses the affine transformation model which was used during the image registration [307]. Let us consider pre and post contrast DCE MRI image as I_{pre} and I_{post} that was generated from the same imaging technique. I_{reg} is the registered image. In our case, pre-contrast image I_{pre} is considered as the fixed image and the post-contrast image I_{post} is the moving image. Also, p and q are the co-ordinates for fixed and moving image. The relationship between $I_{reg}(p)$ and $I_{post}(p)$ is given as shown in Eq. (6.4)

$$I_{reg}(p) = I_{post}(A(q)) \iff I_{post}(q) = I_{reg}(A^{-1}(p)) \tag{6.4}$$

where A is the affine transformation. The affine transformation is the product of four geometric transformations, translation, rotation, scaling and skew as shown in first, second, third and fourth metrics respectively.

$$\begin{bmatrix} 1 & 0 & t_x \\ 0 & 1 & t_y \\ 0 & 0 & 1 \end{bmatrix} . \begin{bmatrix} \theta_c & -\theta_s & 0 \\ \theta_s & \theta_c & 0 \\ 0 & 0 & 1 \end{bmatrix} . \begin{bmatrix} 1 & k & 0 \\ 0 & 1 & 0 \\ 0 & 0 & 1 \end{bmatrix} . \begin{bmatrix} s_x & 0 & 0 \\ 0 & s_y & 0 \\ 0 & 0 & 1 \end{bmatrix}$$

The dot product of these metrics is obtained as shown below:

$$\begin{bmatrix} s_x\theta_c & s_y(k\theta_c - \theta_s) & t_x \\ s_x\theta_s & s_y(k\theta_s + \theta_c) & t_y \\ 0 & 0 & 1 \end{bmatrix}$$

where t_x and t_y are the shift of positive value towards left and up. $\theta$is defined as the rotation which is measured in the clockwise direction. k is a shear factor and s_x, s_y are the change of scale in x and y-direction respectively.

6.2.2 Local phase-preserving denoising

Denoising of DCE MR images is an important process during breast lesion segmentation [308]. Denoising is a process in which the image is transformed into some domain such that the noise component is easily identified. The noise is then removed and transformed back into a noise-free image. Among several denoising algorithms, wavelet transformation is considered very efficient to distinguish between the signal and noise in the image. Also, the image is consist of two important information magnitude and phase. It is seen that the previous denoising mechanism on breast MRI has not considered this important information, phase i.e. phase information is not preserved [65]. Phase information is important not only for the perception but also for the image enhancement.

The phase preservation denoising methodology utilizes the log Gabor wavelet filter. The image is initially decomposed into amplitude and phase information at each point of slices in of DCE MRI. The observation shows that most of the amplitude information is concentrated on the center and the phase information is distributed throughout the image. It is seen that amplitude or phase information alone is not sufficient in reconstructing the noise-free image while preserving the important image features. Hence, we designed a phase preserving technique for breast DCE MRI image that shrinks the amplitude information in different scaling factors and orientations.

Let us consider an image $I(x, y)$ as a signal vector. Response vector for even symmetric (M_n^e) and odd symmetric (M_n^o) wavelets at scale n is given by Eq. (6.5). The amplitude $A_n(x)$ and phase ϕ_n at a wavelet scale n is calculated as Eq. (6.6) and Eq. (6.7) respectively.

$$[Re_n(x, y), Im_n(x, y)] = [I(x, y) \times M_n^e, I(x, y) \times M_n^o] \tag{6.5}$$

where $Re_n(x, y)$,$Im_n(x, y)$ is real and imaginary part of complex valued frequency component.

$$A_n(x,y) = \sqrt{Re_n(x,y)^2 + Im_n(x,y)^2} \tag{6.6}$$

$$\phi_n(x,y) = \text{atan2}(Im_n(x,y)/Re_n(x,y)) \tag{6.7}$$

while denoising, a noise threshold at each wavelet scale is determined and the magnitude of the filtered vector is shrunk leaving phase unchanged. Hence, the complex-valued wavelet response is utilized where the phase is preserved while the amplitude is shrunk over different wavelet scales and orientation. Estimation of a signal can be reconstructed by summing the remaining even-symmetric filter response over all scales and orientations. The estimation of the noise threshold is determined from the mean and variance of Rayleigh distribution. The mean and variance of the Rayleigh distribution $\mathbb{R}$ is given by $\mu_{\mathbb{R}}$ and $\sigma^2_{\mathbb{R}}$ in Eq. (6.9).

$$\mathbb{R}(x,y) = (x,y)/\sigma^2 e^{-(x,y)^2/2\sigma^2} \tag{6.8}$$

$$\mu_{\mathbb{R}} = \sigma\sqrt{\pi/2}, \sigma^2_{\mathbb{R}} = \frac{4-\pi}{2}\sigma^2 \tag{6.9}$$

where σ^2 is the scale parameter of the Rayleigh distribution.The noise threshold is calculated as,

$$\tau_1 = \mu_{\mathbb{R}} + c\sigma_{\mathbb{R}} \tag{6.10}$$

where c specifies the standard deviation values of noise to reject. It is related to the ideal wave shape. It is assumed that the lower value of c produces an ideal wave shape. We tuned the value of c to be fixed and equal to 1.

To make a robust estimation, mean ($\mu_{\mathbb{R}}$) is replaced with the median ($\mathbb{M}$) response of Rayleigh distribution,

$$\mathbb{M} = \sigma\sqrt{-2\ln(1/2)} \tag{6.11}$$

here $\mathbb{M}$ labels median response. In each scale and orientation, the noise threshold is calculated and processed. Finally, the reconstructed image is obtained as I_2.

6.2.3 Adaptive wiener filtering

The edge-preserving denoising technique should be adopted as the edges are the important features during lesion segmentation. Hence, we apply an adaptive Wiener filtering technique to smoothen the image while preserving the edges [259][260].

The adaptive Wiener filter is given by Eq. (6.12) [261]:

$$I_{\text{denoised}}(i,j) = m_{\text{f}} + \frac{\sigma_{\text{f}}^2 - v^2}{\sigma_{\text{f}}^2}(I_{\text{noisy}}(i,j) - m_{\text{f}}) \tag{6.12}$$

where, m_{f} and σ_{f}^2 is the local mean and variance. v^2 is the average value of σ_{f}^2 across noisy image i.e. I_{noisy}. The computation of local mean and m_{f} and variance σ_{f}^2 is provided Eq. (6.13):

$$\begin{aligned} m_{\text{f}} &= (XY)^{-1} \sum_{i,j \in M} I_{\text{noisy}}(i,j) \\ \sigma_{\text{f}}^2 &= (XY)^{-1} \sum_{i,j \in M} (I_{\text{noisy}}^2(i,j) - m_{\text{f}}^2) \end{aligned} \tag{6.13}$$

where X and Y are the horizontal and vertical arrays of pixels in the window mask.

6.2.4 CMF based lesion segmentation

Continuous max flow (CMF) [309] method is a graph-based approach and found to be very effective to label the important regions in the image. Let us consider a problem of partitioning continuous image domain $\Omega$to partition into two region or labels: foreground and background. There are two terminals: source and sink.

There are three concerning flows: F_s, F_t and F are the source, sink and spatial flow as shown in the Fig. 6.1. Let x be the image position and each image position $x \in \Omega$.

$$F_s(x) \leq C_s(x), F_t(x) \leq C_t(x), |F(x)| \leq C(x); \forall x \in \Omega \tag{6.14}$$

and the flows are conserved as

$$F_t - F_s + divF = 0; \forall x \in \Omega \tag{6.15}$$

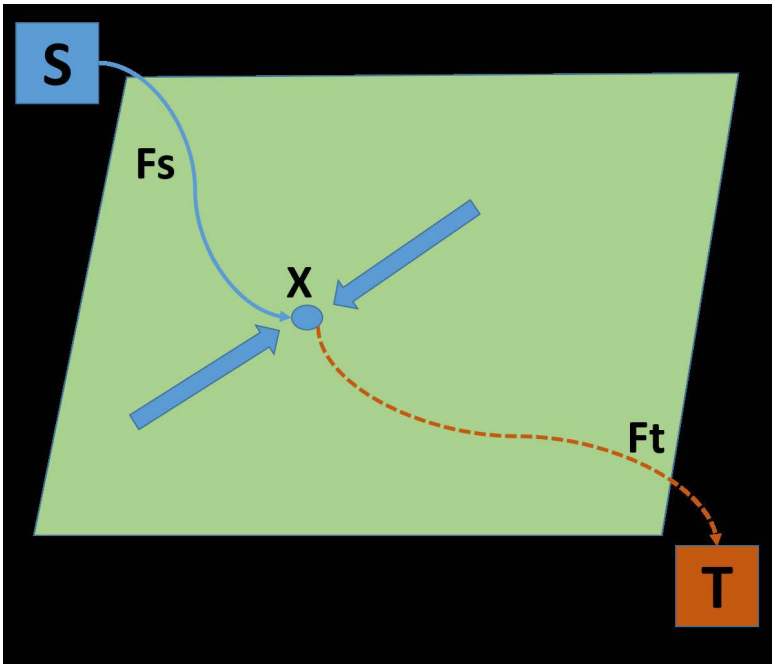

Figure 6.1: Continuous Max flow with two labels.

Hence, the max flow problem for the total flow from source to sink for two labels is given by

$$\max_{F_s,F_t,r} \int_{\Omega} F_s dx \tag{6.16}$$

Let us consider a problem of partitioning continuous image domain Ω to partition for $i = 1.....n$ region or label. There are three concerning flows : $F_s(x), F_i(x) and r_i(x)$ are the source, sink and spatial flow as shown in the Fig. 6.2. Let x be the image position and each image position $x \in \Omega$. In n label max flow model of Ω_i where $i = 1...n$ are given in parallel.

At each position $x \in \Omega$, $F_s(x)$ stream from s to x for each label $i = 1.....n$ Hence, the source field is same and there is no constraint for the source flow $F_s(x)$ for n label partition.

$F_i(x)$ and $r_i(x)$ are constrained by the capacities $\rho(L_i, x)$ and $C_i(x)$, $i = 1.....n$.

The flow are conserved as

$$(divr_i - F_s + F_i)(x) = 0, i = 1.....n \tag{6.17}$$

Hence, the max flow problem for the total flow from source to sink for n labels is given

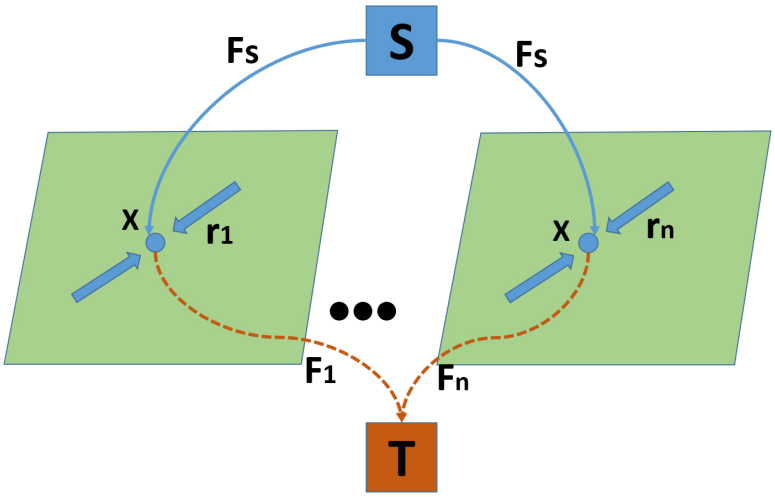

Figure 6.2: Continuous Max flow with n labels.

by

$$\max_{F_s,F,r}\{P(F_s,F,r)\int_\Omega F_s dx\} \tag{6.18}$$

Potts model is considered as a powerful tool for image segmentation [310]. The multi-region segmentation through potts model can be mathematically expressed as shown in Eq. (6.19).

$$\min_{\Omega_{i_{i=1}}^{n}} \sum_{i=1}^{n}\int_{\Omega_i} C_i(x)dx + \alpha\sum_{i=1}^{n}|\partial\Omega_i| \tag{6.19}$$

where $|\partial\Omega_i|$ is the perimeter of each disjoint subdomain $\Omega_i, i = 1...n$. $C_i(x), i = 1...n$ is the cost of assigning the specified position $x \in \Omega$ to the region Ω_i. The segmentation problem can be solved using convex relaxation potts model which is derived from Eq. (6.19) as shown in Eq. (6.20)

$$\min_{u\in S} \sum_{i=1}^{n}\int_\Omega u_i(x)C_i(x)dx + \sum_{i=1}^{n}\int_\Omega \omega(x)|\nabla u_i|dx \tag{6.20}$$

where $u_i(x), i = 1....n$ defines the function of the segmented region Ω_i.S is the convex constrained set of $u(x) = (u_1(x), ...u_n(x))$

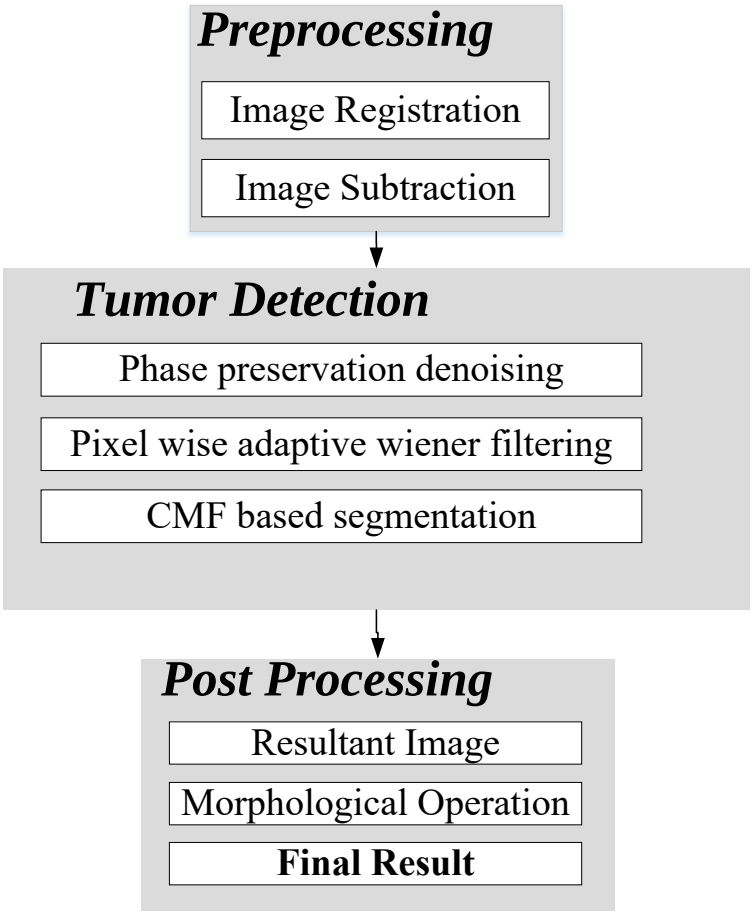

Figure 6.3: The proposed functional diagram of retinal vessel segmentation.

6.3 Proposed lesion segmentation method

The proposed segmentation approach consists of three steps: 1) image pre-processing 2) lesion detection and 3) image post-processing as shown in Fig. 6.3.

6.3.1 Image Pre-processing

This process is used to achieve a more enhanced normalized image to ease the detection of the lesion. It is performed by digitally subtracting the pre-contrast image that is an unenhanced T1 weighted sequence from the post-contrast image obtained after the admission of the contrast agent. Prior to the image subtraction, image registration should be carried out. Image registration resolves the misalignment of the pre and post contrast image originated due to the unintentional movement during imaging. Fig. 6.4 shows that

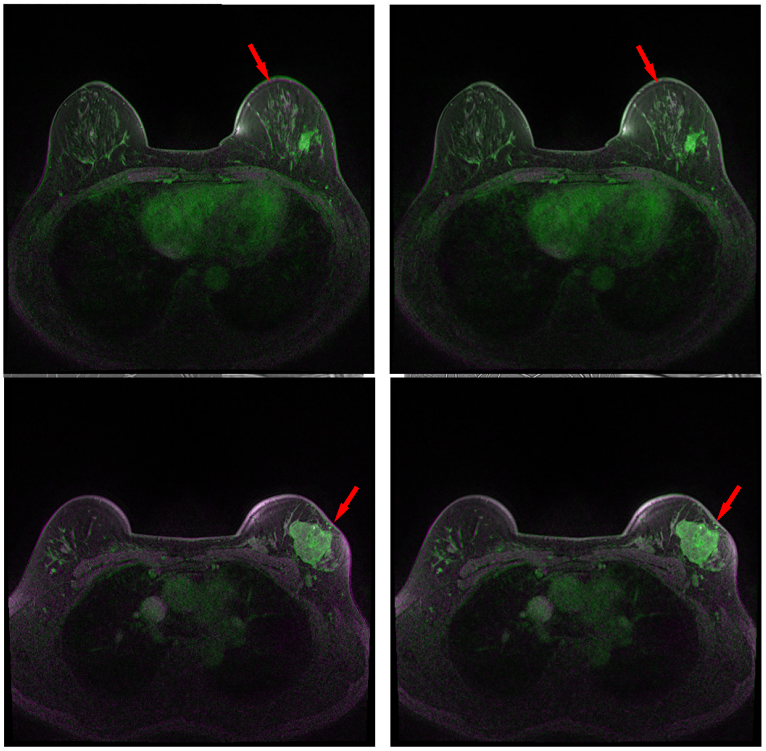

Figure 6.4: Illustration of image registration algorithm in DCE MRI. (a) Image before registration is applied (b) Image after registration is applied.

image before and after the registration.

The subtraction operation removes native T1 signal and hence the remaining enhancement is effective to accurately detect the lesion. This process is seen competent to the image where enhancement is critical to detect the complicated cysts. The Fig. 6.5 illustrates the effectiveness of image subtraction. Fig. 6.5 (a-c) are the pre-contrast, post-contrast and the resultant image after the image subtraction respectively.

6.3.2 Lesion segmentation

DCE MRI contains noise due to the fluctuations in the receiver coil and from the electrically conducting tissue. The presence of noise in the DCE MRI image increases the complexity and leads towards the misinterpretation. It is necessary to remove this noise, minimize the new artifacts and preserve kinetic enhancement information and fine structural details. Therefore following the pre-processing step, the phase preservation denoising method is applied. Also, it is essential to smoothen the image while sharpening the

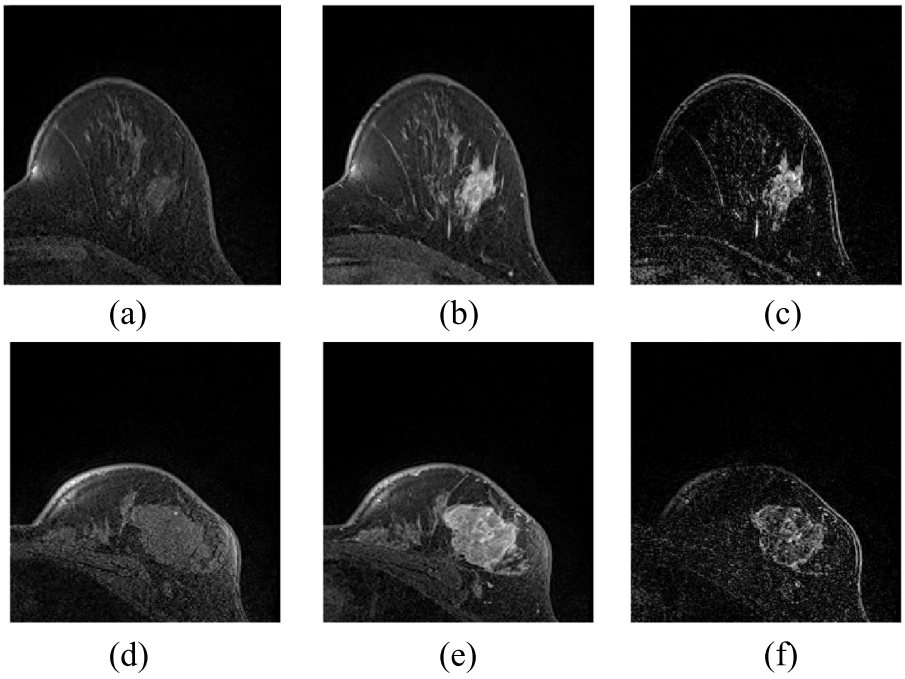

Figure 6.5: Subtraction of the pre-contrast from the post-contrast image. (a), (d) pre-contrast image. (b), (e) Post-contrast image. (c), (f) The resultant image after subtraction of the pre-contrast image from Post-contrast image

edges during the lesion segmentation. Hence, after phase preservation denoising, we applied an adaptive Wiener filtering technique.

There are two important considerations for phase preservation denoising method, orientation and wavelet scaling factor. Low scaling factor refers to filter response to noise is high. Eventually, the increased value of the scaling factor will reduce the filter response to the noise. The selection of scaling factor should be done carefully because the low scaling factor could treat useful information as noise and remove. Also, high scaling filter could be ineffective for noise removal. With several experiments and optimization, we use the scaling factor as 8 which preserves the fine structural details and increase the contrast between the lesion and background. Fig. 6.6shows the filter response of a DCE MRI image via phase preservation denoising with the different scaling factor.

The process of denoising begins with the construction of Gabor features using wavelet filters. The slices of DCE MRI is then convolved with the constructed Gabor features. AS a result feature vector response will be generated. For example, if 2 scales and 15 orientations are considered, it generates 15 different feature vector responses of slices as

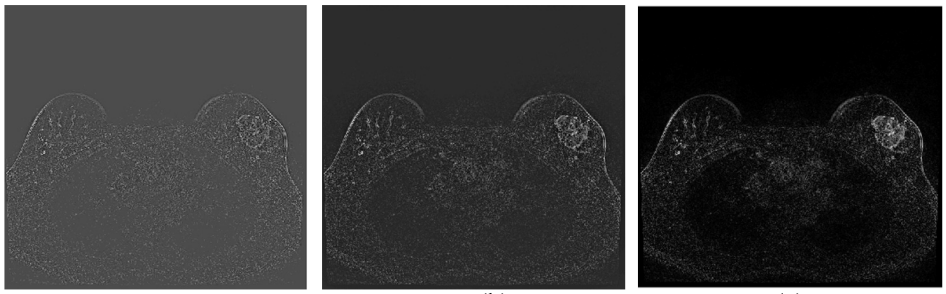

Figure 6.6: Filter responses of the DCE MR images obtained according to different scaling factors. (a) Scaling factor of 1. (b) Scaling factor of 3. (c) Scaling factor of 8.

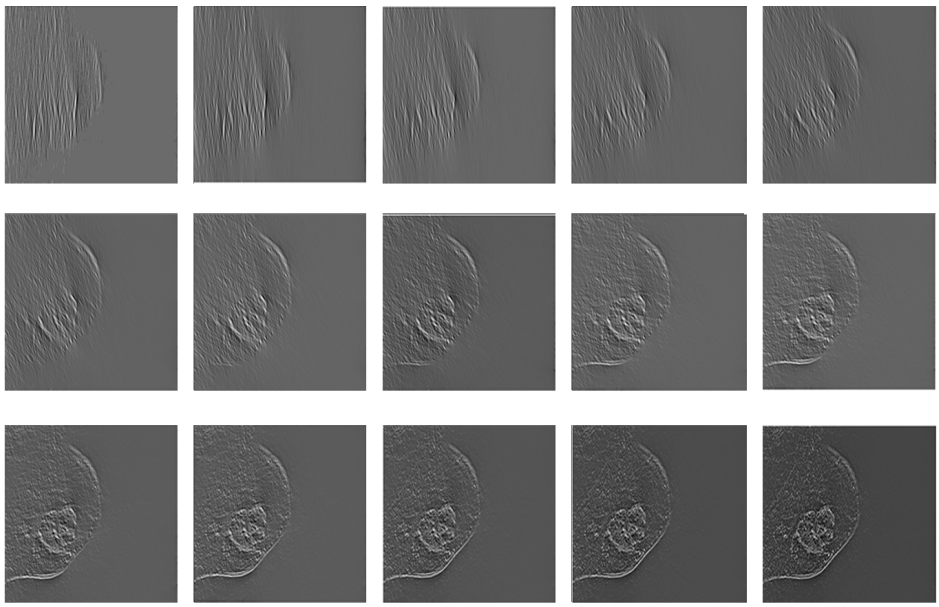

Figure 6.7: Illustration of phase preserved DCE MRI after reconstruction with scaling factor of 2 and 15 orientations using Gabor wavelet filter..

shown in Fig. 6.7. Hence, the final denoised image is obtained by summing the responses over all scales and orientations.

The image is denoised to some extent however, smoothing is required before the application of CMF to achieve the accurate segmentation. At this point, smoothing is required while preserving edges as well as the boundary. Edges and boundaries are the high-frequency areas and bilateral filtering is efficient to remove noise in these areas. Hence, we applied bilateral filtering to preserve edges and boundaries while smoothing the images.

The continuous max-flow algorithm was performed on the denoised MRI image ob-

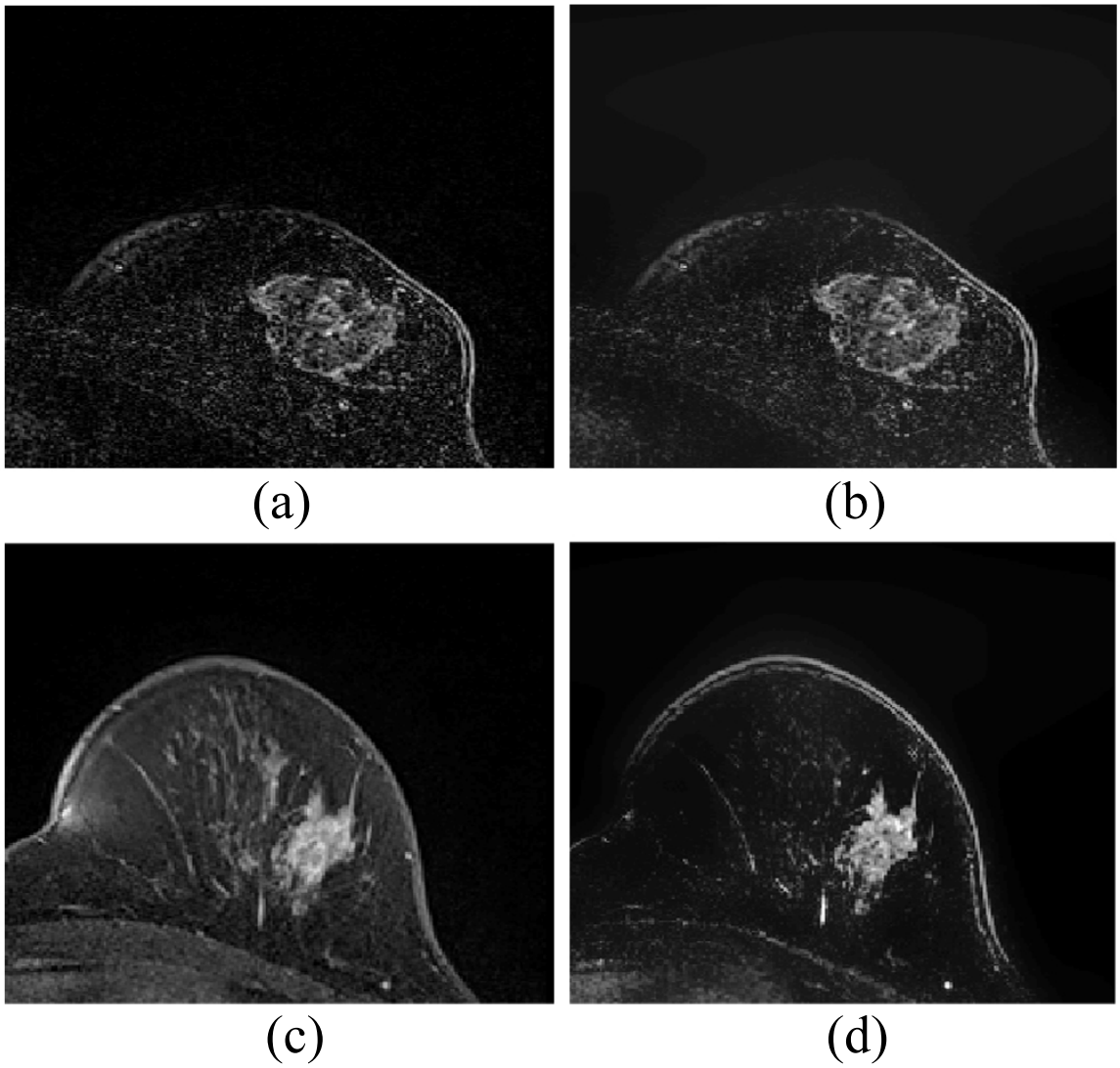

Figure 6.8: Illustration of resultant images obtained without phase-preserving denoising and bilateral filtering. (a), (c) The resultant image from the subtraction of the pre-contrast from the post-contrast image. (b), (c) The resultant image after using phase-preserving denoising and bilateral filtering

tained from the phase preservation denoising. Initially, Each pixel of image slices in the DCE MRI is connected to the source S and sink T in the continuous plane. Also, we consider that each pixel is associated with three flows: source, sink, and spatial flow. The source flow is directed from source S towards sink T. The spatial flow is determined by the strength of interaction with its neighborhood pixels. For the noisy image with low SNR, the capacity values of all the pixels would confine the solutions within local minima thus failing to determine the global optimum. Hence, prior to the application of the CMF method, the phase preservation denoise is used that clears the noise of the image and preserve the important features of the image. Additionally, the use of bilateral filtering on the phase preserved image will smoothen the image while preserving edges.

6.3.3 Image Post-Processing

Based on the observed result from the earlier section, the post-processing of the image is required. Morphological erosion and dilation operation were used to remove the boundary of edges. secondly, the nearby components are connected together and the biggest area among the connected component are searched and preserved. Rest of the areas are considered as noise and removed. The obtained segmented image are compared with manually drawn available ground truth image from the expert. Fig. 6.10, Fig. 6.11, and Fig. 6.12 shows the resultant image obtained after the post-processing. It is observed that post-processing plays a vital role to further precisely segment the lesions.

6.4 Performance evaluation and results

6.4.1 Data acquisition and evaluation criteria

The experiment is conducted on Windows 10 ($\times$64), with Intel Core i5 CPU, 2.9GHZ and 8GB RAM. We validate the proposed algorithm on the image generated from the 1.5T scanner. The imaging parameters for DCE-MRI were: TR/TE = 4.5/1.8 ms, a matrix size = 512 $\times$ 512, with the number of signal averages set to 1, a field of view of 30 cm, and a slice thickness of 1.5 mm. The gray-level range of MRIs is 0–255. There are total 23 cases in with 19 cases with a size of 512 x 512 x 96 and 4 cases with the size of 480 x 480 x 160. All

cases have one pre-contrast and 4 post-contrast imaging frames were acquired. Ground truth images are available for all the cases which are manually labeled by doctors.

The performance of the denoised image before and after phase preservation denoising is demonstrated by calculating the peak signal-to-noise ratios (PSNR).

Furthermore, The quantitative assessment of the proposed algorithm is tested with the eight parameters: area under ROC curve (AUC), accuracy (Acc), sensitivity (Se) or Recall, Specificity (Sp), precision (P), misclassification rate (MR), DICE coefficient (DSC) and Overlap coefficient (Oc). These parameters are based on pixel-based classification technique where each pixel on the slice of DCE MRI is classified as lesion or background. In the pixel-based classification technique, there are four combinations. : two classifications and two misclassifications. Under classification, true positive (TP) and true negative (TN) refers to the pixels which are correctly identified. Misclassification refers to the false positive (FP) and false negative (FN) which are incorrectly identified as a lesion. *SG* signify the segmentations obtained from the proposed methods and *GT*" signify the ground truth which is manually segmented. These metrics are defined as the following equations.

$$\text{Acc} = \frac{\text{TP+TN}}{\text{TP+FP+TN+FN}} \tag{6.21}$$

$$\text{Se} = \frac{\text{TP}}{\text{TP+FN}} \tag{6.22}$$

$$\text{Sp} = \frac{\text{TN}}{\text{TN+FP}} \tag{6.23}$$

$$\text{P} = \frac{\text{TP}}{\text{TP+FP}} \tag{6.24}$$

$$\text{Er} = \frac{\text{FP+FN}}{\text{TP+FP+TN+FN}} \tag{6.25}$$

$$\text{Vs} = 1 - \frac{\text{FN-FP}}{2 * \text{TP+FP+FN}} \tag{6.26}$$

$$\mathrm{DSC} = \frac{2(\mathrm{SG} \cap \mathrm{GT})}{\mathrm{SG} + \mathrm{GT}} * 100\% \tag{6.27}$$

$$\mathrm{JC} = \frac{(\mathrm{SG} \cap \mathrm{GT})}{\mathrm{SG} \cup \mathrm{GT}} * 100\% \tag{6.28}$$

Acc is defined as the total number of classified pixels which are correctly identified to the number of total pixels in an image. Se and Sp are the metrics which are derived from the proportion of positive and negative pixels in the ground truth image that is truly identified. P is the ratio of correctly predicted positive observations and total predicted positive observations.P indicates the reproducible measurements even the value is far from the acceptable range which distinguishes it from the accuracy. A metric error rate (Er) is the misclassification rate which measures the frequency of the wrong prediction. Er is considered excellent when the value is close to zero and positive. Volumetric Similarity is a measure of the volume of the segments that indicated similarity. It is the absolute difference divided by the sum of the compared volumes. DSC is the overlap based metric that measures the similarity between segmented OD via automatic and manual method. To further verify the efficiency of the proposed algorithm, we calculated a metric known as Oc. This metric is the similarity measure related to the Jaccard index which measures the overlap between automatically and manually segmented OD. We calculate metric, AUC from receiving operating characteristics (ROC) curve, which is used to estimate the trade-off between Se and Sp [201]. To achieve this non-parametric performance measurement, the curve is plotted with a false positive rate (1-Sp) on the x-axis and true positive rate (Se) on y-axis using different threshold values within a certain interval. The value greater than 90% is considered to be an excellent result and the ROC curve is considered as an ideal curve when its closer to the top left corner which offers a perfect value i.e. 1.

6.4.2 Results and Discussion

The original DCE MRI image is noisy. The segmentation of the breast lesion from the noisy image degrades the performance of the algorithm. Hence, phase preservation denoising is used to remove the unwanted noise and artifacts from the image. The image

enhancement can be observed visually as shown in Fig. 6.8 and is also tested by calculating the PSNR value before and after denoising as shown in Section 6.4.2. Since the data set consist of an image with two resolution, we have divided the total number of images into two groups (G1 and G2) to test the PSNR value obtained before and after denoising. It is observed that PSNR value in both the group has a significant improvement as shown in Section 6.4.2.

The obtained segmentation results can be observed visually. Fig. 6.9 show the resultant lesion segmentation obtained from the proposed method. The proposed method is able to segment the breast lesion. However, the segmentation result includes some unwanted areas as a false positive which require further processing. Hence, the post-processing step is carried out in the obtained resultant image. Fig. 6.10,Fig. 6.11 and Fig. 6.12 show that the post-processing step is able to remove most of the unwanted areas from the obtained resultant images. The method while compared with the ground-truth image, show that the proposed method is able to efficiently segment the lesion as depicted in Fig. 6.13. Fig. 6.13 (a, d and g) are the manually segmented ground truth image by an expert radiologist. Fig. 6.13 (b, e, and h) are the final result obtained from the proposed method. Fig. 6.13 (c, f and i) show that the overlap between the lesion area in the original image and the result obtained from the proposed method. The result shows that the proposed method is able to segment the lesion area accurately which is further validated by the quantitative analysis as shown in Table 6.2 and Table 6.3.

Table 6.1: Quantitative comparison of performance of lesion segmentation using the proposed method with the ground-truth image.

	Average PSNR	
Dataset	**Subtracted Image**	**After denoising**
G1	21.36 ± 0.7	32.54 ± 0.42
G2	20.82 ± 0.21	34.19 ± 0.53

Table 6.2 and Table 6.3 show the quantitative result obtained from the proposed method when compared with the ground-truth image. In all cases, we have achieved outstanding results. The average result in both the group is highly comparable with the ground-truth image.

The experiment shows that the results obtained from the proposed methods when compared with the results obtained from the recent methods outperform or highly com-

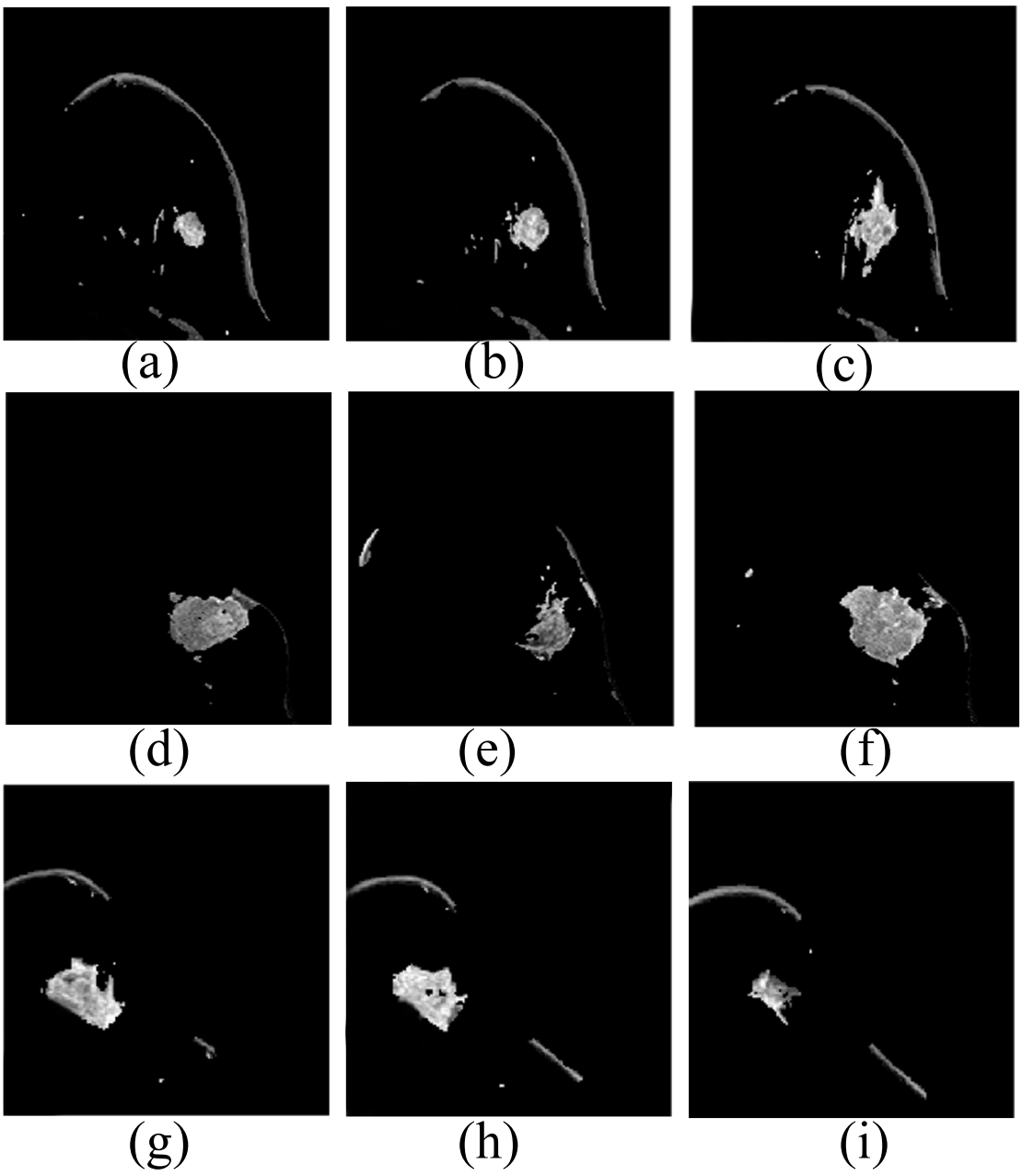

Figure 6.9: Illustration of resultant lesion segmentation obtained by using the proposed method before post-processing. Each row (a)-(b)-(c), (d)-(e)-(f), and (g)-(h)-(i) are the lesion segmented from slices from the same MR images.

parable as shown in Table 6.4. It is observed that Acc, Sp, Vs, and AUC obtained from the proposed method are above 95%, proving the effectiveness of the proposed algorithm. Also, in terms of overlapping metrics (DSC and JC), the obtained result outperforms or highly comparable with the existing methods with an average of 91.63% and 85.35% respectively. When comparing with the result obtained from the recently proposed method,

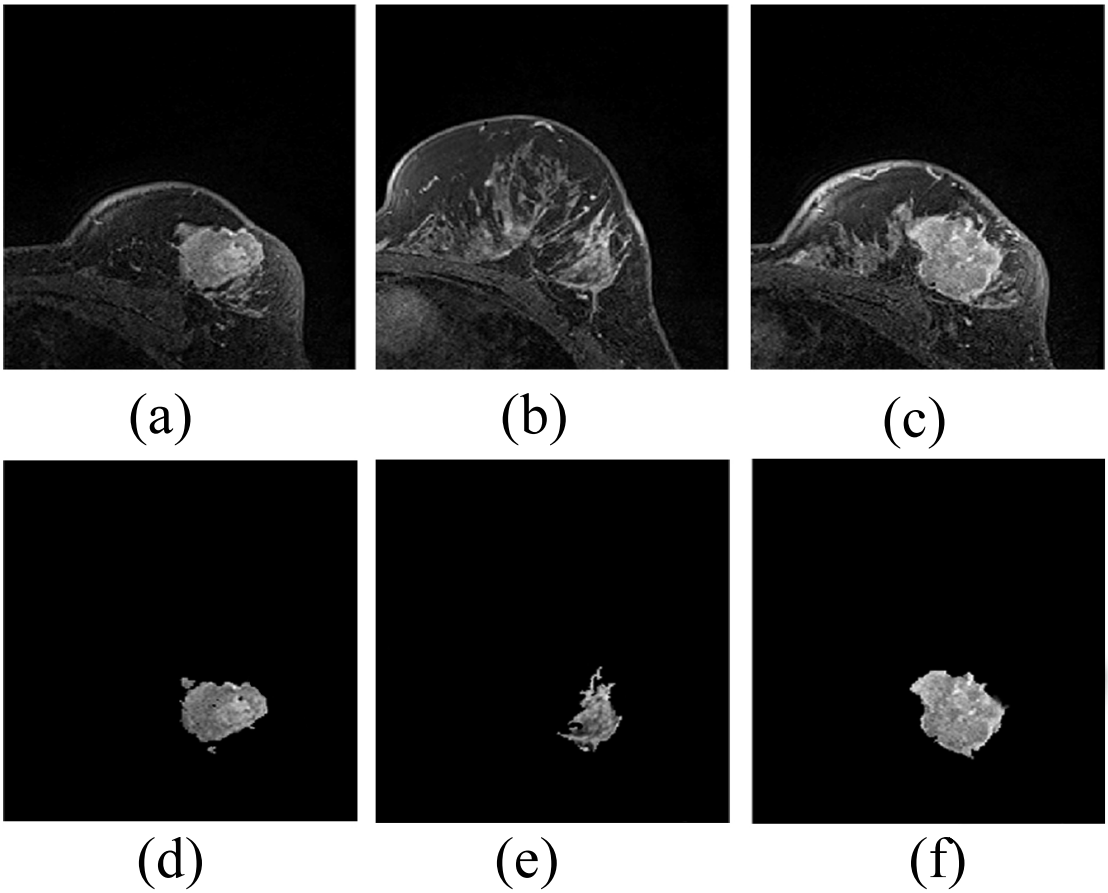

Figure 6.10: Illustration of resultant lesion segmentation obtained by using the proposed method after post-Processing. First row (a, b, c) represents the original image and second row (d, e, f)represents the final result i.e segmented tumors.

Accuracy was observed to be better than all of the other methods except Marrone et al. 2013. However, the result is highly comparable. The result obtained from the proposed method outperforms all the existing methods in terms of DSC and JC with an average value of 91.63% and 85.35%.

Segmentation of lesion from breast DCE MR image is a significant and challenging job. To achieve the level of accuracy as mentioned before we went through several experiments and finally came across the presented solution. The lesion can be found in various shapes and intensity in different slices of DCE MRI. Moreover, DCE MRI images are populated with noises during image acquisition because of untended movement of the object. To overcome this problem, we concluded that image registration is required as the initial step. Furthermore, it is observed that the segmentation process is further

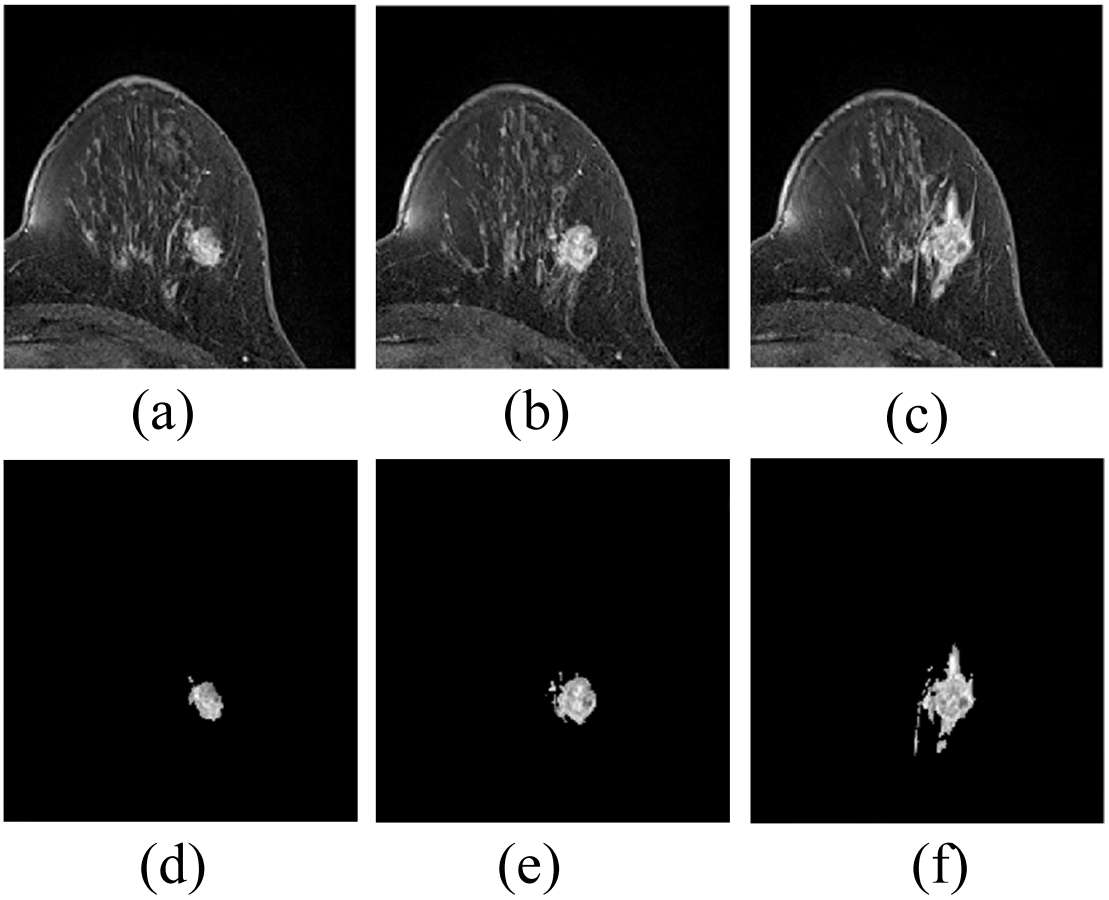

Figure 6.11: Illustration of resultant lesion segmentation obtained by using the proposed method after post-Processing. First row (a, b, c) represents the original image and second row (d, e, f)represents the final result i.e segmented tumors.

complicated by geometric distortion and non-uniform illumination in the tissues. Hence, to preserve most of the useful information of the image while removing the noise, we utilized the phase preservation denoising algorithm in the registered image followed by pixel-wise adaptive Wiener filtering to preserve the sharp edges. Thereafter, we use the graph-based approach i.e CMF to label the important region of the image. This method is found to be effective to solve the segmentation problem while allocating the minimum parameter. Hence, reducing the iteration time to obtain a faster segmentation. However, it was observed that the efficiently this process depends upon the denoising process prior to the application of the CMF algorithm. The CMF algorithm was experimented with or without using the preprocessing step. The experiment shows that the results obtained with the preprocessing steps are accurate in segmenting the lesion area. the result obtained without the preprocessing step includes a lot of unwanted areas, especially near

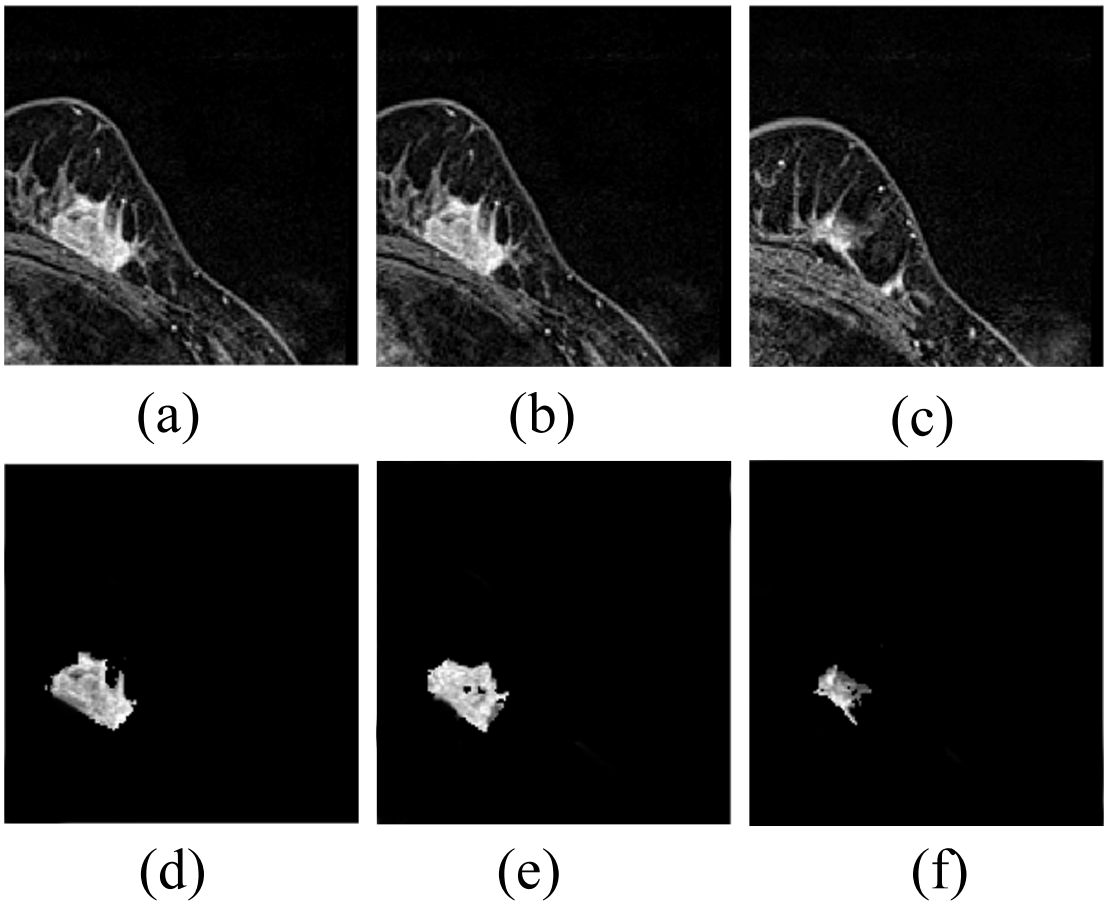

Figure 6.12: Illustration of resultant lesion segmentation obtained by using the proposed method after post-Processing. First row (a, b, c) represents the original image and second row (d, e, f)represents the final results i.e segmented tumors.

the lesion area.

The experiment shows that CMF algorithm was able to produce a resultant image that includes most of the lesion area. However, the image still includes some unwanted area in the image which is depicted in Fig. 6.9. Hence, we have included a post-processing operation to remove the unwanted part. Initially, morphological dilation operation with the disc-shaped structuring element with the radii of 5 pixels is used. This operation allows growing by 5 pixels from the edges along with all directions. This process will preserve the not connected lesion, especially near the lesion area. The process is followed by searching each connected component and preserving the biggest area. The convolution process is carried out with the dilated image with the resultant image to obtain the final lesion segmentation.

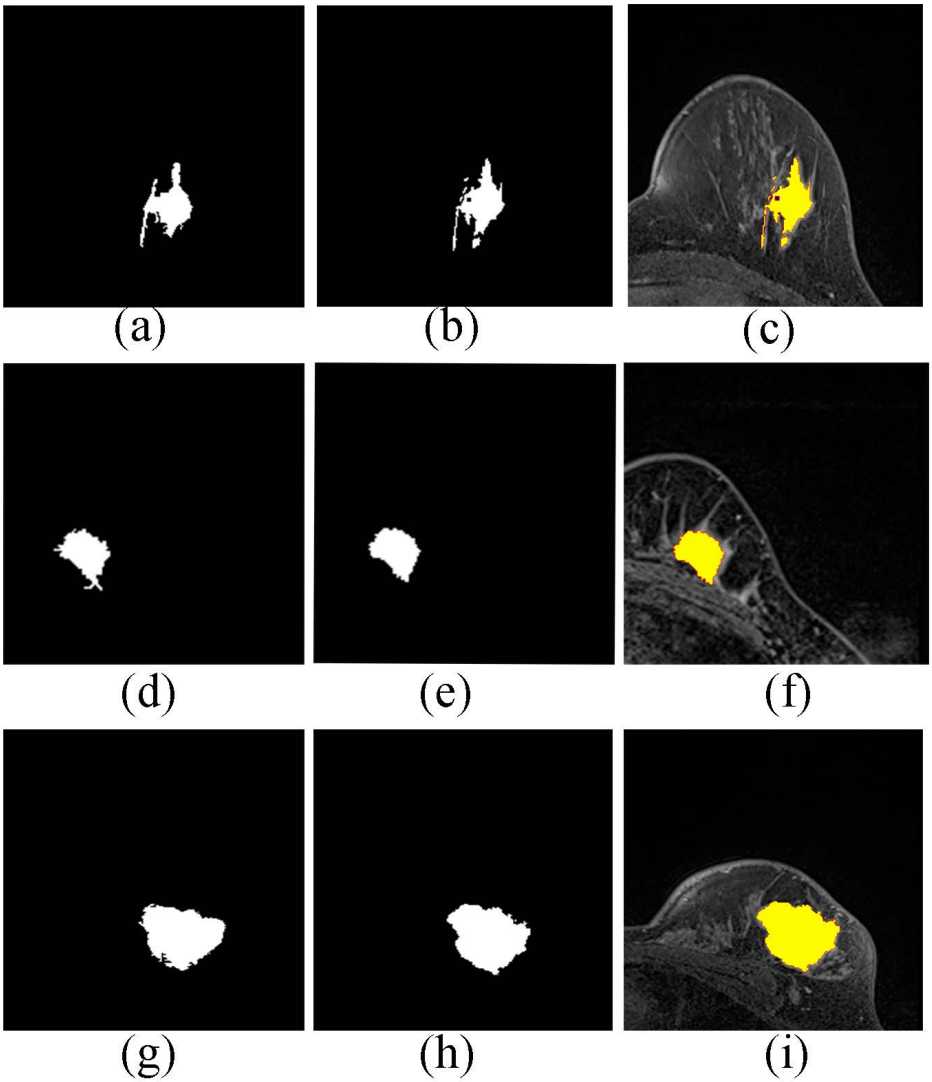

Figure 6.13: Illustration of resultant lesion segmentation obtained by using the proposed method after post-Processing. First row (a, b, c) represents the original image and second row (d, e, f)represents the final results i.e segmented tumors.

6.5 Conclusion

In this chapter, we proposed an automatic and fast lesion segmentation method from breast DCE MRI image. The produce accurate lesion segmentation, we have used image registration before image subtraction as a preprocessing step. Furthermore, a phase preservation denoising and adaptive Wiener filtering followed by CMF technique which is a graph-based approach are applied in the preprocessed image. Finally, post-processing is carried out to remove the unwanted remainings except for lesion. This framework has been tested with 23 different DCE MRI cases with resolutions. The quantitative analy-

Table 6.2: Quantitative comparison of performance of lesion segmentation using the proposed method with the ground-truth image.

Cases (G1)	**Acc**	**Se**	**Sp**	**P**	**Er**	**Vs**	**DICE**	**JC**	**Auc**
1	0.9933	0.9081	0.9968	0.9242	0.0023	0.9912	0.9161	0.8451	0.98
2	0.9921	0.9152	0.9841	0.9365	0.0069	0.9878	0.909	0.8569	0.97
3	0.9789	0.9231	0.9799	0.9388	0.0052	0.9921	0.9256	0.8654	0.96
4	0.9888	0.9012	0.9969	0.9219	0.0042	0.9874	0.9158	0.8475	0.97
5	0.991	0.897	0.9912	0.9127	0.0035	0.9789	0.92	0.8489	0.97
6	0.9699	0.8999	0.9879	0.9099	0.0058	0.9856	0.909	0.8585	0.98
7	0.9956	0.9258	0.9799	0.9123	0.0069	0.9956	0.9158	0.8741	0.99
8	0.9874	0.9265	0.9936	0.9223	0.0063	0.9961	0.9146	0.8461	0.99
9	0.9715	0.9241	0.9752	0.9234	0.0042	0.9816	0.9256	0.849	0.96
10	0.9865	0.9125	0.9858	0.9145	0.0043	0.9777	0.9241	0.851	0.97
11	0.9784	0.8812	0.9912	0.9156	0.0078	0.9713	0.9174	0.8479	0.98
12	0.9953	0.8845	0.9873	0.9215	0.0061	0.9782	0.916	0.859	0.99
13	0.9741	0.9178	0.9932	0.93	0.0039	0.9745	0.9292	0.8513	0.96
14	0.9799	0.9167	0.9889	0.92	0.004	0.9878	0.902	0.8467	0.97
15	0.9898	0.909	0.9798	0.912	0.0043	0.9923	0.9088	0.8419	0.98
16	0.9632	0.8821	0.9712	0.909	0.004	0.9891	0.9087	0.8521	0.98
17	0.9787	0.8928	0.9912	0.9097	0.0047	0.9858	0.9087	0.8484	0.99
18	0.9963	0.9181	0.9963	0.9312	0.0068	0.9799	0.9145	0.8546	0.96
19	0.9879	0.9099	0.9874	0.9012	0.0054	0.9889	0.9191	0.861	0.97
Avg	**0.9845**	**0.9076**	**0.9877**	**0.9195**	**0.0051**	**0.9856**	**0.9158**	**0.8525**	**0.97**

Table 6.3: Quantitative comparison of performance of lesion segmentation using the proposed method with the ground-truth image.

Cases(G2)	**Acc**	**Se**	**Sp**	**P**	**Er**	**Vs**	**DSC**	**JC**	**Auc**
1	0.9674	0.9191	0.9926	0.909	0.0052	0.9826	0.9193	0.8321	0.97
2	0.9874	0.9221	0.9874	0.9258	0.0045	0.9948	0.9201	0.8596	0.99
3	0.9742	0.8989	0.9858	0.9123	0.0054	0.9797	0.9078	0.8679	0.98
4	0.9931	0.9182	0.9745	0.9097	0.0068	0.9889	0.9183	0.8545	0.97
Avg	**0.9805**	**0.9145**	**0.9850**	**0.9142**	**0.0054**	**0.9865**	**0.9163**	**0.8535**	**0.977**

sis in terms of 9 metrics shows that significant improvement of the segmentation quality while compared with the recent segmentation technique. The proposed unsupervised doesn't require any prior knowledge and can work with most of the medical images with a slight modification of the parameters.

Table 6.4: Quantitative comparison of performance of lesion segmentation using the proposed method with the recently developed other approaches.

	Acc	DSC	JC	Sp	Se
Li et al. 2018	x	0.89	0.81	x	0.88
Rasti et al. 2017	0.9639	x	x	0.9487	0.9773
Jayender et. Al 2014	0.9	0.77	x	x	1
Darryl et al. 2014	x	0.76	x	x	x
Marrone et al 2013	98.7	x	x	0.989	0.71
Proposed Method(G1)	**0.9845**	**0.9158**	**0.8525**	**0.9873**	**0.9076**
Proposed Method(G2)	**0.9805**	**0.9163**	**0.8535**	**0.985**	**0.9145**

Chapter 7
Conclusions and Future Directions

7.1 Summary and Conclusions

THIS thesis work mainly focuses on the development of automatic segmentation methods on multidimensional medical images using unsupervised techniques. Medical images analysis especially automatic segmentation process is one of the complex and sensitive tasks that possess several challenges. The major challenges are the noise developed during the image acquisition process, alike intensity tissues all over the image and uncertain boundary. Moreover, high dimensional images often required a huge amount of time and the features in the different areas should be carefully studied to achieve an accurate output. The accuracy and the preciseness should be verified by qualitative and quantitative metrics for the quicker evaluation of the segmentation results.

Automatic segmentation of vital human body parts in the medial images plays an important role in the identification of different diseases and assists doctors for the accurate and fast detection of diseased areas. Hence, the prime motivation for the development of automatic segmentation algorithms on multidimensional medical images is the significant reduction of the cost in terms of processing time and effort taken during the tedious manual segmentation done by experts. Furthermore, automatic segmentation, which is capable of producing an accurate result and is considered as a key job in clinical applications. However, simple segmentation algorithms failed to produce an accurate result. Hence, this research project is focused on addressing issues during image segmentation in two imaging modalities: fundus photography (2D) and DCE MRI (3D).

The fundus photography (2D) is an imaging technique that captures images of the back portion of the human eye. The image produced by fundus photography includes

important landmarks such as optic nerve, blood vessels, macula, and fovea. The study of these landmarks reveals a wide variety of ophthalmic conditions that manifest through the human eye. The study showed that the images, especially with the pathological artifacts such as lesions, exudates, non-uniform illuminations, has high chances of producing unreliable results. This is because of wrongly identified landmarks such as blood vessels, optic nerve, macula, and fovea during automatic segmentation. Hence, the automation of the accurate segmentation process of the above-mentioned landmarks is still a challenging task.

DCE MRI (3D) is an advanced imaging technique that produces detailed images in three dimensions, which are capable of accurate detection, diagnosis and staging of the breast cancer with high precision (including high reproducibility) and low bias. Manual segmentation of lesion in DCE MRI is a tedious task because of the huge amount of data to be analyzed. In addition, the improved system with the lowest false positive (high specificity) should be cheaper for additional treatment and biopsies. The performance of the existing segmentation methods are moderate and has lots of room for the improvement especially during the development of the automatic segmentation method.

Hence, the main objectives of the presented research work is the development of novel algorithms addressing the above-mentioned segmentation challenges in fundus photography and MR images. The developed algorithms are the solutions for:

- Automatic segmentation of blood vessels in fundus photography.
- Localization and detection of Optic Disc in fundus photography.
- Automatic segmentation of BROI and BD in MR Images.
- Automatic breast lesion segmentation in DCE MR Images.

7.2 Addressing the research objective

In this thesis, we have conducted a thorough literature review, proposed novel algorithms and verified the results using several experiments to improve the current state-of-the-art in fundus photography and MR Image. In order to solve the segmentation prob-

lem, we developed four novel segmentation framework including fundus photography and MR images.

In term of fundus photography, firstly, we proposed a novel framework, which is capable of segmenting blood vessels automatically with high accuracy. This method is especially effective in analyzing retinal blood vessels on noisy, pathological and abnormal retinal images. Secondly, we proposed a novel and effective framework for automatic estimation of OD-ROI and segmentation of OD. This proposed algorithm is capable of segmenting OD accurately by using a geometrical model over the edge information of OD and is effective for abnormal retinal images with uneven illumination and several pathological conditions. The efficiency of proposed algorithms is tested with the experiment carried out in publicly available databases. Moreover, the efficiency of both the algorithms is validated in term of quantitative as well as qualitative analysis.

In term of MR image, Firstly, we proposed an automatic method for the accurate segmentation of BROI and BD from breast MR images. This proposed algorithm is highly effective when breast MR images include dense breast tissues. This process can act as a preliminary step during the diagnosis of breast cancer. Secondly, we proposed a novel lesion segmentation algorithm for breast DCE-MR Image. The method is effective in producing an accurate result for noisy DCE MR Images. The efficiency of proposed algorithms is tested with the experiment carried out in MRI databases with available ground truth images. Also, the efficiently of both algorithms are validated in term of quantitative and qualitative analysis.

To sum up, the main contribution of this thesis is as follows:

- **Chapter 1** provides an overview and compressive review for the state-of-art in medical image segmentation. This chapter further elaborates the importance of automatic segmentation in medical images especially in the fundus photography and breast MRI.

- **Chapter 2** provides an overview and compressive review for the state-of-art in medical image segmentation. This chapter further elaborates the importance of automatic segmentation in medical images especially in the retinal image and breast MRI.

- **Chapter 3** discus about the framework for the automatic and accurate segmentation of blood vessel from the retinal fundus images. It discusses the different issues in the retinal image that creates a problem in obtaining accurate segmentation problems and provides solutions. The proposed research work is efficient when compared with the rest of the other methods in the literature.

- **Chapter 4** discus about a novel framework for the automatic and accurate segmentation of optic disc from the retinal fundus images. This chapter identifies the challenges during OD segmentation process and provides an accurate solution. The experimental result shows that the proposed research work is accurate and shown to be superior when compared with the other proposed methods in the state of art.

- **Chapter 5** discus about the framework for the automatic and accurate segmentation of BROI and BD from MR images. It explains the importance of BROI and BD in breast MR images. Furthermore, this chapter explores the challenges during the segmentation process and provide a feasible solution. The experiment results show that the proposed methods can develop high-quality segmentation when compared with the manually drawn BROI and BD.

- **Chapter 6** discus about the framework for the automatic and accurate segmentation of breast lesion from DCE MR images. This paper discusses the challenging issues during breast lesion segmentation. The identification and solution to those challenges are presented in the chapter. Also, the experiment was conducted which proves that the proposed method produces high quality of segmentation results when compared with the manually segmented results.

7.3 Future direction

Although many research efforts have investigated the automatic segmentation techniques in fundus photography and breast MR images, there are still several gaps and challenges to be explored in the future. The algorithms presented in this thesis are unsupervised and hence they are database specific. To test the results with new database, some parameters may required to be adjusted.

The research work presented in this thesis can be directed to following future works for further enhancement in the algorithm development for medical image segmentation.

7.3.1 Automatic segmentation on Fundus photography

The segmentation of different anatomical structure in retinal images such as blood vessels, optic disc, macula, and abnormal lesions is significant for the detection and diagnosis of pathologies that manifest through human eyes. Most importantly, accurate analysis of blood vessel and optic disc provides crucial information for the pathologies such as Diabetic Retinopathy (DR), glaucoma, hypertension, and Age-related Macular Degeneration (AMD). In this thesis, we have presented a novel method for the accurate segmentation of blood vessel and optic disc. The proposed algorithm is only tested with the publicly available databases. The proposed techniques can be further tested with the databases, which are acquired in different environmental conditions and images. If necessary, we can optimize parametric values as well.

The main advantage of the proposed blood vessel segmentation technique is to identify the pixels as vessels and non-vessels, automatically and accurately. The proposed segmentation technique is highly capable of detecting both thick and thin blood vessels in both the healthy and pathological retinal images. The extracted blood vessels can further be used to identify diabetic retinopathy. Diabetic retinopathy occurs when the tiny blood vessels in the back portion of eye deteriorate. The algorithm will also be used for the development of Computer-aided diagnosis tool using artificial intelligence (deep learning). This blood vessel extracted from the algorithm can be classified by experts as either healthy or pathological. Moreover, classified information can be used for the training purpose. In addition, the proposed method can be further used for detecting vessel-like structure in any imaging modalities. However, manipulation of a parameter might be required.

The proposed optic disc segmentation technique is capable of segmenting the optic disc accurately which can be further extended for the segmentation of optic cup. The information of optic disc and optic cup can be used to identify the damage happened on the optic nerve to detect the pathological condition called glaucoma. Glaucoma can cause the cup to get bigger in an oval pattern. Hence, measuring the cup to disc ratio is one

of the effective methods to detect whether the optic nerve is glaucomatous or not. The proposed algorithm can be used for the development of the computer-aided diagnosis system using deep learning, which is considered as one of the effective methods of detecting pathologies. However, there will be a requirement of the optic disc and optic cup segmentation identified as a healthy or pathological for the training purpose. The expert can do the classification manually or an automatic algorithm can be developed for it.

7.3.2 Automatic segmentation on Breast MR Image

In breast MRI analysis, segmentation is used for the visualization of breast anatomical structures especially for evaluating the changes in breast and identifying the pathological regions. Since manual segmentation is tedious and time-consuming; there is always a requirement of developing an automatic segmentation technique. However, the degree of complexity is high for automatic segmentation of any important landmarks in volume images (MRI). Any effective and accurate algorithms can be incorporated into a computer-aided diagnosis system to assist the doctors for the diagnosis of breast cancer. In this thesis, we have presented a novel method for the accurate segmentation of BROI, BD and Breast lesion that can be used for the diagnosis of a pathological condition detected in MR images.

We have developed a novel method that can automatically and efficiently segment the BROI and BD. BROI is the area where the lesion resides. This can be extended for breast lesion detection. Since the breast lesion algorithm runs in a small area, the computation time can be tremendously reduced. On the other hand, we have developed an automatic breast density segmentation algorithm. Breast density is a strong risk factor and the indicator of breast cancer. The study can be further directed for the quantitative measure of textural and morphological features of different patterns and degree of breast density. The study can be directed not only towards the estimation of the quantity of breast dense tissues but can also assist in developing the strategies in fatty and dense regions to observe for the abnormalities at the early stage.

We have developed an automatic segmentation technique for the lesion detection of breast MR images. This technique can accurately segment the suspicious lesions. After the identification of breast lesion, the study can be further extended to classify the ob-

tained result as benign or malignant by the analysis of various textural, morphological or other features. Hence, It can become an important tool for the diagnosis and treatment of breast cancer during the early stages.

Deep learning is considered as one of the effective and widely used methods for the classification of the lesion. However, there are lots of pre-processing work required before the training process. For the development of machine and deep learning approach, manual segmentation of breast ROI is required which can be replaced with our proposed automatic algorithm. This is because the developed algorithm for BROI segmentation presented in this thesis is effective in segmenting the different anatomical structures of breast volume images.

7.4 Final Remarks

Medical image analysis is essential for accurate and fast identification of several pathological conditions. The automatic segmentation method plays a vital role during the medical image analysis to produce an accurate result. In this thesis, we explored and contributed novel automatic segmentation methodologies for two popular imaging modalities: 1) fundus photography and 2) Breast MRI. The automatic segmentation of blood vessel and localization and detection of Optic disc is performed in fundus photography. In the second part of this thesis, the automatic segmentation of breast region of interest, breast density, and breast lesion segmentation is developed. The proposed segmentation techniques are unsupervised and is applicable for multidimensional medical image. The research outcome tested on public and private dataset shows that the proposed techniques are able to produce clear, accurate and concise segmentation result. The obtained result vividly demonstrates that the methodologies presented in this thesis makes a important contribution to the respective state-of-art in terms of fundus photography and breast MR images.

Bibliography

[1] Wikipedia contributors, "Magnetic resonance imaging — Wikipedia, the free encyclopedia," 2019, [Online; accessed 22-May-2019]. [Online]. Available: https://en.wikipedia.org/w/index.php?title=Magnetic_resonance_imaging&oldid=896964944

[2] R. Besenczi, J. Tóth, and A. Hajdu, "A review on automatic analysis techniques for color fundus photographs," *Computational and structural biotechnology journal*, vol. 14, pp. 371–384, 2016.

[3] Y. Jai, R. Ahirwar, and S. Kumar, "Efficient 3-class fuzzy c-means clustering algorithm with thresholding for effective medical image segmentation," *International Journal of Emerging Technology and Advanced Engineering*, vol. 4, no. 10, pp. 546–556, 2014.

[4] U. T. Nguyen, A. Bhuiyan, L. A. Park, and K. Ramamohanarao, "An effective retinal blood vessel segmentation method using multi-scale line detection," *Pattern recognition*, vol. 46, no. 3, pp. 703–715, 2013.

[5] X. Ren and J. Malik, "Learning a classification model for segmentation," in *null*. IEEE, 2003, p. 10.

[6] G. Azzopardi, N. Strisciuglio, M. Vento, and N. Petkov, "Trainable cosfire filters for vessel delineation with application to retinal images," *Medical image analysis*, vol. 19, no. 1, pp. 46–57, 2015.

[7] V. M. Saffarzadeh, A. Osareh, and B. Shadgar, "Vessel segmentation in retinal images using multi-scale line operator and k-means clustering," *Journal of medical signals and sensors*, vol. 4, no. 2, p. 122, 2014.

[8] U. T. Nguyen, A. Bhuiyan, L. A. Park, and K. Ramamohanarao, "An effective retinal blood vessel segmentation method using multi-scale line detection," *Pattern recognition*, vol. 46, no. 3, pp. 703–715, 2013.

[9] K. Doi, "Computer-aided diagnosis in medical imaging: historical review, current status and future potential," *Computerized medical imaging and graphics*, vol. 31, no. 4-5, pp. 198–211, 2007.

[10] S. E. Moss, R. Klein, S. D. Kessler, and K. A. Richie, "Comparison between ophthalmoscopy and fundus photography in determining severity of diabetic retinopathy," *Ophthalmology*, vol. 92, no. 1, pp. 62–67, 1985.

[11] D. Y. Lin, M. S. Blumenkranz, R. J. Brothers, D. M. Grosvenor, and T. D. D. S. Group, "The sensitivity and specificity of single-field nonmydriatic monochromatic digital fundus photography with remote image interpretation for diabetic retinopathy screening: a comparison with ophthalmoscopy and standardized mydriatic color photography," *American journal of ophthalmology*, vol. 134, no. 2, pp. 204–213, 2002.

[12] J. N. Giedd, J. Blumenthal, N. O. Jeffries, F. X. Castellanos, H. Liu, A. Zijdenbos, T. Paus, A. C. Evans, and J. L. Rapoport, "Brain development during childhood and adolescence: a longitudinal mri study," *Nature neuroscience*, vol. 2, no. 10, p. 861, 1999.

[13] J. P. O'Connor, A. Jackson, G. J. Parker, and G. C. Jayson, "Dce-mri biomarkers in the clinical evaluation of antiangiogenic and vascular disrupting agents," *British journal of cancer*, vol. 96, no. 2, p. 189, 2007.

[14] J. A. Jensen, "Field: A program for simulating ultrasound systems," in *10TH NORDICBALTIC CONFERENCE ON BIOMEDICAL IMAGING, VOL. 4, SUPPLEMENT 1, PART 1: 351–353*. Citeseer, 1996.

[15] J. Hsieh *et al.*, "Computed tomography: principles, design, artifacts, and recent advances." SPIE Bellingham, WA, 2009.

[16] F. E.-Z. A. El-Gamal, M. Elmogy, and A. Atwan, "Current trends in medical image registration and fusion," *Egyptian Informatics Journal*, vol. 17, no. 1, pp. 99–124, 2016.

[17] M. Bertero and P. Boccacci, *Introduction to inverse problems in imaging*. CRC press, 1998.

[18] N. K. Medathati, H. Neumann, G. S. Masson, and P. Kornprobst, "Bio-inspired computer vision: Towards a synergistic approach of artificial and biological vision," *Computer Vision and Image Understanding*, vol. 150, pp. 1–30, 2016.

[19] M. J. McAuliffe, F. M. Lalonde, D. McGarry, W. Gandler, K. Csaky, and B. L. Trus, "Medical image processing, analysis and visualization in clinical research," in *Proceedings 14th IEEE Symposium on Computer-Based Medical Systems. CBMS 2001*. IEEE, 2001, pp. 381–386.

[20] D. L. Pham, C. Xu, and J. L. Prince, "Current methods in medical image segmentation," *Annual review of biomedical engineering*, vol. 2, no. 1, pp. 315–337, 2000.

[21] S. D. Olabarriaga and A. W. Smeulders, "Interaction in the segmentation of medical images: A survey," *Medical image analysis*, vol. 5, no. 2, pp. 127–142, 2001.

[22] R. Pohle and K. D. Toennies, "Segmentation of medical images using adaptive region growing," in *Medical Imaging 2001: Image Processing*, vol. 4322. International Society for Optics and Photonics, 2001, pp. 1337–1347.

[23] L. Zhou, M. S. Rzeszotarski, L. J. Singerman, and J. M. Chokreff, "The detection and quantification of retinopathy using digital angiograms," *IEEE transactions on medical imaging*, vol. 13, no. 4, pp. 619–626, 1994.

[24] D. L. Hill, P. G. Batchelor, M. Holden, and D. J. Hawkes, "Medical image registration," *Physics in medicine & biology*, vol. 46, no. 3, p. R1, 2001.

[25] P. Hastreiter and T. Ertl, "Integrated registration and visualization of medical image data," in *Proceedings. Computer Graphics International (Cat. No. 98EX149)*. IEEE, 1998, pp. 78–85.

[26] Wikipedia contributors, "Pixel — Wikipedia, the free encyclopedia," 2019, [Online; accessed 19-May-2019]. [Online]. Available: https://en.wikipedia.org/w/index.php?title=Pixel&oldid=892753578

[27] ——, "Voxel — Wikipedia, the free encyclopedia," 2019, [Online; accessed 19-May-2019]. [Online]. Available: https://en.wikipedia.org/w/index.php?title=Voxel&oldid=893830102

[28] J. Stoitsis, I. Valavanis, S. G. Mougiakakou, S. Golemati, A. Nikita, and K. S. Nikita, "Computer aided diagnosis based on medical image processing and artificial intelligence methods," *Nuclear Instruments and Methods in Physics Research Section A: Accelerators, Spectrometers, Detectors and Associated Equipment*, vol. 569, no. 2, pp. 591–595, 2006.

[29] E. M. Haacke, R. W. Brown, M. R. Thompson, R. Venkatesan *et al.*, *Magnetic resonance imaging: physical principles and sequence design*. Wiley-Liss New York:, 1999, vol. 82.

[30] M. Ferland, J.-p. DesprÉS, A. Tremblay, S. Pinault, A. Nadeau, S. Moorjani, P. J. Lupien, G. ThÉriault, and C. Bouchard, "Assessment of adipose tissue distribution by computed axial tomography in obese women: association with body density and anthropometric measurements," *British Journal of Nutrition*, vol. 61, no. 2, pp. 139–148, 1989.

[31] J. Stewart, G. Kruger, H. Ammon, C. t. DICKINSON, and S. Hall, "The xray system-version of june 1972," Tech. Rep. TR-192. Computer Science Center, Univ. of Maryland, College Park . . . , Tech. Rep., 1972.

[32] R. Damadian, "Tumor detection by nuclear magnetic resonance," *Science*, vol. 171, no. 3976, pp. 1151–1153, 1971.

[33] L. Martincich, F. Montemurro, G. De Rosa, V. Marra, R. Ponzone, S. Cirillo, M. Gatti, N. Biglia, I. Sarotto, P. Sismondi *et al.*, "Monitoring response to primary chemotherapy in breast cancer using dynamic contrast-enhanced magnetic resonance imaging," *Breast cancer research and treatment*, vol. 83, no. 1, pp. 67–76, 2004.

[34] N. Hylton, "Dynamic contrast-enhanced magnetic resonance imaging as an imaging biomarker," *J Clin Oncol*, vol. 24, no. 20, pp. 3293–3298, 2006.

[35] D. J. Foran, W. Chen, and L. Yang, "Automated image interpretation and computer-assisted diagnostics," *Stud Health Technol Inform*, vol. 185, pp. 77–108, 2013.

[36] M. Armaly, "Optic cup in normal and glaucomatous eyes," *Investigative Ophthalmology & Visual Science*, vol. 9, no. 6, pp. 425–429, 1970.

[37] J. Kinyoun, D. Martin, W. Fujimoto, and D. Leonetti, "Ophthalmoscopy versus fundus photographs for detecting and grading diabetic retinopathy." *Investigative ophthalmology & visual science*, vol. 33, no. 6, pp. 1888–1893, 1992.

[38] D. L. Monticciolo, M. S. Newell, L. Moy, B. Niell, B. Monsees, and E. A. Sickles, "Breast cancer screening in women at higher-than-average risk: recommendations from the acr," *Journal of the American College of Radiology*, vol. 15, no. 3, pp. 408–414, 2018.

[39] E. J. Feuer, L.-M. Wun, C. C. Boring, W. D. Flanders, M. J. Timmel, and T. Tong, "The lifetime risk of developing breast cancer," *JNCI: Journal of the National Cancer Institute*, vol. 85, no. 11, pp. 892–897, 1993.

[40] B. E. Dogan, M. E. Scoggins, J. B. Son, W. Wei, R. Candelaria, W. T. Yang, and J. Ma, "American college of radiology–compliant short protocol breast mri for high-risk breast cancer screening: A prospective feasibility study," *American Journal of Roentgenology*, vol. 210, no. 1, pp. 214–221, 2018.

[41] S. C. Agner, S. Soman, E. Libfeld, M. McDonald, K. Thomas, S. Englander, M. A. Rosen, D. Chin, J. Nosher, and A. Madabhushi, "Textural kinetics: a novel dynamic contrast-enhanced (dce)-mri feature for breast lesion classification," *Journal of digital imaging*, vol. 24, no. 3, pp. 446–463, 2011.

[42] W. Venderink, T. M. Govers, M. de Rooij, J. J. Fütterer, and J. M. Sedelaar, "Cost-effectiveness comparison of imaging-guided prostate biopsy techniques: systematic transrectal ultrasound, direct in-bore mri, and image fusion," *American Journal of Roentgenology*, vol. 208, no. 5, pp. 1058–1063, 2017.

[43] S. Lord, W. Lei, P. Craft, J. Cawson, I. Morris, S. Walleser, A. Griffiths, S. Parker, and N. Houssami, "A systematic review of the effectiveness of magnetic resonance imaging (mri) as an addition to mammography and ultrasound in screening young women at high risk of breast cancer," *European journal of cancer*, vol. 43, no. 13, pp. 1905–1917, 2007.

[44] D. D. Patil and S. G. Deore, "Medical image segmentation: a review," *International Journal of Computer Science and Mobile Computing*, vol. 2, no. 1, pp. 22–27, 2013.

[45] N. Sharma and L. M. Aggarwal, "Automated medical image segmentation techniques," *Journal of medical physics/Association of Medical Physicists of India*, vol. 35, no. 1, p. 3, 2010.

[46] F. Jiang, Y. Jiang, H. Zhi, Y. Dong, H. Li, S. Ma, Y. Wang, Q. Dong, H. Shen, and Y. Wang, "Artificial intelligence in healthcare: past, present and future," *Stroke and vascular neurology*, vol. 2, no. 4, pp. 230–243, 2017.

[47] A. Mustaqeem, A. Javed, and T. Fatima, "An efficient brain tumor detection algorithm using watershed & thresholding based segmentation," *International Journal of Image, Graphics and Signal Processing*, vol. 4, no. 10, p. 34, 2012.

[48] Y. Li, L. Jiao, R. Shang, and R. Stolkin, "Dynamic-context cooperative quantum-behaved particle swarm optimization based on multilevel thresholding applied to medical image segmentation," *Information Sciences*, vol. 294, pp. 408–422, 2015.

[49] M. van Eijnatten, R. van Dijk, J. Dobbe, G. Streekstra, J. Koivisto, and J. Wolff, "Ct image segmentation methods for bone used in medical additive manufacturing," *Medical engineering & physics*, vol. 51, pp. 6–16, 2018.

[50] I. Aganj, M. G. Harisinghani, R. Weissleder, and B. Fischl, "Unsupervised medical image segmentation based on the local center of mass," *Scientific reports*, vol. 8, no. 1, p. 13012, 2018.

[51] Y. Luo, L. Liu, Q. Huang, and X. Li, "A novel segmentation approach combining region-and edge-based information for ultrasound images," *BioMed research international*, vol. 2017, 2017.

[52] S. U. Mageswari, M. Sridevi, and C. Mala, "An experimental study and analysis of different image segmentation techniques," *Procedia engineering*, vol. 64, pp. 36–45, 2013.

[53] L. Caponetti, G. Castellano, and V. Corsini, "Mr brain image segmentation: A framework to compare different clustering techniques," *Information*, vol. 8, no. 4, p. 138, 2017.

[54] Z. Yang, F.-L. Chung, and W. Shitong, "Robust fuzzy clustering-based image segmentation," *Applied soft computing*, vol. 9, no. 1, pp. 80–84, 2009.

[55] T. McInerney and D. Terzopoulos, "Deformable models in medical image analysis: a survey," *Medical image analysis*, vol. 1, no. 2, pp. 91–108, 1996.

[56] Y. Wang, Q. Guo, and Y. Zhu, "Medical image segmentation based on deformable models and its applications," in *Deformable Models*. Springer, 2007, pp. 209–260.

[57] H.-F. Ng, "Automatic thresholding for defect detection," *Pattern recognition letters*, vol. 27, no. 14, pp. 1644–1649, 2006.

[58] H. Liu, R. Xiong, J. Zhang, and W. Gao, "Image denoising via adaptive soft-thresholding based on non-local samples," in *Proceedings of the IEEE conference on computer vision and pattern recognition*, 2015, pp. 484–492.

[59] C. H. Li and C. Lee, "Minimum cross entropy thresholding," *Pattern recognition*, vol. 26, no. 4, pp. 617–625, 1993.

[60] H. J. Vala and A. Baxi, "A review on otsu image segmentation algorithm," *International Journal of Advanced Research in Computer Engineering & Technology (IJARCET)*, vol. 2, no. 2, pp. 387–389, 2013.

[61] N. M. Zaitoun and M. J. Aqel, "Survey on image segmentation techniques," *Procedia Computer Science*, vol. 65, pp. 797–806, 2015.

[62] K. Bredies, D. A. Lorenz, and S. Reiterer, "Minimization of non-smooth, non-convex functionals by iterative thresholding," *Journal of Optimization Theory and Applications*, vol. 165, no. 1, pp. 78–112, 2015.

[63] N. Senthilkumaran and S. Vaithegi, "Image segmentation by using thresholding techniques for medical images," *Computer Science & Engineering: An International Journal*, vol. 6, no. 1, pp. 1–13, 2016.

[64] N. Bruce and J. Tsotsos, "Saliency based on information maximization," in *Advances in neural information processing systems*, 2006, pp. 155–162.

[65] D. Pandey, X. Yin, H. Wang, and Y. Zhang, "Accurate vessel segmentation using maximum entropy incorporating line detection and phase-preserving denoising," *Computer Vision and Image Understanding*, vol. 155, pp. 162–172, 2017.

[66] S. Kaur and I. Singh, "Comparison between edge detection techniques," *International Journal of Computer Applications*, vol. 145, no. 15, pp. 15–18, 2016.

[67] T. T. Nguyen and T. Y. Wong, "Retinal vascular changes and diabetic retinopathy," *Current diabetes reports*, vol. 9, no. 4, pp. 277–283, 2009.

[68] N. Bennett, R. Burridge, and N. Saito, "A method to detect and characterize ellipses using the hough transform," *IEEE Transactions on Pattern Analysis and Machine Intelligence*, vol. 21, no. 7, pp. 652–657, 1999.

[69] D. Antolovic, "Review of the hough transform method, with an implementation of the fast hough variant for line detection."

[70] H. Peng, J. Wang, M. J. Pérez-Jiménez, and A. Riscos-Núñez, "An unsupervised learning algorithm for membrane computing," *Information Sciences*, vol. 304, pp. 80–91, 2015.

[71] S. Khanmohammadi, N. Adibeig, and S. Shanehbandy, "An improved overlapping k-means clustering method for medical applications," *Expert Systems with Applications*, vol. 67, pp. 12–18, 2017.

[72] A. Banerjee, C. Krumpelman, J. Ghosh, S. Basu, and R. J. Mooney, "Model-based overlapping clustering," in *Proceedings of the eleventh ACM SIGKDD international conference on Knowledge discovery in data mining*. ACM, 2005, pp. 532–537.

[73] T.-S. Xu, H.-D. Chiang, G.-Y. Liu, and C.-W. Tan, "Hierarchical k-means method for clustering large-scale advanced metering infrastructure data," *IEEE Transactions on Power Delivery*, vol. 32, no. 2, pp. 609–616, 2015.

[74] S. Sankaranarayanan, A. Alavi, C. D. Castillo, and R. Chellappa, "Triplet probabilistic embedding for face verification and clustering," in *2016 IEEE 8th international conference on biometrics theory, applications and systems (BTAS)*. IEEE, 2016, pp. 1–8.

[75] Z.-d. Wu, W.-x. Xie, and J.-p. Yu, "Fuzzy c-means clustering algorithm based on kernel method," in *Proceedings Fifth International Conference on Computational Intelligence and Multimedia Applications. ICCIMA 2003*. IEEE, 2003, pp. 49–54.

[76] S. Kannan, S. Ramathilagam, A. Sathya, and R. Pandiyarajan, "Effective fuzzy c-means based kernel function in segmenting medical images," *computers in biology and medicine*, vol. 40, no. 6, pp. 572–579, 2010.

[77] D. Pandey, X. Yin, H. Wang, M.-Y. Su, J.-H. Chen, J. Wu, and Y. Zhang, "Automatic and fast segmentation of breast region-of-interest (roi) and density in mris," *Heliyon*, vol. 4, no. 12, p. e01042, 2018.

[78] N. Dhanachandra, K. Manglem, and Y. J. Chanu, "Image segmentation using k-means clustering algorithm and subtractive clustering algorithm," *Procedia Computer Science*, vol. 54, pp. 764–771, 2015.

[79] A. Likas, N. Vlassis, and J. J. Verbeek, "The global k-means clustering algorithm," *Pattern recognition*, vol. 36, no. 2, pp. 451–461, 2003.

[80] O. Yim and K. T. Ramdeen, "Hierarchical cluster analysis: comparison of three linkage measures and application to psychological data," *The quantitative methods for psychology*, vol. 11, no. 1, pp. 8–21, 2015.

[81] D. Stutz, A. Hermans, and B. Leibe, "Superpixels: An evaluation of the state-of-the-art," *Computer Vision and Image Understanding*, vol. 166, pp. 1–27, 2018.

[82] R. Achanta, A. Shaji, K. Smith, A. Lucchi, P. Fua, and S. Süsstrunk, "Slic superpixels compared to state-of-the-art superpixel methods," *IEEE transactions on pattern analysis and machine intelligence*, vol. 34, no. 11, pp. 2274–2282, 2012.

[83] D. J. Bora, A. K. Gupta, and F. A. Khan, "Comparing the performance of l* a* b* and hsv color spaces with respect to color image segmentation," *arXiv preprint arXiv:1506.01472*, 2015.

[84] S. Lankton and A. Tannenbaum, "Localizing region-based active contours," *IEEE transactions on image processing*, vol. 17, no. 11, pp. 2029–2039, 2008.

[85] R. Rouhi, M. Jafari, S. Kasaei, and P. Keshavarzian, "Benign and malignant breast tumors classification based on region growing and cnn segmentation," *Expert Systems with Applications*, vol. 42, no. 3, pp. 990–1002, 2015.

[86] M. A. Mohammed, M. K. A. Ghani, R. I. Hamed, M. K. Abdullah, and D. A. Ibrahim, "Automatic segmentation and automatic seed point selection of nasopharyngeal carcinoma from microscopy images using region growing based approach," *Journal of Computational Science*, vol. 20, pp. 61–69, 2017.

[87] J. Yang, Y. He, and J. Caspersen, "Region merging using local spectral angle thresholds: A more accurate method for hybrid segmentation of remote sensing images," *Remote sensing of environment*, vol. 190, pp. 137–148, 2017.

[88] D. Jayadevappa, S. Srinivas Kumar, and D. Murty, "Medical image segmentation algorithms using deformable models: a review," *IETE Technical review*, vol. 28, no. 3, pp. 248–255, 2011.

[89] S. Masood, M. Sharif, A. Masood, M. Yasmin, and M. Raza, "A survey on medical image segmentation," *Current Medical Imaging Reviews*, vol. 11, no. 1, pp. 3–14, 2015.

[90] P. Mesejo, A. Valsecchi, L. Marrakchi-Kacem, S. Cagnoni, and S. Damas, "Biomedical image segmentation using geometric deformable models and metaheuristics," *Computerized Medical Imaging and Graphics*, vol. 43, pp. 167–178, 2015.

[91] J. Dolz, C. Desrosiers, and I. B. Ayed, "3d fully convolutional networks for subcortical segmentation in mri: A large-scale study," *NeuroImage*, vol. 170, pp. 456–470, 2018.

[92] C. Huang and L. Zeng, "An active contour model for the segmentation of images with intensity inhomogeneities and bias field estimation," *PloS one*, vol. 10, no. 4, p. e0120399, 2015.

[93] M. Kass, A. Witkin, and D. Terzopoulos, "Snakes: Active contour models," *International journal of computer vision*, vol. 1, no. 4, pp. 321–331, 1988.

[94] T. F. Chan and L. A. Vese, "Active contours without edges," *IEEE Transactions on image processing*, vol. 10, no. 2, pp. 266–277, 2001.

[95] C. Liu, M. K.-P. Ng, and T. Zeng, "Weighted variational model for selective image segmentation with application to medical images," *Pattern Recognition*, vol. 76, pp. 367–379, 2018.

[96] A. Tsai, A. Yezzi, and A. S. Willsky, "Curve evolution implementation of the mumford-shah functional for image segmentation, denoising, interpolation, and magnification," 2001.

[97] S. Niu, Q. Chen, L. De Sisternes, Z. Ji, Z. Zhou, and D. L. Rubin, "Robust noise region-based active contour model via local similarity factor for image segmentation," *Pattern Recognition*, vol. 61, pp. 104–119, 2017.

[98] F. Gibou, R. Fedkiw, and S. Osher, "A review of level-set methods and some recent applications," *Journal of Computational Physics*, vol. 353, pp. 82–109, 2018.

[99] J. Liu, M. Li, J. Wang, F. Wu, T. Liu, and Y. Pan, "A survey of mri-based brain tumor segmentation methods," *Tsinghua Science and Technology*, vol. 19, no. 6, pp. 578–595, 2014.

[100] P. F. Felzenszwalb and D. P. Huttenlocher, "Efficient graph-based image segmentation," *International journal of computer vision*, vol. 59, no. 2, pp. 167–181, 2004.

[101] X. Chen and L. Pan, "A survey of graph cuts/graph search based medical image segmentation," *IEEE reviews in biomedical engineering*, vol. 11, pp. 112–124, 2018.

[102] C. Bothorel, J. D. Cruz, M. Magnani, and B. Micenkova, "Clustering attributed graphs: models, measures and methods," *Network Science*, vol. 3, no. 3, pp. 408–444, 2015.

[103] B. Peng, L. Zhang, and D. Zhang, "A survey of graph theoretical approaches to image segmentation," *Pattern Recognition*, vol. 46, no. 3, pp. 1020–1038, 2013.

[104] F. Yi and I. Moon, "Image segmentation: A survey of graph-cut methods," in *2012 International Conference on Systems and Informatics (ICSAI2012)*. IEEE, 2012, pp. 1936–1941.

[105] Y. Boykov and M.-P. Jolly, "Graph cuts for binary segmentation of n-dimensional images from object and background seeds," Dec. 6 2005, uS Patent 6,973,212.

[106] Y. Y. Boykov and M.-P. Jolly, "Interactive graph cuts for optimal boundary & region segmentation of objects in nd images," in *Proceedings eighth IEEE international conference on computer vision. ICCV 2001*, vol. 1. IEEE, 2001, pp. 105–112.

[107] D. Freedman and T. Zhang, "Interactive graph cut based segmentation with shape priors," in *2005 IEEE Computer Society Conference on Computer Vision and Pattern Recognition (CVPR'05)*, vol. 1. IEEE, 2005, pp. 755–762.

[108] Y. Zhao, Y. Liu, X. Wu, S. P. Harding, and Y. Zheng, "Retinal vessel segmentation: An efficient graph cut approach with retinex and local phase," *PloS one*, vol. 10, no. 4, p. e0122332, 2015.

[109] Q. Mohamed, M. C. Gillies, and T. Y. Wong, "Management of diabetic retinopathy: a systematic review," *Jama*, vol. 298, no. 8, pp. 902–916, 2007.

[110] D. S. Fong, L. Aiello, T. W. Gardner, G. L. King, G. Blankenship, J. D. Cavallerano, F. L. Ferris, and R. Klein, "Retinopathy in diabetes," *Diabetes care*, vol. 27, no. suppl 1, pp. s84–s87, 2004.

[111] S. Beatty and K. A. Eong, "Acute occlusion of the retinal arteries: current concepts and recent advances in diagnosis and management," *Emergency Medicine Journal*, vol. 17, no. 5, pp. 324–329, 2000.

[112] E. D. C. C. S. Group *et al.*, "Antioxidant status and neovascular age-related macular degeneration," *Arch Ophthalmol*, vol. 111, pp. 104–109, 1993.

[113] M. M. Fraz, P. Remagnino, A. Hoppe, B. Uyyanonvara, A. R. Rudnicka, C. G. Owen, and S. A. Barman, "Blood vessel segmentation methodologies in retinal images–a

survey," *Computer methods and programs in biomedicine*, vol. 108, no. 1, pp. 407–433, 2012.

[114] M. N. J. Staal, M. D. Abramoff and B. v. G. M. A. Viergever, "Ridge-based vessel segmentation in color images of the retina," *IEEE Transactions on Medical Imaging*, vol. 23, no. 4, pp. 501–509, 2004.

[115] R. Nekovei and Y. Sun, "Back-propagation network and its configuration for blood vessel detection in angiograms," *IEEE Transactions on Neural Networks*, vol. 6, no. 1, pp. 64–72, 1995.

[116] C. Kirbas and F. Quek, "A review of vessel extraction techniques and algorithms," *ACM Computing Surveys (CSUR)*, vol. 36, no. 2, pp. 81–121, 2004.

[117] X. Yin, B. W. Ng, J. He, Y. Zhang, and D. Abbott, "Accurate image analysis of the retina using hessian matrix and binarisation of thresholded entropy with application of texture mapping," *PLoS One*, vol. 9, no. 4, p. e95943, 2014.

[118] E. Ricci and R. Perfetti, "Retinal blood vessel segmentation using line operators and support vector classification," *IEEE transactions on medical imaging*, vol. 26, no. 10, pp. 1357–1365, 2007.

[119] C. Bowd, F. A. Medeiros, Z. Zhang, L. M. Zangwill, J. Hao, T.-W. Lee, T. J. Sejnowski, R. N. Weinreb, and M. H. Goldbaum, "Relevance vector machine and support vector machine classifier analysis of scanning laser polarimetry retinal nerve fiber layer measurements," *Investigative ophthalmology & visual science*, vol. 46, no. 4, pp. 1322–1329, 2005.

[120] A. Osareh and B. Shadgar, "An automated tracking approach for extraction of retinal vasculature in fundus images," *Journal of ophthalmic & vision research*, vol. 5, no. 1, p. 20, 2010.

[121] J. Jiang, P. Trundle, and J. Ren, "Medical image analysis with artificial neural networks," *Computerized Medical Imaging and Graphics*, vol. 34, no. 8, pp. 617–631, 2010.

[122] R. Foroozan, P. J. Savino, and R. C. Sergott, "Embolic central retinal artery occlusion detected by orbital color doppler imaging," *Ophthalmology*, vol. 109, no. 4, pp. 744–747, 2002.

[123] J. David, R. Krishnan, and S. Kumar, "Neural network based retinal image analysis," in *2008 Congress on Image and Signal Processing*, vol. 2. IEEE, 2008, pp. 49–53.

[124] M. D. Saleh, C. Eswaran, and A. Mueen, "An automated blood vessel segmentation algorithm using histogram equalization and automatic threshold selection," *Journal of digital imaging*, vol. 24, no. 4, pp. 564–572, 2011.

[125] O. Chutatape, L. Zheng, and S. M. Krishnan, "Retinal blood vessel detection and tracking by matched gaussian and kalman filters," in *Proceedings of the 20th Annual International Conference of the IEEE Engineering in Medicine and Biology Society. Vol. 20 Biomedical Engineering Towards the Year 2000 and Beyond (Cat. No. 98CH36286)*, vol. 6. IEEE, 1998, pp. 3144–3149.

[126] I. Liu and Y. Sun, "Recursive tracking of vascular networks in angiograms based on the detection-deletion scheme," *IEEE Transactions on medical imaging*, vol. 12, no. 2, pp. 334–341, 1993.

[127] A. F. Frangi, W. J. Niessen, K. L. Vincken, and M. A. Viergever, "Multiscale vessel enhancement filtering," in *International conference on medical image computing and computer-assisted intervention*. Springer, 1998, pp. 130–137.

[128] V. Mahadevan, H. Narasimha-Iyer, B. Roysam, and H. L. Tanenbaum, "Robust model-based vasculature detection in noisy biomedical images," *IEEE Transactions on Information Technology in Biomedicine*, vol. 8, no. 3, pp. 360–376, 2004.

[129] K. A. Vermeer, F. M. Vos, H. G. Lemij, and A. M. Vossepoel, "A model based method for retinal blood vessel detection," *Computers in biology and medicine*, vol. 34, no. 3, pp. 209–219, 2004.

[130] L. Espona, M. J. Carreira, M. Ortega, and M. G. Penedo, "A snake for retinal vessel segmentation," in *Iberian Conference on Pattern Recognition and Image Analysis*. Springer, 2007, pp. 178–185.

[131] F. Zana and J.-C. Klein, "Segmentation of vessel-like patterns using mathematical morphology and curvature evaluation," *IEEE transactions on image processing*, vol. 10, no. 7, pp. 1010–1019, 2001.

[132] ——, "A multimodal registration algorithm of eye fundus images using vessels detection and hough transform," *IEEE transactions on Medical Imaging*, vol. 18, no. 5, pp. 419–428, 1999.

[133] N. Katz, M. Nelson, M. Goldbaum, S. Chaudhuri, and S. Chatterjee, "Detection of blood vessels in retinal images using two-dimensional matched filters," *IEEE Trans. Med. Imaging*, vol. 8, no. 3, pp. 263–269, 1989.

[134] P. Siddalingaswamy and K. G. Prabhu, "Automatic localization and boundary detection of optic disc using implicit active contours," *International Journal of Computer Applications*, vol. 1, no. 7, pp. 1–5, 2010.

[135] C. Kondermann, D. Kondermann, and M. Yan, "Blood vessel classification into arteries and veins in retinal images," in *Medical Imaging 2007: Image Processing*, vol. 6512. International Society for Optics and Photonics, 2007, p. 651247.

[136] U. M. Akram and S. A. Khan, "Automated detection of dark and bright lesions in retinal images for early detection of diabetic retinopathy," *Journal of medical systems*, vol. 36, no. 5, pp. 3151–3162, 2012.

[137] L. Sukkaew, B. Uyyanonvara, S. Barman, A. Fielder, and K. Cocker, "Automatic extraction of the structure of the retinal blood vessel network of premature infants," *Journal of the Medical Association of Thailand = Chotmaihet thangphaet*, vol. 90, pp. 1780–92, 10 2007.

[138] A. Hoover and M. Goldbaum, "Locating the optic nerve in a retinal image using the fuzzy convergence of the blood vessels," *IEEE transactions on medical imaging*, vol. 22, no. 8, pp. 951–958, 2003.

[139] C. L. Passaglia and J. B. Troy, "The impact of noise on retinal coding of visual signals," *Journal of neurophysiology*, 2004.

[140] M. Al-Rawi, M. Qutaishat, and M. Arrar, "An improved matched filter for blood vessel detection of digital retinal images," *Computers in Biology and Medicine*, vol. 37, no. 2, pp. 262–267, 2007.

[141] C.-H. Wu, G. Agam, and P. Stanchev, "A general framework for vessel segmentation in retinal images," in *2007 International Symposium on Computational Intelligence in Robotics and Automation*. IEEE, 2007, pp. 37–42.

[142] A. M. Mendonca and A. Campilho, "Segmentation of retinal blood vessels by combining the detection of centerlines and morphological reconstruction," *IEEE transactions on medical imaging*, vol. 25, no. 9, pp. 1200–1213, 2006.

[143] L. Xu and S. Luo, "A novel method for blood vessel detection from retinal images," *Biomedical engineering online*, vol. 9, no. 1, p. 14, 2010.

[144] J. Staal, M. Abramoff, M. Niemeijer, M. Viergever, and B. van Ginneken, "Ridge based vessel segmentation in color images of the retina," *IEEE Transactions on Medical Imaging*, vol. 23, no. 4, pp. 501–509, 2004.

[145] A. Hoover, V. Kouznetsova, and M. Goldbaum, "Locating blood vessels in retinal images by piece-wise threshold probing of a matched filter response." in *Proceedings of the AMIA Symposium*. American Medical Informatics Association, 1998, p. 931.

[146] C. G. Owen, A. R. Rudnicka, R. Mullen, S. A. Barman, D. Monekosso, P. H. Whincup, J. Ng, and C. Paterson, "Measuring retinal vessel tortuosity in 10-year-old children: validation of the computer-assisted image analysis of the retina (caiar) program," *Investigative ophthalmology & visual science*, vol. 50, no. 5, pp. 2004–2010, 2009.

[147] J. Odstrcilik, R. Kolar, A. Budai, J. Hornegger, J. Jan, J. Gazarek, T. Kubena, P. Cernosek, O. Svoboda, and E. Angelopoulou, "Retinal vessel segmentation by improved matched filtering: evaluation on a new high-resolution fundus image database," *IET Image Processing*, vol. 7, no. 4, pp. 373–383, 2013.

[148] P. Kovesi, "Phase preserving denoising of images," *signal*, vol. 4, no. 1, 1999.

[149] S. Fischer, F. Šroubek, L. Perrinet, R. Redondo, and G. Cristóbal, "Self-invertible 2d log-gabor wavelets," *International Journal of Computer Vision*, vol. 75, no. 2, pp. 231–246, 2007.

[150] X. Xie and K.-M. Lam, "An efficient illumination normalization method for face recognition," *Pattern Recognition Letters*, vol. 27, no. 6, pp. 609–617, 2006.

[151] T. Fawcett, "An introduction to roc analysis," *Pattern recognition letters*, vol. 27, no. 8, pp. 861–874, 2006.

[152] J. V. Soares, J. J. Leandro, R. M. Cesar, H. F. Jelinek, and M. J. Cree, "Retinal vessel segmentation using the 2-d gabor wavelet and supervised classification," *IEEE Transactions on medical Imaging*, vol. 25, no. 9, pp. 1214–1222, 2006.

[153] D. Marín, A. Aquino, M. E. Gegúndez-Arias, and J. M. Bravo, "A new supervised method for blood vessel segmentation in retinal images by using gray-level and moment invariants-based features," *IEEE Transactions on medical imaging*, vol. 30, no. 1, pp. 146–158, 2011.

[154] M. M. Fraz, P. Remagnino, A. Hoppe, B. Uyyanonvara, A. R. Rudnicka, C. G. Owen, and S. A. Barman, "An ensemble classification-based approach applied to retinal blood vessel segmentation," *IEEE Transactions on Biomedical Engineering*, vol. 59, no. 9, pp. 2538–2548, 2012.

[155] M. E. Martinez-Perez, A. D. Hughes, S. A. Thom, A. A. Bharath, and K. H. Parker, "Segmentation of blood vessels from red-free and fluorescein retinal images," *Medical image analysis*, vol. 11, no. 1, pp. 47–61, 2007.

[156] B. Al-Diri, A. Hunter, and D. Steel, "An active contour model for segmenting and measuring retinal vessels," *IEEE Transactions on Medical imaging*, vol. 28, no. 9, pp. 1488–1497, 2009.

[157] B. S. Lam, Y. Gao, and A. W.-C. Liew, "General retinal vessel segmentation using regularization-based multiconcavity modeling," *IEEE Transactions on Medical Imaging*, vol. 29, no. 7, pp. 1369–1381, 2010.

[158] Y. Zhao, L. Rada, K. Chen, S. P. Harding, and Y. Zheng, "Automated vessel segmentation using infinite perimeter active contour model with hybrid region information with application to retinal images," *IEEE transactions on medical imaging*, vol. 34, no. 9, pp. 1797–1807, 2015.

[159] H. Yu, S. Barriga, C. Agurto, G. Zamora, W. Bauman, and P. Soliz, "Fast vessel segmentation in retinal images using multi-scale enhancement and second-order local entropy," in *Medical Imaging 2012: Computer-Aided Diagnosis*, vol. 8315. International Society for Optics and Photonics, 2012, p. 83151B.

[160] H. Annuziata, A. Garzelli, L. Ballerini, A. Mecocci, and E. Trucco, "Fast vessel segmentation in retinal images using multi-scale enhancement and second-order local entropy," vol. 20, no. 4. IEEE, 2016, pp. 1129–1138.

[161] M. D. Abràmoff, M. K. Garvin, and M. Sonka, "Retinal imaging and image analysis," *IEEE reviews in biomedical engineering*, vol. 3, pp. 169–208, 2010.

[162] M. D. Pinazo-Durán, V. Zanón-Moreno, J. J. García-Medina, J. F. Arévalo, R. Gallego-Pinazo, and C. Nucci, "Eclectic ocular comorbidities and systemic diseases with eye involvement: a review," *BioMed research international*, vol. 2016, 2016.

[163] H. Yu, E. S. Barriga, C. Agurto, S. Echegaray, M. S. Pattichis, W. Bauman, and P. Soliz, "Fast localization and segmentation of optic disk in retinal images using directional matched filtering and level sets," *IEEE Transactions on information technology in biomedicine*, vol. 16, no. 4, pp. 644–657, 2012.

[164] J. Jack and B. Brad, "Kanski clinical ophthalmology, a systematic approach," 2006.

[165] A. Almazroa, R. Burman, K. Raahemifar, and V. Lakshminarayanan, "Optic disc and optic cup segmentation methodologies for glaucoma image detection: a survey," *Journal of ophthalmology*, vol. 2015, 2015.

[166] D. Welfer, J. Scharcanski, and D. R. Marinho, "A morphologic two-stage approach for automated optic disk detection in color eye fundus images," *Pattern Recognition Letters*, vol. 34, no. 5, pp. 476–485, 2013.

[167] S. Morales, V. Naranjo, J. Angulo, and M. Alcañiz, "Automatic detection of optic disc based on pca and mathematical morphology," *IEEE transactions on medical imaging*, vol. 32, no. 4, pp. 786–796, 2013.

[168] G. D. Joshi, J. Sivaswamy, and S. Krishnadas, "Optic disk and cup segmentation from monocular color retinal images for glaucoma assessment," *IEEE transactions on medical imaging*, vol. 30, no. 6, pp. 1192–1205, 2011.

[169] H.-K. Hsiao, C.-C. Liu, C.-Y. Yu, S.-W. Kuo, and S.-S. Yu, "A novel optic disc detection scheme on retinal images," *Expert Systems with Applications*, vol. 39, no. 12, pp. 10 600–10 606, 2012.

[170] J. Cheng, J. Liu, Y. Xu, F. Yin, D. W. K. Wong, N.-M. Tan, D. Tao, C.-Y. Cheng, T. Aung, and T. Y. Wong, "Superpixel classification based optic disc and optic cup segmentation for glaucoma screening," *IEEE transactions on Medical Imaging*, vol. 32, no. 6, pp. 1019–1032, 2013.

[171] X. Zhu and R. M. Rangayyan, "Detection of the optic disc in images of the retina using the hough transform," in *Engineering in Medicine and Biology Society, 2008. EMBS 2008. 30th Annual International Conference of the IEEE*. IEEE, 2008, pp. 3546–3549.

[172] P. Siddalingaswamy and K. G. Prabhu, "Automatic localization and boundary detection of optic disc using implicit active contours," *International Journal of Computer Applications*, vol. 1, no. 7, pp. 1–5, 2010.

[173] F. Yin, J. Liu, S. H. Ong, Y. Sun, D. W. Wong, N. M. Tan, C. Cheung, M. Baskaran, T. Aung, and T. Y. Wong, "Model-based optic nerve head segmentation on retinal fundus images," in *Engineering in Medicine and Biology Society, EMBC, 2011 Annual International Conference of the IEEE*. IEEE, 2011, pp. 2626–2629.

[174] S. Lu, "Accurate and efficient optic disc detection and segmentation by a circular transformation," *IEEE Transactions on medical imaging*, vol. 30, no. 12, pp. 2126–2133, 2011.

[175] H. Tjandrasa, A. Wijayanti, and N. Suciati, "Optic nerve head segmentation using hough transform and active contours," *Indonesian Journal of Electrical Engineering and Computer Science*, vol. 10, no. 3, pp. 531–536, 2012.

[176] M. Abdullah, M. M. Fraz, and S. A. Barman, "Localization and segmentation of optic disc in retinal images using circular hough transform and grow-cut algorithm," *PeerJ*, vol. 4, p. e2003, 2016.

[177] D. Marin, M. E. Gegundez-Arias, A. Suero, and J. M. Bravo, "Obtaining optic disc center and pixel region by automatic thresholding methods on morphologically processed fundus images," *Computer methods and programs in biomedicine*, vol. 118, no. 2, pp. 173–185, 2015.

[178] A. Basit and M. M. Fraz, "Optic disc detection and boundary extraction in retinal images," *Appl. Opt.*, vol. 54, no. 11, pp. 3440–3447, Apr 2015.

[179] C. Agurto, V. Murray, E. Barriga, S. Murillo, M. Pattichis, H. Davis, S. Russell, M. Abràmoff, and P. Soliz, "Multiscale am-fm methods for diabetic retinopathy lesion detection," *IEEE transactions on medical imaging*, vol. 29, no. 2, pp. 502–512, 2010.

[180] A. Borji, M.-M. Cheng, H. Jiang, and J. Li, "Salient object detection: A benchmark," *IEEE transactions on image processing*, vol. 24, no. 12, pp. 5706–5722, 2015.

[181] L. Lu and G. D. Hager, "Dynamic foreground/background extraction from images and videos using random patches," in *Advances in Neural Information Processing Systems*, 2007, pp. 929–936.

[182] H. Yao, Q. Duan, D. Li, and J. Wang, "An improved k-means clustering algorithm for fish image segmentation," *Mathematical and Computer Modelling*, vol. 58, no. 3-4, pp. 790–798, 2013.

[183] A. C. Bovik and S. T. Acton, "Basic linear filtering with application to image enhancement," in *The Essential Guide to Image Processing*. Elsevier, 2009, pp. 225–239.

[184] R. Achanta, A. Shaji, K. Smith, A. Lucchi, P. Fua, and S. Süsstrunk, "Slic superpixels," Tech. Rep., 2010.

[185] P. P. Mondal, K. Rajan, and I. Ahmad, "Filter for biomedical imaging and image processing," *JOSA A*, vol. 23, no. 7, pp. 1678–1686, 2006.

[186] H. Ng, S. Ong, K. Foong, P. Goh, and W. Nowinski, "Medical image segmentation using k-means clustering and improved watershed algorithm," in *Image Analysis and Interpretation, 2006 IEEE Southwest Symposium on*. IEEE, 2006, pp. 61–65.

[187] F. Ter Haar, "Automatic localization of the optic disc in digital colour images of the human retina," *Utrecht University*, 2005.

[188] S. J. K. Pedersen, "Circular hough transform," *Aalborg University, Vision, Graphics, and Interactive Systems*, vol. 123, p. 123, 2007.

[189] S. Biswas, D. Ghoshal, and R. Hazra, "A new algorithm of image segmentation using curve fitting based higher order polynomial smoothing," *Optik-International Journal for Light and Electron Optics*, vol. 127, no. 20, pp. 8916–8925, 2016.

[190] E. J. Carmona, M. Rincón, J. García-Feijoó, and J. M. Martínez-de-la Casa, "Identification of the optic nerve head with genetic algorithms," *Artificial Intelligence in Medicine*, vol. 43, no. 3, pp. 243–259, 2008.

[191] E. Decencière, X. Zhang, G. Cazuguel, B. Lay, B. Cochener, C. Trone, P. Gain, R. Ordonez, P. Massin, A. Erginay *et al.*, "Feedback on a publicly distributed image database: the messidor database," *Image Analysis & Stereology*, vol. 33, no. 3, pp. 231–234, 2014.

[192] M. Niemeijer, X. Xu, A. V. Dumitrescu, P. Gupta, B. Van Ginneken, J. C. Folk, and M. D. Abramoff, "Automated measurement of the arteriolar-to-venular width ratio in digital color fundus photographs," *IEEE Transactions on medical imaging*, vol. 30, no. 11, pp. 1941–1950, 2011.

[193] M. Niemeijer, J. Staal, B. Ginneken, M. Loog, and M. Abramoff, "Drive: digital retinal images for vessel extraction," *Methods for Evaluating Segmentation and Indexing Techniques Dedicated to Retinal Ophthalmology*, 2004.

[194] M. M. Fraz, P. Remagnino, A. Hoppe, B. Uyyanonvara, A. R. Rudnicka, C. G. Owen, and S. A. Barman, "An ensemble classification-based approach applied to retinal

blood vessel segmentation," *IEEE Transactions on Biomedical Engineering*, vol. 59, no. 9, pp. 2538–2548, 2012.

[195] T. Kauppi, V. Kalesnykiene, J.-K. Kamarainen, L. Lensu, I. Sorri, H. Uusitalo, H. Kälviäinen, and J. Pietilä, "Diaretdb0: Evaluation database and methodology for diabetic retinopathy algorithms," *Machine Vision and Pattern Recognition Research Group, Lappeenranta University of Technology, Finland*, vol. 73, 2006.

[196] R. Kälviäinen and H. Uusitalo, "Diaretdb1 diabetic retinopathy database and evaluation protocol," in *Medical Image Understanding and Analysis*, vol. 2007. Citeseer, 2007, p. 61.

[197] S. Roychowdhury, D. D. Koozekanani, S. N. Kuchinka, and K. K. Parhi, "Optic disc boundary and vessel origin segmentation of fundus images," *IEEE journal of biomedical and health informatics*, vol. 20, no. 6, pp. 1562–1574, 2016.

[198] C. Parker, "An analysis of performance measures for binary classifiers," in *Data Mining (ICDM), 2011 IEEE 11th International Conference on*. IEEE, 2011, pp. 517–526.

[199] K. J. Van Stralen, V. S. Stel, J. B. Reitsma, F. W. Dekker, C. Zoccali, and K. J. Jager, "Diagnostic methods i: sensitivity, specificity, and other measures of accuracy," *Kidney international*, vol. 75, no. 12, pp. 1257–1263, 2009.

[200] M. M. Fraz, P. Remagnino, A. Hoppe, B. Uyyanonvara, A. R. Rudnicka, C. G. Owen, and S. A. Barman, "Blood vessel segmentation methodologies in retinal images–a survey," *Computer methods and programs in biomedicine*, vol. 108, no. 1, pp. 407–433, 2012.

[201] T. Fawcett, "An introduction to roc analysis," *Pattern recognition letters*, vol. 27, no. 8, pp. 861–874, 2006.

[202] M. N. Zahoor and M. M. Fraz, "A correction to the article "fast optic disc segmentation in retina using polar transform"," *IEEE Access*, vol. 6, pp. 4845–4849, 2018.

[203] B. Dashtbozorg, A. M. Mendonça, and A. Campilho, "Optic disc segmentation using the sliding band filter," *Computers in biology and medicine*, vol. 56, pp. 1–12, 2015.

[204] A. G. Salazar-Gonzalez, D. Kaba, Y. Li, and X. Liu, "Segmentation of the blood vessels and optic disk in retinal images." *IEEE J. Biomedical and Health Informatics*, vol. 18, no. 6, pp. 1874–1886, 2014.

[205] A. Basit and M. M. Fraz, "Optic disc detection and boundary extraction in retinal images," *Applied optics*, vol. 54, no. 11, pp. 3440–3447, 2015.

[206] A. Jemal, R. Siegel, J. Xu, and E. Ward, "Cancer statistics, 2010," *CA: a cancer journal for clinicians*, vol. 60, no. 5, pp. 277–300, 2010.

[207] J. Ferlay, D. Parkin, and E. Steliarova-Foucher, "Estimates of cancer incidence and mortality in europe in 2008," *European journal of cancer*, vol. 46, no. 4, pp. 765–781, 2010.

[208] F. Lalloo and D. G. Evans, "Familial breast cancer," *Clinical Genetics*, vol. 82, no. 2, pp. 105–114, 2012. [Online]. Available: https://onlinelibrary.wiley.com/doi/abs/10.1111/j.1399-0004.2012.01859.x

[209] C. E. DeSantis, S. A. Fedewa, A. Goding Sauer, J. L. Kramer, R. A. Smith, and A. Jemal, "Breast cancer statistics, 2015: Convergence of incidence rates between black and white women," *CA: a cancer journal for clinicians*, vol. 66, no. 1, pp. 31–42, 2016.

[210] H. Weedon-Fekjær, P. R. Romundstad, and L. J. Vatten, "Modern mammography screening and breast cancer mortality: population study," *Bmj*, vol. 348, p. g3701, 2014.

[211] R. M. Mann, C. K. Kuhl, K. Kinkel, and C. Boetes, "Breast mri: guidelines from the european society of breast imaging," *European radiology*, vol. 18, no. 7, pp. 1307–1318, 2008.

[212] S. G. Orel and M. D. Schnall, "Mr imaging of the breast for the detection, diagnosis, and staging of breast cancer," *Radiology*, vol. 220, no. 1, pp. 13–30, 2001.

[213] Y. Zheng, S. Baloch, S. Englander, M. D. Schnall, and D. Shen, "Segmentation and classification of breast tumor using dynamic contrast-enhanced mr images," in *International Conference on Medical Image Computing and Computer-Assisted Intervention*. Springer, 2007, pp. 393–401.

[214] X.-X. Yin, S. Hadjiloucas, J.-H. Chen, Y. Zhang, J.-L. Wu, and M.-Y. Su, "Tensor based multichannel reconstruction for breast tumours identification from dce-mris," *PloS one*, vol. 12, no. 3, p. e0172111, 2017.

[215] X.-X. Yin, B.-H. Ng, Q. Yang, A. Pitman, K. Ramamohanarao, and D. Abbott, "Anatomical landmark localization in breast dynamic contrast-enhanced mr imaging," *Medical & biological engineering & computing*, vol. 50, no. 1, pp. 91–101, 2012.

[216] N. Saidin, H. A. M. Sakim, U. K. Ngah, and I. L. Shuaib, "Segmentation of breast regions in mammogram based on density: a review," *arXiv preprint arXiv:1209.5494*, 2012.

[217] A. Eng, Z. Gallant, J. Shepherd, V. McCormack, J. Li, M. Dowsett, S. Vinnicombe, S. Allen, and I. dos Santos-Silva, "Digital mammographic density and breast cancer risk: a case–control study of six alternative density assessment methods," *Breast cancer research*, vol. 16, no. 5, p. 439, 2014.

[218] J. Yao, J. Chen, and C. Chow, "Breast tumor analysis in dynamic contrast enhanced mri using texture features and wavelet transform," *IEEE Journal of selected topics in signal processing*, vol. 3, no. 1, pp. 94–100, 2009.

[219] K. Ganesan, U. R. Acharya, K. C. Chua, L. C. Min, and K. T. Abraham, "Pectoral muscle segmentation: a review," *Computer methods and programs in biomedicine*, vol. 110, no. 1, pp. 48–57, 2013.

[220] B. Zheng, J. H. Sumkin, M. L. Zuley, X. Wang, A. H. Klym, and D. Gur, "Bilateral mammographic density asymmetry and breast cancer risk: a preliminary assessment," *European journal of radiology*, vol. 81, no. 11, pp. 3222–3228, 2012.

[221] G. Ertaş, H. Ö. Gülçür, O. Osman, O. N. Uçan, M. Tunacı, and M. Dursun, "Breast mr segmentation and lesion detection with cellular neural networks and 3d template matching," *Computers in biology and medicine*, vol. 38, no. 1, pp. 116–126, 2008.

[222] D. Raba, A. Oliver, J. Martí, M. Peracaula, and J. Espunya, "Breast segmentation with pectoral muscle suppression on digital mammograms," in *Iberian Conference on Pattern Recognition and Image Analysis*. Springer, 2005, pp. 471–478.

[223] N. Just, "Improving tumour heterogeneity mri assessment with histograms," *British journal of cancer*, vol. 111, no. 12, p. 2205, 2014.

[224] M. Lin, J.-H. Chen, X. Wang, S. Chan, S. Chen, and M.-Y. Su, "Template-based automatic breast segmentation on mri by excluding the chest region," *Medical physics*, vol. 40, no. 12, 2013.

[225] J. J. Heine, M. Kallergi, S. M. Chetelat, and L. P. Clarke, "Multiresolution wavelet approach for separating the breast region from the background in high resolution digital mammography," in *Digital Mammography*. Springer, 1998, pp. 295–298.

[226] R. Ferrari, A. Frere, R. Rangayyan, J. Desautels, and R. Borges, "Identification of the breast boundary in mammograms using active contour models," *Medical and Biological Engineering and Computing*, vol. 42, no. 2, pp. 201–208, 2004.

[227] A. Q. Al-Faris, U. K. Ngah, N. A. M. Isa, and I. L. Shuaib, "Computer-aided segmentation system for breast mri tumour using modified automatic seeded region growing (bmri-masrg)," *Journal of digital imaging*, vol. 27, no. 1, pp. 133–144, 2014.

[228] B. Keller, D. Nathan, Y. Wang, Y. Zheng, J. Gee, E. Conant, and D. Kontos, "Adaptive multi-cluster fuzzy c-means segmentation of breast parenchymal tissue in digital mammography," in *International Conference on Medical Image Computing and Computer-Assisted Intervention*. Springer, 2011, pp. 562–569.

[229] W. Chen, M. L. Giger, and U. Bick, "A fuzzy c-means (fcm)-based approach for computerized segmentation of breast lesions in dynamic contrast-enhanced mr images1," *Academic radiology*, vol. 13, no. 1, pp. 63–72, 2006.

[230] N. Petrick, H.-P. Chan, B. Sahiner, and M. A. Helvie, "Combined adaptive enhancement and region-growing segmentation of breast masses on digitized mammograms," *Medical physics*, vol. 26, no. 8, pp. 1642–1654, 1999.

[231] Y. Cao, X. Hao, X. Zhu, and S. Xia, "An adaptive region growing algorithm for breast masses in mammograms," *Frontiers of Electrical and Electronic Engineering in China*, vol. 5, no. 2, pp. 128–136, 2010.

[232] L. Wang, K. Filippatos, O. Friman, and H. K. Hahn, "Fully automated segmentation of the pectoralis muscle boundary in breast mr images," in *Medical Imaging 2011: Computer-Aided Diagnosis*, vol. 7963. International Society for Optics and Photonics, 2011, p. 796309.

[233] F. Khalvati, C. Gallego-Ortiz, S. Balasingham, and A. L. Martel, "Automated segmentation of breast in 3-d mr images using a robust atlas," *IEEE transactions on medical imaging*, vol. 34, no. 1, pp. 116–125, 2015.

[234] A. Gubern-Merida, M. Kallenberg, R. M. Mann, R. Marti, and N. Karssemeijer, "Breast segmentation and density estimation in breast mri: a fully automatic framework," *ieee journal of biomedical and health informatics*, vol. 19, no. 1, pp. 349–357, 2015.

[235] J. Milenković, O. Chambers, M. M. Mušič, and J. F. Tasič, "Automated breast-region segmentation in the axial breast mr images," *Computers in biology and medicine*, vol. 62, pp. 55–64, 2015.

[236] P. T. Fwu, J.-H. Chen, Y. Li, S. Chan, and M.-Y. Su, "Quantification of regional breast density in four quadrants using 3d mri—a pilot study," *Translational oncology*, vol. 8, no. 4, pp. 250–257, 2015.

[237] Q. Yang, L. Li, J. Zhang, G. Shao, C. Zhang, and B. Zheng, "Computer-aided diagnosis of breast dce-mri images using bilateral asymmetry of contrast enhancement between two breasts," *Journal of digital imaging*, vol. 27, no. 1, pp. 152–160, 2014.

[238] J. H. Hipwell, V. Vavourakis, L. Han, T. Mertzanidou, B. Eiben, and D. J. Hawkes, "A review of biomechanically informed breast image registration," *Physics in Medicine & Biology*, vol. 61, no. 2, p. R1, 2016.

[239] R. Azmi, N. Norozi, R. Anbiaee, L. Salehi, and A. Amirzadi, "Impst: a new interactive self-training approach to segmentation suspicious lesions in breast mri," *Journal of medical signals and sensors*, vol. 1, no. 2, p. 138, 2011.

[240] M. J. Yaffe, "Mammographic density. measurement of mammographic density," *Breast Cancer Research*, vol. 10, no. 3, p. 209, 2008.

[241] R. Llobet, M. Pollán, J. Antón, J. Miranda-García, M. Casals, I. Martínez, F. Ruiz-Perales, B. Pérez-Gómez, D. Salas-Trejo, and J.-C. Pérez-Cortés, "Semi-automated and fully automated mammographic density measurement and breast cancer risk prediction," *Computer methods and programs in biomedicine*, vol. 116, no. 2, pp. 105–115, 2014.

[242] J. J. Heine, M. J. Carston, C. G. Scott, K. R. Brandt, F.-F. Wu, V. S. Pankratz, T. A. Sellers, and C. M. Vachon, "An automated approach for estimation of breast density," *Cancer Epidemiology and Prevention Biomarkers*, vol. 17, no. 11, pp. 3090–3097, 2008.

[243] F. Habte, S. Budhiraja, S. Keren, T. C. Doyle, C. S. Levin, and D. S. Paik, "In situ study of the impact of inter-and intra-reader variability on region of interest (roi) analysis in preclinical molecular imaging," *American journal of nuclear medicine and molecular imaging*, vol. 3, no. 2, p. 175, 2013.

[244] C.-H. Wei, Y. Li, P. J. Huang, C.-Y. Gwo, and S. E. Harms, "Estimation of breast density: An adaptive moment preserving method for segmentation of fibroglandular tissue in breast magnetic resonance images," *European journal of radiology*, vol. 81, no. 4, pp. e618–e624, 2012.

[245] S. Wu, S. Weinstein, and D. Kontos, "Atlas-based probabilistic fibroglandular tissue segmentation in breast mri," in *International Conference on Medical Image Computing and Computer-Assisted Intervention*. Springer, 2012, pp. 437–445.

[246] L.-J. W. Lu, T. K. Nishino, R. F. Johnson, F. Nayeem, D. G. Brunder, H. Ju, M. H. Leonard Jr, J. J. Grady, and T. Khamapirad, "Comparison of breast tissue measurements using magnetic resonance imaging, digital mammography and a mathematical algorithm," *Physics in Medicine & Biology*, vol. 57, no. 21, p. 6903, 2012.

[247] Y. Wang, G. Morrell, M. E. Heibrun, A. Payne, and D. L. Parker, "3d multi-parametric breast mri segmentation using hierarchical support vector machine with coil sensitivity correction," *Academic radiology*, vol. 20, no. 2, pp. 137–147, 2013.

[248] J. A. Rosado-Toro, T. Barr, J.-P. Galons, M. T. Marron, A. Stopeck, C. Thomson, P. Thompson, D. Carroll, E. Wolf, M. I. Altbach *et al.*, "Automated breast segmenta-

tion of fat and water mr images using dynamic programming," *Academic radiology*, vol. 22, no. 2, pp. 139–148, 2015.

[249] M. Kazubek, "Wavelet domain image denoising by thresholding and wiener filtering," *IEEE Signal Processing Letters*, vol. 10, no. 11, pp. 324–326, 2003.

[250] J. S. Lim, "Two-dimensional signal and image processing," *Englewood Cliffs, NJ, Prentice Hall, 1990, 710 p.*, 1990.

[251] T. Kanungo, D. M. Mount, N. S. Netanyahu, C. D. Piatko, R. Silverman, and A. Y. Wu, "An efficient k-means clustering algorithm: Analysis and implementation," *IEEE Transactions on Pattern Analysis & Machine Intelligence*, no. 7, pp. 881–892, 2002.

[252] T. F. Chan and L. A. Vese, "Active contours without edges," *IEEE Transactions on image processing*, vol. 10, no. 2, pp. 266–277, 2001.

[253] D. Pandey, X. Yin, H. Wang, and Y. Zhang, "Accurate vessel segmentation using maximum entropy incorporating line detection and phase-preserving denoising," *Computer Vision and Image Understanding*, vol. 155, pp. 162–172, 2017.

[254] C. J. Kuo, C.-H. Yeh, and S. F. Odeh, "Polynomial search algorithms for motion estimation," in *ISCAS'99. Proceedings of the 1999 IEEE International Symposium on Circuits and Systems VLSI (Cat. No. 99CH36349)*, vol. 4. IEEE, 1999, pp. 215–218.

[255] Y. Yang, C. Zheng, and P. Lin, "Image thresholding via a modified fuzzy c-means algorithm," in *Iberoamerican Congress on Pattern Recognition*. Springer, 2004, pp. 589–596.

[256] J. V. Manjón, "Mri preprocessing," in *Imaging Biomarkers*. Springer, 2017, pp. 53–63.

[257] M. Basu, "Gaussian-based edge-detection methods-a survey," *IEEE Transactions on Systems, Man, and Cybernetics, Part C (Applications and Reviews)*, vol. 32, no. 3, pp. 252–260, 2002.

[258] T. Qiu, A. Wang, N. Yu, and A. Song, "Llsure: local linear sure-based edge-preserving image filtering," *IEEE Transactions on Image Processing*, vol. 22, no. 1, pp. 80–90, 2013.

[259] C. V. Cannistraci, A. Abbas, and X. Gao, "Median modified wiener filter for nonlinear adaptive spatial denoising of protein nmr multidimensional spectra," *Scientific reports*, vol. 5, p. 8017, 2015.

[260] V. Strela, "Denoising via block wiener filtering in wavelet domain," in *European Congress of Mathematics*. Springer, 2001, pp. 619–625.

[261] R. K. Carl Fredrik Westin, Hans Knutsson, "Adaptive image filtering." in *Handbook of medical image processing and analysis*. Elsevier, 2000, pp. 3208–3212.

[262] M. M. Ahmed and D. B. Mohamad, "Segmentation of brain mr images for tumor extraction by combining kmeans clustering and perona-malik anisotropic diffusion model," *International Journal of Image Processing*, vol. 2, no. 1, pp. 27–34, 2008.

[263] J. Petitot, "An introduction to the mumford–shah segmentation model," *Journal of Physiology-Paris*, vol. 97, no. 2-3, pp. 335–342, 2003.

[264] R. Boss, K. Thangavel, and D. Daniel, "Automatic mammogram image breast region extraction and removal of pectoral muscle," *arXiv preprint arXiv:1307.7474*, 2013.

[265] A. Rampun, P. J. Morrow, B. W. Scotney, and J. Winder, "Fully automated breast boundary and pectoral muscle segmentation in mammograms," *Artificial intelligence in medicine*, vol. 79, pp. 28–41, 2017.

[266] H. Wang and B. Fei, "A modified fuzzy c-means classification method using a multiscale diffusion filtering scheme," *Medical image analysis*, vol. 13, no. 2, pp. 193–202, 2009.

[267] R. Suganya and R. Shanthi, "Fuzzy c-means algorithm-a review," *International Journal of Scientific and Research Publications*, vol. 2, no. 11, p. 1, 2012.

[268] R. Parikh, A. Mathai, S. Parikh, G. C. Sekhar, and R. Thomas, "Understanding and using sensitivity, specificity and predictive values," *Indian journal of ophthalmology*, vol. 56, no. 1, p. 45, 2008.

[269] A. A. Taha and A. Hanbury, "Metrics for evaluating 3d medical image segmentation: analysis, selection, and tool," *BMC medical imaging*, vol. 15, no. 1, p. 29, 2015.

[270] K. Hajian-Tilaki, "Sample size estimation in diagnostic test studies of biomedical informatics," *Journal of biomedical informatics*, vol. 48, pp. 193–204, 2014.

[271] S. Wu, S. P. Weinstein, E. F. Conant, M. D. Schnall, and D. Kontos, "Automated chest wall line detection for whole-breast segmentation in sagittal breast mr images," *Medical physics*, vol. 40, no. 4, 2013.

[272] M. Peng, Q. Xie, H. Wang, Y. Zhang, and G. Tian, "Bayesian sparse topical coding," *IEEE Transactions on Knowledge and Data Engineering*, 2018.

[273] H. Wang, Y. Zhang *et al.*, "Detection of motor imagery eeg signals employing naïve bayes based learning process," *Measurement*, vol. 86, pp. 148–158, 2016.

[274] J. He, J. Rong, L. Sun, H. Wang, Y. Zhang, and J. Ma, "D-ecg: a dynamic framework for cardiac arrhythmia detection from iot-based ecgs," in *International Conference on Web Information Systems Engineering*. Springer, 2018, pp. 85–99.

[275] K. H. Zou, S. K. Warfield, A. Bharatha, C. M. Tempany, M. R. Kaus, S. J. Haker, W. M. Wells III, F. A. Jolesz, and R. Kikinis, "Statistical validation of image segmentation quality based on a spatial overlap index1: scientific reports," *Academic radiology*, vol. 11, no. 2, pp. 178–189, 2004.

[276] C. G. Ortiz and A. Martel, "Automatic atlas-based segmentation of the breast in mri for 3d breast volume computation," *Medical physics*, vol. 39, no. 10, pp. 5835–5848, 2012.

[277] S. J. Doran, J. H. Hipwell, R. Denholm, B. Eiben, M. Busana, D. J. Hawkes, M. O. Leach, and I. d. S. Silva, "Breast mri segmentation for density estimation: Do different methods give the same results and how much do differences matter?" *Medical physics*, vol. 44, no. 9, pp. 4573–4592, 2017.

[278] A. Fooladivanda, S. B. Shokouhi, and N. Ahmadinejad, "Localized-atlas-based segmentation of breast mri in a decision-making framework," *Australasian physical & engineering sciences in medicine*, vol. 40, no. 1, pp. 69–84, 2017.

[279] S. Thakran, S. Chatterjee, M. Singhal, R. K. Gupta, and A. Singh, "Automatic outer and inner breast tissue segmentation using multi-parametric mri images of breast tumor patients," *PloS one*, vol. 13, no. 1, p. e0190348, 2018.

[280] M. Akram, M. Iqbal, M. Daniyal, and A. U. Khan, "Awareness and current knowledge of breast cancer," *Biological research*, vol. 50, no. 1, p. 33, 2017.

[281] H. G. Welch, P. C. Prorok, A. J. O'Malley, and B. S. Kramer, "Breast-cancer tumor size, overdiagnosis, and mammography screening effectiveness," *New England Journal of Medicine*, vol. 375, no. 15, pp. 1438–1447, 2016.

[282] M. Abdel-Nasser, J. Melendez, A. Moreno, O. A. Omer, and D. Puig, "Breast tumor classification in ultrasound images using texture analysis and super-resolution methods," *Engineering Applications of Artificial Intelligence*, vol. 59, pp. 84–92, 2017.

[283] J.-Z. Cheng, D. Ni, Y.-H. Chou, J. Qin, C.-M. Tiu, Y.-C. Chang, C.-S. Huang, D. Shen, and C.-M. Chen, "Computer-aided diagnosis with deep learning architecture: applications to breast lesions in us images and pulmonary nodules in ct scans," *Scientific reports*, vol. 6, p. 24454, 2016.

[284] H. Li, Y. Zhu, E. S. Burnside, E. Huang, K. Drukker, K. A. Hoadley, C. Fan, S. D. Conzen, M. Zuley, J. M. Net *et al.*, "Quantitative mri radiomics in the prediction of molecular classifications of breast cancer subtypes in the tcga/tcia data set," *NPJ Breast Cancer*, vol. 2, p. 16012, 2016.

[285] J. Zhang, A. Saha, Z. Zhu, and M. A. Mazurowski, "Hierarchical convolutional neural networks for segmentation of breast tumors in mri with application to radiogenomics," *IEEE transactions on medical imaging*, vol. 38, no. 2, pp. 435–447, 2019.

[286] T. Wan, J. Cao, J. Chen, and Z. Qin, "Automated grading of breast cancer histopathology using cascaded ensemble with combination of multi-level image features," *Neurocomputing*, vol. 229, pp. 34–44, 2017.

[287] Y. Zhuge, A. V. Krauze, H. Ning, J. Y. Cheng, B. C. Arora, K. Camphausen, and R. W. Miller, "Brain tumor segmentation using holistically nested neural networks in mri images," *Medical physics*, vol. 44, no. 10, pp. 5234–5243, 2017.

[288] M. Angulakshmi and G. Lakshmi Priya, "Automated brain tumour segmentation techniques—a review," *International Journal of Imaging Systems and Technology*, vol. 27, no. 1, pp. 66–77, 2017.

[289] D. Bzdok, M. Krzywinski, and N. Altman, "Points of significance: Machine learning: supervised methods," 2018.

[290] S. Du, F. Zhang, and X. Zhang, "Semantic classification of urban buildings combining vhr image and gis data: An improved random forest approach," *ISPRS journal of photogrammetry and remote sensing*, vol. 105, pp. 107–119, 2015.

[291] Z. Shi, P. Siva, and T. Xiang, "Transfer learning by ranking for weakly supervised object annotation," *arXiv preprint arXiv:1705.00873*, 2017.

[292] H. Fabelo, S. Ortega, E. Casselden, J. Loh, H. Bulstrode, A. Zolnourian, P. Grundy, G. M. Callico, D. Bulters, and R. Sarmiento, "Svm optimization for brain tumor identification using infrared spectroscopic samples," *Sensors*, vol. 18, no. 12, p. 4487, 2018.

[293] A. Kendall and Y. Gal, "What uncertainties do we need in bayesian deep learning for computer vision?" in *Advances in neural information processing systems*, 2017, pp. 5574–5584.

[294] M. Havaei, A. Davy, D. Warde-Farley, A. Biard, A. Courville, Y. Bengio, C. Pal, P.-M. Jodoin, and H. Larochelle, "Brain tumor segmentation with deep neural networks," *Medical image analysis*, vol. 35, pp. 18–31, 2017.

[295] A. Kapoor and A. Singhal, "A comparative study of k-means, k-means++ and fuzzy c-means clustering algorithms," in *2017 3rd International Conference on Computational Intelligence & Communication Technology (CICT)*. IEEE, 2017, pp. 1–6.

[296] Z. Yang, P. Wang, Y. Wang, W. Xu, and R. Nevatia, "Every pixel counts: Unsupervised geometry learning with holistic 3d motion understanding," in *Proceedings of the European Conference on Computer Vision (ECCV)*, 2018, pp. 0–0.

[297] D. Chudasama, T. Patel, S. Joshi, and G. I. Prajapati, "Image segmentation using morphological operations," *International Journal of Computer Applications*, vol. 117, no. 18, 2015.

[298] R. Kashyap and V. Tiwari, "Energy-based active contour method for image segmentation." *IJEH*, vol. 9, no. 2/3, pp. 210–225, 2017.

[299] F.-X. Tang and Y.-F. Yang, "Research of color image segmentation algorithm based on asymmetric kernel density estimation," *Journal of Computational Methods in Sciences and Engineering*, vol. 17, no. 3, pp. 455–462, 2017.

[300] K. H. Cha, L. Hadjiiski, R. K. Samala, H.-P. Chan, E. M. Caoili, and R. H. Cohan, "Urinary bladder segmentation in ct urography using deep-learning convolutional neural network and level sets," *Medical physics*, vol. 43, no. 4, pp. 1882–1896, 2016.

[301] L. Gao, J. Song, F. Nie, F. Zou, N. Sebe, and H. T. Shen, "Graph-without-cut: An ideal graph learning for image segmentation," in *Thirtieth AAAI Conference on Artificial Intelligence*, 2016.

[302] S. Ekström, F. Malmberg, H. Ahlström, J. Kullberg, and R. Strand, "Fast graph-cut based optimization for practical dense deformable registration of volume images," *arXiv preprint arXiv:1810.08427*, 2018.

[303] X. Chen, J. K. Udupa, U. Bagci, Y. Zhuge, and J. Yao, "Medical image segmentation by combining graph cuts and oriented active appearance models," *IEEE Transactions on Image Processing*, vol. 21, no. 4, pp. 2035–2046, 2012.

[304] J. Yuan, E. Bae, and X.-C. Tai, "A study on continuous max-flow and min-cut approaches," in *2010 ieee computer society conference on computer vision and pattern recognition*. IEEE, 2010, pp. 2217–2224.

[305] K. Villringer, R. Serrano-Sandoval, U. Grittner, I. Galinovic, A. Schneider, A.-C. Ostwaldt, P. Brunecker, A. Rocco, and J. B. Fiebach, "Subtracted dynamic mr perfusion source images (smrp-si) provide collateral blood flow assessment in mca occlusions and predict tissue fate," *European radiology*, vol. 26, no. 5, pp. 1396–1403, 2016.

[306] K. K. Brock, S. Mutic, T. R. McNutt, H. Li, and M. L. Kessler, "Use of image registration and fusion algorithms and techniques in radiotherapy: Report of the aapm radiation therapy committee task group no. 132," *Medical physics*, vol. 44, no. 7, pp. e43–e76, 2017.

[307] C. Su, J. Li, S. Zhang, J. Xing, W. Gao, and Q. Tian, "Pose-driven deep convolutional model for person re-identification," in *Proceedings of the IEEE International Conference on Computer Vision*, 2017, pp. 3960–3969.

[308] S. Vaishali, K. K. Rao, and G. S. Rao, "A review on noise reduction methods for brain mri images," in *2015 International Conference on Signal Processing and Communication Engineering Systems*. IEEE, 2015, pp. 363–365.

[309] G. Hou, H. Pan, R. Zhao, Z. Hao, and W. Liu, "Image segmentation via the continuous max-flow method based on chan-vese model," in *Chinese Conference on Image and Graphics Technologies*. Springer, 2017, pp. 232–242.

[310] X. Bresson, X.-C. Tai, T. F. Chan, and A. Szlam, "Multi-class transductive learning based on ℓ 1 relaxations of cheeger cut and mumford-shah-potts model," *Journal of mathematical imaging and vision*, vol. 49, no. 1, pp. 191–201, 2014.